

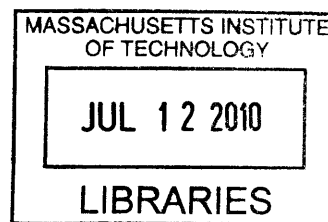
A Microfluidic Platform for the Genome-Wide Analysis of Electrical Phenotype: Physical Theories and Biological Applications

by

Michael D. Vahey

B. S. Electrical and Computer Engineering
Carnegie Mellon University, 2004

S. M. Electrical Engineering and Computer Science
Massachusetts Institute of Technology, 2006



ARCHIVES

SUBMITTED TO THE DEPARTMENT OF ELECTRICAL ENGINEERING AND COMPUTER SCIENCE IN PARTIAL FULFILLMENT OF THE REQUIREMENTS FOR THE DEGREE OF

DOCTOR OF PHILOSOPHY IN ELECTRICAL ENGINEERING AND COMPUTER SCIENCE
AT THE
MASSACHUSETTS INSTITUTE OF TECHNOLOGY


JUNE 2010

© MASSACHUSETTS INSTITUTE OF TECHNOLOGY, 2010
All rights reserved

Signature of Author

Department of Electrical Engineering and Computer Science
May 21, 2010

Certified by: _____


Joel Voldman
Associate Professor of Electrical Engineering and Computer Science
Thesis Supervisor

Accepted by: _____


Terry P. Orlando
Professor of Electrical Engineering and Computer Science
Chairman, Committee for Graduate Students

A Microfluidic Platform for the Genome-Wide Analysis of Electrical Phenotype: Physical Theories and Biological Applications

by

Michael D. Vahey

Submitted to the Department of Electrical Engineering and Computer Science in partial fulfillment of the requirements for the Degree of Doctor of Philosophy in Electrical Engineering and Computer Science

ABSTRACT

This thesis presents the development of a new microfluidic method for separating and characterizing cells based upon differences in their electrical properties. The objective of this work is to obtain a genome-wide mapping of genotype to electrical phenotype in the budding yeast *Saccharomyces cerevisiae*. Towards this end, we present: (1) the development of a novel equilibrium gradient separation method, called isodielectric separation (IDS); (2) the development of physical theories describing how interactions between particles effect microscale separations; and (3) the application of IDS to a screen for electrical phenotypes in the yeast deletion library.

Despite the variety of technologies available for cell sorting, a relative lack of *intrinsic* separation methods – those which separate cells according to their natural, unmodified characteristics - persists. To address this need, we have developed isodielectric separation. IDS separates cells according to differences in their intrinsic electrical properties. Using dielectrophoresis in a medium with spatially varying electrical conductivity, IDS drives cells to the locations where their polarization charges vanish, spatially resolving cells with different electrical properties. Our implementation of IDS offers label-free, continuous-flow separation, and is capable of resolving graded differences in electrical properties. Additionally, we demonstrate the ability to extract quantitative information from samples during separation, establishing IDS as an analytical technique as well as a preparative one.

Any platform for performing genetic screens must have high throughput. Although satisfying this requirement would be greatly facilitated by using high cell densities, physical interactions between cells under these conditions can affect the performance of devices used for screening. Although pervasive, interactions between cells or particles are challenging to describe quantitatively, especially in the confined environments typical of microfluidic devices. By studying the effects of electrostatic and hydrodynamic interactions between particles in a microfluidic device, we have found that ensembles of interacting particles exhibit emergent behaviors that we are able to predict through numerical simulations and a simple analytic model based on hydrodynamic coupling. Applying these theoretical tools to IDS and other microfluidic separation methods has provided insight into how particle interactions can profoundly influence separation performance in counterintuitive ways.

Having demonstrated the performance metrics necessary for a genetic screen, we apply IDS to the genome-wide analysis of electrical properties in the budding yeast *S. cerevisiae*. Although others have studied changes in electrical properties induced by drastic changes in gene expression (*e.g.* in differentiation) or by specific mutations in a small number of genes, a systematic and comprehensive analysis of the relationship between genotype and electrical phenotype has yet to be performed. Using IDS, we have screened the ~5000 strains in the yeast deletion collection for altered electrical phenotype. This work has identified a number of genes associated with distinct electrical properties, and, by analyzing known interactions and correlations between these genes, we have identified pathways and morphologies that appear to be primary determinants of electrical phenotype.

Thesis Supervisor: Joel Voldman

Title: Associate Professor of Electrical Engineering and Computer Science

Acknowledgements

The work presented in this thesis was made possible by remarkable people who I am tremendously grateful to know and to have worked with. My attempt to express this gratitude begins with my advisor, Professor Joel Voldman. Beyond the obvious technical expertise that he brings to the role of advisor, he has created and maintained a work environment that manages the difficult balance of being both stimulating and comfortable. The diversity of his interests, reflected by the projects and academic backgrounds of the group's members, has been a tremendous asset that I have happily tried to exploit over the years. I would also like to thank Joel for demonstrating the patience and trust to put up with some of my academic detours. Should I someday find myself with students of my own to advise, I hope to be able to transfer some of what I have learned about mentoring from Joel.

I have also been the beneficiary of a number of close collaborations over the years, with people from my lab as well as people from other labs, departments, and universities. Within the Voldman Lab, I have worked particularly closely with Dr. Salil Desai. It has been an honor to observe (and aspire to) Salil's ability to approach and dissect scientific challenges with insights and perspectives drawn from multiple disciplines. I hope that I might continue to benefit from his input in the years ahead. I am also grateful for the advice and assistance of Peter Svensson and Laia Quiros Pesudo, from Professor Leona Samson's laboratory. With patience and enthusiasm, Peter and Laia have provided considerable guidance (not to mention yeast strains) to an electrical engineer just beginning to appreciate the APYG. I'd also like to acknowledge Marco Carminati, Bob Barsotti, and Ryan Wartena, collaborators whose fresh perspective and enthusiasm for science and technology I respect and admire.

My colleagues in the Voldman lab deserve recognition, not only for their technical contributions and accomplishments, but also for putting up with me and keeping me sane over the past six years. In addition to Salil, whose personality I admire as much as his scientific ability and integrity, I would like to thank (deep breath) Katarina Blagovic, whose intellectual dexterity (from E&M to bioMEMS), love of the outdoors, and indefatigable work ethic and good humor are inspirational; Nitzan Gadish, who was a colleague for only one year out of six, but then proceeded to spend the remaining five as an incomparable friend and inspiration; Lily Kim, whose ability to pick fascinating hobbies, and whose insights on matters scientific and otherwise have been a big influence; Joseph Kovac, who has stretched my experiences as a graduate student further than they would have otherwise gone, and whose commitment to the eradication of "smoke and mirrors" was constantly refreshing; Nikhil Mittal, whose good nature and hospitality is exemplified by (among other things) his not objecting when I asked him for the thousandth time if anything exciting was going on today; Laralynne Przybyla, whose advice, sense of humor, and good taste in music helped me throughout; Somponnat Sampattavanich, whose tireless work ethic, enthusiasm, and intellectual curiosity I can genuinely call contagious; Brian Taff, a pioneer and founding father of the lab, who taught me how to be a graduate student; and Hasan Celiker, Melanie Hoehl, Hsu-Yi Lee, Katarzyna Puchala, Adam Rosenthal, Alison Skelley, Tao Sun, Yi-Chin Toh, and Wei Mong Tsang, each of whom I am honored to have gotten to know and to have worked with.

I am also indebted to a number of facilities and the outstanding faculty and staff that organize and run them. In particular, I wish to acknowledge the Microsystems Technology Laboratory and its outstanding staff, especially Dave Terry and Paul Tierney. On the biological side of things, I wish to acknowledge the MIT BioMicro Center, and Allison Perrotta and Kevin Thai in particular. Without the expertise of these individuals, much of the work in this thesis simply would not have been possible.

A final, special recognition belongs to my family – my father, David; my mother, Linda; and my brother Brian – who have sustained me throughout this and all other chapters of my life with infinite patience, grace, and kindness. I can never repay all that they have given me, and a few sentences will do nothing to change that; instead, I offer my deepest thanks for a lifetime of support and guidance.

TABLE OF CONTENTS

Commonly Used Symbols and Notations.....	12
Chapter 1: Background and Motivation.....	13
Introduction.....	13
Genetic Screens.....	13
Intrinsic Separations and Equilibrium Gradient Methods	15
Dielectrophoresis and the Electrical Properties of Cells.....	16
Isodielectric Separation as a Platform for Genome-wide Cell Analysis.....	20
Thesis Overview	22
Chapter 2: Device Modeling, Design, and Characterization	25
Models for Device Operation.....	25
Motivation.....	25
Mass Transport.....	25
Electric Fields.	27
Thermal Model.....	27
Electrohydrodynamic Flows.	28
Force Balance.....	29
Device Fabrication and Packaging.....	31
Device Characterization.....	32
Preparation of Cell and Bead Suspensions	32
Fluorescent Imaging, Data Acquisition and Processing.	32
Electrical Characterization of Cells.	32
Electrical Characterization of Beads.....	33
Calculating the Separation Resolution.....	33
Separation of Polystyrene Beads Based Upon Electrical Properties.	33
Separation of viable from non-viable <i>S. cerevisiae</i>	35
Discussion.	37
Electrically Addressable Giant Unilamellar Vesicles.....	38
Controlling and Characterizing the Size and Conductivities of GUVs.	38
Alternative Implementations of IDS.....	41
Conductivity Sources and Sinks.	42
Long-Range Dielectrophoresis.	43
Appendix to Chapter 2	47

Fabrication Process Flow.....	47
Chapter 3: Performing Analytical Separations	49
Introduction.....	49
Theory	51
Mass transport.....	52
Force Balance.....	52
Particle and cell heterogeneity	53
Influence of non-specific forces.....	54
Materials and Methods.....	55
Cell culture and bead preparation.....	55
Fluorescence Microscopy and Data Acquisition.....	55
Analysis of Results.....	56
Results.....	56
Particle Separation and characterization.....	56
Polystyrene Beads.....	56
Viable Yeast Cells.....	58
Heat Treated Yeast Cells.....	59
Discussion.....	61
Chapter 4: Particle interactions in microfluidic systems	63
Introduction.....	63
Results.....	64
Numerical Model.....	64
Microscopic Emergent Behavior.....	64
Macroscopic Emergence: Particle Concentration and Separation.....	65
Separating Particles.....	70
Interactions between non-spherical particles.....	73
Discussion.....	78
Materials and Methods.....	79
Device Fabrication, Packaging and Preparation.....	79
Particle characterization.....	79
Fluorescence imaging.....	80
Appendix to Chapter 4.....	81
Matlab Scripts.....	81
Chapter 5: Genome-wide electrical profiling in <i>Saccharomyces cerevisiae</i>	99

Introduction.....	99
Results.....	100
Selection of strains for the pilot screen.....	100
IDS analysis of strains with distinct crossover frequencies.....	102
Corroboration of pairwise results with pooled separations.....	103
The complete pooled deletion library: sampling strains in collection and sequencing.	104
The complete pooled deletion library: corroboration with the 83 strain pilot screen.	105
Sequencing results for the pooled deletion collection.	107
Discussion.....	108
Cell morphology and electrical phenotype.	108
Electrical Phenotype of the KRE9 DAmP Strain.	110
Candidate strains identified through barcode sequencing.	111
Categorization of candidate strains by morphology.	111
Categorization of candidate strains by biological function.....	111
Genetic interactions and electrical phenotype.	112
Materials and Methods.....	114
Measuring Crossover Frequencies.....	114
Pairwise Comparison of Strains Using IDS.....	114
Separations of the Pooled Pilot Screen Strains.....	115
Separations of the Pooled Deletion Collection.....	115
Analysis of Sequencing Results.....	116
Mapping Genetic Interactions to Electrical Phenotype.	116
Appendix to Chapter 5.....	118
DNA Extraction and Purification.....	120
Amplification of Strain Barcodes for Quantitative PCR.	120
Amplification of Strain Barcodes for Sequencing.....	121
Purification of PCR Product for Sequencing.....	122
Electrically Distinct Strains Identified from Barcode Sequencing.....	123
Classification of Strains by Morphology.....	127
Classification of Strains by Biological Function.....	128
Chapter 6: Contributions and Future Directions.....	129
Contributions.....	129
Design rules for isodielectric separation.....	129
Demonstration of important figures of merit.....	129

Combining analytical and preparative separations using IDS.	129
Tools for understanding particle interactions in microfluidic devices.....	129
Identification of yeast strains exhibiting distinct electrical phenotypes.	130
Electrogenomic profiling with IDS.....	130
Future Directions	130
Bibliography	137

TABLE OF FIGURES

Chapter 1

Figure 1- 1: General approaches to genetic screening	14
Figure 1- 2: Equilibrium gradient separations	15
Figure 1- 3: Polarization of a particle in an external electric field	17
Figure 1- 4: Electrical properties of cells and the dielectric spectrum	17
Figure 1- 5: Sensitivity of different regions of the dielectric spectrum of a yeast cell to variations in different lumped parameters.	19
Figure 1- 6: Concept and implementation of IDS.	21

Chapter 2

Figure 2- 1: Coordinate systems used in modeling different aspects of the device.....	25
Figure 2- 2: Modeling fields, forces and flows.....	29
Figure 2- 3: Design curves for IDS devices targeting different types of particles.	31
Figure 2- 4: Simultaneous separation of three types of polystyrene beads based upon differences in surface conductance.....	34
Figure 2- 5: Separation of polystyrene beads based upon differences in surface conductivity in the presence or absence of modification with charged carboxyl groups	35
Figure 2- 6: Live/dead separations of <i>S. cerevisiae</i>	36
Figure 2- 7: Biasing GUV size.....	38
Figure 2- 8: Controlling the dielectric spectra of GUVs.....	40
Figure 2- 9: Performing separations using positive dielectrophoresis.....	42
Figure 2- 10: Using conductivity sources and sinks to create a conductivity gradient.....	43
Figure 2- 11: Long-range, reconfigurable dielectrophoresis..	45
Figure 2- 12: Focusing particles and cells by superposing signals of different frequencies	46

Chapter 3

Figure 3- 1: Analytical separations using IDS.....	50
Figure 3- 2: Modeling and interpreting the distribution of particle trajectories	54
Figure 3- 3: Analytical separations of polystyrene beads.....	58
Figure 3- 4: Analytical separations of viable and heat-treated yeast.....	60
Figure 3- 5: Analytical separations of mammalian cells	61

Chapter 4

Figure 4- 1: Emergent behavior of particle suspensions subjected to electric and hydrodynamic fields.....	65
Figure 4- 2: Particle trapping landscape as a function of concentration and applied force	67
Figure 4- 3: Comparison of numerical trapping curves with the sigmoidal approximation.....	68
Figure 4- 4: Particle concentration and hydrodynamic cooperativity.....	70
Figure 4- 5: Comparison of the hydrodynamic cooperativity model to experimental results for separation.....	71
Figure 4- 6: Leveraging dynamic operating conditions to improve separation performance.....	72
Figure 4- 7: Dissociation of particle aggregates under dynamic operating conditions.....	73
Figure 4- 8: Interactions between non-spherical particles	75
Figure 4- 9: Dielectrophoretic field flow fractionation (DEP-FFF).	75
Figure 4- 10: Simulations of DEP-FFF using different numbers of particles.....	76
Figure 4- 11: Polarizability based separation.....	77
Figure 4- 12: Simulations of polarizability-based separations using different numbers of particles.....	78

Chapter 5

Figure 5- 1: Crossover frequency measurements for the strains used in the pilot screen..... 101

Figure 5- 2: Pairwise comparisons of deletion/DAmP strains to wildtype using IDS..... 102

Figure 5- 3: Quantifying the abundance of different deletion strains in an 83-strain pool sorted using IDS 103

Figure 5- 4: Quantifying the abundance of specific barcodes using PCR..... 106

Figure 5- 5: Quantitative PCR results for a separation of the complete deletion pool 106

Figure 5- 6: Enrichment of deletion strains across four sorted fractions relative to the original unsorted pool..... 107

Figure 5- 7: Cell shape and the dielectric spectra 110

Figure 5- 8: Pairwise comparisons between wildtype and KRE9 DAmP strains 110

Figure 5- 9: Illustration of a subnetwork of interactions among genes whose deletion confers increased electrical conductivity..... 112

Figure 5- 10: PCR products from barcode-specific primers run on a 1.5% agarose gel 121

Figure 5- 11: UV shadowing of a polyacrylamide gel..... 122

Chapter 6

Figure 6- 1: Particle interactions across the dielectrophoretic spectrum..... 131

Figure 6- 2: Improving separation through the use of carrier particles 132

Figure 6- 3: Automated control system for IDS 134

Commonly Used Symbols and Notations

General Notation	
n	Scalar field or constant
\mathbf{n}	Vector or tensor field
\tilde{n}	Dimensionless variable
\underline{n}	Complex variable

Scalar Fields	
φ	Electric Potential
T	Temperature
ρ	Charge Density
p	Probability Density
c	Concentration

Vector Fields	
\mathbf{F}	Imposed Force
\mathbf{f}	Interaction force
\mathbf{p}	Dipole Moment
\mathbf{E}	Electric Field
\mathbf{u}	Fluid Velocity

Material Properties / Physical Attributes	
ε	Electrical Permittivity
σ	Electrical Conductivity
κ	Thermal Conductivity
D	Diffusivity
μ	Viscosity
K_S	Surface Conductance
a	Cell or Particle Radius
K	Electrical Polarizability
ϕ	Volume fraction

Geometric / Operational Constants	
w	Channel Width
h	Channel Height
ℓ	Channel Length
d	Electrode Spacing
θ	Electrode Angle
ω	Angular Frequency
U_0	Average Fluid Velocity
Q_0	Volumetric Flow Rate
V_0	Voltage (zero-to-peak)

Chapter 1: Background and Motivation

Introduction

As the ability to address biological questions at a genome-wide scale has become increasingly available, a tremendous opportunity to better understand the genetic basis for the physical and biochemical properties of cells has arisen. This thesis presents the development, analysis, and demonstration of a new method for separating and characterizing cells based upon differences in their electrical properties.

Electrical properties - in particular, conductivity and permittivity - are intrinsic to the structure and composition of a cell, and encode biophysical information relevant to the cell's state: its electrical phenotype. A better understanding of the mapping between genotype and electrical phenotype offers advantages to both pure and applied biology. For the pure biologist, the ability to screen cells for altered physical properties - and to quantify the extent to which these properties have been altered - could provide more detailed information than functional studies alone. For the biotechnologist, understanding the genetic basis of electrical properties could lead to the systematic development of assays for isolating cells of particular scientific or commercial interest.

To realize these goals, a number of requirements must be satisfied. First, the technology used to screen for electrically distinct cells must exhibit *high specificity*; for example, properties such as cell volume which vary considerably as a cell grows and divides can obscure the genetic basis for electrical properties. Accordingly, a primary goal in the development of our screening platform is insensitivity to cell volume. Second, the screening method should exhibit *high resolution* and dynamic range, so that a library of cells can be finely categorized and strong outliers easily identified. Finally, a third stringent requirement imposed by the need to screen large libraries of cells is *high throughput*; the screening technology must be capable of handling biologically relevant numbers of cells ($>10^6$) in a reasonable amount of time (on the order of a few hours).

In the following chapter, we will describe the separation method we have developed for screening electrical phenotypes, called isodielectric separation (IDS), and place it in the context of other screening and separation technologies. In addition, we will discuss the general basis and significance of the electrical properties of cells, and how they can be used as a basis for cell sorting. Next, we will address our efforts to satisfy the three screening requirements - specificity, resolution, and throughput - outlined above. These themes will be returned to and elaborated on throughout subsequent chapters in an effort to describe the physical basis of IDS - and, more generally, of microfluidic separations of concentrated suspensions - and its application to cell characterization and the genome-wide analysis of a cell library.

Genetic Screens

Extracting information from large numbers of cells typically requires the ability to identify and study the small fraction of those cells which exhibit a property of interest. Genetic or phenotypic screens illustrate some of the potential difficulties in this process². Since studying the cells targeted in such a screen typically requires that they be physically isolated, one way to categorize genetic screens is by whether cells are screened individually and remain isolated throughout, or screened as a pool and isolated afterwards. For the case where cells are screened individually, cells subjected to different genetic or environmental perturbations are grown in isolation; for example, each well across multiple plates could contain a distinct strain or cell line, and the fate of these cells in an altered environmental condition could be studied and related back to the genetic perturbation that gave rise to that outcome (Figure 1- 1, left). Alternatively, the cell line could be identical in each well, and the environmental perturbation varied. In either case, this approach has the obvious advantage of greatly simplifying the process of identifying cell types or perturbations associated with a certain outcome, since each well is uniquely associated with a particular strain or condition. However, working with large numbers of strains requires an equally large

number of isolated wells. For example, libraries of relatively modest size in the budding yeast *Saccharomyces cerevisiae* consist of strains numbering in the thousands^{3,4}, and libraries for RNA interference (RNAi) in mammalian cells can number in the tens of thousands⁵. While screening libraries of this size in separate cultures is possible using robotics or by sequentially isolating smaller subpopulations of the total library, in the case of prohibitively large collections of cells, such as those produced by randomized methods^{6,7}, other approaches are necessary.

Pooled screens and selections offer an alternative to screening cells individually.

Here, all cells are subjected to a common set of conditions and those of interest are then, by some means, physically isolated from the background for further analysis. In the case of selection, the means of isolation is competitive growth; cells exhibiting a higher level of fitness under the given conditions will grow to dominate the culture over time, performing the task of isolation automatically (Figure 1- 1, center). This approach has been applied, for example, to determine *S. cerevisiae* genes essential for optimal growth under several stress-inducing environmental conditions³. Of course, some phenotypes are not associated directly with growth and thus are not easily amenable to selection. In these cases, screening is necessary and requires an external mechanism to physically sort the cells of interest (Figure 1- 1, right). One common approach to this challenge employs a technique known as fluorescence activated cells sorting (FACS). FACS leverages fluorescent labeling to interrogate cells as they serially flow past a laser coupled to an optical sensor. Cells exhibiting fluorescent emission at the targeted frequency and intensity are then directed to a separate outlet for collection. The fluorescent label may be either introduced to the cell externally (as in antibody staining) or genetically programmed into the cell (as in GFP-tagged proteins, which themselves may be expressed constitutively or only in response to particular environmental cues), enabling the use of FACS in a wide variety of assays. FACS offers the further advantages of sorting as many as $\sim 10^4$ cells per second at purities limited primarily by the specificity and uniformity of the fluorescent label, and its amenability to multiplexing⁸. These capabilities have established FACS as an important technique at the center of a wide variety of assays and screens.

Despite its advantages, however, there remain a number of applications for which FACS is not ideally suited. For example, bacteria and other small cells - for which the fluorescent signal integrated over the cell volume is typically weaker than for larger eukaryotic cells - are difficult to sort using FACS, and the development of a fluorescent label for a new assay may be a time- and resource-intensive process. Although other technologies exist for marker-specific separations that can be applied to smaller cells, including magnetically-activated cell sorting (MACS)⁹, these techniques share with FACS the fundamental reliance on cell labeling.

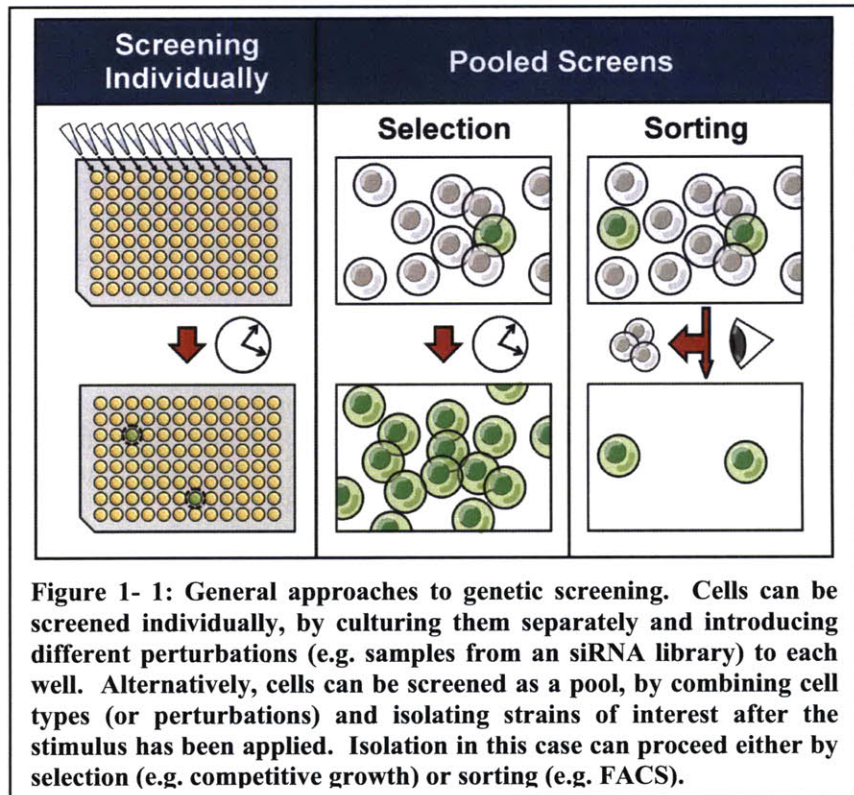


Figure 1- 1: General approaches to genetic screening. Cells can be screened individually, by culturing them separately and introducing different perturbations (e.g. samples from an siRNA library) to each well. Alternatively, cells can be screened as a pool, by combining cell types (or perturbations) and isolating strains of interest after the stimulus has been applied. Isolation in this case can proceed either by selection (e.g. competitive growth) or sorting (e.g. FACS).

In between the automatic isolation achieved by selection and the marker-specific (and potentially labor-intensive) isolation enabled by FACS or MACS, there are relatively few means of separating cells with the specificity, resolution, and throughput appropriate for a genetic screen. To circumvent the need for cell labeling, *intrinsic* separation methods are necessary.

Intrinsic Separations and Equilibrium Gradient Methods

Intrinsic separation methods – those which sort cells or particles according to their unperturbed physical properties – circumvent some of the limitations of marker-specific separation methods by removing the need for labeling altogether. In the context of cell sorting, the wide variety of physical properties available for separations – including size¹⁰, shape^{11,12}, density¹³, acoustic compressibility¹⁴, electrical charge¹⁵, permittivity¹⁶ and conductivity¹⁷ – cover a wealth of different phenotypes and increase the likelihood that some technique is applicable to a particular assay. By acting upon the naturally occurring properties of the cells, intrinsic separation methods not only remove the need to label cells, but they also enable analytic separations, in which the property being selected for is quantified concurrent with the separation.

A subset of intrinsic separations is collectively known as equilibrium gradient methods. Equilibrium gradient separation refers to a class of separation techniques that segregate molecules or cells to a position in a force field where the net force on the object is zero, and where the zero-force position is stable^{18,19} (Figure 1- 2). Two common examples are density-gradient centrifugation (DGC)¹³ and iso-electric focusing (IEF)²⁰.

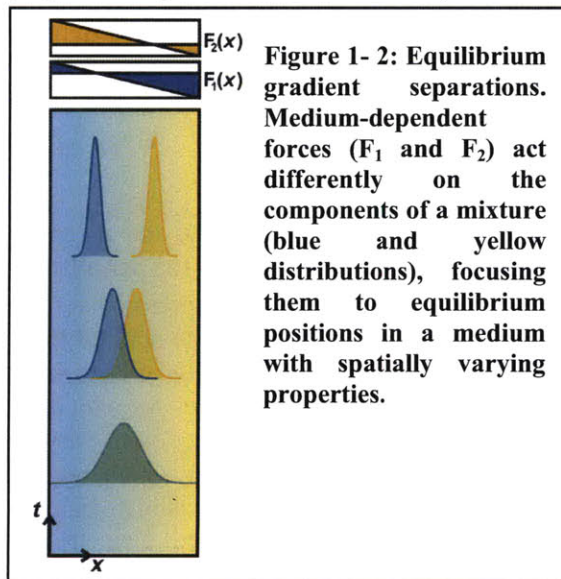


Figure 1- 2: Equilibrium gradient separations. Medium-dependent forces (F_1 and F_2) act differently on the components of a mixture (blue and yellow distributions), focusing them to equilibrium positions in a medium with spatially varying properties.

In DGC, the objects to be separated (e.g., cellular organelles) are placed in a centrifugal force field in the presence of a spatial density gradient. Different objects migrate to the position in the separation vessel (e.g., tube) where their density is equal to the surrounding density. In IEF, the force is instead the Coulomb force on a charged molecule, and the objects (e.g., proteins) are placed in a pH gradient. The Coulomb force directs them to their iso-electric point, where their charge (and hence net force) goes to zero. The common characteristic of both DGC and IEF is the guidance of particles by a force field to stable equilibrium positions; when the objects are in a region where the pH or density is lower than the object's equilibrium point, they will feel a net force toward higher pH or density, while if they are in a region of relatively high pH or density, they will feel a force in the opposite direction.

One of the primary advantages of equilibrium gradient methods is that the analytes – cells, particles, or molecules – are resolved into a continuous spatial distribution according to their properties. While marker specific separations, especially MACS, are often predicated on a binary decision – either a cell exhibits the label or it does not – equilibrium methods enable separations based upon continuous variations in the targeted property. This not only increases the capacity of the separation, but may also reduce the need for sample preparation, since contaminating particles can be resolved from the target particles more easily than in a binary separation.

Although equilibrium methods are not strictly constrained to sort cells by intrinsic properties, an important advantage results when the two classes of techniques are combined; because the separation is based upon the native physical properties of the cell, and because the cells are sorted into a continuum of physical locations determined by these properties, it is possible to extract direct quantitative information regarding the cells' physical states. This capability establishes a separation method as being *analytic*,

where the objective is to characterize the components of a mixture, as opposed to *preparative*, where the objective is to fractionate a sample (commonly in large volumes) for collection and subsequent use ²¹. Because equilibrium methods may be both preparative and analytic, they have the potential to be more versatile than other approaches to separation. The objective of this thesis is to leverage the advantages inherent in equilibrium separations to develop a new method for sorting cells based upon their electrical polarizability.

Dielectrophoresis and the Electrical Properties of Cells

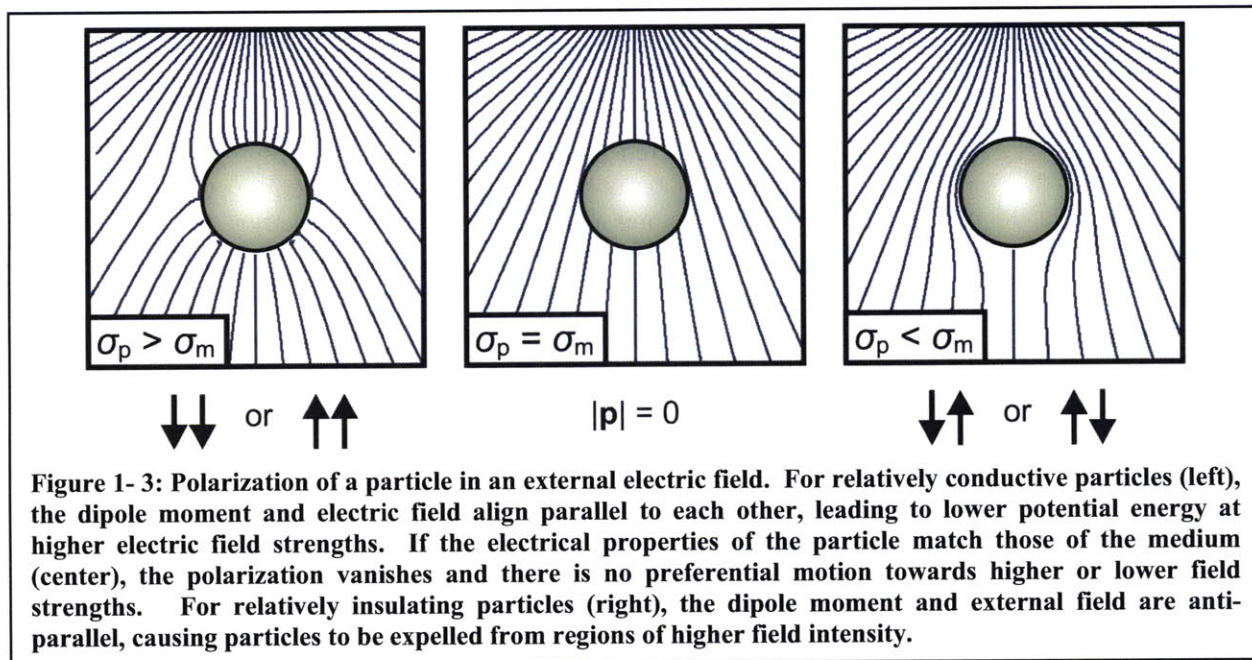
In an external electric field, polarization charge induced at the interface of a particle and the surrounding medium induces a dipole moment aligned either parallel or anti-parallel to the applied field (Figure 1- 3) ²². The orientation of the induced dipole with respect to the field depends upon the electrical properties of the particle and medium, and determines the direction of the translational force acting on the particle. For the case of a lossless particle and medium, this dielectrophoretic (DEP) force is conservative and may be expressed in terms of the potential energy of a dipole with moment \mathbf{p} in an electric field \mathbf{E} :

$$\mathbf{F} = -\nabla U = \mathbf{p} \cdot \nabla \mathbf{E} \quad (1- 1)$$

The force acts to minimize the energy of the system; if the moment and field are anti-parallel ($\mathbf{p} \cdot \mathbf{E} = -|\mathbf{p}||\mathbf{E}|$), the particle is pushed in the direction of decreasing field intensity, whereas a parallel moment and field ($\mathbf{p} \cdot \mathbf{E} = |\mathbf{p}||\mathbf{E}|$) results in the particle being pulled in the direction of increasing field intensity. Although Eq. 1 derives from a conservative system in which the particle and medium are purely dielectric (i.e. there is no energy dissipation from conduction), it also applies to lossy systems, provided that the induced dipole moment is appropriately defined as ²³:

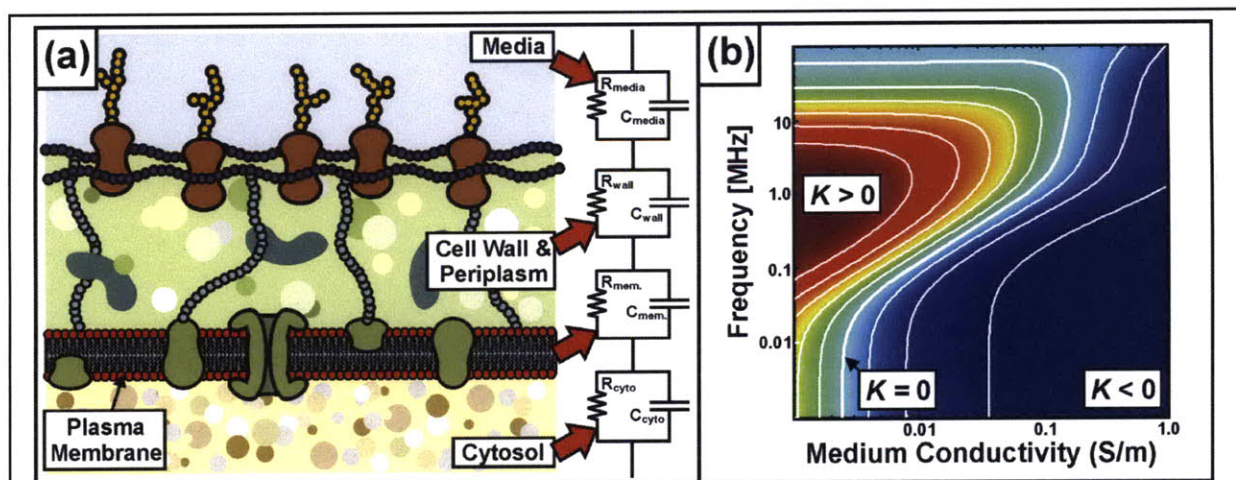
$$\mathbf{p} = 4\pi\alpha^3 \varepsilon_m K \mathbf{E} \quad \text{where} \quad K = \text{Re} \left\{ \frac{\underline{\sigma}_p - \underline{\sigma}_m}{\underline{\sigma}_p + 2\underline{\sigma}_m} \right\} \quad (1- 2)$$

Here, $\underline{\sigma}_p$ and $\underline{\sigma}_m$ denote the complex conductivity of the particle and medium, respectively, and are given by $\underline{\sigma}_{p,m} = \sigma_{p,m} + i\omega\varepsilon_{p,m}$, where $\sigma_{p,m}$ is the conductivity of the particle or medium, $\varepsilon_{p,m}$ is the permittivity of the particle or medium, and ω is the frequency of the applied electric field. This expression for the induced polarization of a particle may exhibit a strong dependence on the frequency of the applied field. For example, in the case of a layered particle, the thickness, conductivity, and permittivity of each layer determine the particle's complex conductivity. This gives rise to the possibility of particles for which the sign of the polarizability (and thus the direction of the DEP force acting on it) alternates with varying frequency. These particles are characterized by one or more crossover frequencies, at which the net polarization vanishes. The information contained in a cell's frequency-dependent polarizability enables the dielectric spectrum to serve as an effective means of probing a cell's structure. Indeed, dielectric, or impedance, spectroscopy has been widely used as a means of characterizing populations of cells and particles ^{24,25}.



The dielectric spectrum of a cell depends on its structure and composition in a complicated manner. This is simplified greatly by approximating the cell cytoplasm, membrane and wall (where applicable) as consisting of uniform, homogeneous media with well-defined conductivity and permittivity²³ (Figure 1-4a). One way to effectively homogenize a heterogeneous layered particle is through the Maxwell-Garnett mixing formula. For spherical inclusions (or layered particles comprised of concentric spheres), this has the form:

$$\underline{\sigma}'_n = \underline{\sigma}_n \left[\frac{1 + 2\phi_{n-1,n} \underline{K}_{n-1,n}}{1 - \phi_{n-1,n} \underline{K}_{n-1,n}} \right] \quad (1-3)$$



Here, $\phi_{n-1,n}$ represents the volume fraction of component $n-1$ (the inclusion) within component n , and $\underline{K}_{n-1,n}$ is defined as in equation (1- 2), taking the inclusion to be the particle, and component n to be the medium in which it is dispersed (with complex conductivity $\underline{\sigma}_n$ in this case). For concentric spheres with an inner radius a and an outer radius $a+\delta$, the volume fraction becomes $[a/(a+\delta)]^3$, and the familiar equation for the effective conductivity of a layered particle is recovered. Applying equation (1- 3) iteratively from the innermost layer to the outermost layer gives the effective conductivity of a heterogeneous cell. Substituting this into the expression for polarizability (equation (1- 2)) gives the dielectric spectrum of the cell. Figure 1- 4b gives the spectrum for a yeast cell as a function of medium conductivity and electric field frequency, using typical parameter values from the literature^{26,27}.

Underlying the form of a cell's dielectric spectrum are the material properties of its constitutive layers, which in turn depend on structure and composition. The electrical conductivity of a solution (e.g. a simple model for the cytosol) is determined by the concentration (c), valence charge (z), and mobility (u) of each solute present, according to:

$$\sigma \equiv F \sum_i z_i^2 u_i c_i \quad (1- 4)$$

Here, F denotes the Faraday constant (≈ 96485 C/mol), and the sum is over all ionic species present. In a cell's cytoplasm, this includes small ions (~ 400 mM) and macromolecules such as protein (~ 0.1 - 1 mM), RNA and DNA, in addition to charged carbohydrates, amino acids, and high energy phosphates²⁸. Despite the diversity of contributors to the cytoplasmic conductivity, the dominant contribution likely arises from small ions present at high concentrations and low valence throughout the cytoplasm^a. Accordingly, we do not expect translational levels of a particular protein or transcriptional levels of a particular RNA to be directly detectable as a change in a cell's electrical properties. Nonetheless, proteins (as well as mRNA) may contribute *indirectly* to a cell's conductivity; one possible example of this is relevant for microorganisms with a cell wall. Here, high concentrations of fixed, negatively-charged, glycoproteins can enhance the concentration of positive counterions in the porous crosslinked structure of the wall, increasing its conductivity.

^a In addition to small ions, macromolecules (mostly negatively charged), present at low concentrations but with relatively large valence charge, may also contribute. These include DNA, RNA, and proteins; of these, DNA may be considered largely immobile ($u \sim 0$), while RNA occurs at very low concentrations ($\sim \mu$ M). Proteins are composed from 20 amino acids, of which two are negatively charged (glutamate and aspartate) and two are positively charged (arginine and lysine); assuming equal representation of amino acids on average, each residue in a protein has a 10% chance of being positive and a 10% chance of being negative (i.e. $p(z = 1) = 0.1$, $p(z = -1) = 0.1$), giving a variance in z of 0.2 for a single residue. If a protein contains N amino acids, its valence will then scale as $|z| \sim \sqrt{0.2N}$, or ~ 8 for $N = 300$. Since proteins are far less abundant than small ions and typically have a considerably lower mobility (by up to $\sim 100\times$), an increase in valence charge of order 10 is not sufficient to match the contribution of small ions to the overall cytoplasmic conductivity.

An important conclusion of this is that electrical conductivity is *sensitive* to a variety of parameters at the molecular level, but, as a consequence, is *specific* to none of them. Accordingly, it is most convenient to define a cell's electrical phenotype in terms of more general, macroscopic quantities, such as the conductivity or permittivity of the cell wall, cell membrane, or cytoplasm. Figure 1- 5 illustrates how different regions of a cell's dielectric spectrum, calculated for a cell comprised of cytoplasm, a cell membrane, and a cell wall using equation (1- 2), are sensitive to these parameters. By varying the frequency of the interrogating electric field or the conductivity of the medium in which the cell is suspended, it is possible to address some cell layers independent of others; for example, high frequencies and medium conductivities provide sensitivity to cytoplasmic conductivity and permittivity, whereas lower frequencies and conductivities can be used to probe the external layers of a cell. Thus although polarizability does not generally provide molecular specificity, it does afford some specificity with regard to broader macroscopic properties.

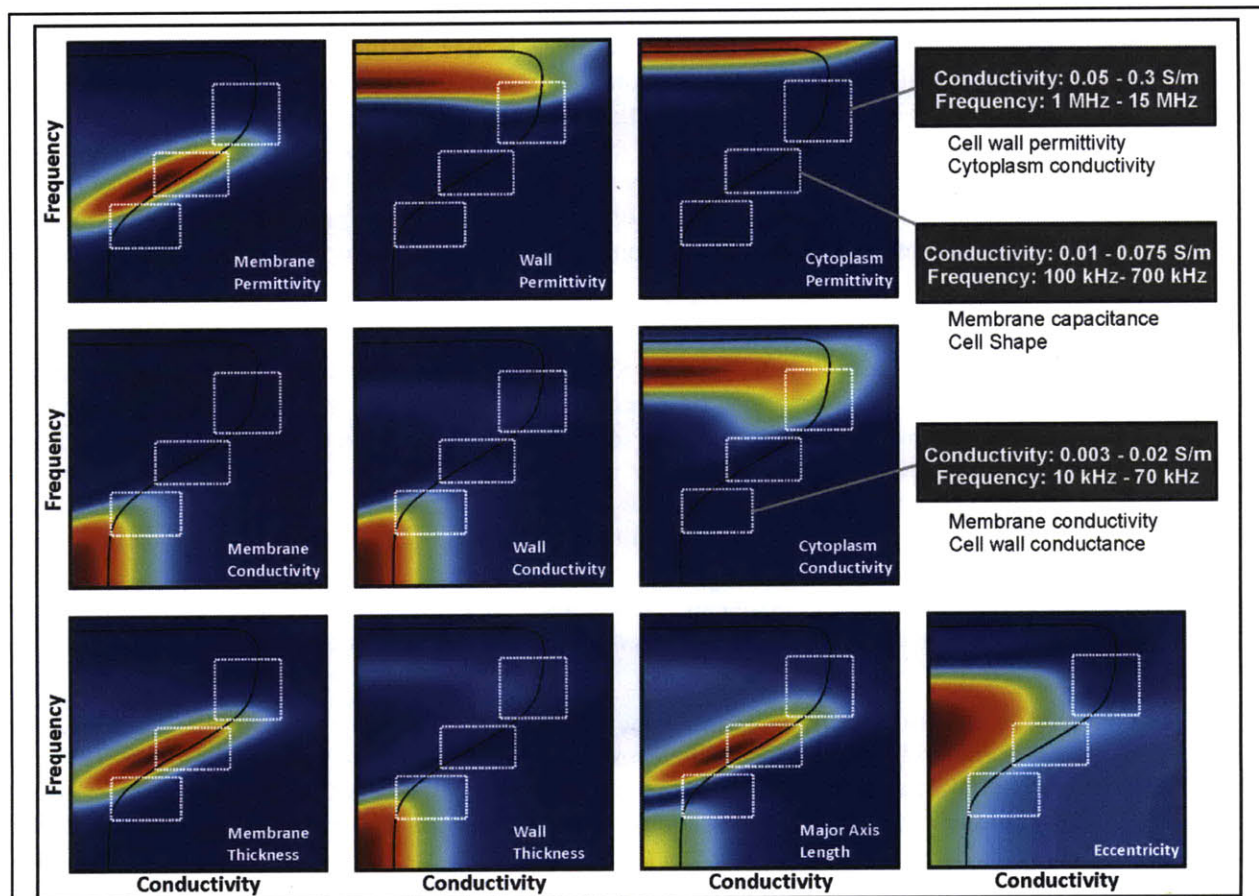


Figure 1- 5: Sensitivity of different regions of the dielectric spectrum of a yeast cell to variations in different lumped parameters. Each panel shows the magnitude of the partial derivative of the cell's polarizability (defined according to equation (1- 2)) taken with respect to one physical characteristic. By operating at low-to-intermediate frequencies and conductivities, it is possible to probe external cell structure (i.e. the wall and membrane). Alternatively, operating at higher conductivities and frequencies increases sensitivity to cytoplasmic properties. In addition to being able to tune sensitivity to different cell layers, it is also possible to tune sensitivity to cell shape (i.e. the eccentricity or major axis length).

Isodielectric Separation as a Platform for Genome-wide Cell Analysis

The ability of differences in gene expression to alter a cell's electrical properties is dramatically illustrated by the significant differences in dielectric spectra observed for genetically identical cells that have differentiated²⁹, or which have become cancerous³⁰. However, in these cases, changes in gene expression are drastic, making it difficult to systematically understand the mechanisms by which the cell's physical properties are altered. At the opposite extreme, other researchers have studied how specific mutations affecting a single gene alter electrical properties^{26,31}; however, these studies have largely been limited to a small number of cases involving one or a few genes. Accordingly, the question of how genetic differences in a single gene may affect electrical properties has not been comprehensively addressed at a genome-wide scale. To address this question, we have developed a new separation method to satisfy the requirements for performing a genetic screen.

The foundation of our method is the ability to use cell polarization in an electric fields to both interrogate the properties of those cell, as well as to actuate them, using dielectrophoresis. This ability to simultaneously interrogate and position cells and particles is one of the more attractive features of electrical methods for separation and characterization. Unlike methods in which interrogation must be coupled to downstream separation (e.g. FACS), DEP essentially combines the two steps, leading to potentially faster screens that are further simplified by not requiring cell labeling. We have leveraged these advantages of electrical methods and the ability to position particles in different locations according to differences in their electrical properties by developing a new separation and characterization method called iso-dielectric separation (IDS). In IDS, cells and particles are dielectrophoretically concentrated to the regions in an electrical conductivity gradient where their polarization charge and the resulting DEP force vanishes.

Figure 1- 6 illustrates the concept of IDS. We create a monotonic gradient in electrical conductivity across the width of a microfluidic channel by injecting one solution of relatively high conductivity containing the cell mixture and a second solution of relatively low conductivity into a device with a diffusive mixer (Figure 1- 6a, top left). This mixer generates a smooth monotonic conductivity profile that flows directly into a channel containing electrodes arranged across the diagonal (Figure 1- 6a, bottom left). These electrodes guide the cells in the direction of decreasing medium conductivity – a one-sided approach to equilibrium – until the DEP force becomes sufficiently small that it is overwhelmed by hydrodynamic drag and the barrier is breached. The cells then continue downstream unobstructed for collection. Sampling cells from different portions along the channel width thus segregates cells according to their electrical properties.

In the past decade, several groups have developed noteworthy devices for using DEP to sort large numbers of cells. A method referred to as Dielectrophoretically Activated Cell Sorting (DACS) was recently developed at UC Santa Barbara³², in which cells presenting specific surface proteins were conjugated to polystyrene beads coated with complementary proteins. The strong polarization of the beads relative to the freely suspended cells then served as a handle by which cells could be isolated via DEP according to their surface markers. Although this technique achieves high throughput and specificity, it requires the use of labels (i.e. antibody-coated polystyrene beads) and is an essentially binary method – cells either express the surface marker at some threshold level and are isolated, or they do not. Accordingly, it is not possible to use DACS to directly quantify the level of expression of individual cells.

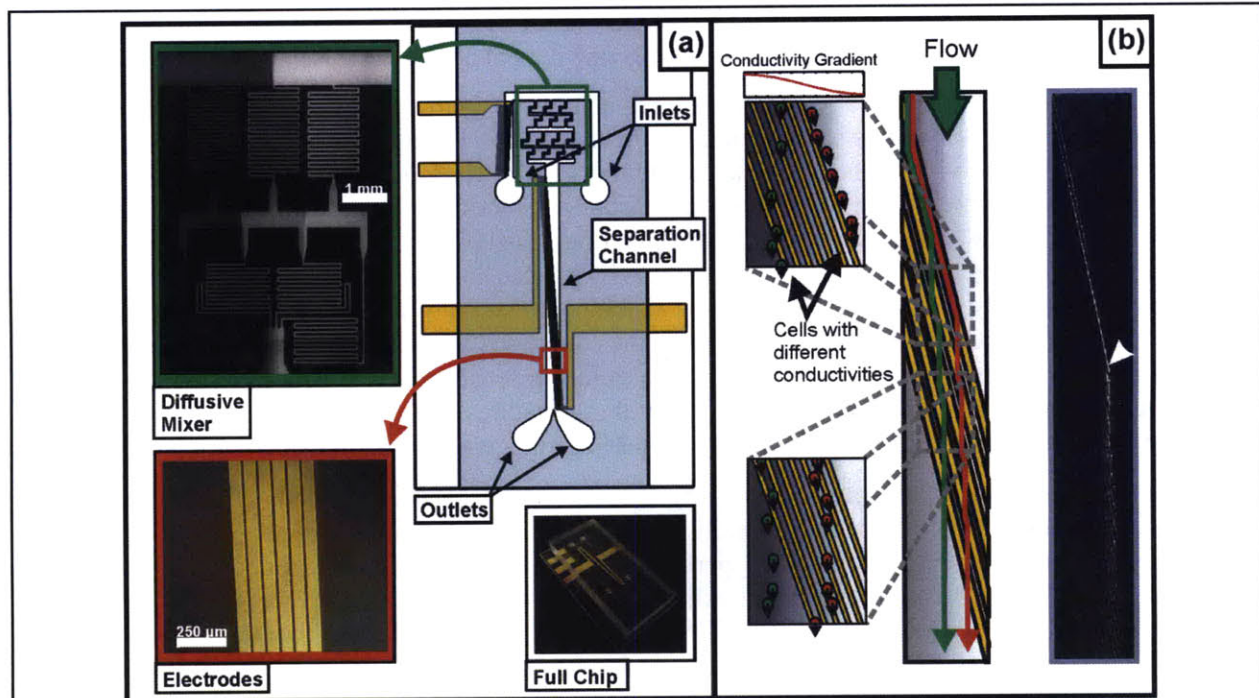


Figure 1- 6: Concept and implementation of IDS. (a) Layout of the device, consisting of two inlets, a diffusive mixer to establish the electrical conductivity gradient, and a separation channel, along which diagonal pairs of electrodes are arranged. (b) Operation of the device: cells are carried by flow to electrodes across the channel diagonal. The DEP force resolves with hydrodynamic drag to direct the particle across the width of the channel, in the direction of decreasing conductivity and thus towards the iso-dielectric point (IDP). To the right is a fluorescence micrograph of polystyrene beads deflected by the electrodes prior to reaching their IDP (arrow).

An alternate approach to DEP separations – 3D insulative DEP³³ – uses geometric constrictions to create gradients in an electric field applied along the axis of a microfluidic channel. By shaping these constrictions appropriately, it is possible to create a force gradient across the width of the channel, so that particles with different polarizabilities traverse different distances along the channel’s width. Because the force gradient is continuous and separation occurs perpendicular to the direction of flow, this approach is able to perform analog separations of cells and particles under continuous flow. However, because separation is determined by the magnitude of particle polarizability, it is highly sensitive to particle size and thus limited to applications in which either the particles are uniformly sized, or size is the property being selected for. An additional limitation of insulative DEP is its restriction to low frequencies; this is a consequence of the large electric potentials ($\sim 10^3$ V) needed to create strong electric fields across large distances ($\sim 10^{-2}$ m), and constrains the use of this approach to applications involving the external structure of the cell, as illustrated by Figure 1- 5.

Yet another technique developed to sort cells is dielectrophoretic field flow fractionation (DEP-FFF)^{34,35}. Here, a plug of cells is injected into a channel with an array of interdigitated electrodes along the bottom. When an electric field is applied in the absence of any flow, the cells levitate to equilibrium heights determined by the balance between the uniform downward gravitational force and the upward DEP force (which decays away from the electrodes). When a pressure gradient is applied along the channel, a parabolic velocity profile is created in the fluid, which carries cells with different equilibrium heights to the outlet at different rates. Separation is then achieved by timing the collection of samples from the outlet according to the elution times of the targeted cells. Because both gravitational and DEP forces are volumetric, this dependence is canceled out in determining the equilibrium height, and DEP-FFF

has the attractive feature of being insensitive to the size of the cell or particle; however, because it is an inherently batch mode separation method, sorting cells one plug at a time, its throughput is limited.

With IDS, our goal is to leverage the advantages of these existing approaches while avoiding their specific limitations. This amounts to developing a method that is label-free, operates under continuous-flow, is capable of resolving cells across a continuum of electrical differences, and is insensitive to variations in cell size which often overwhelm more subtle, genetically induced differences in electrical properties. While the first three features (label-free, continuous-flow, and high-resolution) follow directly from the implementation we have outlined, insensitivity to size follows from the nature of equilibrium separations. Specifically, although the magnitude of the polarization of a cell (and thus the magnitude of the dielectrophoretic force) depends on cell volume, the conditions under which polarizability vanishes do not. As a result, separations based upon a cell or particle's approach to these equilibrium conditions are not strongly dependent on cell volume. Combining these features of IDS provides a platform with the specificity, resolution, and throughput necessary for performing genetic screens.

In addition to the specific limitations that apply to each of the separation methods discussed earlier, all microfluidic technologies have been generally constrained by an incomplete understanding of how interactions between particles affect their performance. This is particularly important when high-throughput - and thus high concentrations of cells - are necessary, as in a genetic screen. Accordingly, a critical component of understanding how IDS operates at high cell concentrations has been the development of analytical and numerical tools to understand how colloidal particles interact when they are subjected to electric and hydrodynamic fields. These tools and their experimental validation therefore comprise an additional focus of this thesis.

Thesis Overview

The work described in this thesis builds off of work described in the author's Masters Thesis³⁶. This prior work focused primarily on the design of the device, culminating in an initial proof of concept for IDS. In the present document, we have attempted to minimize duplication of material, placing the emphasis on reducing the device to practice and developing a more rigorous understanding of its operation. This emphasis can be broadly categorized into four specific aims:

1. Designing, fabricating and characterizing an isodielectric separation device.
2. Demonstrating the broad applicability of IDS as an analytical technique by characterizing a variety of cell types and particles.
3. Developing analytical and numerical tools for understanding particle interactions in microfluidic devices, and validating these tools experimentally.
4. Demonstrating the feasibility of performing genetic screens using IDS by searching for electrically distinct phenotypes in the *Saccharomyces cerevisiae* gene deletion library.

Each of these four aims comprises a chapter in the body of this thesis. In Chapter 2, we discuss the fundamental considerations underlying device design and operation, and how they determine separation performance. Chapter 2 also contains proof-of-concept demonstrations for IDS, and discusses the development and characterization of giant unilamellar vesicles as new dielectrophoretic metrology tools. The chapter then concludes with an analysis of alternative implementations of IDS.

Chapter 3 extends the work presented in Chapter 2 to demonstrate IDS as an analytical separation technique, capable of simultaneously sorting and characterizing suspensions of cells and particles. To specifically demonstrate the broad applicability of IDS, this chapter describes the characterization of cells and particles spanning three orders of magnitude in volume and conductivity.

We proceed in Chapter 4 to explore more generally the operation of microfluidic devices at high particle concentrations, through the development of analytical and numerical models combined with experiments. Specifically, this chapter discusses how local interaction rules involving only a few

particles propagate to larger scales, affecting the performance of devices designed to sort and concentrate cells. Chapter 4 concludes with a case study illustrating the implications of our findings to separation methods operating by different mechanisms (DEP-FFF and IDS).

Chapter 5 describes the initial stages of a pooled genetic screen of the *Saccharomyces cerevisiae* deletion library for electrically distinguishable phenotypes. Specifically, we describe a pilot screen in which we survey 82 strains sampled from the full library, followed by separations of the complete deletion collection and preparation for genome-wide analysis of electrical phenotypes in yeast. The results of this chapter demonstrate the feasibility of using IDS as a screening platform.

Finally, we conclude in Chapter 6 with a discussion of the contributions of this work and some of the avenues for scientific research and technology development that it has engendered.

Chapter 2: Device Modeling, Design, and Characterization

This chapter begins by describing physical models for IDS, developed to predict and optimize the operation and design of devices. These models take into account electrostatics, heat and mass transport, and fluid dynamics, in an effort to understand the coupling between these physical domains. From these models, we proceed to discuss the design, fabrication, and characterization of the first generation of IDS devices, using charged polystyrene beads and viable and non-viable yeast (*Saccharomyces cerevisiae*) to demonstrate its functionality. We then expand on this discussion to describe the development of giant unilamellar vesicles (GUVs) as new metrology tools for characterizing dielectrophoretic systems, especially IDS. The chapter then concludes by analyzing alternative implementations of IDS that exhibit some promise but were not pursued in this thesis.

The material in this chapter includes work published in *Analytical Chemistry*³⁷. In addition, the work with GUVs was performed in collaboration with Dr. Salil P. Desai; a more complete description of this part of the chapter can be found in an article we have published in *Langmuir*³⁸.

Models for Device Operation

Motivation. The successful design of a device for IDS requires understanding and managing the coupling between the multiple physical domains relevant to the method's operation. Specifically, the primary physical domains we consider in designing the device are mass transport (i.e. how convection and diffusion of ions establishes a conductivity profile), electrostatics, and fluid dynamics. To take advantage of different symmetries, we will develop these models in two different coordinate systems, (x,y,z) , and (ξ,η,z) shown in Figure 2- 1; the cartesian coordinates (x,y,z) are convenient of describing the channel's width (x -axis), length (y -axis), and depth (z -axis), whereas the coordinates (ξ,η,z) are rotated by an angle θ such that ξ and η are, respectively, perpendicular and parallel to the electrode axis. Specifically, this transformation amounts to:

$$\begin{bmatrix} \xi \\ \eta \\ z \end{bmatrix} = \begin{bmatrix} \cos \theta & -\sin \theta & 0 \\ \sin \theta & \cos \theta & 0 \\ 0 & 0 & 1 \end{bmatrix} \begin{bmatrix} x \\ y \\ z \end{bmatrix} \quad (2- 1)$$

While the (x,y,z) coordinates are well suited to describing the conductivity profile throughout the channel, it is convenient to model force balance using (ξ,η,z) . Throughout this chapter, we will alternate between these two coordinate systems.

Mass Transport. The first domain we consider is that governing the transport of dissolved ions in the separation medium; in effect, its electrical conductivity. The IDS device must operate in a convection-dominated transport regime to ensure that the conductivity gradient is preserved over the channel length. This requirement is quantified by the dimensionless Péclet number ($Pe \equiv UL/D$, where U denotes the characteristic velocity of the fluid, L denotes the relevant length scale, and D is the diffusivity of the

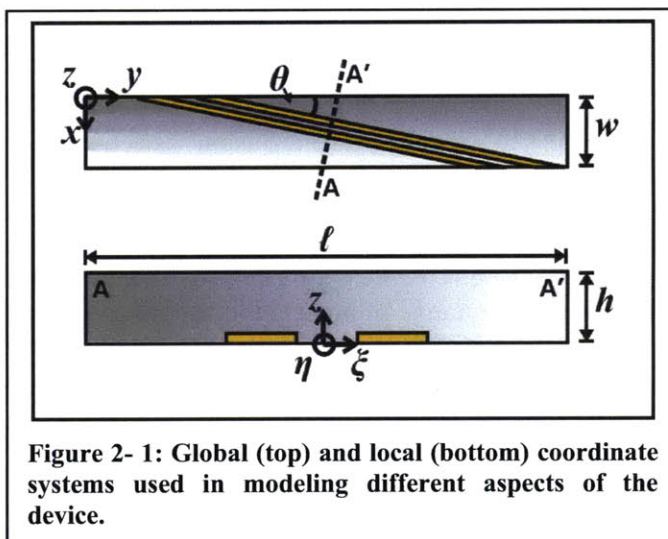


Figure 2- 1: Global (top) and local (bottom) coordinate systems used in modeling different aspects of the device.

chemical species of interest)^b which increases with the significance of convection. The two length scales we are interested in are the channel width, w , from which the timescale for diffusion is obtained ($\sim w^2/D$), and the channel length, ℓ , which enters through the convective time constant ($\sim \ell/U$). This suggests that transport in the device is best parameterized in terms of the modified Péclet number, $w^2U/D\ell$, allowing us to define for a given separation a critical number, Pe_0 , below which that separation is no longer possible.

To study the relationship between transport (as parameterized by the Péclet number) and the range of electrical conductivities available for a separation further, we solve for the conductivity profile at the outlet of the device as a function of the Péclet number. To do this, we use a two-dimensional model for mass transport throughout the device; use of a two-dimensional model (rather than 3-D) is motivated by the rapid equilibration of the conductivity over the depth of the shallow channel. Solving the steady-state conservation equation for conductivity ($\mathbf{u} \cdot \nabla \sigma = \nabla^2 \sigma$, where \mathbf{u} is the fluid velocity vector and σ is the conductivity) in dimensionless form gives:

$$\tilde{\sigma} \equiv \frac{\sigma - \sigma_\ell}{\sigma_h - \sigma_\ell} = \frac{1}{2} + \sum_{n=1}^{\infty} a_n \cos(n\pi\tilde{x}) \exp(k_n\tilde{y}) \quad (2-2)$$

Here, the x and y coordinates have been scaled according to the channel width and length, respectively (so that $\tilde{x} = x/w$ and $\tilde{y} = y/\ell$). The conductivity at the entrance of the device is bounded by high and low values of σ_h and σ_ℓ , respectively. Defining the dimensionless groups $Pe = w^2U/D\ell$ and $\gamma = \ell/w$ and assuming the conductivity at $y = 0$ (the entrance of the chamber) consists of M equally spaced levels ($M = 3$ in our architecture), we have $k_n = \frac{1}{2}(\gamma^2 Pe - [(\gamma^2 Pe)^2 + 4\gamma^2(n\pi)^2]^{1/2})$ and $a_n = \sum_{m=1}^{M-1} 2 \frac{\sin(mn\pi/M)}{(M-1)n\pi}$. For cases in which $Pe \gg 2\pi\gamma^{-1}$, axial diffusion can be neglected and k_n simplifies to $k_n = -(n\pi)^2/Pe$. Combining this with equation (2-2) allows us to solve for the range of conductivities preserved along the separation channel as a function of Pe . Since the separation is based upon a mapping of the effective conductivity of a particle to the position along the channel width where it matches the solution conductivity, there is a direct correspondence between the range of conductivities preserved in the device and the maximum range of conductivities that can be simultaneously resolved. In effect, Pe determines the *dynamic range* of the separation. For example, if a sample contains particles varying in conductivity by a factor of 5, Pe must be maintained above ~ 18 to accommodate the full range, independent of other parameters and operating conditions.

Equation (2-2) is easily solved, due to the rectangular symmetry of the device we are considering. A modeling approach not used in this thesis (but potentially useful for more complicated device geometries) exploits the conformal invariance of certain coupled systems of equations. One such system of equations is:

^b The diffusivity referred to here and throughout this thesis is the effective diffusivity describing the flux of electrical conductivity in the presence of a conductivity difference. The electrical conductivity of a solution is determined by the concentration, valence charge, and mobility of each solute present, as described by equation (1-4). The transport of each of these solutes is in turn governed by the Nernst-Planck equation, in which each ionic species is coupled by the electric fields created by the charged solute. For the case of a binary electrolyte, positive and negative species can be replaced by an equivalent salt concentration, with an effective diffusivity, $D = (z_+ - z_-)D_+D_-/(z_+D_+ - z_-D_-)$. Since an electrolyte composed of a single dissolved salt has an electrical conductivity proportional to the salt concentration, this effective diffusivity allows us to model the evolution of conductivity gradients independent of the electric fields coupling positive and negative ions together. Since in our work, conductivities are established using PBS (predominantly NaCl), our electrolyte solutions are monovalent in addition to binary, and the effective diffusivity becomes $D = 2D_{Na}D_{Cl}/(D_{Na} + D_{Cl})$. In all of the following discussion, D refers to this effective diffusivity.

$$\begin{aligned}\nabla^2\psi &= 0 \\ \text{Pe}[\nabla\psi \cdot \nabla\Theta] &= \nabla^2\Theta\end{aligned}\tag{2-3}$$

The quantity ψ can be interpreted as a velocity potential (i.e. $\mathbf{u} \equiv \nabla\psi$), such that the first equation describes an irrotational flow ($\nabla \times \mathbf{u} = 0$), while the second equation describes steady convection and diffusion within this flow. Although velocity fields in microfluidic devices are generally not irrotational, for a sufficiently shallow channel the depth-averaged velocity reduces to a Hele-Shaw flow and is thus mathematically equivalent to a potential flow. These coupled equations are therefore a more general form of a drift-diffusion equation, applicable to thin microfluidic channels. Since we have already obtained a solution to these equations for a rectangular geometry (equation (2-2)), it is possible to obtain accurate approximations for concentration profiles in shallow devices with arbitrary planar geometries by mapping this solution to the new channel shape.

Electric Fields. After determining how the electrical conductivity varies throughout the device, we proceed to solving for the electric fields. The coplanar electrode geometry introduced in chapter 1 permits conformal mapping solutions in the ξ - z plane³⁹ if we assume the medium conductivity can be treated as locally homogeneous. This assumption is justified provided the distance over which the electric potential varies is considerably smaller than that over which the medium conductivity varies. Since these distances are, respectively, the electrode gap ($d \sim 10\text{-}20 \mu\text{m}$) and the channel width ($w \sim 2\text{-}3 \text{mm}$), disturbances to the electric field due to the heterogeneous conductivity will be of order $d/w \sim 10^{-2}$ times smaller than the baseline electric field determined through conformal mapping. This is an important aspect of the design we use, since the ability to decouple the length scales over which mass transport and electrical conductance occurs is fundamental to the operation of these devices. Given the electric field, the dielectrophoretic force can be determined to arbitrary order either analytically or numerically, using custom scripts for efficiently calculating the multipolar DEP force⁴⁰.

Thermal Model. Electrical conduction within the device dissipates power and can lead to temperature rises. Having determined the electric fields, we can proceed to modeling the significance of this heating under different operating conditions. The primary difficulty in modeling heat transfer in the device is establishing accurate boundary conditions. While all of the boundaries act to sink heat away from the channel in which it is generated, their thermal properties and how they couple to the external (ambient) environment are not easily definable. To attempt to account for this ambiguity, we consider two different models. In the first, the glass substrate acts as the primary heat sink, with a linear profile connecting the temperature in the channel to the ambient temperature (the much thicker PDMS channel ceiling is treated as thermal insulation). In the second model, we treat the electrodes as perfect heat sinks (maintained at the ambient temperature), with the glass substrate and PDMS channel ceiling acting as thermal insulation. The primary advantage of the second approach is that it establishes a conformally invariant system of equations for the electric potential and temperature, analogous to what we obtained for the conductivity profile in a potential flow (equation (2-3)). In terms of dimensionless quantities:

$$\tilde{\nabla}^2 \tilde{\varphi} = 0 \tag{2-4}$$

$$\nabla^2 \tilde{T} + 1/2(\tilde{\nabla} \tilde{\varphi} \cdot \tilde{\nabla} \tilde{\varphi}) = 0 \tag{2-5}$$

(The alternate formulation cannot be treated in this way because the Robin boundary conditions are not conformally invariant). The primary outcome of comparing these two approaches is that the former results in a larger temperature but smaller temperature gradient, whereas the latter results in a lower temperature but larger temperature gradient. On both of these points, treating the electrodes as ideal heat sinks appears more physically realistic with respect to experiments (for example, in typical operating conditions it predicts a temperature rise of 1-2K as opposed to 10-20K). Because it offers more physically realistic predictions (with the added advantage of being more mathematically elegant), we use the electrode-as-heat-sink model throughout. To a good approximation, using conformal mapping and the method of reflections, the temperature (in the ξ - z plane around the electrodes) is given by:

$$T(\xi, z) = \frac{\sigma_m V_0^2}{4\kappa\pi^2} \left[\frac{\pi^2}{4} - \operatorname{Re} \left\{ \sin^{-1} \left(\frac{z}{d} (\xi + iz) \right) \right\}^2 \right] + \sum_{n=1}^{\infty} \left[\frac{\operatorname{Re} \left\{ \sin^{-1} \left(\frac{z}{d} (\xi + (-1)^{n+1} iz + i2hn) \right) \right\}^2}{\operatorname{Re} \left\{ \sin^{-1} \left(\frac{z}{d} (\xi + (-1)^n iz + i2hn) \right) \right\}^2} - \dots \right] \quad (2-6)$$

Interestingly, because the spacing of the electrodes (d) determines how much power is dissipated in the device as well as the proximity of the heat sinks to each other, the maximum temperature rise ($= \sigma_m V_0^2 / 16\kappa$) is independent of the electrode spacing, as well as the height of the channel.

Electrohydrodynamic Flows. Mass transport, electric fields, and heat transfer combine to induce convection within the device. IDS is distinct from many other gradient separation methods in the extent to which the separation medium (the conductivity gradient) couples to the electric fields driving the separation. This coupling is bi-directional, as gradients in the properties of the medium can perturb the electric field, while the electric field can simultaneously perturb the medium, through both Joule heating and induced flow. While electrokinetics have been leveraged to mix and pump fluids at the microscale^{41,42}, in the context of separations, they exert non-specific forces that can undermine the ability to resolve different cells or particles. Although Pethig et al. demonstrated cell sorting in a *time-varying* conductivity⁴³, we believe that the difficulties attendant to the strong coupling between electric fields and spatial variations in the fluid's electrical properties is why IDS has not previously been demonstrated.

To predict the significance of induced convection within the device, we consider the influence of induced charge electroosmosis (ICEO) and electrohydrodynamics, the latter of which may be driven by polarization of both the imposed conductivity gradient (electrical hydrodynamics, EHD) as well as gradients in conductivity and permittivity induced by Joule heating (electrothermal hydrodynamics, ETHD). These flows are all described by the Navier-Stokes equation with an electrical body force, and are distinguished from each other by the form of the space charge density, ρ :

$$0 = -\nabla p + \mu \nabla^2 \mathbf{u} + \rho \mathbf{E} - \frac{1}{2} (\mathbf{E} \cdot \mathbf{E}) \nabla \epsilon_m \quad (2-7)$$

For the case of ICEO, ρ is created by polarization at the electrode surface, making it convenient to reformulate the electrical body force as an appropriate "slip" boundary condition at the electrode-liquid interface. The strong frequency dependence of ICEO suggests that it will be negligible when the electrodes are driven in excess of ~ 10 kHz⁴⁴ for the medium conductivities and electrode geometries we are using. For both EHD and ETHD, the space charge density results from the polarization of the bulk fluid as a result of gradients in conductivity and permittivity, and can be written as:

$$\rho = \frac{\sigma_m \nabla(\epsilon_m / \sigma_m) \cdot \mathbf{E}}{1 + i\omega(\epsilon_m / \sigma_m)} \quad (2-8)$$

(As a general operating principle, IDS requires frequencies well below the inverse charge relaxation time for the medium, so that the denominator is ~ 1 in all cases of interest). For EHD and ETHD flows, we nondimensionalize the governing equations and solve numerically for the induced flow as a regular perturbation series. This approach is contingent on two primary assumptions. The first assumption is that the frequency is sufficiently high that we may use time-averaged quantities for the polarization force and Joule heating, both of which depend on the square of the electric field and thus will have both an AC and DC component when the applied voltage is sinusoidal in time. The second assumption is that the conductivity varies over distances considerably larger than the applied electric field. This motivates us to formulate the problem using regular perturbation, in which the small parameter is taken as the fractional change in conductivity over the region of large electric field. For the case of the imposed conductivity gradient, this parameter is of order $h/w \sim 10^{-2}$ (h = channel height, w = channel width; we are assuming here that $h \sim d$, the electrode spacing), and is thus universally valid. For thermally induced gradients in conductivity and permittivity, validity of the perturbation analysis is contingent on the temperature rise being reasonably modest ($\Delta T < 10$ K, typically).

The 0th order term in the perturbation series corresponds to the behavior of the different physical domains (electric field, conductivity profile and fluid velocity) in the absence of any coupling. The fluid velocity, \mathbf{u}_0 , is Poiseuille, the electric field, $\mathbf{E}_0 = -\nabla\phi$, is solenoidal, and the conductivity and permittivity are, to 0th order, uniform in the ξ - z plane around the electrodes. After scaling the governing system of equations and eliminating higher-order terms, the first correction for the fluid velocity, \mathbf{u} , is governed by:

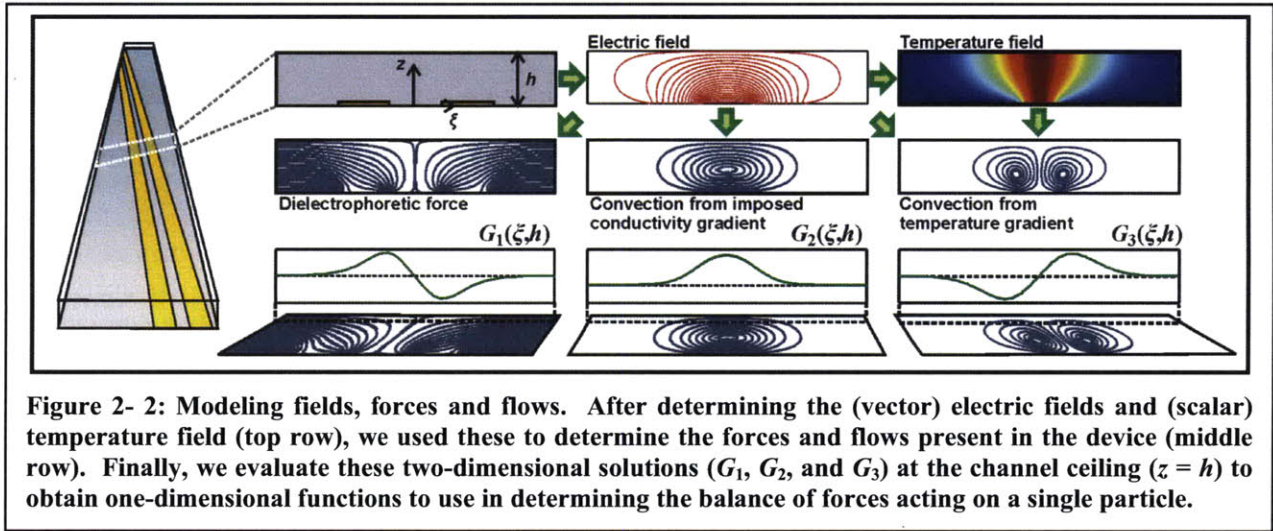
$$0 = -\tilde{\nabla}\tilde{p} + \tilde{\nabla}^2\tilde{\mathbf{u}} + \frac{1}{2}\left[\frac{\varepsilon V_0^2}{\mu h U}\lambda(\eta)\right]\left[\left(\frac{\partial\tilde{\phi}_0}{\partial\xi}\right)\tilde{\nabla}\tilde{\phi}_0\right] \quad (2-9)$$

$$0 = -\tilde{\nabla}\tilde{p} + \tilde{\nabla}^2\tilde{\mathbf{u}} + \frac{1}{2}\left[\frac{\varepsilon V_0^4\beta}{\mu h \kappa U}\sigma_m(\eta)\right]\left[\left(\tilde{\nabla}\tilde{T}\cdot\tilde{\nabla}\tilde{\phi}_0\right)\tilde{\nabla}\tilde{\phi}_0 - \frac{1}{12}\left(\tilde{\nabla}\tilde{\phi}_0\cdot\tilde{\nabla}\tilde{\phi}_0\right)\tilde{\nabla}\tilde{T}\right] \quad (2-10)$$

in addition to continuity ($\tilde{\nabla}\cdot\tilde{\mathbf{u}}=0$). The constant β ($=\varepsilon_m^{-1}(\partial\varepsilon_m/\partial T)-\sigma_m^{-1}(\partial\sigma_m/\partial T)$) is a material property related to the temperature coefficients of conductivity ($=-0.004\text{K}^{-1}$) and permittivity ($=0.02\text{K}^{-1}$). In equation (2-9), we have introduced the dimensionless function, $\lambda(\eta)$, given by:

$$\lambda(\eta) \equiv \frac{(h/\sigma_m)}{\left[1+(\omega\varepsilon_m/\sigma_m)^2\right]}\frac{\partial\sigma_m}{\partial\xi}\bigg|_{\xi=0} \approx \frac{h}{\sigma_m}\frac{\partial\sigma_m}{\partial\xi}\bigg|_{\xi=0} \quad (2-11)$$

Solving these equations yields the EHD and ETHD velocities. Since the equations have been linearized, the superposition of these solutions is equal to the solution of a single equation with the forces superimposed. The total induced convection will therefore be the sum of the EHD and ETHD velocity fields.



Force Balance. Once we have solved for the dielectrophoretic force and induced fluid velocity in the ξ - z plane, we can combine the results to determine where particles will pass through the electrode barrier: the effective iso-dielectric point. This methodology is illustrated in Figure 2-2. Each of the forces can be expressed as separable functions of (ξ, z) and η :

$$F_\xi^{DEP} = \pi\varepsilon_m V_0^2 (a/h)^3 K(\eta)G_1(\xi, z) \quad (2-12)$$

$$F_\xi^{iEHD} = 3\pi\varepsilon_m V_0^2 (a/h)\lambda(\eta)G_2(\xi, z) \quad (2-13)$$

$$F_\xi^{eEHD} = 3\pi\varepsilon_m V_0^4 (a/h)\beta\kappa^{-1}\sigma_m(\eta)G_3(\xi, z) \quad (2-14)$$

$$F_\xi^{HD} = 6\pi\mu a U_0 \sin(\theta)G_4(z) \quad (2-15)$$

In the above, $K(\eta)$ is the real part of the Clausius-Mossoti factor (and thus a function of the local medium conductivity, $\sigma_m(\eta)$), and G_i ($i = 1..4$) are dimensionless functions that depend only on ξ and z (G_1 , G_2 and G_3 are plotted in the second row of Figure 2- 2). Since particles are strongly levitated by the z -

component of the dielectrophoretic force, we assume for simplicity that $z = h-a$ (i.e. particles are pressed against the ceiling of the channel). For small particles ($a \ll h$), this allows us to expand around $z = h$ to further simplify the force calculations. Based upon numerical results, we have:

$$G_1(\xi, z) \approx [-0.2 + O(a^2/h^2)] G_1(\xi, h) \quad (2-16)$$

$$G_2(\xi, z) \approx [2 \times 10^{-2}(a/h) + O(a^2/h^2)] G_2(\xi, h) \quad (2-17)$$

$$G_3(\xi, z) \approx [2 \times 10^{-3}(a/h) + O(a^2/h^2)] G_3(\xi, h) \quad (2-18)$$

$$G_4(z) \approx 8.22(a/h) \quad (2-19)$$

Plots of these functions along with surface plots of the associated forces are depicted in the bottom rows of Figure 2-2. Using these expressions, it is possible to determine which forces will dominate in determining the trajectory of a particle over a broad range of operating conditions and geometries. For optimal performance, we would like the maximum magnitude of F^{DEP} to dominate all other forces except where $K \sim 0$, (the iso-dielectric point). Since we have normalized all $G_i(\xi, h)$ to have a maximum magnitude of 1, they do not contribute appreciably to the relative importance of the different forces:

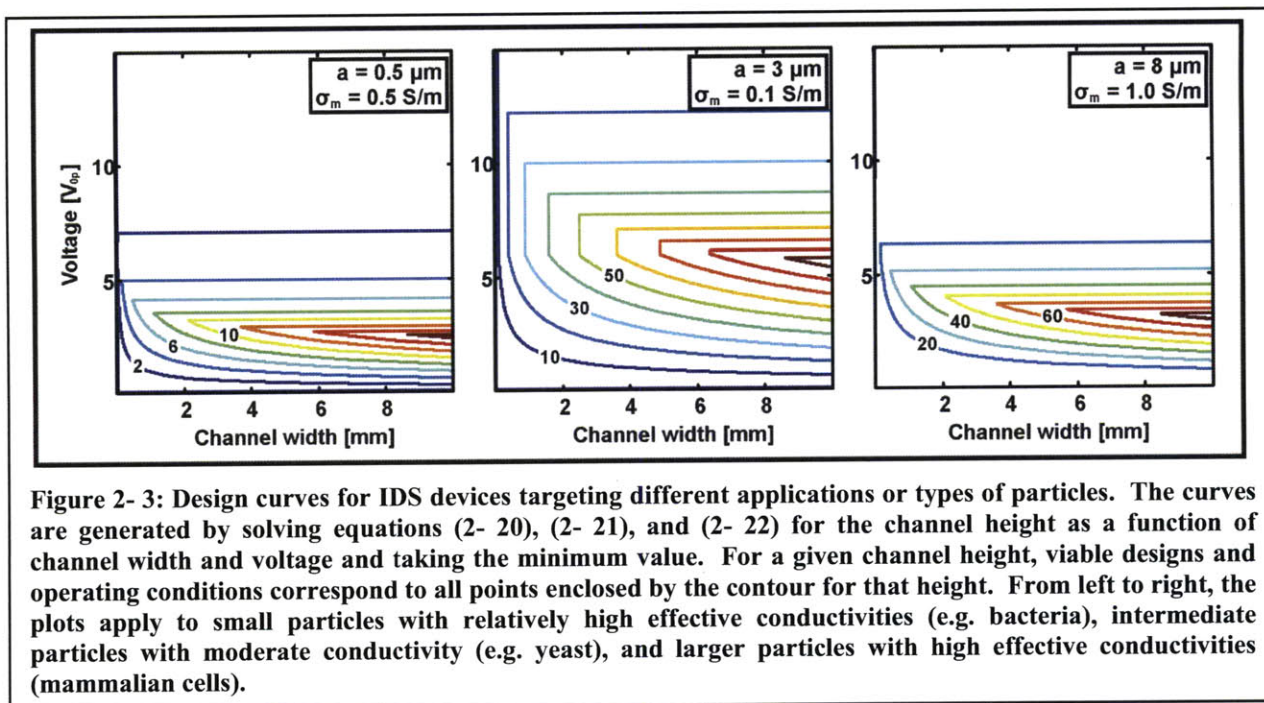
$$F_\xi^{\text{DEP}} / F_\xi^{\text{IEHD}} \approx \frac{10aw}{3h^2} K(\eta) \quad (2-20)$$

$$F_\xi^{\text{DEP}} / F_\xi^{\text{IEHD}} \approx \frac{a(10^3 \text{ W/m})}{hV_0^2 \sigma_m(\eta)} K(\eta) \quad (2-21)$$

$$F_\xi^{\text{DEP}} / F_\xi^{\text{HD}} \approx \frac{\epsilon_m V_0^2 a \ell}{250 \mu h Q_0} K(\eta) = \frac{\epsilon_m V_0^2 a w}{250 \mu h^2 \text{DPe}} K(\eta) \quad (2-22)$$

In the above, we have replaced $\sin(\theta)$ with w/ℓ (assuming that $w \gg \ell$), and U_0 with either Q_0/wh (since it is ultimately the volumetric flowrate, Q_0 , that determines throughput) or Pe (since this determines the extent to which the gradient is preserved). These three expressions represent the constraints for force balance; maximizing the coefficients of $K(\eta)$ (subject to the additional constraint of maintaining an appropriate conductivity gradient) will optimize the performance of the device. From this analysis, it becomes clear that the controlling design parameter is the channel height, h . Making the channel shallower has favorable effects on all three elements of force balance (it is important to note, however, that we have assumed that the electrode spacing is comparable to the channel height; if this relationship no longer holds, the above relationships would need to be modified). In addition to decreasing h , increasing the channel width (w) and length (ℓ) are advantageous in individual cases (equations (2-20) and (2-22), respectively), with no detriment in others. Another design rule that arises from the scaling of forces is that maintaining a constant ratio of particle size to channel height will not work for arbitrarily large particles, even for the limiting case of $a/h = 1/2$; regardless of particle size, the device will no longer function if the particles become too large. Accordingly, IDS is a fundamentally microscale separation method.

Figure 2- 3 shows design curves under different conditions; those typical of bacterial separations ($a \sim 0.5\mu\text{m}$, $\sigma_m \sim 0.5 \text{ S/m}$), those typical for yeast ($a \sim 3\mu\text{m}$, $\sigma_m \sim 0.1 \text{ S/m}$), and those typical for mammalian cells ($a \sim 8\mu\text{m}$, $\sigma_m \sim 1.0 \text{ S/m}$). The contours give the maximum channel height (in microns) that is allowable for a given zero-to-peak operating voltage and channel width. In generating these curves, we have taken $Pe = 20$, and $|K| = 0.1$, providing a sufficient conductivity range and specificity. Despite the number of approximations made in deriving these design curves, they provide useful guidelines in determining the range of possible separations. In particular, they suggest that the constraints presented by working with bacterial cells are considerably stronger than those for both yeast and mammalian cells. While a $20\mu\text{m} \times 2\text{mm}$ channel operating at 7V would be operational for both yeast and mammalian cells, working with bacteria at this voltage would require a $2.5\mu\text{m} \times 2\text{mm}$ channel, owing primarily to the constraints of electrothermal flows.



Device Fabrication and Packaging.

The application-specific design curves in Figure 2- 3 indicate that separations of eukaryotic cells are generally achievable with a channel $>1\text{mm}$ wide and $< 30 \mu\text{m}$ deep. These dimensions are well within the range of those easily achieved by molding PDMS on photolithographically patterned silicon wafers. Similarly, since the electrode gap is roughly equal to the channel height for our design space, the resolution required in patterning the electrodes (minimum features on the order of $10 \mu\text{m}$) is not constraining. This facilitates device fabrication at the expense of working only with eukaryotic cells. Given the range of applications involving yeast and mammalian cells, this is not particularly limiting; this notwithstanding, there is no fundamental reason that IDS could not be applied to bacterial separations.

To enable broader coverage of the accessible design space, we fabricate devices with widths ranging from 0.5mm to 3mm , at heights from $10 - 25 \mu\text{m}$, using an identical process for each. Complete process flows are available in the appendix to this chapter. Briefly, we pattern planar electrodes on $6''$ Pyrex wafers using e-beam evaporation of 2000-\AA Au/ 100-\AA Ti and a standard liftoff process using NR-7 negative photoresist. The electrode spacing and line width are $15 \mu\text{m}$ and $60 \mu\text{m}$, respectively. For the microfluidic channels, we use PDMS replica molding from an SU-8 patterned silicon master (SU-8 2015, Microchem, Newton MA) to create channels with width of $0.5\text{-}3 \text{ mm}$ and heights ranging from $10 - 25 \mu\text{m}$, achieving $\sim 5\%$ uniformity in film thickness over the area of the wafer in all cases. Devices with a 1-

mm-wide by 15-mm-long channel generally gave the best performance, and were used in the experiments throughout this chapter. After dicing the glass wafer and manually drilling fluidic access holes, we plasma bond the PDMS channel to the chip. The PDMS channels are designed to be used once, mitigating any issues with fouling and contamination; for subsequent uses we strip the PDMS channel (Nanostrip 2X, Rockwood Electronic Materials, Derbyshire, UK) and bond a new channel in its place. We then affix the device to a custom printed circuit board, where we make the remainder of the electrical and fluidic connections. A more detailed process flow is included in the appendix.

Device Characterization

With the fabricated and packaged devices, we proceeded to characterize their performance using charged polystyrene beads and viable and non-viable yeast as test particles. This section describes the process through which we carried out this characterization and the results we obtained. The results of this section collectively demonstrate the ability to perform size-insensitive, non-binary separations using IDS.

Preparation of Cell and Bead Suspensions. We culture the budding yeast *Saccharomyces cerevisiae* at 30°C for two days in a medium comprised of 1% Yeast extract, 2% peptone and 2% glucose. After harvesting the cells, we centrifuge and resuspend them in deionized water. We then transfer cells to be heat treated to a glass vial which we place on a hot plate set to 90°C for ~20 minutes. Live/dead staining using Syto 9 (S-34854, Invitrogen, Carlsbad, CA) and propidium iodide (P1304MP, Invitrogen, Carlsbad, CA) confirms that 100% of cells are non-viable after heat treatment, whereas typically >95% of the untreated cells remain viable. After staining, we wash the cells three times in a solution of deionized water, 0.1% BSA, and PBS mixed to the desired conductivity. For experiments involving polystyrene beads, we use three different types: blue fluorescent (17686-5, Polysciences, Inc. Warrington, PA, $1.6 \pm 0.04 \mu\text{m}$ true diameter), red fluorescent (19508, Polysciences, Inc. Warrington, PA, $1.755 \pm 0.055 \mu\text{m}$ true diameter), and green fluorescent (FS04F/6845, Bangs Laboratories, Inc. Fishers IN, $1.90 \pm 0.22 \mu\text{m}$ true diameter).

Fluorescent Imaging, Data Acquisition and Processing. We image the device using an upright Zeiss Axioplan 2M microscope (Zeiss, Thornwood, NY) coupled to a LaVision Imager 3 QE CCD Digital Camera (LaVision GmbH, Goettingen, Germany) using DAPI, FITC, and Cy3 filters. We record videos of particle separations under $5\times$ magnification at the outlet of the device. To represent the trajectories of ensembles of particles over time in a 2D image, we process the videos using a first-order difference filter. We apply a uniform threshold, so that each particle receives identical weighting in the composite image, and average the video over the total number of frames to produce the final image.

Electrical Characterization of Cells. To determine the optimal conditions (i.e. conductivity range and frequency) for separation, we measure the cross-over frequencies of viable and non-viable *S. cerevisiae*. We stain cells for viability using Syto 9 (S-34854, Invitrogen, Carlsbad, CA) and propidium iodide (P1304MP, Invitrogen, Carlsbad, CA). By viewing cells under a triple band filter (61000v2, Chroma Technology Corp., Rockingham, VT), we are able to distinguish live and dead cells from one another simultaneously, enabling concurrent measurements under identical conditions. After staining, we wash the cells $3\times$ in solutions of deionized water doped to the desired conductivity using Dulbecco's phosphate buffered saline (Gibco, Carlsbad, CA). We then place the cell suspension in a sealed gasket above an array of interdigitated electrodes and vary the frequency until minimal response to the electric field is observed. We summarize the data in Table 2- 1.

Medium Conductivity [S/m]	Viable	Non-Viable
	Frequency [kHz]	Frequency [kHz]
0.0105	50 ± 10	25 ± 10
0.019	150 ± 25	100 ± 25
0.033	325 ± 25	-
0.04	375 ± 25	-
0.055	600 ± 50	-

Table 2- 1: Crossover frequency measurements for viable and heat-treated *S. cerevisiae* (A ‘-’ denotes conditions under which no crossover was observed).

Electrical Characterization of Beads. We characterize the electrical properties of beads using the same technique as for cells. We wash and suspend the mixture of beads (diameters of 1.6, 1.75, and 1.9 μm) in a solution of known conductivity and search for the frequency at which the DEP force is minimized. We summarize the results from these measurements in Table 2- 2.

Medium Conductivity [S/m]	1.60 μm Beads	1.75 μm Beads	1.90 μm Beads
	Frequency [kHz]	Frequency [kHz]	Frequency [kHz]
0.0033	180 ± 20	120 ± 20	40 ± 10
0.0063	120 ± 10	70 ± 10	40 ± 10
0.0092	100 ± 20	50 ± 10	-
0.0121	80 ± 10	-	-

Table 2- 2: Crossover frequency measurements for beads.

Calculating the Separation Resolution. To estimate the degree to which we are able to separate viable from non-viable cells, we record videos of multiple separations immediately before the outlet of the device and obtain fluorescence intensity profiles, corresponding to the average distribution for $\sim 10^4$ cells. From these fluorescence profiles, we obtain the separation resolution, R_s :

$$R_s = \frac{|X_1^{IDP} - X_2^{IDP}|}{2(\sigma_1 + \sigma_2)} \quad (2- 23)$$

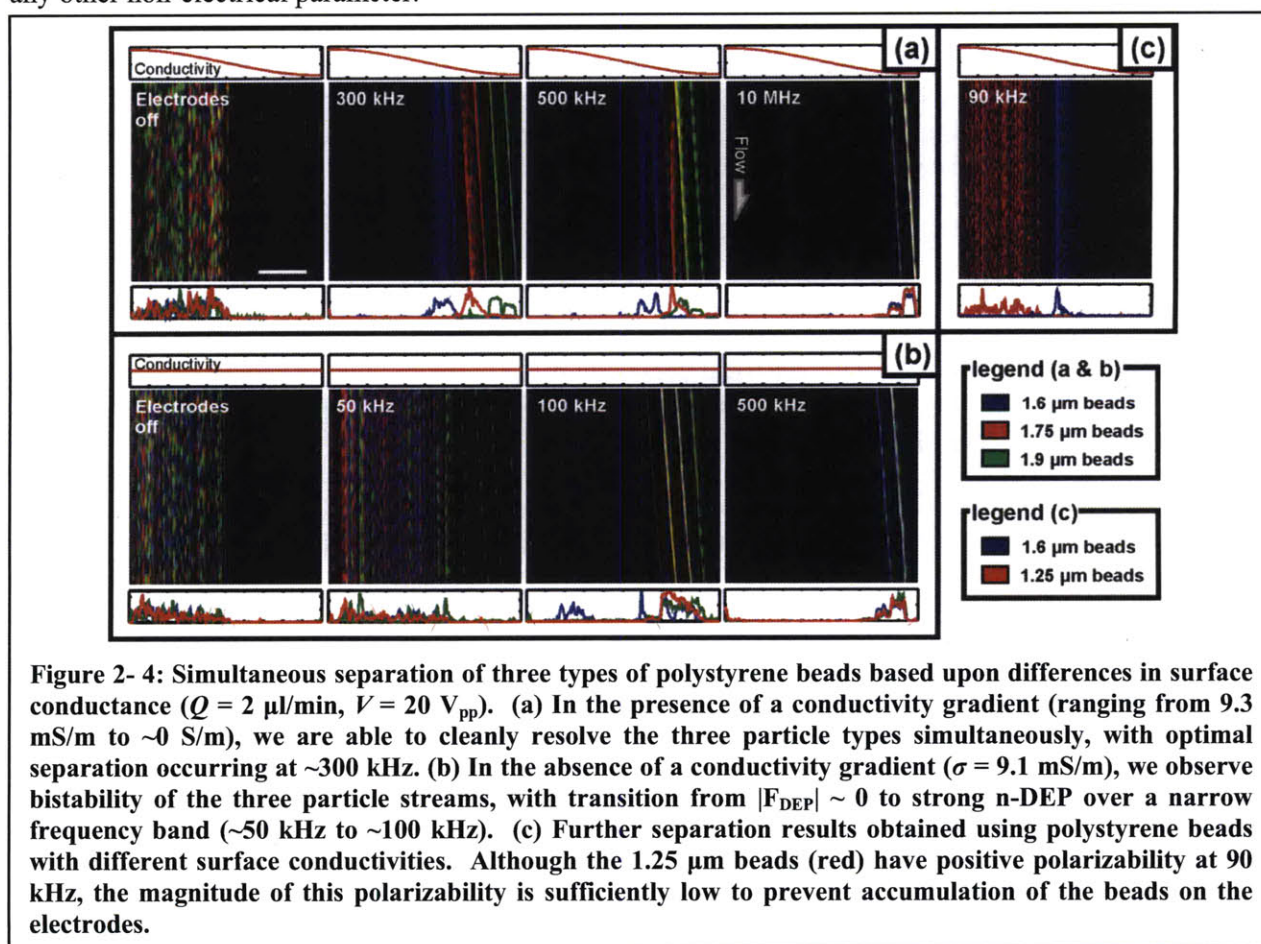
Here, $X_{1,2}^{IDP}$ denotes the point around which the cells are centered, and $\sigma_{1,2}$ is the standard deviation of the distribution (not to be confused with electrical conductivity). By interpreting the fluorescence intensity plots as probability densities, $p_L(x)$ and $p_D(x)$, we determine the mean and standard deviations for the particle distributions using $\langle f(x) \rangle = \int f(x)p_{L,D}(x)dx$ with $X^{IDP} = \langle x \rangle$ and $\sigma = [\langle x^2 \rangle - \langle x \rangle^2]^{1/2}$. Since striations in the distributions of cells created by the electrode gaps (where the concentration of cells is enhanced) cause the distributions to have considerable higher-order moments, we account for the non-Gaussian shape of the distributions by using an alternate interpretation of the standard deviation, integrating over the distribution and finding the width of the region over which the central most 68% of the cells are located.

Separation of Polystyrene Beads Based Upon Electrical Properties. We demonstrate the ability to resolve complex mixtures of micron-scale particles based upon differences in conductivity by using a mixture of three types of polystyrene beads in the device. Although bulk polystyrene is essentially dielectric, the effects of surface conductance can dominate for smaller beads, where the surface-to-volume ratio is greater⁴⁵⁻⁴⁷. This allows us to modulate the effective electrical properties of particles indirectly through size. Our characterization of the beads indicates that, for media conductivities less than ~ 10 mS/m, crossover frequency varies inversely with size, supporting the hypothesis that the surface-to-volume ratio provides an avenue for modulating the electrical properties of the beads (Table 2- 2).

Importantly, although the complex interfacial phenomena that give rise to a particle's surface conductance are not fully understood, we observe that the DEP force on different particles vanishes at different combinations of frequency and medium conductivity. Thus, independent of the physical mechanism underlying their electrical properties, it should be possible to separate these particles using IDS.

We wash the beads in medium with a conductivity of 9.1 mS/m and inject this and a low conductivity solution (comprised of deionized water) into the device. As we vary the frequency from 100 kHz to 10 MHz, the beads are resolved into three distinct flow streams, with the cleanest separation observed at 300 kHz (Figure 2- 4a). Increasing the frequency further results in deflection to successively lower conductivities, until the DEP force becomes independent of the fluid and particle conductivities, culminating in the complete deflection of all particles across the channel at a frequency of 10 MHz. We observe similar results in separations involving 1.25 μm beads (Figure 2- 4c), which have a crossover frequency at the conductivity of interest of ~ 5 MHz, and thus separate into higher conductivity than the 1.6 μm blue beads in Figure 2- 4a.

To confirm that the order of elution of the beads is based upon differences in their dielectrophoretic equilibrium rather than differences in particle size leading to different magnitudes of polarization, we repeat the assay with the solution conductivity held constant throughout the device (Figure 2- 4b). In the uniformly conducting medium, we observe bistable behavior, with particles abruptly switching from zero to negative polarizability over a narrow frequency range (~ 50 -100 kHz). The necessity of a conductivity gradient in resolving these beads supports the conclusion that the separation is based upon differences in the equilibrium positions of the beads in a conductivity gradient rather than differences in bead volume and thus the magnitude of the DEP force. Additionally, the requirement for the conductivity gradient and the variation of the separation with frequency together preclude the possibility that the separation is due to any other non-electrical parameter.



To further verify that the separation we observe is based upon surface conductivity as opposed to other properties that differ between the particles, we have performed complementary experiments in which we sort beads with comparable sizes but different surface coatings. For carboxyl-modified beads with comparable surface charge densities, differences in surface conductivity arise from differences in surface-to-volume ratio. Accordingly, smaller COOH-modified beads exhibit higher conductivities than larger, similarly functionalized beads and separate into higher conductivity solution, as illustrated in Figure 2. Alternatively, the absence of COOH surface modification should decrease the surface conductivity and hence the effective conductivity of the beads. This is exactly what is observed in Figure 3. Here small unmodified polystyrene beads exhibit lower effective conductivities than their larger and more highly charged counterparts (Figure 2- 5). These experiments demonstrate that IDS may be used to separate particles according to their electrical properties, even in the presence of competing differences in the sizes of the particles.

Separation of viable from non-viable *S. cerevisiae*. A live/dead separation using *S. cerevisiae* demonstrates the feasibility of IDS for biological assays. To determine the appropriate conductivity range for the separation, we characterize viable and non-viable (heat treated) cells by measuring their crossover frequencies (Table 2- 1). Consistent with previous observations¹, we observe the homogenization of the DEP spectra of yeast cells upon heat treatment, a combined effect of increased membrane conductance and decreased cytoplasmic conductivity in non-viable versus viable cells. These measurements prescribe a conductivity that decreases from ~50 mS/m to ~10 mS/m across the channel and an applied frequency of ~500 kHz.

After staining the cells and suspending them in the higher conductivity fluid (40 – 50 mS/m), they are injected into the device along with the less conductive (10 mS/m) blank solution. Figure 4a depicts a sequence in which frequency is varied. Prior to the activation of the electrodes, both live and dead cells flow downstream uninhibited. Driving the electrodes at 200 kHz produces a deflection to lower conductivities for both live and dead cells. As we increase the frequency through ~600 kHz, the electric field bypasses the membrane, probing the internal properties of the cell. Since viable cells retain the small ions that lend their cytoplasm its relatively high conductivity (~0.2 S/m) while permeabilized cells do not, the effective conductivity of viable yeast increases with increasing frequency in this regime. Accordingly, we observe the stream of live cells relax into more conductive fluid as the frequency is increased. This trend continues until the effective conductivity of the cells exceeds that of the most conductive fluid in the channel (occurring at around 700 kHz for a maximum medium conductivity of 50 S/m), and the cells undergo p-DEP upon reaching the electrode barrier. If the frequency is increased further still (>10 MHz), we exceed the inverse of the dielectric relaxation time associated with the polarization of the cytoplasm. In this limit, the DEP force becomes independent of the medium and particle conductivities, depending instead only on the relative permittivities. Because the

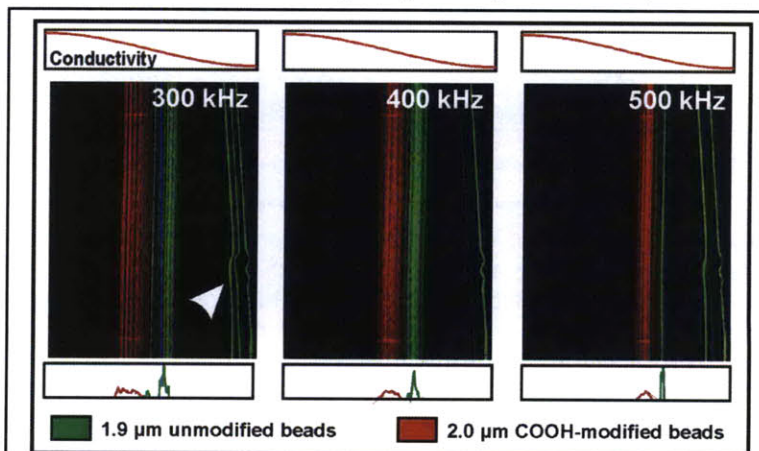


Figure 2- 5: Separation of polystyrene beads based upon differences in surface conductivity, as determined by the presence or absence of modification with charged carboxyl (COOH) groups. Beads without carboxyl modification exhibit lower effective conductivities, despite competing differences in surface-to-volume ratio. The arrow in the leftmost panel indicates particle aggregates which do not pass through the electrode barrier.

fluid permittivity across the channel is essentially uniform and greater than the permittivities of both live and dead cells, the cells are unable to pass over the electrode barrier. Although heat treatment of yeast is known to reduce the cell size by ~5-10%, our observations cannot be attributed to size dependence, since it is the non-viable cells that undergo the greatest deflection.

In further studies, we have confirmed the separations observed under flow by collecting cells and imaging the separated samples under a coverslip (Figure 2- 6b). Also, we have observed that separation and enrichment of rare cells is not contingent on having comparable numbers of viable and non-viable cells, or on those cells being subjected to heat treatment protocol outlined previously. Specifically, we have achieved separation of live and dead yeast taken directly from culture, such that only a small percentage (<5%) are non-viable (Figure 2- 6c).

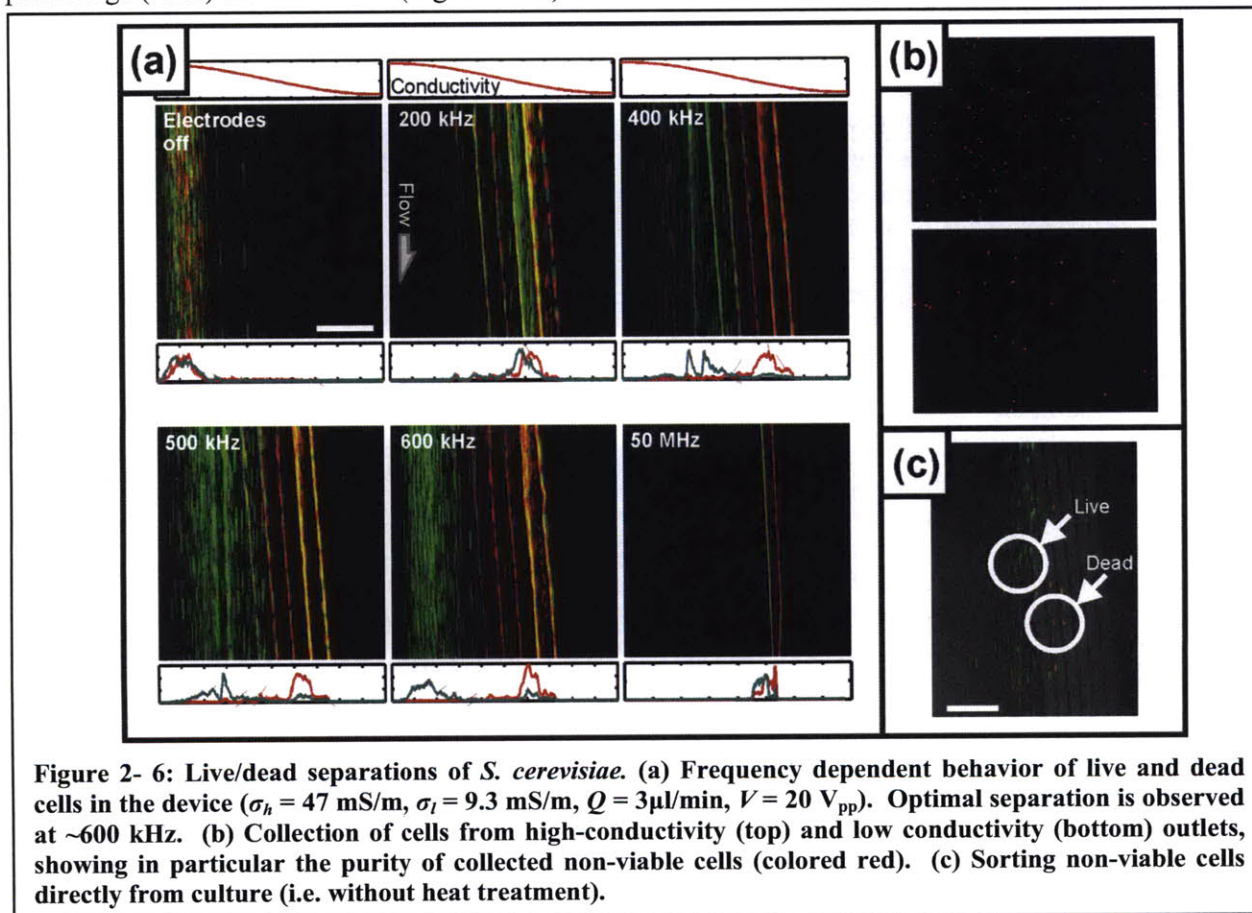


Figure 2- 6: Live/dead separations of *S. cerevisiae*. (a) Frequency dependent behavior of live and dead cells in the device ($\sigma_h = 47$ mS/m, $\sigma_l = 9.3$ mS/m, $Q = 3\mu\text{l}/\text{min}$, $V = 20$ V_{pp}). Optimal separation is observed at ~600 kHz. (b) Collection of cells from high-conductivity (top) and low conductivity (bottom) outlets, showing in particular the purity of collected non-viable cells (colored red). (c) Sorting non-viable cells directly from culture (i.e. without heat treatment).

We determined throughput and resolution for separations of viable and non-viable yeast by performing the assay at multiple flowrates using different cultures of cells in the same IDS device. At a frequency of 500 kHz and flowrates of 1.0 and 1.5 $\mu\text{l}/\text{min}$ (for throughputs of 10^4 and 1.5×10^4 cells/min), we estimate the separation resolution (equation (2- 23)) to be 1.12 ± 0.15 and 1.25 ± 0.30 respectively. For separations performed in a frequency range over which the cells are purely conductive, this would correspond to a minimum resolvable difference in conductivity of ~7.5 mS/m (corresponding to $R_s \approx 0.5$). The observation that a 50% increase in flowrate results in essentially no change in resolution suggests that the quality of the separation under these conditions is more strongly determined by intrinsic variability in the electrical properties of the cells than by non-specific parameters, such as size (for which we measure these cells to have a coefficient of variation of 17%). We have additionally observed that the separation depends upon the concentration of cells injected into the device. While at 10^7 cells/ml, separation resolution falls to $\sim 0.6 \pm 0.05$ at a flowrate of 2 $\mu\text{l}/\text{min}$, decreasing the concentration to $\sim 0.5 \times 10^6$ cells/ml enables separation at flowrates up to 3 $\mu\text{l}/\text{min}$ (Figure 2- 6a, $R_s \sim 1.5$ at 600 kHz). This suggests that

optimum throughput is achieved for high sample concentrations processed at moderately lower flowrates. The relationship between separation performance and sample concentration is explored in considerably more detail in Chapter 4.

Besides resolution, a second metric for characterizing separations of complex mixtures is the peak capacity, which gives the maximum number of peaks that could be fit within the separation window²¹. Peak capacity is most commonly used to describe the performance of batch-mode separations, where the objective is to analyze the composition of the sample rather than sort it for collection. However, because IDS may be used as an analytic method as well as a preparative one, peak capacity serves as a relevant metric in evaluating the analytic potential of IDS. We estimate peak capacities of ~6 and ~4 for optimized separations of polystyrene beads and yeast, respectively. The increased predicted peak capacity for beads over yeast is not surprising, given that monodisperse, synthetic particles are likely to exhibit more narrowly distributed electrical properties than biological cells. Indeed, for applications in which the intrinsic variability of the particles' conductivities is very low, we would expect further improvement in peak capacity. We also note that, if the width of the particle distribution is limited by intrinsic conductivity differences, the peak capacity can be enhanced by using a larger range of conductivities, stabilized against diffusion and induced flow by adopting a correspondingly wider channel.

Discussion. Equilibrium separations can be broadly defined as consisting of a medium with spatial non-uniformities combined with an imposed force field, giving rise to equilibrium positions to which particles stably converge. Within this common framework, however, exists considerable diversity. For example, the specificity of any equilibrium method is fundamentally connected to the nature of the equilibrium it is based upon; the number of intrinsic parameters to which the separation is sensitive will typically increase with the number of forces that combine to create the equilibrium. While the equilibrium position in DGC¹³ is determined by ρ and thus specific to ρ density alone, DEP-FFF³⁴ relies upon the balance between counteracting gravitational and DEP forces, and is therefore sensitive to both density and electrical properties. Accordingly, it is worth distinguishing between methods that achieve equilibrium through counteracting forces and those which exploit a single forcing mechanism that vanishes at some point in the medium, since the latter tend to offer greater specificity. Equilibrium methods may also be categorized according to such interrelated issues as whether they operate in batch or continuous mode, whether they are micro- or macro-scale, and the particular physics that they exploit. The equilibrium in IDS – the IDP – is established by a single forcing mechanism, and, in the implementation we present here, particles are directed towards this equilibrium under continuous flow. Although the operation mode (batch or continuous) is not fundamentally constrained, IDS is inherently a microscale technology, as dictated by the strong dependence of DEP and fluid flow on geometric scale.

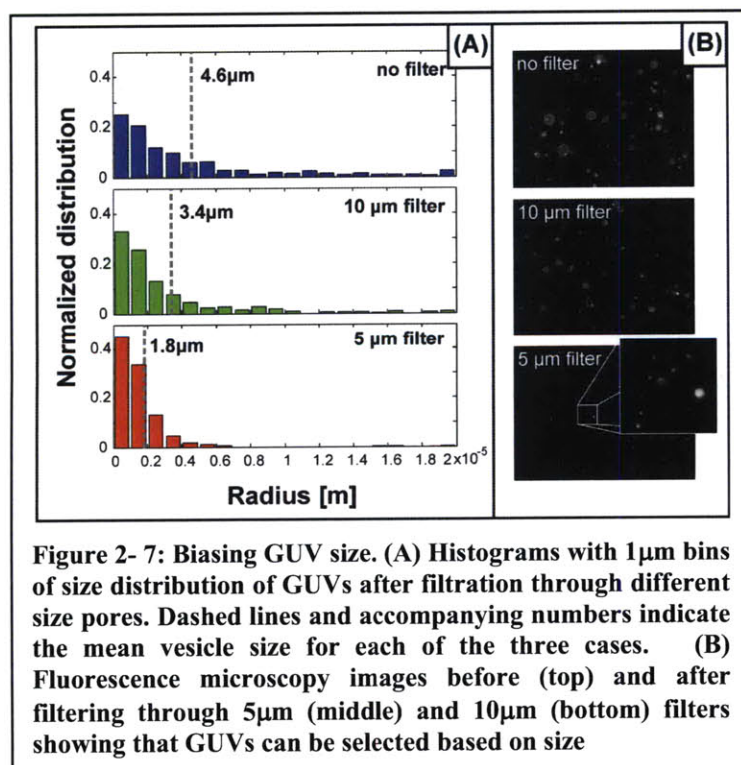
Direct comparison of the resolution and peak capacity of IDS to similar parameters typical of equilibrium separations of biological molecules is complicated by the physically distinct mechanisms that limit performance in each case. While the resolution of molecular separations is fundamentally constrained by thermodynamics, the trajectories of individual particles in IDS are deterministic and directly measurable. Performance limits in IDS are thus largely determined by the intrinsic variability of the cells. Indeed, this feature of IDS could be leveraged as an analytical tool, capable of performing high-throughput measurements of distributions of electrical properties across large populations of cells. Despite these constraints, we are able to achieve $R_s > 1$ reproducibly over several months across several devices. Although the optimal conditions (e.g. frequency and flowrate) for a particular separation may vary from trial to trial, an initial calibration of the device prior to each separation can be performed to assure optimal conditions. This is done by simply observing the separation under different conditions and choosing those that are most effective.

The new physical methodology we present – dielectrophoresis in the presence of non-uniform medium conductivity giving rise to particle-specific equilibrium positions – can be generalized to different architectures with different modes of operation. We envision IDS as a platform allowing researchers to

proceed directly from the creation of a mutant library to screening for a target phenotype with a minimum of intermediate steps, since the separation is intrinsic and no labels are required. Simultaneously, IDS could be used as a quantitative tool; measuring the IDP of particles as a function of frequency, for example, would provide an avenue for determining the impedance spectra for heterogeneous populations of cells, characterizing their electrical phenotype. Realizing these goals will be aided by full characterization of the device's performance, especially in the limits of small particle size and high average media conductivities. The role of higher-order effects, such as the electrostatic and hydrodynamic interactions between particles being sorted, must also be investigated further if IDS is to be extended into a fully quantitative analytic technique⁴⁸. Although we have focused in this work on particles with sizes of $\sim 1 \mu\text{m}$, we expect that IDS can be scaled for separations of smaller or larger specimens (e.g. viruses and mammalian cells, respectively) with modifications to the size and architecture of the current device.

Electrically Addressable Giant Unilamellar Vesicles

One of the greatest challenges in characterizing systems using dielectrophoresis is finding particles with well-defined electrical properties with which to test them. In collaboration with Salil P. Desai, I developed and validated giant unilamellar vesicles (GUVs) as a platform for dielectrophoresis metrology. The following sections describe my specific contributions to this collaboration, consisting of the formation of GUVs with different aqueous interiors and the characterization of these vesicles' sizes and electrical properties. I also present theoretical results prescribing rules for forming vesicles with distinct dielectric dispersions in the presence of polydispersity. The electrically addressable vesicles presented in this work could present a particularly valuable resource for characterizing IDS devices, where polydispersity is less of a limitation, and where it is difficult to find particles whose bulk (as opposed to interfacial) electrical properties can be precisely controlled. For a more detailed description of this work, please refer to the paper published in Langmuir³⁸.



Controlling and Characterizing the Size and Conductivities of GUVs.

Using particles whose dielectrophoretic response is dominated by their interfacial properties to characterize an IDS device is inherently difficult, as these properties will generally change as the composition of their suspending medium changes. We will return to this subject in more detail in Chapter 3. An alternative to these tunable-interface particles that offered tunable and medium-independent *bulk* electrical properties would simplify device characterization considerably. GUVs are promising candidates, in that they may be formed in solutions with a wide range of electrical conductivities, and then resuspended in a different medium. Because the phospholipid bilayer defining the surface of each vesicle is impermeable to ions, as long as the external solution balances the

osmolarity of the encapsulated solution, each vesicle will maintain a constant internal conductivity equal to that of the solution in which it was formed. An additional feature of GUVs is that fluorescent markers

can be incorporated directly within the membrane, or dissolved in the encapsulated medium. This facilitates the creation of vesicle mixtures with distinct electrical properties that can be distinguished using fluorescence microscopy.

The properties of GUVs described above apply regardless of how they are formed, techniques for which vary⁴⁹⁻⁵¹. For simplicity, we have adopted a conventional electroformation protocol. This produces a high yield of polydisperse vesicles with sizes ranging from 100's of nanometers to ~100 μm . While this high degree of polydispersity is potentially limiting for many applications, we have shown that the size distribution can be biased through simple filtration (Figure 2- 7). For characterizing IDS, however, particles with precisely defined electrical conductivity but broadly distributed sizes could provide a useful means of characterizing the size-independence of a separation. This is enabled by the broad range of frequencies over which the dielectrophoretic spectrum of a GUV is dependent almost entirely on the electrical conductivity of its interior, independent of the (size-dependent) capacitance of its membrane.

This is illustrated by considering the mathematical form of a vesicles' complex polarizability. For a vesicle of radius a encapsulating a core of conductivity σ_c and permittivity ϵ_c , and surrounded by an electrically insulating membrane with permittivity ϵ_{mem} and thickness δ , this is given by:

$$\underline{K}(\omega) = \frac{-\sigma_m \sigma_c + i\omega[ac_m(\sigma_c - \sigma_m) - (\sigma_c \epsilon_m + \sigma_m \epsilon_c)] - \omega^2[ac_m(\epsilon_c - \epsilon_m) - \epsilon_c \epsilon_m]}{2\sigma_m \sigma_c + i\omega[ac_m(\sigma_c + 2\sigma_m) + 2(\sigma_c \epsilon_m + \sigma_m \epsilon_c)] - \omega^2[ac_m(\epsilon_c + 2\epsilon_m) + 2\epsilon_c \epsilon_m]} \quad (2- 24)$$

Here, σ_m and ϵ_m represent the conductivity and permittivity of the suspending medium, and we have distilled the membrane properties into a specific capacitance, $c_m = \epsilon_{\text{mem}}/\delta$. This spectrum can be divided according to two dispersions, ω_L and ω_H , and three polarizabilities, K_1 ($\approx \text{Re}\{\underline{K}(\omega \ll \omega_L)\}$), K_2 ($\approx \text{Re}\{\underline{K}(\omega_L \ll \omega \ll \omega_H)\}$), and K_3 ($\approx \text{Re}\{\underline{K}(\omega_H \ll \omega)\}$). From equation (2- 24), the dispersions are:

$$\omega_L = \frac{2\sigma_m \sigma_c}{ac_m(\sigma_c + 2\sigma_m) + 2(\sigma_c \epsilon_m + \sigma_m \epsilon_c)} \quad \omega_H = \frac{ac_m(\sigma_c + 2\sigma_m) + 2(\sigma_c \epsilon_m + \sigma_m \epsilon_c)}{ac_m(\epsilon_c + 2\epsilon_m) + 2\epsilon_c \epsilon_m} \quad (2- 25)$$

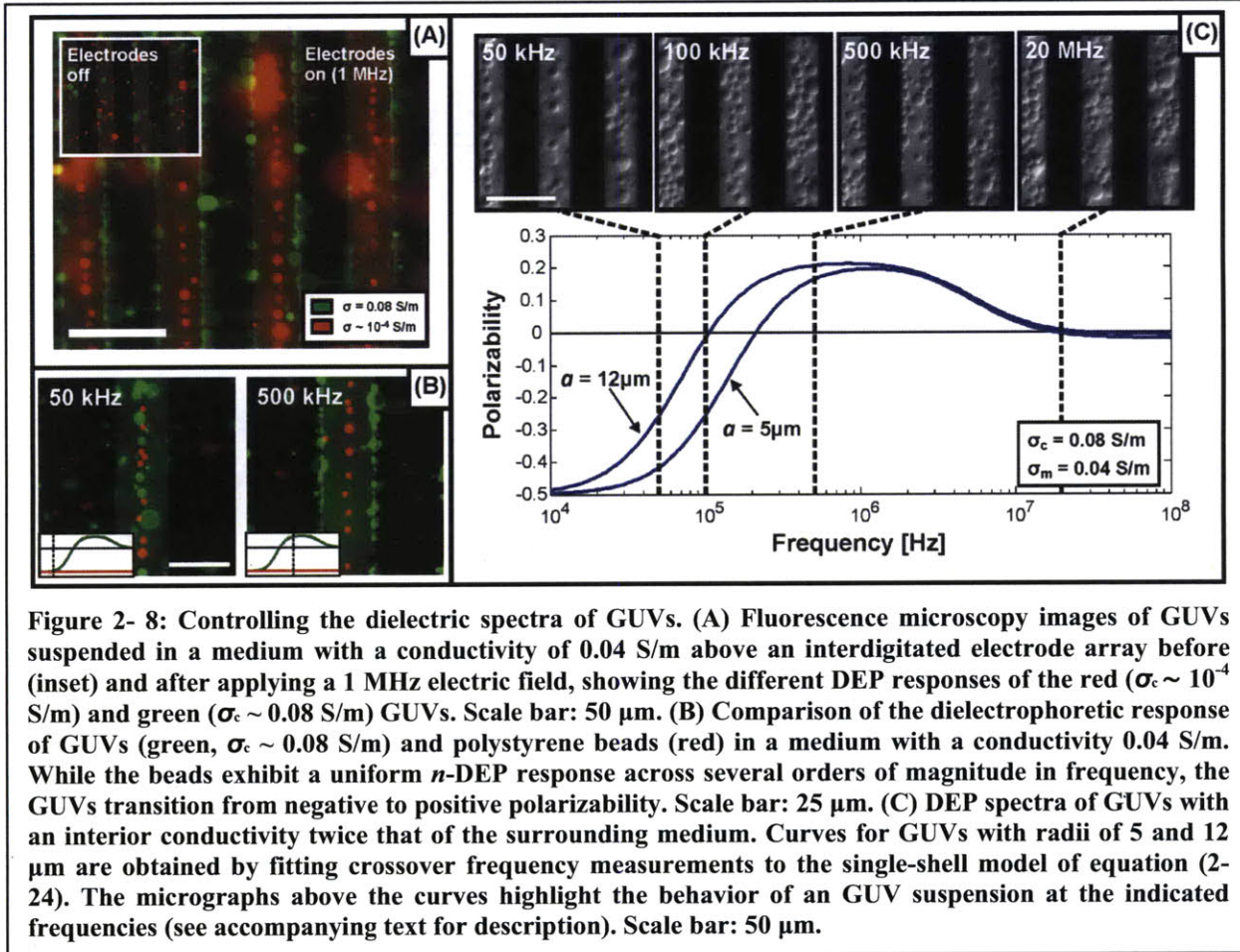
Likewise, the characteristic polarizabilities are:

$$K_1 = -\frac{1}{2} \quad K_2 = \frac{ac_m(\sigma_c - \sigma_m) - (\sigma_c \epsilon_m + \sigma_m \epsilon_c)}{ac_m(\sigma_c + 2\sigma_m) + 2(\sigma_c \epsilon_m + \sigma_m \epsilon_c)} \quad K_3 = \frac{ac_m(\epsilon_c - \epsilon_m) - \epsilon_c \epsilon_m}{ac_m(\epsilon_c + 2\epsilon_m) + 2\epsilon_c \epsilon_m} \quad (2- 26)$$

Of these three polarizabilities, only K_2 is conductivity dependent and thus of direct relevance to IDS. To simplify K_2 and the other expressions, we use the idea that the chemical stability of a vesicle requires a strongly polar solvent on its interior and exterior, such in relevant cases $\epsilon_c \approx \epsilon_m \approx 80\epsilon_0$. Provided that $ac_m \gg 80\epsilon_0$, K_2 reduces to the form of a purely conductive particle suspended in a purely conductive medium, and is independent of the vesicle size. More generally, the vesicle's DEP spectrum will be roughly independent of ac_m for $\omega \gg \omega_L$. Expressing c_m as a function of membrane properties, the requirement for a size-independent, conductivity-specific polarization regime to exist becomes $a/\delta \gg 10$. Assuming $\delta \sim 10\text{nm}$, this is satisfied for any particle larger than $\sim 1\mu\text{m}$.

For frequencies satisfying $\omega_L \ll \omega \ll \omega_H$, the effective conductivity of all vesicles in a suspension larger than $\sim 1\mu\text{m}$ vesicles is simply σ_c , and thus their polarizabilities can be tightly controlled even in the presence of significant polydispersity. Figure 2- 8a shows a mixture of two types of vesicles, one (green) with $\sigma_c = 0.08 \text{ S/m}$, and the other (red) with $\sigma_c \sim 10^{-4} \text{ S/m}$. Suspended in a medium of 0.04 S/m and subjected to an electric field at 1MHz , the more conductive vesicles are attracted to the electrode edges ($K(\omega) \approx K_2 > 0$), whereas the less conductive vesicles are repelled from the electrode edges ($K(\omega) \approx K_2 < 0$). This type of addressability cannot easily be achieved using alternative synthetic particles (e.g. polystyrene beads) since these tend to exhibit flat dielectrophoretic responses when the particle surface-to-volume ratio becomes too small (Figure 2- 8b). Varying the frequency of the electric field applied to a

suspension of vesicles with matching core conductivities illustrates how dielectrophoretic response varies as the frequency passes through the two dispersions (Figure 2- 8c). At low frequencies (50kHz; $\omega < \omega_L$), vesicles of all sizes are repelled from the electrodes; as the frequency is increased through ω_L (~500kHz), larger vesicles begin to localize at the electrode edges, while smaller ones are still repelled; for $\omega_L < \omega < \omega_H$, the vesicles are attracted to the electrode edges, although crowding excludes some of them; finally, as the high frequency dispersion is reached (20MHz), none of the vesicles respond strongly to the applied field.



The illustrative spectra in Figure 2- 8c show the predictions of equation (2- 24) for two vesicles of different radii, showing the size independence for $\omega \gg \omega_L$. To test the validity of the model on which equation (2- 24) is based, we measured the radius and crossover frequencies (ω_0 , such that $K(\omega_0) = 0$) of different vesicles, and used these measurements to determine the effective membrane thickness of each vesicle. Solving for δ as a function of ω_0 gives:

$$\delta = 2a\epsilon_{mem} \frac{(\sigma_c - \sigma_m)(\sigma_c + 2\sigma_m)}{\sigma_c(\sigma_c\epsilon_m + \sigma_m\epsilon_c)} \left[4 \frac{\sigma_m}{\sigma_c} - 1 + 3 \left[1 + \frac{8\sigma_m^2(\sigma_c - \sigma_m)(\sigma_c + 2\sigma_m)}{9\omega_0^2(\sigma_c\epsilon_m + \sigma_m\epsilon_c)^2} \right]^{1/2} \right]^{-1} \quad (2- 27)$$

Measuring crossover frequency across different core and medium conductivities (σ_c and σ_m), and across different batches of electroformed EAVs yields an effective membrane thickness of 9.3 ± 4.3 nm. The sensitivity of δ to ω_0 for typical parameters is such that a 10% change in crossover frequency produces a change of ~8% in predicted membrane thickness. Our measurements are in reasonable agreement with expectation for the thickness of a lipid bilayer and support the validity of this simple model for vesicle polarizability. Specifically, we find that extracted values of δ are fairly independent of

the vesicle radius (correlation coefficient: -0.0026 across 80 individual vesicles) as well as the crossover frequency (correlation coefficient: 0.18). While low coefficients of correlation are not sufficient to prove independence, they do suggest that our measurements are consistent with the functional dependencies of δ on these parameters given by equation (2- 30). Additionally, we find that the specific fluorophore incorporated in the membrane does not lead to a change in electrical properties, with carboxyfluorescein-labeled and rhodamine-labeled vesicles exhibiting no observable difference in crossover frequency (not shown).

Beyond the considerations discussed here, vesicles offer additional advantages as test particles through their mechanical properties. Unlike microspheres of comparable size made of metal or polystyrene, GUVs can be made neutrally buoyant. For particles larger than 10 μm , this prevents rapid sedimentation out of the suspension. Additionally, the ability of GUVs to undergo deformations prevents devices from clogging and enables volume fractions orders of magnitude higher than would be practical for rigid particles of the same size. These characteristics complement their unique DEP spectra, which could not easily be achieved by any other means. Although we have not applied electrically addressable GUVs to a thorough characterization of IDS, our experiments suggest that doing so should be possible.

Alternative Implementations of IDS

In addition to exploring alternative test particles with which to characterize IDS, we have explored alternative implementations of IDS itself. One of the constraints imposed by IDS is that the conductivity gradient must stably persist for a sufficient amount of time to allow particles to be dielectrophoretically driven to their equilibrium positions. In the continuous-flow implementation of IDS that is the focus of this thesis, convective transport is used both to create a temporally stable conductivity gradient as well as to aid in particle actuation. Although the DEP force is highly localized in our device, convection enables long range transport of particles by pressing them into the high-field region as they are steadily deflected across the conductivity gradient. Essentially, the use of convection allows us to decouple the length scales over which the electric field and the conductivity gradient vary. The drawback of this approach is that the strength of the convection limits the degree to which particles converge to their absolute equilibrium positions (see, for example, equation (2- 22), in which equilibrium signifies $K = 0$). Implementation of a convection-free system for IDS could therefore enable greater specificity, but would require that the conductivity gradient in which particles are resolved and the electric field intensity gradient that drives the separation vary over similar length scales. In the course of this thesis, I have considered a number of possible implementations of a “batch-mode” (as opposed to continuous-flow) IDS device. In the following sections, I will briefly outline the most promising of these ideas.

IDS Using Positive Dielectrophoresis. Although the device we have described in this chapter was designed to be operated using negative dielectrophoresis, it is also possible to reverse the direction of the gradient and use positive dielectrophoresis to perform separations. Figure 2- 9 illustrates this concept. Using negative dielectrophoresis, particles are repelled from the electrode gap and trapped upstream of the electrodes, at the channel ceiling (Figure 2- 9a, $K < 0$); with positive dielectrophoresis, particles are generally retained close to the edge of the downstream electrode (Figure 2- 9a, $K > 0$). Figure 2- 9b shows 1.6 μm polystyrene beads (blue) being separated from 1.9 μm polystyrene beads (green). As in Figure 2- 5, the smaller blue beads have a higher effective conductivity, passing through the electrode barrier *later* in this case (4 kHz) than the less conductive 1.9 μm beads. Alternatively, at 35 kHz the larger beads are negatively polarizable across the full range of conductivities (and thus do not pass through the electrode barrier), while the polarizability of the 1.6 μm becomes ~ 0 . Although this alternate mode of operation is feasible and has some notable advantages – in particular, the DEP force will generally be much larger for a given voltage – we do not pursue it further for a number of reasons. First, it is conducive to fouling over time, since particles may become stuck along the electrode edge. Second, when working with cells, it generally prohibits keeping them suspended in culture medium prior to their

separation. A device designed specifically for this more of operation could potentially overcome these limitations.

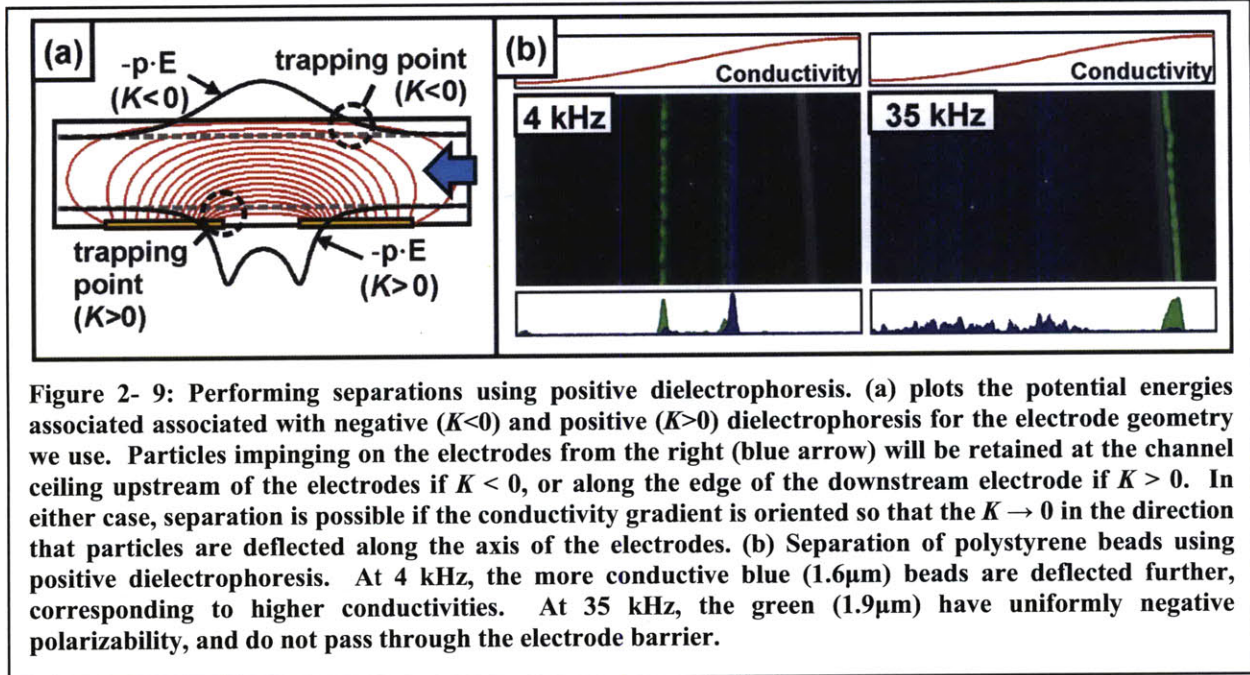


Figure 2- 9: Performing separations using positive dielectrophoresis. (a) plots the potential energies associated with negative ($K<0$) and positive ($K>0$) dielectrophoresis for the electrode geometry we use. Particles impinging on the electrodes from the right (blue arrow) will be retained at the channel ceiling upstream of the electrodes if $K < 0$, or along the edge of the downstream electrode if $K > 0$. In either case, separation is possible if the conductivity gradient is oriented so that the $K \rightarrow 0$ in the direction that particles are deflected along the axis of the electrodes. (b) Separation of polystyrene beads using positive dielectrophoresis. At 4 kHz, the more conductive blue ($1.6\mu\text{m}$) beads are deflected further, corresponding to higher conductivities. At 35 kHz, the green ($1.9\mu\text{m}$) have uniformly negative polarizability, and do not pass through the electrode barrier.

Conductivity Sources and Sinks. If a steady state concentration gradient can be maintained in the absence of convection, constraints on the magnitude of the dielectrophoretic force are relaxed considerably. One way to achieve this is through the use of concentration sources and sinks that are hydrodynamically isolated from the separation chamber through, for example, a nanoporous membrane. One plausible implementation could consist of two layers of overlapping microfluidic channels with a membrane separating them. Solute exchange between the two fluidic layers could be controlled by perfusing the source/sink layer at a high rate relative to the separation layer, allowing steady conductivity gradients to form. Flow within the separation layer could then be modulated (or stopped altogether) without complete attenuation of the gradient.

A two-dimensional (shallow-channel) model for this class of devices can be constructed by averaging the steady state conservation equation for conductivity over the depth of the channel:

$$\mathbf{u} \cdot \nabla \sigma = D \nabla^2 \sigma + \frac{D_{mem}}{h\delta} (\sigma_s - \sigma) s(x, y) \quad (2-28)$$

Here, \mathbf{u} and σ are functions of x and y only, and the source term arises from the flux of positive and negative ions (conductivity) from a source or sink maintained at conductivity σ_s across a membrane with diffusion coefficient D_{mem} and thickness δ . The function $s(x, y)$ captures the geometry of the overlapping regions of source/sink channels with the separation channel ($s = 1$ where there is an overlap and $s = 0$ otherwise). Whereas before, the conductivity profile was fully determined by one dimensionless parameter (the Peclet number, Pe), the source/sink term introduces a second. Taking as our length scale the distance over which the conductivity varies ($= w$), equation (2-28) becomes:

$$Pe \tilde{\nabla} \tilde{\sigma} = \tilde{\nabla}^2 \tilde{\sigma} + \frac{w^2 D_{mem}}{h\delta D} (\tilde{\sigma}_s - \tilde{\sigma}) s \quad (2-29)$$

The new dimensionless parameter (“ λ ” for simplicity) depends on the relative diffusivity of ions inside the membrane versus in the bulk electrolyte (D_{mem}/D), as well as the geometric ratio $w^2/h\delta$. Depending on

the magnitudes of Pe and λ , either convection, diffusion, or solute exchange through the membrane could dominate the conductivity profile.

One limiting case is that in which $Pe \cdot \nabla\sigma = 0$, so that the gradient is determined from the balance between diffusion and exchange with the source and sink channels. For the simple geometry shown in Figure 2- 9a, a solution is:

$$\tilde{\sigma} = \frac{(\sigma - \sigma_l)}{(\sigma_h - \sigma_l)} = \begin{cases} \frac{1}{2} \left[\frac{\sinh(\lambda^{\frac{1}{2}}/2)}{\cosh(\lambda^{\frac{1}{2}}/2)} \sinh(\lambda^{\frac{1}{2}}\tilde{x}) + \cosh(\lambda^{\frac{1}{2}}\tilde{x}) \right] & -1/2 < \tilde{x} < 0 \\ 1 + \frac{1}{2} \left[\frac{\sinh(\lambda^{\frac{1}{2}}/2)}{\cosh(\lambda^{\frac{1}{2}}/2)} \sinh(\lambda^{\frac{1}{2}}\tilde{x}) - \cosh(\lambda^{\frac{1}{2}}\tilde{x}) \right] & 0 < \tilde{x} < 1/2 \end{cases} \quad (2- 30)$$

Using this result, we can calculate the transfer efficiency of solute from the source/sink channels to the separation channel as a function of λ in the absence of the effects of convection. The normalized difference between the range of conductivities within the separation channel and the range spanned by the source and sink channels is given by $\tilde{\sigma}(1/2) - \tilde{\sigma}(-1/2) = 1 - \cosh(\sqrt{\lambda}/2)^{-1}$. For large λ (>10), this simplifies to $1 - 2\exp[-(\sqrt{\lambda}/2)]$, suggesting that at $\lambda \sim 36$ the conductivity will be maintained with 90% of the target value. Although this result was derived for a simple rectangular geometry, it should provide general design guidelines for any such device operating under the same principle.

In this discussion, I have focused on a two-layer geometry with a permeable membrane dividing the two layers. Such devices have been demonstrated in the literature for other purposes⁵², and the fabrication and assembly techniques should be applicable to building an IDS device. However, other techniques could be applied as well, including using dialysis tubing as the walls of a microfluidic channel⁵³.

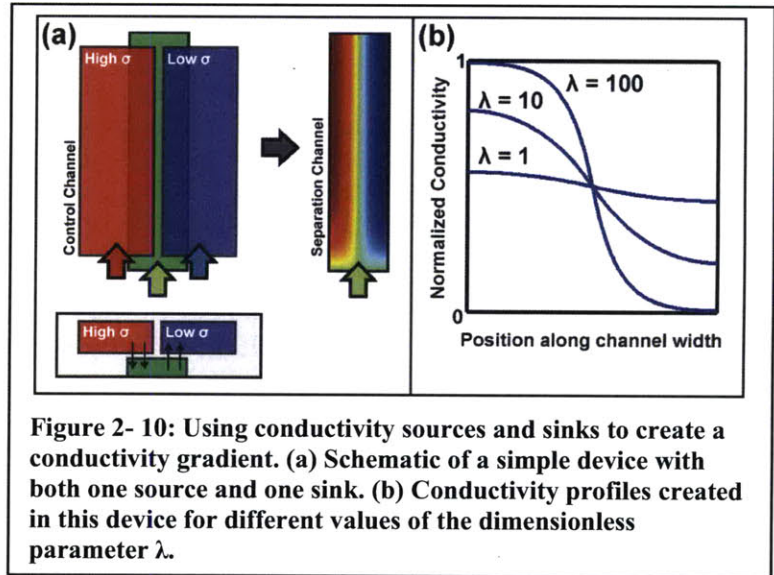


Figure 2- 10: Using conductivity sources and sinks to create a conductivity gradient. (a) Schematic of a simple device with both one source and one sink. (b) Conductivity profiles created in this device for different values of the dimensionless parameter λ .

Long-Range Dielectrophoresis. Although conductivity sources and sinks present a solution to one challenge – creating stable and persistent gradients in electrical conductivity – the challenge of creating a long range dielectrophoretic force to drive the separation remains. This challenge is illustrated by the typical scaling with length of the DEP force as L^{-3} , where L is a characteristic length of the electrode geometry. Confined electrodes give stronger forces, but lower range of actuation.

One approach to relaxing this constraint which I have explored is to decouple the lengths over which the electric potential and electric field intensity vary. The device consists of two parallel plate electrodes, coated with a thin film of indium tin oxide (ITO), which act as the ceiling and floor of a shallow ($\sim 50 \mu\text{m}$) microfluidic channel. Although electrically conducting, these ITO layers have a non-negligible (for our purposes) resistivity of $\sim 50 \Omega$ per square. On top of the ITO film, we pattern additional electrodes using gold, which act as perfect conductors. By applying voltage differences both *across* an ITO electrode as well as *between* the ITO electrodes, it is possible to shape electric field gradients to generate long-range dielectrophoretic forces driven by a high-intensity electric field. For example, if the voltage across the

lower electrode decreases linearly from 1 to 0 across the width of the chamber, the electric potential is given by:

$$\varphi(\tilde{x}, \tilde{z}) = \frac{1}{2} \left[1 - \tilde{z}/\varepsilon \right] + \sum_{\substack{n=1 \\ n \text{ odd}}}^{\infty} \frac{4}{(n\pi)^2} \left[\cosh(n\pi\tilde{z}) - \frac{\sinh(n\pi\tilde{z})}{\tanh(n\pi\varepsilon)} \right] \cos(n\pi\tilde{x}) \quad (2-31)$$

Here, x and z have been normalized by the channel width and height, respectively, so that $\varepsilon = h/w$. If we ignore the boundary conditions at $\tilde{x} = 0$ and $\tilde{x} = 1$ and assume $\varepsilon \ll 1$, the convenient approximation $\varphi = (1 - \tilde{z}/\varepsilon)(1 - \tilde{x})$ can be used (more generally, this is $\varphi = (1 - \tilde{z}/\varepsilon)v(\tilde{x}, \tilde{y})$, where v is the voltage in the x - y plane of the lower ITO substrate; throughout this section, we assume that insufficient current is drawn through the liquid in the chamber to appreciably alter this voltage). The advantage of this approach is that it introduces two distinct length scales, parameterized by ε , over which the electric field varies: the chamber height and width. This enables the creation of an electric field with a high intensity ($\propto h^{-2}$) that varies steadily over a large distance (w). An additional advantage of this geometry is that the electric field is primarily oriented orthogonal to the direction in which the DEP force acts, and thus the direction in which the conductivity would vary. This helps to minimize polarization of the fluid (equation (2-8)) and thus reduce electrohydrodynamic convection. Although other geometries – for example, a wedge-shaped channel – can achieve high-intensity fields that vary over large distances, these are considerably more difficult to make using conventional microfabrication. One limitation of this approach is that particles are polarized along the axis normal to the conductive plane of the ITO electrodes, and are attracted to their electrostatic image in these plains. Because the x -directed DEP force vanishes as $\tilde{z} \rightarrow \varepsilon$, these devices work best with particles whose size is comparable to the chamber height, so that they are sterically confined to the region where the x -directed force is larger. Electrically addressable vesicles, discussed previously, are ideal for characterizing these systems due to their size (up to tens of microns in diameter) and the ability to control the conductivity of their aqueous core.

This concept can be generalized to more complicated imposed voltages on the ITO electrode. For example, if one ITO electrode is held uniformly at ground while the other carries multiple superimposed signals $v(x, y) = \sum_n v_n(x, y)e^{i\omega_n t}$, the electric field intensity (for a shallow chamber) will be approximately v^2/h^2 . Although this non-linearity introduces mixing of the different frequencies, ω_n , only terms with matching frequencies will produce a non-zero time average and contribute to the dielectrophoretic force. Accordingly, the trajectory of a particle can be determined from:

$$\frac{d\mathbf{x}}{dt} = \alpha \sum_n K(\omega_n) v_n \nabla v_n \quad (2-32)$$

where $K(\omega_n)$ denotes the polarizability of the particle at frequency ω_n . This shows that the time-averaged DEP force arising from superimposed signals is the same as the superposition of the DEP forces arising from each signal separately.

The ability to pattern and superimpose different signals on the ITO substrate to shape electric field intensity gradients enables particles to be routed in complex configurations. For example, by grounding both sides of one ITO slide while switching the polarity of the voltage drop across the other ITO slide, it is possible to move vesicles back and forth across the chamber at speeds of $\sim 30 \mu\text{m/s}$ (Figure 2- 10b). Introducing additional electrical contacts allows particles to be moved anywhere within the two-dimensional plane of the chamber by altering the configuration of active and ground electrodes (Figure 2- 10c). Because this method of manipulation is strongly size dependent (due to the volumetric dependence of dielectrophoresis combined with the tendency of particles to move to the ITO surfaces), only the largest vesicles are affected. This could be used for high sensitivity filtration of large vesicles or to manipulate large, payload-bearing vesicles relative to smaller cells before rupturing the vesicle by pulsing with a short, high-amplitude electric field.

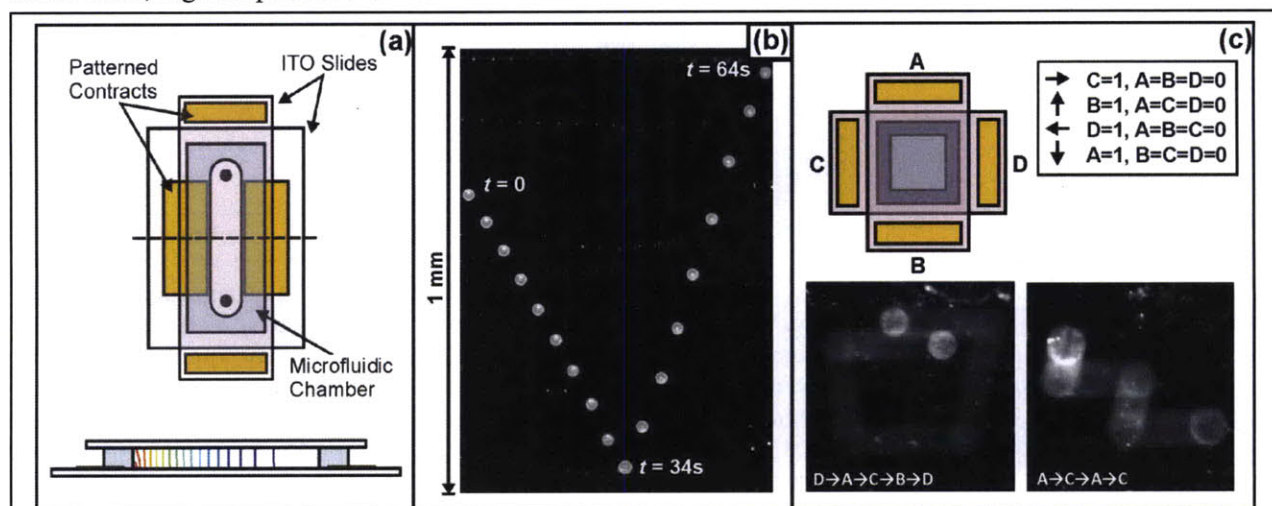


Figure 2- 11: Long-range, reconfigurable dielectrophoresis. (a) A schematic of the device (top and side views), consisting of two ITO-coated slides, each with two electrical contacts, and a microfluidic channel, defined by a gasket placed between the slides. (b) Tiled snapshots of a movie showing the dielectrophoretic actuation of a GUV in both directions across a 1-mm-wide channel. Note that smaller vesicles visible in the background are not appreciably deflected from frame to frame. (c) A more complex reconfigurable scheme, in which vesicles can be moved anywhere within the two-dimensional plane of the device by altering which electrical contact is high (denoted as '1'), and which are grounded ('0'). The two lower images show time-averaged trajectories of vesicles obtained in this way.

Additional functionality can be achieved by superimposing signals at different frequencies on the same ITO substrate. In particular, if the two signals counteract each other, they can be used to focus particles to an equilibrium position that depends on their polarizabilities at the selected frequencies. This approach to separation has recently been demonstrated in a different platform⁵⁴. In our particular implementation, we ground the upper ITO electrode and apply signals of different frequency on opposite sides of the lower ITO electrode. Accordingly, for a particle at the either side of the chamber, one frequency will dominate; choosing these frequencies appropriately (i.e. such that the particles have a negative polarizability at both frequencies, but possibly of different magnitudes) results in particles focused somewhere in the middle of the chamber. Figure 2- 11a shows steady state images of fluorescent polystyrene beads deflected to either side of the chamber when the signals are applied separately, and focused in the middle when they are superimposed. Similarly, Figure 2- 11b shows two different cell types (HL60s, green; and BA/F3s, red) focused in this way.

As is evident in Figure 2- 11b, we did not observe any separation of the two cell types. Although this may be due to inherently similar electrical properties, it is more likely due to two significant but surmountable limitations to this approach. First, because these experiments are performed in cell culture media ($\sigma \sim 1.5$ S/m), significant current is diverted through the medium as opposed traveling directly through the ITO as would occur if the liquid were a pure dielectric. This causes the voltage drop across the lower substrate to attenuate more rapidly, making the focusing of particles less sharp. Second, although focused particles are in equilibrium under the counteracting forces, they remain strongly polarized by the superposed electric field, and thus interact with each other through their induced dipole moments (oriented along the axis out of plane). This effectively leads to a roughened energy landscape in which particles become jammed (Figure 2- 11c). In conductivity gradient IDS, the equilibrium position is characterized by vanishing polarizability, and thus the absence of electrostatic interactions between particles; the same device using a single frequency and a conductivity gradient could offer superior performance. A second approach to improving the focusing and separation of particles is to introduce time-varying forces with zero mean (for example, a slowly oscillating velocity field), so that the arrangement of cells could sample different configurations, and thus converge more closely to the optimum global state. This is analogous to Brownian motion, but for cells and particles too large ($\sim 10\mu\text{m}$) to be affected by thermal forces. In the continuous-flow implementation of IDS that is the focus of the rest of this thesis, hydrodynamic interactions between particles serve as this surrogate to thermal forces, allowing tightly coupled aggregates of particles to sample different spatial configurations. This phenomenon is discussed in more detail in Chapter 4.

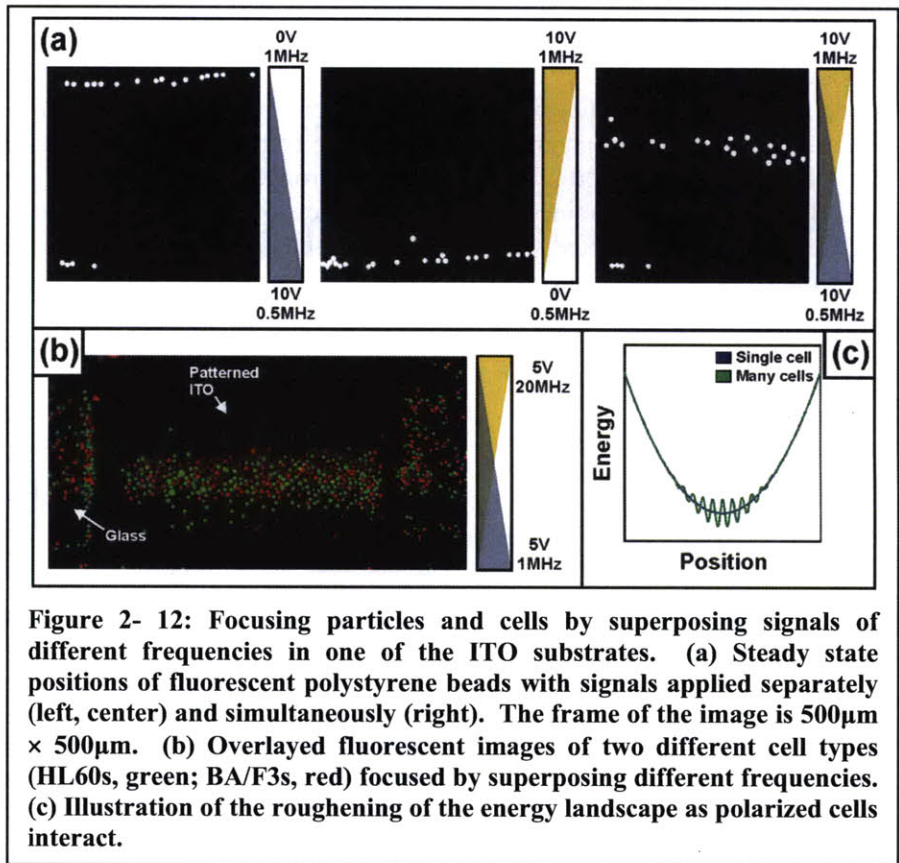


Figure 2- 12: Focusing particles and cells by superposing signals of different frequencies in one of the ITO substrates. (a) Steady state positions of fluorescent polystyrene beads with signals applied separately (left, center) and simultaneously (right). The frame of the image is $500\mu\text{m} \times 500\mu\text{m}$. (b) Overlaid fluorescent images of two different cell types (HL60s, green; BA/F3s, red) focused by superposing different frequencies. (c) Illustration of the roughening of the energy landscape as polarized cells interact.

Appendix to Chapter 2

Fabrication Process Flow

Starting Materials:

- 150-mm-diameter, 762- μm -thick Pyrex wafers (Bullen Ultrasonics, Eaton, OH)
- 150-mm-diameter, 650- μm -thick Silicon wafers (WaferNet, Inc., San Jose, CA)

Step	Description	TRL Machine	Parameters
Electrode Patterning, 6" Pyrex wafer			
1	Piranha clean	Acid hood	
2	Dehydration bake	HMDS oven	120°C, 30 min
3	HMDS	HMDS oven	Recipe 4
4	Photoresist coat	Coater	NR-7 photoresist: - spread 6s, 750 rpm - spin 30s, 2500 rpm
5	Prebake	Hotplate station	155°C (plate setting), 90s
6	UV expose	EV1	10s continuous, hard contact
7	Post-expose bake	Hotplate station	120°C (plate setting), 2 min
8	Develop, rinse and spin dry	Photo-wet bench	RD6 in a shallow beaker: - Gently agitate for 25-30s - Rinse with dH ₂ O - Use fresh RD6 with each wafer
9	Metal evaporation	E-beam	100Å Ti, 2000Å Au
10	Liftoff metal	Solvent-Au	
11	Protective resist coat	Coater	AZ 5214E, 500 rpm final speed
12	Bake	Hotplate station	120°C, 2 min
13	Dice wafer	Die saw	

Microfluidic Channel Patterning, 6" Silicon wafer			
1	Dehydration bake	Hotplate station	200°C, 30min
2	SU-8 Spin	SU8-spinner	SU-8 2015 (20 µm thickness): Dispense ~6ml SU-8 (1ml per inch diameter) Ramp to 500 rpm at 100 rpm/sec accel and hold for 5-10 seconds Ramp to 2250 rpm at 300 rpm/second and hold for total of 30 seconds
3	Prebake	Hotplate station	Slow ramp from 60°C to 95°C, hold at 95°C for 2 min; cool to ambient
4	UV expose	EV1	Flow chamber mask, 12 sec, 30 µm separation
5	Post-expose bake	Hotplate station	Slow ramp from 60°C to 95°C, hold at 95°C for 2 min; cool to ambient
6	Develop	Solvent-Au	~3-5 min soak in PM Acetate 30s spin while spraying with PMA 30s spin while spraying with IPA 30s spin dry
7	Silanize wafer	EML acid hood	Put 3-4 drops of HMDS into cup in vacuum jar. Lean wafer against wall of jar, exposing both front and back Close jar, turn on vacuum for 5-10 minutes, Turn vacuum off, let sit ~30 minutes.

Chapter 3: Performing Analytical Separations

Separations can be broadly categorized as *preparative*, where the objective is to extract purified quantities of a sample from a complex mixture, or *analytical*, where the goal is to determine and quantify the contents of the original mixture. This chapter describes the development of IDS into an analytical method, capable of measuring the electrical properties of cells and particles as a function of electric field frequency and medium conductivity. Specifically, we discuss the mathematical model used to obtain quantitative information from experimental data, as well as the application of IDS to measure the electrical properties of polystyrene microspheres, viable and non-viable yeast (*Saccharomyces cerevisiae*), and murine pro B cells, including how these electrical properties vary with the electrical conductivity of the surrounding solvent.

Much of the content of this chapter is taken from the second of two papers published in Analytical Chemistry⁵⁵. It is important to acknowledge the help of Susan Lindquist and Salil P. Desai in providing and transfecting the BA/F3 mouse pro B cells used in this chapter.

Introduction

Electrical properties, such as conductivity and permittivity, offer both insight into the composition and structure of cells and particles, as well as provide an intrinsic handle upon which separations can be based. Over the past several decades, dielectrophoresis (DEP)³¹, electrorotation^{47,56} and impedance spectroscopy^{24,25} have emerged as effective techniques for characterizing the charge, conductivity, and permittivity of cells over a broad range of conditions. Simultaneously, related techniques – in particular, dielectrophoresis - have also proven effective as mechanisms for cell sorting^{57,58}. Still, for electrical separations to be most effective requires a more extensive understanding and characterization of cell properties. This improved understanding – a mapping of genetic and phenotypic information to the electrical properties of individual or groups of cells - could lead to new applications; however it requires techniques for measuring cell properties that are high throughput, adaptable to a wide range of cell types, and capable of rapidly exploring a large parameter space of environmental conditions. Despite the need for such measurements and the fundamental connection between cell characterization and cell sorting, to date, previous technology has focused on either cell separation or on cell characterization, with exceptionally few attempts to combine these two functionalities to create an analytic cell separation method.

We have recently developed a new method, called iso-dielectric separation (IDS), capable of performing *preparative* separations of cells and particles based upon their electrical properties over a range of frequencies and medium conductivities⁵⁹. An analogy can be drawn between IDS and iso-electric focusing (IEF), a widely used analytic separation method for sorting and characterizing mixtures of biomolecules. In IEF, molecules with a pH-dependent charge are focused by an electric field in a pH gradient to equilibrium – the iso-electric point, where the net charge vanishes. In IDS, dielectrophoresis – the translational force on a polarizable body in a spatially non-uniform electric field²² - is used to drive cells and particles in an electrical conductivity gradient to the iso-dielectric point, or IDP, where the net *polarization* charge vanishes. We have previously demonstrated the efficacy of IDS for separating mixtures of synthetic polystyrene beads according to surface conductance, as well as biological cells according to a phenotypic marker (i.e. viable and non-viable cells of *S. cerevisiae*)⁵⁹. In the present work, we focus on the use of IDS as an *analytical* tool for characterizing the electrical properties of cells and particles, including functionalized and non-functionalized polystyrene beads, viable and heat treated yeast, and mammalian white blood cells.

Figure 3- 1 illustrates the concept of IDS. The principle of operation is identical to that described previously. Briefly, the device consists of a microfluidic channel into which we load a high conductivity solution, containing the suspension of cells or particles, and a low conductivity solution, free of particles. These solutions pass through a diffusive mixer, which establishes a smoothly varying conductivity profile

at the entrance to a separation channel. The separation channel contains electrodes arranged across the bottom surface at a shallow angle with respect to the direction of flow in the channel. Because the particles are initially suspended in a high-conductivity solution, in which they exhibit negative polarizability, the non-uniform electric field created by the electrodes deflects the particles across the width of the channel, in the direction of decreasing medium conductivity. As the medium conductivity surrounding the particle decreases, so too does the particle's polarization. This continues until the imposed drag force, acting along the axis of the channel, overwhelms the dielectrophoretic force created by the electrode barrier, allowing the particles to flow downstream unobstructed. Here, the particles may either be imaged (if the objective is to record their positions for the purpose of characterization), collected from one of a number of outlets (four in our architecture, though more could easily be added), or both. In this work, we are focused primarily on demonstrating the ability to characterize particles and thus imaged them at the outlet. Because the position along the width of the channel that a particle exits the device can be related back to the conductivity of the medium, the spatial distribution of particles at the outlet of the device encodes information about those particles' electrical properties. In its use of a variable medium conductivity, IDS is superficially similar to a technique developed by Marx *et al.*²²; however, while this previous approach leveraged a temporally applied "gradient" and was not extended to particle measurement, the conductivity gradient in our work is applied spatially (and is therefore a true gradient), and we focus in the current work on extending IDS as a tool for measuring cellular properties.

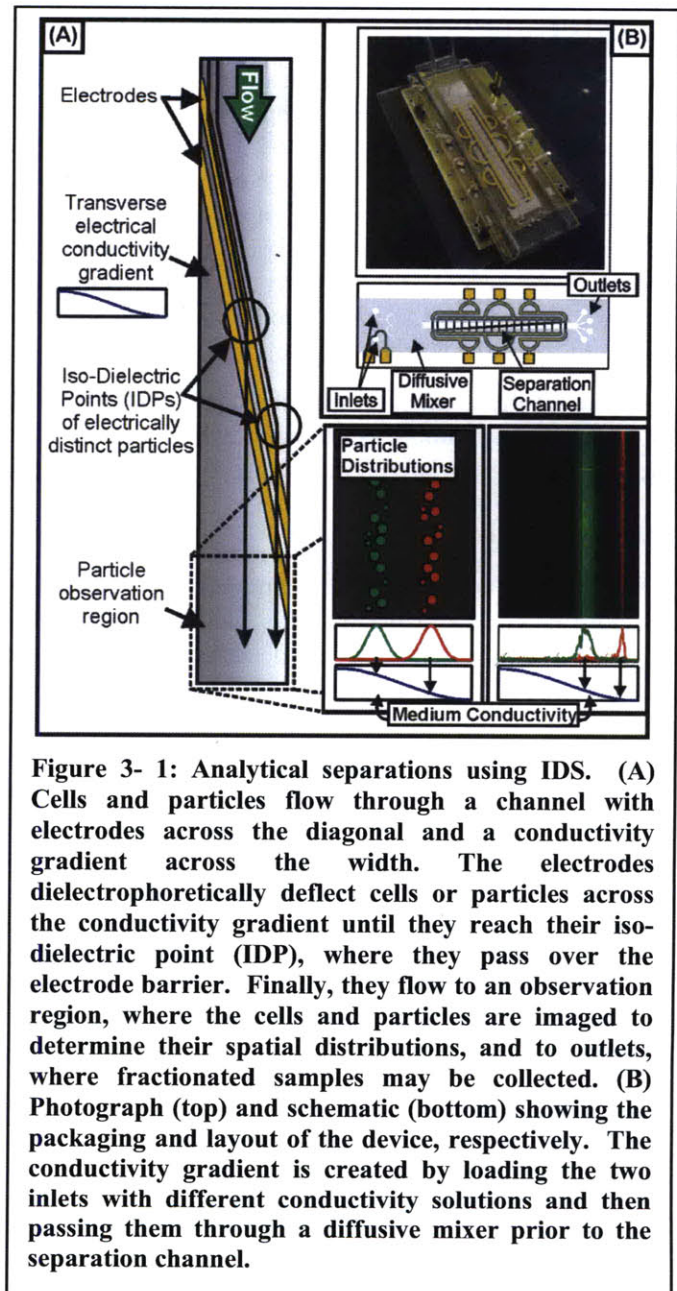


Figure 3- 1: Analytical separations using IDS. (A) Cells and particles flow through a channel with electrodes across the diagonal and a conductivity gradient across the width. The electrodes dielectrophoretically deflect cells or particles across the conductivity gradient until they reach their iso-dielectric point (IDP), where they pass over the electrode barrier. Finally, they flow to an observation region, where the cells and particles are imaged to determine their spatial distributions, and to outlets, where fractionated samples may be collected. (B) Photograph (top) and schematic (bottom) showing the packaging and layout of the device, respectively. The conductivity gradient is created by loading the two inlets with different conductivity solutions and then passing them through a diffusive mixer prior to the separation channel.

Based on the characterization results presented in Chapter 2, we designed a second-generation IDS device that more effectively takes advantages of the scaling laws we derived (equations (2- 20) through (2- 22)) in order to improve performance. Specifically, we doubled both the channel width (to 2 mm) and length (to 3 cm); this reduces the significance of electrohydrodynamic flows (equation (2- 20)) while simultaneously doubling the potential throughput or sensitivity (corresponding to Q_0 and $1/K$ in equation (2- 22), respectively). These new devices, shown in Figure 3- 1B, have a larger footprint than previous designs, with the pyrex chip being the size of a standard microscope slide (25mm \times 75mm).

One feature of using IDS for measuring particle properties is its insensitivity to particle volume. Because the dielectrophoretic force is volumetric, most methods that use DEP are very sensitive to cell

size. It is more difficult to specifically measure the electrical properties of cells, which manifest themselves as the effective conductivity and permittivity of the cell, embedded in the dimensionless Clausius-Mossotti factor, $\underline{K}(\omega)$:

$$\underline{K}(\omega) = \frac{\underline{\sigma}_p - \underline{\sigma}_m}{\underline{\sigma}_p + 2\underline{\sigma}_m} \quad (3-1)$$

Here, $\underline{\sigma}_p$ is the complex (frequency dependent) conductivity of the particle, given by $\underline{\sigma}_p \equiv \sigma_p + i\omega\varepsilon_p$. When $\text{Re}\{\underline{K}\} = 0$, the particle is no longer polarized by the applied field, and the translational force vanishes. Importantly, the location of this iso-dielectric point in the conductivity gradient is determined only by the conductivity and permittivity of the cell and the surrounding medium, *independent of the cell volume or other parameters*. As a result, by observing convergence of cells to this point in the gradient, we obtain a more specific measurement of a cell's electrical properties than is typically possible using dielectrophoresis.

A second feature of IDS is that it operates in a continuous flow manner, enabling the rapid characterization of $>10^4$ cells per minute, including both the mean and variance of properties across a population. This is in contrast to techniques such as electrorotation⁴⁷, from which one must obtain detailed spectra for individual cells somewhat laboriously, or bulk impedance measurements⁶⁰, which only provide electrical properties averaged over large populations. While microfluidic impedance spectroscopy techniques have recently been developed to achieve high-throughput measurements of a broad range of the dielectric spectra of cells²⁵, these methods consider only a single media conductivity at a time, whereas IDS enables rapid measurements of electrical properties subjected to variable medium conditions. Because particles with sizes of $\sim 1 - 10 \mu\text{m}$ typically reach diffusive equilibrium on a timescale of $\sim 1-100 \text{ ms}$ (a^2/D) while residence time in the separation channel is typically $\sim 10 \text{ s}$, particles can be treated as instantaneously adjusting to variations in the external medium. This allows us to simultaneously map out the frequency and conductivity dependence of $\text{Re}\{\underline{K}\}$ by varying the conditions (i.e. applied voltage, frequency, and flowrate) of the separation. Examples of cells and particles for which electrical properties depend sensitively on the external environment are pervasive, including any particle or cell for which the outermost layer supports fixed charge and/or is porous. In these (nearly ubiquitous) cases, the ability to measure the dependence of polarizability on frequency and medium conductivity in a way that is essentially simultaneous complements existing characterization methods²⁵ that focus on high-bandwidth measurements of electrical properties across varying frequencies. The combined advantages of insensitivity to variations in non-specific parameters (e.g. volume, density, etc.), high-throughput measurements of population averages and variation, and the ability to consider a range of frequencies and medium conductivities in a single experiment make IDS a promising tool for particle characterization and separation, and an effective complement to existing techniques well suited to obtaining high-resolution spectra of cells and particles at single conductivities.

Theory

Interpreting the results of a separation to obtain quantitative information about the cells or particles being analyzed requires quantitative understanding of how the device operates. In general, the characteristics of a separation are determined by the contributions of both specific and non-specific forces acting on the particles. Here, a specific force refers to any force which depends upon the property of the particle being targeted for separation. Since IDS separates particles according to their effective electrical conductivity, dielectrophoresis represents the specific force within the system, whereas all other forces (hydrodynamic, gravitational, etc.) comprise non-specific forces, and thus interfere with the purity of the separation and undermine the potential for analysis. In Chapter 2, we developed models for designing devices capable of creating electric fields in conductivity gradients while mitigating electrohydrodynamic flows, as required for IDS. In this section, we expand on these models to address the task of

quantitatively correlating particle position in the device to that particle's electrical properties in the face of specific and non-specific forces.

Mass transport. Because the DEP force depends on the conductivity throughout the device's separation channel, specifying the forces acting on particles requires the analysis of mass transport in the system. We have described previously⁵⁹ the normalized steady-state conductivity profile $\tilde{\sigma}_m$ obtained throughout the separation channel. Taking equation (2- 2) from Chapter 2 and setting $y = (\ell/w)x$ (or, in terms of dimensionless coordinates, $\tilde{y} = \tilde{x}$), we can obtain an expression for the conductivity in the frame of a particle as it is being deflected along the electrodes:

$$\tilde{\sigma}_m(\tilde{x}) = \frac{1}{2} + \sum_{n=1}^{\infty} a_n \cos(n\pi\tilde{x}) \exp\left[-\frac{(n\pi)^2}{\text{Pe}} \tilde{x}\right] \quad (3- 2)$$

This expression provides a means for mapping the position of a particle along the channel width (x) to the medium conductivity at which it reaches its threshold polarizability (σ_m). To extend this analysis to determining the electrical properties of the cells, we must relate this medium conductivity to the threshold polarizability, K , at which particles pass through the DEP barrier. For this, we can use equations (2- 20)-(2- 22) from Chapter 2.

Force Balance. The threshold polarizability of a particle is determined from the balance between drag and dielectrophoretic forces. The force on a particle in a shallow channel, subject to an imposed external force and Poiseuille flow is given by⁶¹:

$$\mathbf{F}_{DEP} = 6\pi\mu a \left[\xi_1 \mathbf{u}_p - \xi_2 \mathbf{U}_0 \right] \quad (3- 3)$$

where \mathbf{F}_{DEP} denotes the DEP force, \mathbf{u}_p denotes the particle velocity, and \mathbf{U}_0 denotes the average velocity of the imposed Poiseuille flow. The parameters ξ_1 and ξ_2 are dimensionless corrections for the Stokes drag coefficient, necessitated by the nonuniform fluid velocity and the presence of the channel floor and ceiling. Integrating \mathbf{u}_p with respect to time determines the trajectory of a particle subject to drag and DEP forces (Figure 3- 2A, *left*). Because the particle polarizability and thus the DEP force vary with the conductivity, as particles approach their iso-dielectric points, $\mathbf{F}_{DEP} \approx 0$ and the particles pass through the DEP barrier. This will occur when the polarizability reaches a threshold value, $\text{Re}\{K\} = K_0$, such that the particle is no longer deflected along the axis of the electrodes. This corresponds to the condition that:

$$U_{DEP}^{\max} = [\xi_2 \sin \theta] U_0 \quad (3- 4)$$

Here, the angle θ denotes the inclination of the electrodes with respect to the direction of flow, and we have defined the dielectrophoretic “velocity”, \mathbf{U}_{DEP} , of a particle of radius a in a fluid of viscosity μ as $(6\pi\mu a)^{-1} \mathbf{F}_{DEP}$, which has a maximum magnitude of U_{DEP}^{\max} . To calculate \mathbf{U}_{DEP} we use the conformal mapping solutions available for the coplanar electrode geometry³⁹ to calculate the electric field, combined with custom scripts for efficiently calculating the multipolar DEP force⁶². The use of conformal mapping in determining the electric field assumes that the medium conductivity can be treated as locally homogeneous. This assumption is motivated by the disparate length scales characterizing variation in the conductivity (which varies over the width of the channel, $w = 2 \text{ mm}$) and the electric field (which varies over the width and spacing of the electrodes, $\sim 60 \mu\text{m}$). Given the electric field, the dipole contribution to the DEP velocity is determined from:

$$\mathbf{U}_{DEP} = \frac{a^2 \varepsilon_m}{3\mu} K(\omega) \nabla(\mathbf{E} \cdot \mathbf{E}) \quad (3- 5)$$

To make this calculation consistent with our models for mass transport (in which we neglect any variation along the depth of the channel), we evaluate the DEP force one particle radius below the channel ceiling, where we define the dimensionless field intensity gradient for a channel of height h as $\tilde{\mathbf{G}}(a/h) \equiv V_{rms}^{-2} h^3 \nabla(\mathbf{E} \cdot \mathbf{E})$. This simplification is motivated by the strong levitational force exerted on the particles, and is also invoked in obtaining a more convenient expression for the dimensionless drag coefficient, ξ_2 , from equation (3- 4):

$$\xi_2 \approx 8.22 \frac{a}{h} \left[1 - 0.039 \frac{a}{h} \right] \approx 8.22 \frac{a}{h} \quad (3- 6)$$

This dimensionless correction for the drag on a particle levitated to the channel ceiling in Poiseuille flow is valid for $0 < a/h < 1/2$; for the common case where $a/h \ll 1$, this may be linearized to further simplify analysis.

Equations (3- 4) through (3- 6) allow us to determine K_0 , the threshold polarizability at which particles flow past the DEP barrier:

$$K_0(\omega) = 49.32 \frac{\mu h^2 \sin(\theta) U_0}{a \epsilon_m V_0^2 \tilde{\mathbf{G}}(a/h)} \quad (3- 7)$$

In the limit of small particles ($a/h \rightarrow 0$), $\tilde{\mathbf{G}}$ reduces to a constant (≈ -0.2), and equation (3- 7) reduces to:

$$K_0(\omega) \approx -250 \frac{\mu h^2 \sin(\theta) U_0}{a \epsilon_m V_0^2} \quad (3- 8)$$

We use equation (3- 8) to calculate the threshold polarizability that determines where particles pass through the electrode barrier. By equating K_0 from equation (3- 8) with $\text{Re}\{\underline{K}\}$ as given by equation (3- 1) and calculating the medium conductivity from equation (3- 2) and the observed locations of the particles, we are able to relate the threshold polarizability of a particle to its electrical properties, embodied by the effective (frequency dependent) particle conductivity, σ_p . This effective conductivity may then be interpreted in terms of the thickness, conductivity and permittivity of the different layers comprising a particle.

Particle and cell heterogeneity. Since the size and electrical properties of each particle in a suspension are not identical, the threshold polarizability (equation (3- 8)) and the medium conductivity at which it is reached will typically vary, giving rise to a spatial distribution of particles as they flow to the outlet of the device. By observing this distribution (denoted as $p(x)$, where x is the position along the width of the channel), it is possible to study how the particle's properties are distributed. Although the number of parameters contributing to the effective conductivity of a particle is typically large (consisting of, for example, the size, conductivity, and permittivity of each layer), for simple particles, or particles in which different layers can be isolated by performing measurements over a particular frequency range, we can use IDS to rapidly measure the variance of the properties of large numbers of cells or particles ($>10^4$ per minute).

We consider a suspension of particles whose IDP is determined by the combination of N properties (in addition to the device's operating conditions), which we denote as $\{q_i\}$, ($i = 1 \dots N$). The properties of the particles in the suspension are thus described by the joint probability distribution function $p(q_1, q_2, \dots q_N)$. We wish to relate the distribution of the N particle properties to $p(x)$, the spatial distribution of particles at the outlet of the device. Given a measurement of the spatial distribution, we may then determine property distributions which are consistent with our observations.

To determine how $p(x)$ is related to $p(q_1, q_2, \dots, q_N)$, we express one of the N parameters (q_N , for example) as a function of the remaining $N-1$ parameters and the outlet position, x , and calculate the following integral

$$p(x) = \int p(q_1, q_2, \dots, q_N(q_1, q_2, \dots, q_{N-1}, x)) \frac{\partial q_N}{\partial x} dq_1 dq_2 \dots dq_{N-1} \quad (3-9)$$

For the simplest case of a single parameter, q_1 , with distribution $p_1(q_1)$, the distributions are related by $p(x) = p_1\{q_1(x)\} \frac{dq_1}{dx}$. Figure 3-2 illustrates this transformation from distributions of physical properties (two in this case – particle radius and conductivity) to distributions of positions. The trajectories of individual particles (Figure 3-2A, right) are determined by both the physical properties of the cell (through equation (3-1)) as well as the operating conditions of the device (through equations (3-2) and (3-8)), and can be summarized by the IDP – the position of the particle at the device outlet. Although the electrical properties of a particle uniquely determine that particle’s IDP for a given set of operating conditions, the position at the outlet does not uniquely

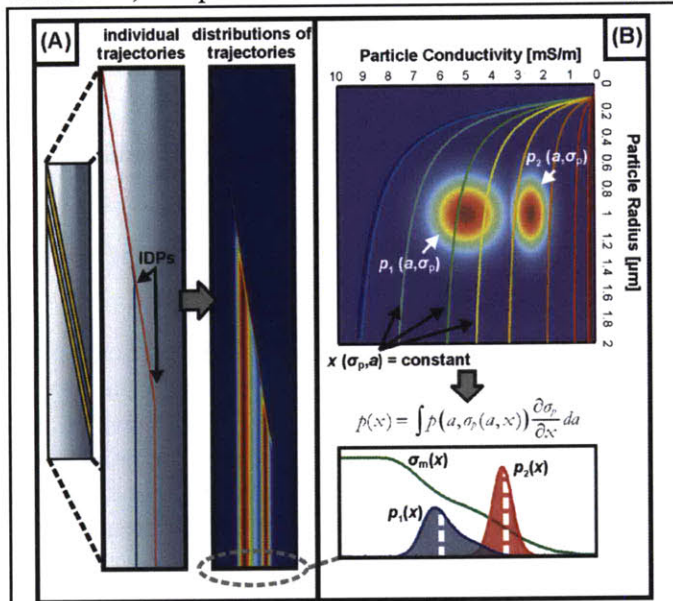


Figure 3-2: Modeling and interpreting the distribution of particle trajectories through the device. (A) Simulations to determine individual particles' trajectories (left) and distributions of these trajectories (right) for suspensions containing particles with a distribution of sizes (a) and conductivities (σ_p). (B) Relating the distribution of physical properties (size and conductivity, in this case), to the spatial distribution of particles at the outlet ($p(x)$) by integrating the property distributions (appropriately weighted) over contours of constant outlet positions. By fitting spatial distributions from this model to the observed distributions, we are able to infer how certain physical properties are distributed across the suspension.

as an example, for a suspension containing particles with variable sizes (a) and conductivities (σ_p), there will exist a family of sizes and conductivities which produce the same IDP (the curves labeled $x(\sigma_p, a) = \text{constant}$ in Figure 3-2B). Equation (3-9) amounts to integrating the probability distribution $p(a, \sigma_p)$ over these contours, inversely weighted according to how sensitive the IDP is to variations in particle conductivity (for this particular case). The result is distributions $p(x)$ which match the property distributions for the appropriate set of operating conditions (Figure 3-2B, bottom).

Although the mapping of one parameter (the IDP) to several (size, conductivity, etc.) is inherently underspecified, in practice, it is often possible to eliminate all but the dominant source of variation, or to use orthogonal methods to determine the variation in one or more of the relevant properties (e.g. particle size). In all of our calculations, we assume that the properties are distributed narrowly enough that the physical properties all follow a normal distribution, although it would be straightforward to use more realistic one-sided distribution functions. Under this assumption, the task of determining the distribution of physical properties is reduced to finding their mean and variance.

Influence of non-specific forces. The primary non-specific forces that can interfere

with particle separation and characterization in IDS arise from electrohydrodynamics (EHD)^{44,63-65} and particle interactions⁶⁶ in the system. Based on previous modeling (equation (2-21)) and observations of

EHD in our system⁵⁹, we have found that for the maximum conductivities and voltages we would use while operating with polystyrene beads, yeast, or mammalian cells, thermally induced EHD produces a force of magnitude $< 20\%$ that of DEP in all cases. Accordingly, for similar or less stringent operating conditions (e.g. larger particles, lower conductivities, or lower voltages) EHD should not appreciably influence device performance.

Non-specific forces arising from electric or hydrodynamic interactions between particles can be avoided by operating at sufficiently low particle concentrations. This is further aided by the separation mechanism in IDS, which minimizes the disturbance caused by particles to the medium. For example, while the DEP force acting on a particle is linearly proportional to the real part of the particle's CM factor, K , dipole interactions between two electrically similar particles vary as approximately K^2 . Thus, as particles approach their IDPs ($K \rightarrow 0$), interparticle forces decay more rapidly than the DEP force arising from the external field. By operating within the constraints imposed by these non-specific forces, it is possible to accurately neglect these contributions to the particle trajectories. This influence of particle interactions in IDS and other separation methods at *high* particle concentrations is discussed in detail in Chapter 4.

Materials and Methods

Cell culture and bead preparation. We cultured the budding yeast *Saccharomyces cerevisiae* at 30 °C for two days in a medium comprised of 1% Yeast extract, 2% peptone and 2% glucose. After harvesting the cells, we centrifuged and resuspended them in deionized water. Cells to be heat treated were transferred to a glass vial and placed on a hot plate set to 90°C for ~20 minutes. Live/dead staining using Syto 9 (S-34854, Invitrogen, Carlsbad, CA) and propidium iodide (P1304MP, Invitrogen, Carlsbad, CA) confirmed that 100% of cells were non-viable after heat treatment, whereas typically $>95\%$ of the untreated cells remained viable. After staining, cells were washed three times in a solution of deionized water, 0.1% BSA, and PBS mixed to the desired conductivity.

For experiments involving polystyrene beads, three different types were used: green fluorescent carboxylate-modified (09719, Polysciences, Inc. Warrington, PA, $1.646 \pm 0.069 \mu\text{m}$ true diameter), red fluorescent carboxylate-modified (F8825, Molecular Probes Eugene, OR, $2.0 \mu\text{m}$ true diameter, ~1% CV estimated by manufacturer), and green fluorescent (FS04F/6845, Bangs Laboratories, Inc. Fishers IN, $1.90 \pm 0.22 \mu\text{m}$ true diameter).

For experiments with mammalian cells we use BA/F3 mouse pro B cells provided by Susan Lindquist (Whitehead Institute, Cambridge, MA). The cell line was transfected and cultured as described in⁶⁷. To assess the viability of mammalian cells after passing through the device, we collected samples from the device (operating at 6 V_{pp} and 10 MHz and a flowrate of 4 $\mu\text{l}/\text{min}$) and stained with Syto 9 and propidium iodide before manually counting viable and non-viable cells. Using this simple assay, we found no significant difference in viability before and after the cells were passed through the device with viability $>85\%$ in both cases. The lack of adverse effects on cell viability is consistent with the brief residence time of the cells in the device (~16 s under these operating conditions) and operation in a frequency range in which the transmembrane voltage is small.

Fluorescence Microscopy and Data Acquisition. Imaging is performed using an upright Zeiss Axioplan 2M microscope (Zeiss, Thornwood, NY) coupled to a LaVision Imager 3 QE CCD Digital Camera (LaVision GmbH, Goettingen, Germany) using FITC and Cy3 filters. We record videos of particle separations under $5\times$ magnification at the outlet of the device. To represent the trajectories of ensembles of particles over time in a 2D image, we process the videos using a first-order difference filter. We apply a uniform threshold, so that each particle receives identical weighting in the composite image, and average the video over the total number of frames to produce the final image.

Analysis of Results. After determining the one dimensional cell or particle distributions at the outlet of the device, we calculate the IDP (defined as the mean of the distribution) from $x_{IDP} = \int_0^w xp(x)dx$. Substituting x_{IDP} into equation (3- 2) for the conductivity along the axis of the electrodes gives σ_m , the local medium conductivity at the particle IDP. Using equation (3- 8), we predict the value of $\text{Re}[\underline{K}(\omega)]$ at which the particles pass through the electrode barrier. Combining this result with the local medium conductivity, we may calculate the conductivity or permittivity of different layers of the particle or cell by using an appropriate model for the particle we are considering.

Results

Particle Separation and characterization. We use IDS and the model described above to separate and characterize particles covering a broad range of sizes ($\sim 1 - 10 \mu\text{m}$) and conductivities ($\sim 10^{-3} - 1 \text{ S/m}$). Our technique enables us to rapidly measure both the frequency and conductivity dependence of the electrical properties for large numbers ($\sim 10^4 - 10^5$) of particles and cells. As our first demonstration of this capability, we determine the surface conductance, K_s , of functionalized and non-functionalized polystyrene beads at varying medium conductivities. These beads offer a widely studied example of particles whose electrical properties vary depending upon their interactions with the external solution. From this, we proceed to study biological cells both with and without a cell wall (the budding yeast *S. cerevisiae* and the BA/F3 murine pro B cell line, respectively). The charged, porous structure of the yeast cell wall presents a second example of system in which electrical properties are directly dependent upon the external medium.

Polystyrene Beads. The ability to control both the surface-to-volume ratio and surface chemistry of polystyrene (PS) beads has made them an attractive tool for chemical sensing and concentration^{68,69}, as well as more general characterization of microfluidic and dielectrophoretic devices^{70,71}. Despite this wide use, the surface properties of these particles are often difficult to characterize, and the physical basis for these properties remains an area of active research⁷². In the context of AC electrical measurements, DEP and electrorotation have been used to determine the surface conductance of PS and latex beads^{47,73}; however, the throughput of these measurements – typically performed in non-continuous flow devices or laboriously on single particles – is prohibitive for applications in which one wishes to quantify changes in surface conductance associated with chemical modification to the surface of a large number of (potentially heterogeneous) particles.

The electrical conductivity of a PS bead is given by $\sigma_p = \sigma_{bulk} + 2K_s/a$, where σ_{bulk} denotes the bulk conductivity of polystyrene, a is the particle radius, and K_s is the surface conductance⁴⁷. Following others, we assume $\sigma_{bulk} \approx 0$, such that the surface conductance and particle size are the sole determinants of the particle's conductivity. A simple model for the surface conductance assumes that K_s is proportional to the net charge of the particle divided by the thickness of the layer over which counterions balance this charge: $K_s \propto \rho_s/\delta$ ⁷⁴. In considerably more detail, Mangelsdorf and White proposed that K_s is composed of contributions from both the stagnant (Stern) layer as well as the diffuse layer surrounding the particle⁷⁵, and others have shown that describing a particle's total surface conductance as the sum of two terms, one increasing with and one independent of the external medium conductivity are consistent with experimental results⁷⁶. This suggests that at very low medium conductivity, where the diffuse layer becomes relatively thick, the surface conductance is determined primarily from the stagnant layer conductance. Accordingly, K_s is expected to be independent of the medium conductivity for low values of σ_m , and increase with the medium conductivity at higher values of σ_m , as the contribution of the diffuse layer conductance becomes more significant.

We have used IDS to simultaneously separate and characterize the surface conductance of PS beads with different sizes and surface chemistries. Representative particle distributions from these experiments are presented in Figure 3- 3A&B. We can use these distributions to solve for K_s by substituting the expression for the beads' effective conductivity into equation (3- 1) and equating the result with the

threshold polarizability given by equation (3- 8). For the green carboxylate-modified beads, red carboxylate-modified beads and unmodified green beads, we find average values for K_s of 2.27 ± 0.23 nS, 2.34 ± 0.33 nS, and 1.64 ± 0.30 nS, respectively. We may also match individual measurements of the beads' surface conductance with the medium conductivity at which they localized under particular conditions to study how the surface conductance depends on the medium conductivity. Our measurements show an increase in surface conductance from ~ 1 -3 nS with increasing medium conductivity (Figure 3- 3C) over the range 2 – 10 mS/m. Previous studies of surface conductance, performed using electrorotation, report values of K_s independent of the medium conductivity for σ_m from 0.2 – 1.6 mS/m, with values ranging from 0.2 – 2.1 nS⁴⁷. This may be attributable to the Stern layer conductance in the model of Mangelsdorf and White. Additionally, although they do not report specific results, the authors of this study observe the onset of a dependence upon the medium conductivity at higher conductivities, consistent with our observations. In obtaining our results, measurement of the non-functionalized beads was complicated by the larger CV of these beads (11% as provided from the vendor) and their tendency to form aggregates, possibly due to their lower surface charge. In our analysis, we have excluded this subpopulation which does not pass through the electrode barrier (Figure 3- 3B); as a result, the numbers we report for non-functionalized beads may vary significantly from those that would be determined from a population average while enabling the discrimination of subpopulations (e.g. particle aggregates) from a nominally homogeneous, monodisperse suspension.

Because IDS measures the properties of many particles at once, we can extract information about particle properties from the shapes of the particle distributions measured at the outlet. Using equation (3- 9) with the variable parameters taken to be particle radius (a) and surface conductance (K_s), we fit our model to the measured distributions. For the carboxylate-modified beads, approximate CV's obtained from the vendors are 4.2% for the 1.6 μm beads and 1% for the 2.0 μm beads. For the non-functionalized 1.9 μm beads, since we exclude the fraction of the population which does not pass over the electrodes, we fit the distributions by allowing the CVs for both particle size and surface conductance to vary. Following this procedure, we obtain CVs of $11.4 \pm 5.4\%$ and $5.8 \pm 3.9\%$ for the K_s values of green and red carboxylate-modified beads, respectively. For the non-functionalized beads, best fits are obtained for a 1-2% variation in size with a 7.5% variation in surface conductance. Plots of measured and fitted particle distributions are presented in Figure 3- 3A&B. These results suggest that the surface properties of these particles are approximately as homogeneous as their distributions in size. The larger variation in surface conductance for particles with smaller diameters may be attributable to the increased sensitivity of K_s to variations in the number of charged groups on the particle surface as the total number of these groups decreases.

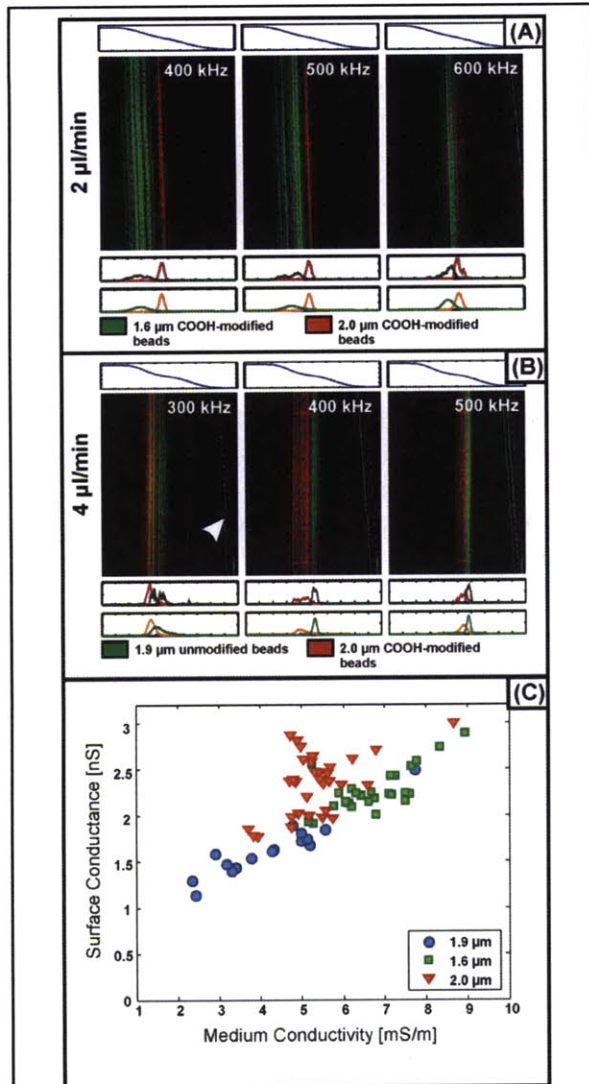


Figure 3- 3: (A) Measured distributions of red (2.0- μm diameter) and green (1.6- μm diameter) carboxylate-modified polystyrene beads. (B) Measured distributions of red (2.0- μm diameter) carboxylate-modified and green (1.9- μm diameter) unmodified polystyrene beads. Along with each fluorescence micrograph in both A and B, the conductivity (above, predicted from Eq. 2 with a high conductivity of 10 mS/m and a low conductivity of ~ 0 S/m) is plotted, as well as the one-dimensional measured (below, top) and modeled (below, bottom) particle distributions. The arrow in the leftmost panel in B indicates particle aggregates which do not pass through the electrode barrier. (C) Values for the surface conductance (K_s) of the three types of polystyrene beads as a function of medium conductivity extracted from measurements using IDS.

Yeast Cells. The budding yeast *Saccharomyces cerevisiae* has been the focus of fundamental and applied research, from genetics and bioinformatics to antifungal drug development. Each of these applications seek to map the phenotype of particular cells to either their genotype or to the environmental conditions to which they have been subjected, an analysis that requires the ability to perform quantitative measurements on the cells. Accordingly, a common approach over the past several decades has been to study the dielectric spectra of mutant or environmentally perturbed yeast^{1,77,78}.

While others have used electrorotation or bulk impedance measurements to characterize the spectra of individual cells or population averages across frequency^{47,56}, IDS offers the ability to measure property distributions over a continuous range of medium conductivities spanning several orders of magnitude on a large number of cells. To investigate the possibility of using IDS to separate and characterize yeast with environmentally altered phenotype, we apply the technique to the study of viable and non-viable cells with emphasis on the electrical properties of the cell envelope; this measurement is particularly well suited to IDS, since, as with the polystyrene beads, the electrical properties of the porous, charged cell wall have been shown to depend sensitively on the conductivity of the external medium⁷⁹. Since the equilibration of mobile carriers within the wall occurs over a timescale on the order of the charge relaxation time ($\sim 0.1 \mu\text{s}$ under typical conditions), whereas the medium conductivity surrounding a cell evolves over the course of the convective timescale ($\sim 1-10$ s), the electrical properties of the cell wall during the separation should be pseudosteady, changing essentially instantaneously with the medium conductivity.

Viable Yeast Cells. To determine the electrical properties of viable yeast cells, we use the parameters given in Table 3- 1. Assuming literature values for some of the cell layers (cytoplasmic conductivity and permittivity, cell wall thickness and permittivity, and cell membrane thickness and conductivity), as well as using direct measurements of the cell radius obtained using a Coulter counter, constrains the fitting problem and allows us to focus on the characteristics of the cell envelope. With the exception of the cytoplasmic conductivity,

	Membrane	Cell Wall	Cytoplasm
Viable Cells	2.5×10^{-7} S/m*	$\sigma_w/\sigma_m = 0.12 \pm 0.03$	0.5 S/m
	$10\epsilon_0$	$60\epsilon_0^*$	$50\epsilon_0^*$
	8 nm*	$0.25 \mu\text{m}^*$	$2.0 \mu\text{m}$
Heat Treated Cells	1.6×10^{-4} S/m*	$\sigma_w/\sigma_m = 0.43 \pm 0.24$	0.05 S/m ($= \sigma_{high}$)
	$10\epsilon_0$	$60\epsilon_0^*$	$50\epsilon_0^*$
	8 nm*	$0.25 \mu\text{m}^*$	$2.0 \mu\text{m}$

Table 3- 1: Parameters used in and determined from fitting the distributions of yeast at the outlet of the IDS device. Parameters labeled with ‘*’ are taken from ¹. The values and error estimates for σ_w/σ_m are obtained by fitting the data in Figure 3- 4B to a straight line (corresponding to the assumption that $\sigma_m \gg c_f^w u^0$ in equation (3- 10)), and determining how much variation in the slope of this line is necessary to capture 70% of the scattered points.

measurements of which vary considerably through the literature (from 0.2 – 1.2 S/m), property values are taken from¹. For the cytoplasmic conductivity, we use an approximate median value from the literature of 0.5 S/m. Because of the difficulty associated with determining the cytoplasmic conductivity, we also performed fitting for values of 0.25 S/m and 1.0 S/m. In both cases, the extracted cell wall conductivities changed by less than 10% from the results obtained using 0.5 S/m, confirming that the conditions for this

measurement are not strongly dependent on the cell’s interior properties.

A common model for the conductivity of a charged, porous material such as the yeast cell wall, is of the form⁷⁹:

$$\sigma_w \approx c_f^w u^w \left[1 + \left(2\sigma_m / c_f^w u^0 \right)^2 \right]^{1/2} \quad (3- 10)$$

At sufficiently low medium conductivities, the wall conductivity is determined by the concentration of fixed charges (c_f^w) and the mobility of counterions in the cell wall (u^w). At high medium conductivities, σ_w varies linearly with σ_m , with a slope depending upon the porosity of the cell wall, as parameterized by the mobility of ions inside the cell wall relative to their mobility in the bulk solvent (u^0). We have characterized multiple cell cultures in conductivity gradients spanning both high ($\sigma_h = 0.33$ S/m, corresponding to the cells’ growth medium) and low ($\sigma_h = 0.05$ S/m) values. Figure 3- 4A depicts representative distributions observed for viable and heat-treated yeast cells at the lower conductivity range. Comparison of the values of σ_w extracted from these measurements to equation (3- 10) suggests that at media conductivities as low as ~ 0.02 S/m, the concentration of fixed charge in the wall is much less than the concentration of ions in the electrolyte (Figure 3- 4B), as suggested by the approximately linear increase in σ_w with σ_m . Additionally, interpreting the slope of the curve ($\Delta\sigma_w/\Delta\sigma_m$) as relating the mobility of ions in the bulk solution to ions in the porous wall suggests an effective porosity for the cell wall of roughly 6%. This agrees with measurements presented elsewhere in the literature, for example the value of $\sim 5\%$ measured via impedance analysis reported in⁷⁷.

Heat Treated Yeast Cells. Heating the cell suspension to 90 °C for ~ 20 minutes renders the cells non-viable and is accompanied by several drastic changes in cell structure. It is believed, for example, that heat treatment permeabilizes the cell membrane, increasing membrane conductance as well as allowing the internal contents of the cell to equilibrate with the external medium¹. In addition, it is expected that extreme heat treatment may alter the structure and composition of the cell wall through denaturation. To investigate this, we use IDS to characterize heat-treated cells from multiple cultures following the same procedure as for viable cells. Our results suggest that the cell wall conductivity is more nearly proportional to the medium conductivity (Figure 3- 4B, from which we obtain $\sigma_w \sim (0.43 \pm 0.16) \sigma_m$).

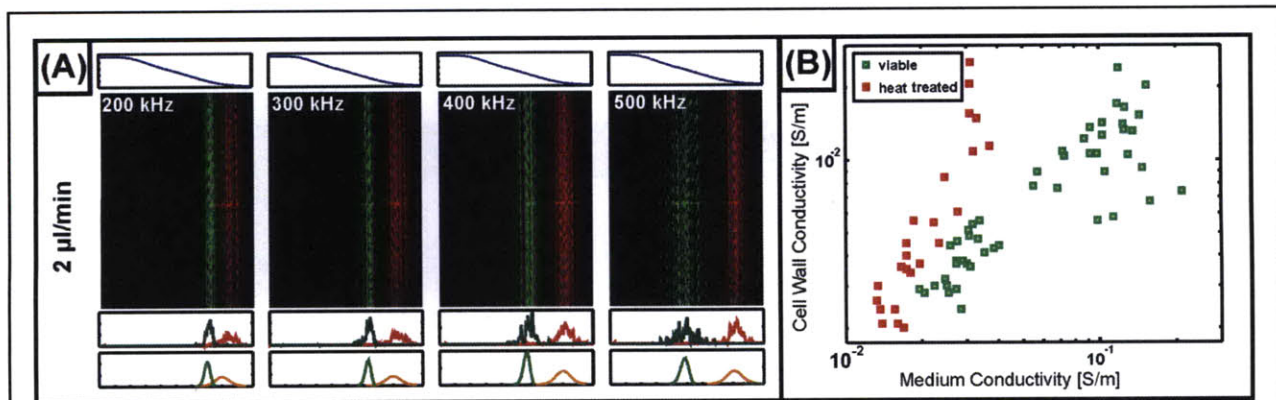


Figure 3- 4: (A) Measured distributions of viable (green) and non-viable (heat-treated) yeast cells. Along with each fluorescence micrograph, the conductivity (above, predicted from equation (3- 2) with a high conductivity of 50 mS/m and a low conductivity of 10 mS/m) is plotted as well as 1-D measured and modeled (below, with fits determined using the parameters from Table 3- 1) particle distributions. (B) Values for the yeast cell wall conductivity as a function of medium conductivity determined for viable (green) and heat-treated (red) cells obtained using IDS and the parameters from Table 3- 1.

Since we generally cannot decouple the influence between the conductivity and thickness of the cell wall, this observation may also be attributable to the decreases in the cell wall thickness from heat treatment. It is also worth noting that in our analysis, we take the internal conductivity of the permeabilized cells to be equal to the high conductivity used in establishing the gradient (50 mS/m); this assumes that the internal conductivity does not equilibrate with its surroundings over times on the order of a few seconds. Since the validity of this assumption depends upon the porosity of the permeabilized cell membrane, we have also considered a model in which the internal conductivity equals the medium conductivity at all times (not shown). This leads to a similar conclusion ($\sigma_w \sim 0.5 \sigma_m$), but with an increase in the scatter of the data.

Mammalian Cells. Finally, to demonstrate the feasibility of characterizing the electrical properties of larger, more physiologically sensitive cells, we use IDS to determine the membrane and cytoplasmic electrical properties of mammalian (BA/F3) cells. Mammalian cells are commonly modeled as a relatively conductive core, representing a lumped model for the cells' cytoplasm and internal structure, surrounding by a thin (~ 5 nm) primarily insulating membrane²³. Despite the simplicity of these models, they have provided an indicator of phenotype in screens for apoptotic cells^{80,81}, multidrug resistance reversal⁸², or tumor cells⁸³. One of the primary obstacles in the electrical characterization of mammalian cells is the inability of these cells to maintain ion homeostasis in a medium with low ionic strength^{84,85}; in any effort to characterize the electrical response of a cell, it is thus essential to control for the aspects of the electrical response which are inextricably connected to the measurement technique. Our approach largely circumvents this challenge by keeping cells suspended in a high-conductivity solution (e.g. cell culture media) until seconds before the measurement is performed. Since we do not expect ion leakage over such a short time scale to be appreciable, cell characterization using IDS has the potential to reveal unperturbed cytoplasm and membrane properties.

Figure 3- 5 displays representative results for distributions of BA/F3 cells along with theoretical distributions generated from fitting the cytoplasmic conductivity and membrane capacitance using the model for device operation. Using a two-shell model for a mammalian cell suggests values of 0.58 S/m and 2.3 $\mu\text{F}/\text{cm}^2$ for the cytoplasmic conductivity and membrane capacitance, respectively, both in agreement with values reported elsewhere for white blood cells⁸⁶. Importantly, we find that these parameters do not vary appreciably with the conductivity of the medium into which the cells localize (Figure 3- 5B). This suggests that the cells maintain ion homeostasis for the duration of the measurement, enabling us to observe the unperturbed electrical properties of the cells. We also note that the typical peak width observed for these cells exceeds those measured for other particle and cell types. This may be attributed in part to the lower voltages used in these experiments as compared to those for yeast (3-5 V

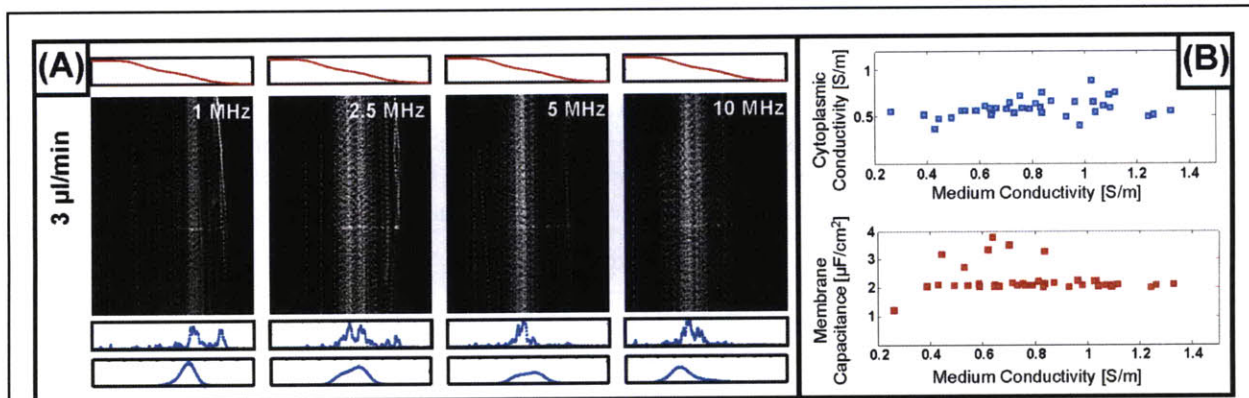


Figure 3- 5: (A) Measured distributions of BA/F3 cells in a conductivity gradient ranging from 1.5 S/m (corresponding to the growth medium of the cells) to an osmotically balanced sucrose solution that we treat as ~ 0 S/m. Beneath each image we plot the 1-D measured and modeled particle distributions, from which we obtain a cytoplasmic conductivity of 0.58 S/m and a membrane capacitance of 2.3 $\mu\text{F}/\text{cm}^2$. (B) Values for the cytoplasmic conductivity and membrane capacitance of BA/F3 cells determined from fitting to the particle distributions. The independence of both of these properties on the medium conductivity suggests that the exposure of the cells to low conductivity solutions is sufficiently short to avoid substantial disturbances of the cells' ion homeostasis.

zero-to-peak amplitude as compared to 7-10 V for yeast). Thus despite the larger size of these cells, they do not converge as fully to equilibrium ($K \sim 0$), and thus exhibit a greater sensitivity to variations in cell size. In addition, we expect the electrical properties of the cells to be distributed over a finite range. Combining the different sources of variance, we estimate from the peak width a CV of $\sim 10\%$ for the cytoplasm and membrane electrical properties.

Discussion

Analytic separation techniques can be broadly categorized as one of two types: those in which characterization may be coupled to downstream separation (e.g. impedance cytometry), and those in which the method of isolating particles in time or space is the fundamental mechanism of their characterization (e.g. iso-electric focusing, electrophoresis). While this latter category is well represented by molecular separation methods, there are exceptionally few analytic methods of this type for separating and analyzing cells. By using dielectrophoresis to both interrogate the electrical properties of cells as well as physically effect their separation, IDS fits into the category of analytic techniques that intrinsically also separate. The relative benefits of each of this approach to characterization depends on the application at hand; the rate at which measurements may be taken using IDS, for example, is constrained by the speed of separation - residence time of a cell in the device. For our architecture, this means that different conditions can be probed no faster than one every ~ 10 s. In contrast, measurements of a single cell's impedance at 512 frequencies in ~ 1 ms using impedance cytometry has been reported⁸⁷. However, IDS offers the ability to characterize particles over two dimensions - frequency and conductivity - without the need to change the sample. This is advantageous in cases, such as those considered here of yeast and charged colloidal particles, where the dependence of electrical properties on the surrounding medium offers insight into the physical structure of a cell or particle's surface. The ability to rapidly measure the interfacial electrical properties of particles for which these properties are inextricable from the external medium represents an advance over traditional approaches, and is enabled by the rapid equilibration of small particles with their immediate environment. Combining this ability with the ability to obtain full spatial distributions of the sample through the device in seconds allows for high throughput and high content characterization.

A second class of measurements for which IDS is well suited and which we have begun to explore here are those in which the cells being characterized may be perturbed from their native state by the environmental conditions. For example, although it is often advantageous to measure the electrical properties of mammalian cells in low medium conductivities, the stress that this places on the cell leads to changes in its electrical properties, as its ability to maintain ion homeostasis is compromised. Using IDS, it is possible to limit the exposure of cells to environmental stresses (such as low conductivities) to a few seconds, enabling measurements of the native properties of the cells under non-native conditions.

Although some of the experiments presented here have used fluorescent labels to better track subpopulations of cells in mixtures (e.g. viable and non-viable yeast), this is not a fundamental requirement of the technique. For example, results shown in Figure 3- 5 for the BA/F3 cell line were obtained by using the constitutive DsRed expression engineered into this cell line in place of cell staining. Furthermore, we have performed experiments (not shown) in which bright field imaging has been used in place of fluorescence to track particle distributions. This imaging approach appears to be robust for particles $\sim 5 \mu\text{m}$ in diameter (e.g. yeast); however, we have not attempted this for particles substantially smaller than this, and for which it may prove difficult.

Regarding device design, the principle behind IDS is not specific to one particular architecture and thus allows for a broad range of implementations. Our design was guided by the objective of creating a device compatible with particles covering a broad range of sizes and conductivities, but different electrode dimensions and geometries may be better suited for applications targeting a specific type of cell or particle. Relevant considerations may include not only the force the electrodes are capable of imparting on a particle, but also factors such as the total power and power density dissipated in a particular design, as well as the ease of fabrication. As an example of the possible tradeoffs, assuming coplanar electrodes operated at a fixed voltage, the highest holding force is produced by using an electrode spacing much less than the channel height, regardless of the specific channel height used. However, too small of a gap will lead to excessive Joule heating and electrothermal convection, especially when higher conductivity buffers are used. A second example is the choice between coplanar electrodes and electrodes arranged parallel to each other on the top and bottom of the channel. While the parallel geometry leads to higher throughput in many (though not all) cases, it requires a more difficult fabrication process. Accordingly, the constraints and requirements of any specific application should be used to inform the device design.

We have demonstrated the feasibility of using IDS to better understand the electrical properties of cells and particles, especially regarding their dependence on the conductivity of the surrounding medium. Still, we believe that this approach to particle characterization and separation holds additional advantages for applications more advanced than those demonstrated here. The ability to combine characterization with separation could be used, for example, to screen cells according to their response to an environmental stressor, such as osmotic or thermal shock, or exposure to alkylating agents. With IDS, it would be possible to select cells of any level of resistance or susceptibility, provided that the stress response altered the electrical phenotype of the cell. Furthermore, the wide applicability of IDS which we have demonstrated here – characterizing cells and particles spanning several orders of magnitude in both volume and conductivity – suggests that its use is not limited to one type of cell, but could be applied to assays involving either prokaryotic or eukaryotic cells.

Chapter 4: Particle interactions in microfluidic systems

Having described the initial development of isodielectric separation in the previous two chapters, we shift our focus at this point to address a subject that applies not only to IDS, but to other microfluidic separation methods that seek to operate at high particle concentrations as well. The effects of high particle concentrations on separation methods is an issue central to their implementation. Given the scale of most biological applications – even the simplest genetic screens involve ~5000 genetically distinct mutants - high throughput is a necessary feature of any technology for screening cells and requires maximizing the particle concentration through the device. Some times in conflict with this goal, however, is the fact that cells and colloidal particles placed in an energy landscape interact with each other, giving rise to complex dynamic behavior that affects the ability to process and manipulate suspensions of these particles. These interactions propagate across multiple scales, from the local behavior of 10's of particles, to non-local behavior encompassing $>10^6$ particles. Although pervasive, particle interactions are challenging to describe quantitatively, especially in the confined environments typical of microfluidic devices. This chapter focuses on experiments and simulations we have performed involving a simple microfluidic device in which hydrodynamic and electrostatic forces are leveraged to concentrate and separate particle mixtures. We find that ensembles of interacting particles exhibit emergent behavior with features of dynamical frustration and cooperativity that influence the ability to concentrate and sort suspensions. Finally, we present a simple analytic model based on hydrodynamic coupling that captures important features of strongly interacting particle suspensions. Following this more general discussion of how particle interactions hold implications for generic microfluidic devices, I will conclude by discussing how it specifically affects iso-dielectric separation.

Included in the appendix to this chapter are several Matlab scripts representative of those used throughout this part of the thesis.

Introduction

The collective behavior of systems of interacting objects is relevant to a broad range of fields, including condensed matter physics (superconductivity, ferromagnetism), biology (molecular and cellular networks, protein folding, morphogenesis), and colloidal dynamics (suspension rheology, nanotechnology). These examples of many-body, non-linear systems are characterized by their complexity and the emergent phenomena that they engender, including, for example, pattern formation⁸⁸⁻⁹⁰, cooperativity⁹¹⁻⁹³, hysteresis⁹⁴, synchronization^{95,96}, and frustration⁹⁷⁻⁹⁹. Here, we demonstrate the applicability of these concepts to the field of microfluidics; specifically, we show how emergent behavior arises in microfluidic devices designed to handle cells and micron-scale colloidal particles, and how these behaviors collectively affect the performance of these devices. Taking a device using electric and hydrodynamic fields to manipulate particles as a specific example, we find that the forms of cooperativity, hysteresis, and dynamical frustration that emerge can be leveraged to significantly improve the performance of devices designed to concentrate and separate cells or colloidal particles.

To date, particle interactions and their implications have largely been neglected in the design of microfluidic devices. This has persisted despite their relevance to a wide range of applications – including cell enrichment and purification^{57,58}, droplet/bubble generation and control¹⁰⁰⁻¹⁰², and sample preparation^{103,104}. Although previous treatments have dealt with electrostatic interactions and particle aggregation under static conditions¹⁰⁵ (i.e. no hydrodynamic interactions), have developed continuum theories^{106,107}, or have focused on the rigorous calculation of the trajectories of specific arrangements of interacting particles¹⁰⁸, the emergence and implications of collective behavior across multiple scales (i.e. from a few to many particles) in microfluidic systems remains unexplored. To better understand and predictively quantify these effects, we approach particle interactions from an experimental and theoretical perspective, through the use of experiments, Brownian dynamics simulations, and the development of a statistical model. This approach provides a simple platform for studying collective behaviors and emergence in a many-body system where the interaction rules between particles may be controlled.

Additionally, because the emergent patterns of particles retain some memory of the conditions under which they were formed, we are able to explore how the path-dependence of these systems can be leveraged to design higher-performance microfluidic devices.

The characteristics of many-body systems are determined by the mechanisms through which the constitutive particles interact. In a confined microfluidic device, these interactions may be (for example) electrical, magnetic, optical, or hydrodynamic in origin, and may occur either between particles coupling with each other directly or through their images in the system's boundaries¹⁰⁹. As a platform for studying collective behavior and its practical implications, electric and hydrodynamic interactions have a number of attractive features: they are applicable to a wide variety of recently developed devices^{110,111}; they are anisotropic, giving rise to more complex patterns; and they are determined by external fields which can be controlled both geometrically and dynamically (through operating conditions such as voltage, frequency, and flowrate). To exploit these advantages, we take as our experimental platform a shallow microfluidic channel (height = 18 μm) overlaying a microfabricated array of interdigitated electrodes (width = 50 μm , pitch = 50 μm), through which we flow particles perpendicular to the axis of the electrodes (Figure 4- 1a). In operation, a voltage applied across the electrodes polarizes particles and exerts a negative dielectrophoretic force; this force counteracts hydrodynamic drag, retaining the particles if the voltage is large enough. By observing the dynamics of one to thousands of particles simultaneously in this environment, we are able to identify emergent behavior across multiple length scales.

Results

Numerical Model. Brownian and Stokesian dynamics simulations^{112,113} present an approach to modeling collections of interacting particles. We first specify the imposed electric field, \mathbf{E}_0 , and fluid velocity, \mathbf{u}_0 , together with the positions of N interacting particles, $\mathbf{x}_i(t)$ ($i = 1 \dots N$). To self-consistently determine the electric and hydrodynamic fields given each particle's position, polarization, and velocity relative to the surrounding medium, we use:

$$\mathbf{E}(\mathbf{x}) = \mathbf{E}_0(\mathbf{x}) + \sum_{i=1 \dots N} \mathbf{G}_{\text{es}}(\mathbf{x}; \mathbf{x}_i) \mathbf{E}(\mathbf{x}_i) \quad (4-1)$$

$$\mathbf{v}(\mathbf{x}) = \mathbf{u}_0(\mathbf{x}) + \sum_{i=1 \dots N} \mathbf{G}_{\text{hd}}(\mathbf{x}; \mathbf{x}_i) \mathbf{F}(\mathbf{x}_i) \quad (4-2)$$

Here, $\mathbf{F}(\mathbf{x}_i)$ denotes the net external force acting on the i^{th} particle, and the Green's functions \mathbf{G}_{ES} and \mathbf{G}_{HD} represent electrostatic and hydrodynamic coupling between particles and to the system's boundaries¹¹⁴. Given the self-consistent electric field (\mathbf{E}), the dielectrophoretic contribution to the external force is given by:

$$\mathbf{F}_i = \mathbf{p}_i \cdot \nabla \mathbf{E}(\mathbf{x}_i) = 4\pi\epsilon_m a_i^3 K_i [\mathbf{E}(\mathbf{x}_i) \cdot \nabla \mathbf{E}(\mathbf{x}_i)] \quad (4-3)$$

where a_i and K_i denote the radius and polarizability of the i^{th} particle, respectively. In addition, the net external force contains a steric contribution, preventing overlap between contacting particles and/or surfaces. Using the net force, we calculate the velocity of each particle \mathbf{x}_j using:

$$\mathbf{v}_j^p = \mathbf{u}_0(\mathbf{x}_j) + (6\pi\mu a_i)^{-1} \mathbf{F}(\mathbf{x}_i) + \sum_{i=1}^N \mathbf{G}_{\text{hd}}(\mathbf{x}_j; \mathbf{x}_i) \mathbf{F}(\mathbf{x}_i) \quad (4-4)$$

Microscopic Emergent Behavior. Hydrodynamic and electrostatic Green's functions define the local interaction rules which determine the dynamic patterns of particles that form at a microscopic level (i.e. a scale encompassing ~ 1 -10 particles). We use experiments and simulations to study these patterns, observing 1- to 4- μm -diameter colloidal particles in the presence of externally imposed electric and hydrodynamic fields to test the accuracy of our simulations. We repeatedly observe a variety of behaviors that vary as the number of particles incident on the electrode barrier is increased.

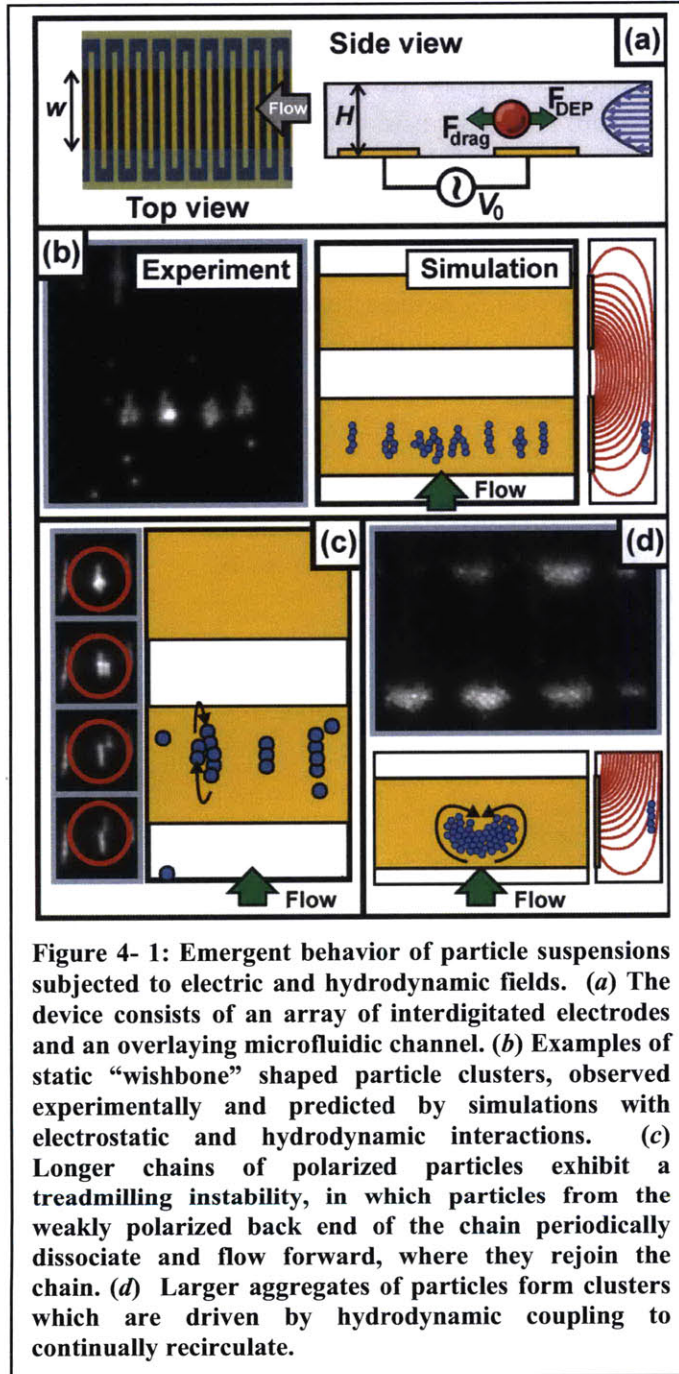


Figure 4- 1: Emergent behavior of particle suspensions subjected to electric and hydrodynamic fields. (a) The device consists of an array of interdigitated electrodes and an overlaying microfluidic channel. **(b)** Examples of static “wishbone” shaped particle clusters, observed experimentally and predicted by simulations with electrostatic and hydrodynamic interactions. **(c)** Longer chains of polarized particles exhibit a treadmilling instability, in which particles from the weakly polarized back end of the chain periodically dissociate and flow forward, where they rejoin the chain. **(d)** Larger aggregates of particles form clusters which are driven by hydrodynamic coupling to continually recirculate.

As aggregates of a few to several particles begin to form, they take the form of chains aligned to the electric field. As a result of hydrodynamic interactions¹¹⁵, these chains are more stably held against the flow than single particles in isolation, and entrain incoming particles through dipole interactions. As these chains lengthen, the rear of the chain is exposed to a weaker external field and is more subject to perturbations off the axis of the chain. Disturbances to the back of the chain allow additional branches to form, giving rise to inverted ‘Y’ shaped structures (Figure 4- 1b). A second response we observe in lengthening chains is the detachment of particles from the weakly polarized back end, which are then carried forward by flow, where they rejoin the strongly polarized front end of the chain, producing a periodic “treadmilling” behavior (Figure 4- 1c). Finally, as the particle aggregate grows increasingly large, the chain structure is lost in favor of a closely packed cluster of particles which continually recirculates under hydrodynamic forces (Figure 4- 1d).

The dynamic patterns we observe exhibit features of dynamical frustration^{97,99}, where the components of a system periodically cycle through a series of states, unable to reach a stable equilibrium. In the present case, the frustration arises through the tendency of particles to disrupt the balance of forces on their nearest neighbors. The qualitative agreement between the dynamic behavior observed in both experiments and the results of simulations suggests that our modeling approach captures the essential physical aspects of interacting colloidal systems.

Macroscopic Emergence: Particle Concentration and Separation. The collective behavior we observe on the scale of ~ 10 particles propagates to larger length scales, influencing such “macroscopic” properties as the performance of a particle concentrator. To study the implications of particle interactions on a scale directly relevant to device performance, we measured the effect of changing the particle concentration on the ability to retain particles against flow. As a means of quantifying this ability, we define a function $\Theta(c,v)$ representing the fraction of particles retained for a given particle concentration (c) and voltage (v) . At infinite dilution $(c = 0)$, the minimum voltage necessary to retain a particle is

deterministic and well defined ($v = V_0$). However, as the particle concentration increases, cooperative behavior tends to (probabilistically) decrease the voltage necessary for particles to accumulate.

We constructed a statistical model to describe semiquantitatively the cooperativity that emerges in systems of interacting particles. Specifically, we explore a model where a particle is surrounded by N neighbors with which it interacts. These neighbors lie within a distance R_0 of the particle, and the overall concentration of particles is defined as $c \equiv N_T/A_T$, where N_T and A_T are the total number of particles and the total area, respectively. In our model, we assume that the contribution to the mobility matrix ($= m$) of any of these N particles is randomly distributed according to $p(m) = ke^{-km}$. Here, k is a constant equal to the inverse of the expectation value of m . For a given overall particle concentration and a uniform distribution of particles, the number of neighbors, N , is distributed according to:

$$p[N] = \frac{N_T!}{N!(N_T - N)!} \left[\frac{\pi R_0^2}{A_T} \right]^N \left[1 - \frac{\pi R_0^2}{A_T} \right]^{N_T - N} \quad (4-5)$$

where $N = 0 \dots N_T$. Since $\pi R_0^2 \ll A_T$ and $N \ll N_T$ in all realistic cases, $p[N]$ is accurately approximated by $p[N] = [(\pi R_0^2 c)^N / N!] e^{-\pi R_0^2 c}$. Since each of the N particles contributes to the net mobility of the central particle, to find the distribution of the net mobility, we convolve $p(m)$ with itself N times:

$$p_N(m) = k \frac{(km)^{N-1}}{(N-1)!} e^{-km} \quad (4-6)$$

In the special case where $N = 0$, m is identically 0, since there are no neighboring particles to interact with. The joint probability distribution, i.e. the probability of having N particles and a net mobility (summed over these N particles) of m , is given by:

$$p[N, m] = \begin{cases} e^{-\pi R_0^2 c} & N = 0 \\ (\pi R_0^2 ck) e^{-\pi R_0^2 c - km} \left[\frac{(\pi R_0^2 ck m)^{N-1}}{N!(N-1)!} \right] & N > 0 \end{cases} \quad (4-7)$$

To determine the probability of having a net mobility m for a given overall particle concentration c , we sum $p[N, m]$ over all N :

$$p(m) = e^{-\pi R_0^2 c} \left[\delta(m) + \frac{(\pi R_0^2 ck) e^{-km}}{\sqrt{\pi R_0^2 ck m}} \left[I_1 \left\{ 2\sqrt{\pi R_0^2 ck m} \right\} \right] \right] \quad (4-8)$$

Here, I_1 is a modified Bessel function of the first kind ($\nu = 1$), and the impulse, $\delta(m)$, accounts for the case where $N = 0$. For convenience, from this point on we replace $\pi R_0^2 c$ with c ; this dimensionless concentration is equivalent to $\langle N \rangle$, the expected number of interactions a particle shares with its neighbors.

A particle is retained if its net mobility has been altered enough to hold it against the external flow. As a result, the fraction of particles retained can be calculated from:

$$\Theta(c) = 1 - e^{-c} u(m) - c k e^{-c} \int_0^m dm' \left[\frac{e^{-km'}}{\sqrt{ckm'}} I_1 \left\{ 2\sqrt{ckm'} \right\} \right] \quad (4-9)$$

Or, written in somewhat simpler form with the change of variable $x \equiv 2\sqrt{ckm}$:

$$\Theta(c) = 1 - e^{-c} \left[u(m) + c^{1/2} \int_0^{2\sqrt{ckm}} e^{-(x/2)^2} I_1 \left\{ c^{1/2} x \right\} dx \right] \quad (4-10)$$

Here, $u(m)$ is the unit step function, where m corresponds to the net contribution from other particles necessary for trapping, and is related to the forces in the system by $m = (u_0 - \mu_0 F_0) / \mu_0 F_0$. Here, the external force acting on a particle (with mobility μ_0) is F_0 and the external fluid velocity that the force opposes is u_0 . Accordingly, m describes the degree to which the applied force is sub-threshold; note that if $(u_0 - \mu_0 F_0)$ is negative, the external force is strong enough to retain a single particle, resulting in $\Theta(c)$

= 1 for all c . The appropriate concentration to use in these equations depends on the manner in which the force is applied. For example, if the force is highly localized in space or time, then the input concentration can be used directly in these equations. Alternatively, if the force is distributed over space or time, the particle concentration will reach an enhanced steady state value, although the force may remain sub-threshold. This enhanced concentration (c') will then be related to the input concentration (c)

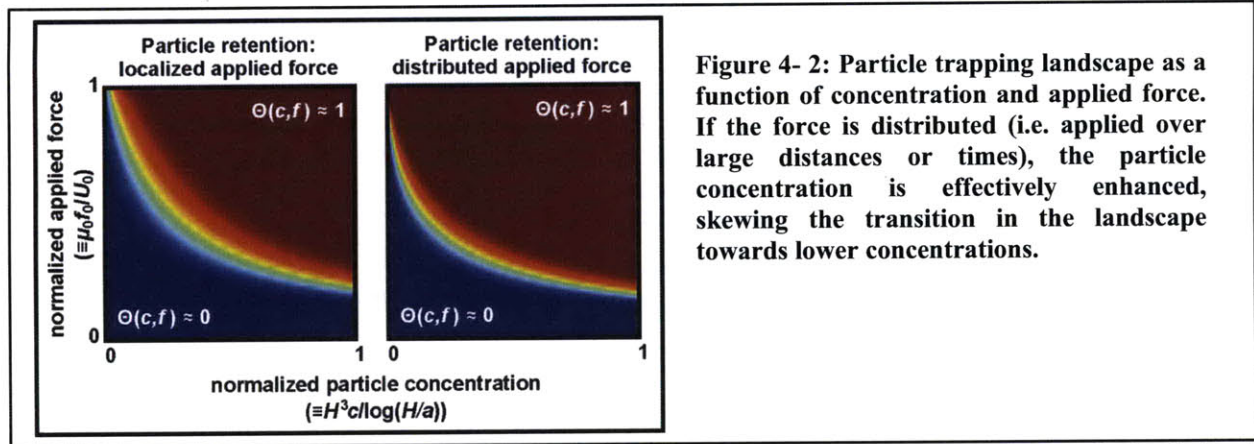


Figure 4- 2: Particle trapping landscape as a function of concentration and applied force. If the force is distributed (i.e. applied over large distances or times), the particle concentration is effectively enhanced, skewing the transition in the landscape towards lower concentrations.

according to $c' = cu_0/(u_0 - \mu_0 F_0)$. Figure 4- 2 shows the effective trapping landscape for both local and distributed forces, as a function of input concentration and the magnitude of the applied force.

Approximate Expressions for $\Theta(c, f)$. Although there is no closed-form expression for the integral in equation (4- 10), if $2\sqrt{ckm}$ is small, then it simplifies to $\Theta(c) \approx 1 - e^{-c}[1 + c(1 - e^{-km})]u(m)$. Alternatively, for large values of $2\sqrt{ckm}$, we can use an asymptotic approximation for the Bessel function and Laplace's method¹¹⁶. Specifically, we replace I_1 in equation (4- 10) using $I_1\{c^{1/2}x\} \sim (2\pi c^{1/2}x)^{-1/2} e^{c^{1/2}x}$ and obtain:

$$\begin{aligned} \Theta(c) &\sim 1 - e^{-c} - c^{1/4} \int_0^{2\sqrt{km}} (2\pi x)^{-1/2} e^{-[\frac{x}{2} - \sqrt{c}]^2} dx \\ &\approx (4\pi)^{-1/2} \int_0^{2\sqrt{km}} e^{-[\frac{x}{2} - \sqrt{c}]^2} dx \\ \Theta(c) &\sim 1 - e^{-c} + \frac{1}{2} \operatorname{erf}\{\sqrt{c} - \sqrt{km}\} - \frac{1}{2} \operatorname{erf}\{\sqrt{c}\} \end{aligned} \quad (4- 11)$$

This suggests that the inflection in $\Theta(c)$ will occur at $c \approx km$. If we treat this inflection as the onset of appreciable particle trapping, we can express the trapping efficiency in a form similar to that of cooperative binding:

$$\Theta(c) \approx \frac{c^n}{K_D^n + c^n} \quad (4- 12)$$

To determine the effective value of the constants K_D and n , we expand around the concentration at half saturation, use $\Theta(K_D) = 1/2$ and $\Theta'(K_D) = n/4K_D$. An approximation valid for all concentrations and forces is $K_D \approx km + \log 2$ and $n \approx 2\sqrt{km/\pi} + (\log 2)^2$, so that:

$$\Theta(c) \approx \frac{c^{2\sqrt{km/\pi} + (\log 2)^2}}{(km + \ln 2)^{2\sqrt{km/\pi} + (\log 2)^2} + c^{2\sqrt{km/\pi} + (\log 2)^2}} \quad (4- 13)$$

In terms of the forces present in the system:

$$K_D \approx k[(u_0 - \mu_0 F_0)/\mu_0 F_0] + \log 2 \quad (4-14)$$

$$n \approx 2\sqrt{[k(u_0 - \mu_0 F_0)/\pi\mu_0 F_0] + (\log 2)^2} \quad (4-15)$$

In equation (4-14), K_D remains dimensionless. Figure 4-3 compares the numerically determined trapping curves with this sigmoidal approximation.

We are interested in systems using dielectrophoresis as the primary force, in which case $F_0 \sim \alpha v^2$, where v is the applied voltage. Similarly, we can recast u_0 in terms of the voltage needed to retain particles against flow at infinite dilution, V_0 . This amounts to replacing $m = (u_0 - \mu_0 F_0)/\mu_0 F_0$ with the equivalent expression $m = (V_0^2 - v^2)/v^2$. For a distributed force (as in our experiments) the enhanced concentration approximation for the trapping landscape is appropriate. By setting $K_D = cV_0^2/(V_0^2 - v^2)$ in equation (4-14) and neglecting the additive constant $\log(2)$ (amounting to the assumption that the

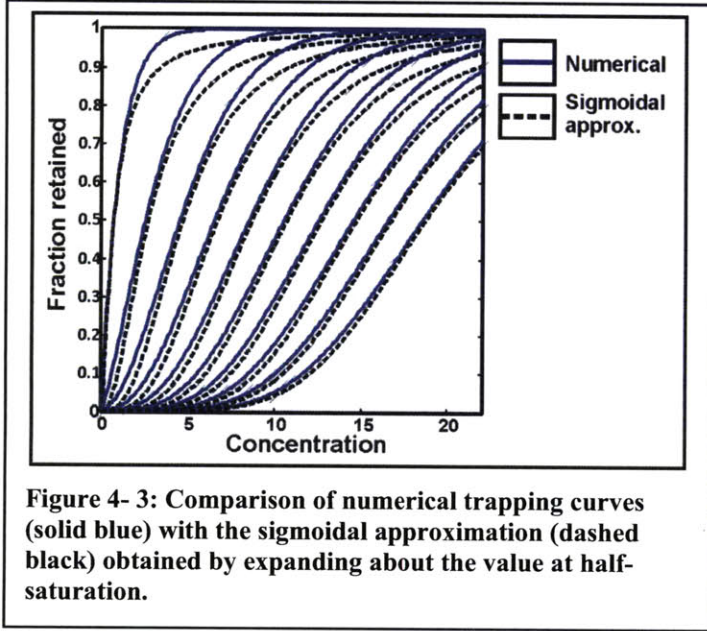


Figure 4-3: Comparison of numerical trapping curves (solid blue) with the sigmoidal approximation (dashed black) obtained by expanding about the value at half-saturation.

the voltage v is well below V_0), we can evaluate the threshold voltage for particle trapping as a function of the dimensionless particle concentration ($v^*(c)$):

$$\frac{v^*}{V_0} = \left[\frac{\pi h R_0^2 c}{4k} + 1 \right]^{\frac{1}{2}} - \left[\frac{\pi h R_0^2 c}{4k} \right]^{\frac{1}{2}} \quad (4-16)$$

Here, we have restored the dimensions to c , so that it represents particles per unit volume for a channel with depth h . Note that the interaction force also contributes to concentration enhancement, but has not been taken into account here; accordingly, this can be thought of as a first-order correction to the model.

To make more physical sense of the parameter k , we look at the implications of

taking a Poisson distribution for $p(m)$, as we did earlier. Specifically, this is consistent with a mobility that depends logarithmically on the distance between particles:

$$\langle M_{ij} \rangle_\theta = -\frac{2}{k} \log \left[\frac{r_{ij}}{R_0} \right] \quad (4-17)$$

As before, R_0 is the distance at which we truncate the θ -averaged hydrodynamic interactions (i.e. $m = 0$ for $r > R_0$). In addition, the maximum coupling between particles occurs when particles are in contact ($r = 2a$). Defining the corresponding mobility as m_0 , this gives:

$$k = -\frac{2}{m_0} \log \left[\frac{2a}{R_0} \right] \quad (4-18)$$

The value of m_0 should be comparable to but less than one, requiring for self-consistency that k be significantly larger than one, and thus that R_0 be at least an order of magnitude larger than the particle radius, a . It seems reasonable to expect R_0 to be a few times the depth of the channel (h), based on the far-field approximation developed in¹¹⁷. Accordingly, as a general guideline, we take $R_0 \approx 2h$, such that $k \sim 3 \log[h/a]$. For our typical geometry and particle size, this gives $k \sim 9$. Using this result in equations (4-14) and (4-15) (and taking $\pi/3 \approx 1$) gives expressions for K_D (dimensional) and n (dimensionless):

$$K_D \approx \left(\log(h/a)/4h^3 \right) \left[(V_0/v)^2 - 1 \right] \quad (4-19)$$

$$n \approx \sqrt{(12/\pi) \left[(V_0/v)^2 - 1 \right] \log(h/a) + (2 \log 2)^2} \quad (4-20)$$

Traditionally, $n = 1$ implies no cooperativity, with $n > 1$ indicating positive cooperativity. In our case, as v decreases, the ability to retain particles becomes more sensitive to the number of particles interacting with each other, increasing cooperativity. The lower limit for n in this model, approached as $v \rightarrow V_0$, is $2 \log 2$ (≈ 1.39) – comparable with but not equal to the case of no cooperativity, a difference likely attributable to the simplifications inherent in the model. Using these expressions for k and R_0 in equation (4-16) gives the characteristic voltage, v^* , for retaining particles in terms of concentration and well-defined geometric parameters for the case of a *distributed* applied force:

$$\frac{v^*}{V_0} \approx \left[\frac{h^3 c}{\log(h/a)} + 1 \right]^{\frac{1}{2}} - \left[\frac{h^3 c}{\log(h/a)} \right]^{\frac{1}{2}} \quad (4-21)$$

Figure 4-4a superimposes $v^*(c)$ (dashed line) and experimentally determined voltage thresholds for particle retention (boxes) on a plot of $\Theta(c, v)$ (shading). The form of equation (4-21) suggests that $\log(h/a)/h^3$ is an important scale for particle concentration in confined device geometries; below this concentration, the threshold voltage decreases rapidly with increasing concentration, while at higher particle concentrations, the characteristic voltage decreases more slowly, proportional to $c^{-1/2}$. The sensitivity at low c suggests that, even at very low concentrations ($c \ll \log(h/a)/h^3$), treating a suspension as infinitely dilute may be inaccurate, because fluctuations in the number of particles arriving at the barrier may lead to spurious particle trapping. Although this model should be treated as only semiquantitative, it offers insight into the relationship between the concentration of particles and their retention in an external force field, making more explicit the notion of hydrodynamic cooperativity.

In obtaining equation (4-21) above, we assumed that the applied force was distributed, so that an enhanced particle concentration was established. For the case of a highly *localized* force, the trapping threshold is obtained by setting $K_D = c$ directly in equation (4-14) (recast in terms of voltages) and solving to obtain:

$$\frac{v^*}{V_0} \approx \left[\frac{k}{c+k} \right]^{\frac{1}{2}} = \left[\frac{3 \log(h/a)}{4\pi h^3 c + 3 \log(h/a)} \right]^{\frac{1}{2}} \quad (4-22)$$

Finally, we note that taking the square of equation (4-21) or equation (4-22) yields a corresponding expression for f^*/F_0 , where the threshold is expressed more generally as a force as opposed to an applied voltage.

Because the threshold for retaining particles decreases with increasing particle concentration, devices for handling concentrated suspensions exhibit hysteresis (Figure 4- 4b). If the flux of particles into a device is constant, particles will accumulate to a steady state concentration that depends on the strength of the concentrating force along with the capacity of the device. Sequentially increasing and then decreasing the applied voltage at a rate sufficiently slow to allow the particle concentration to reach steady state results in a concentration – voltage hysteresis loop.

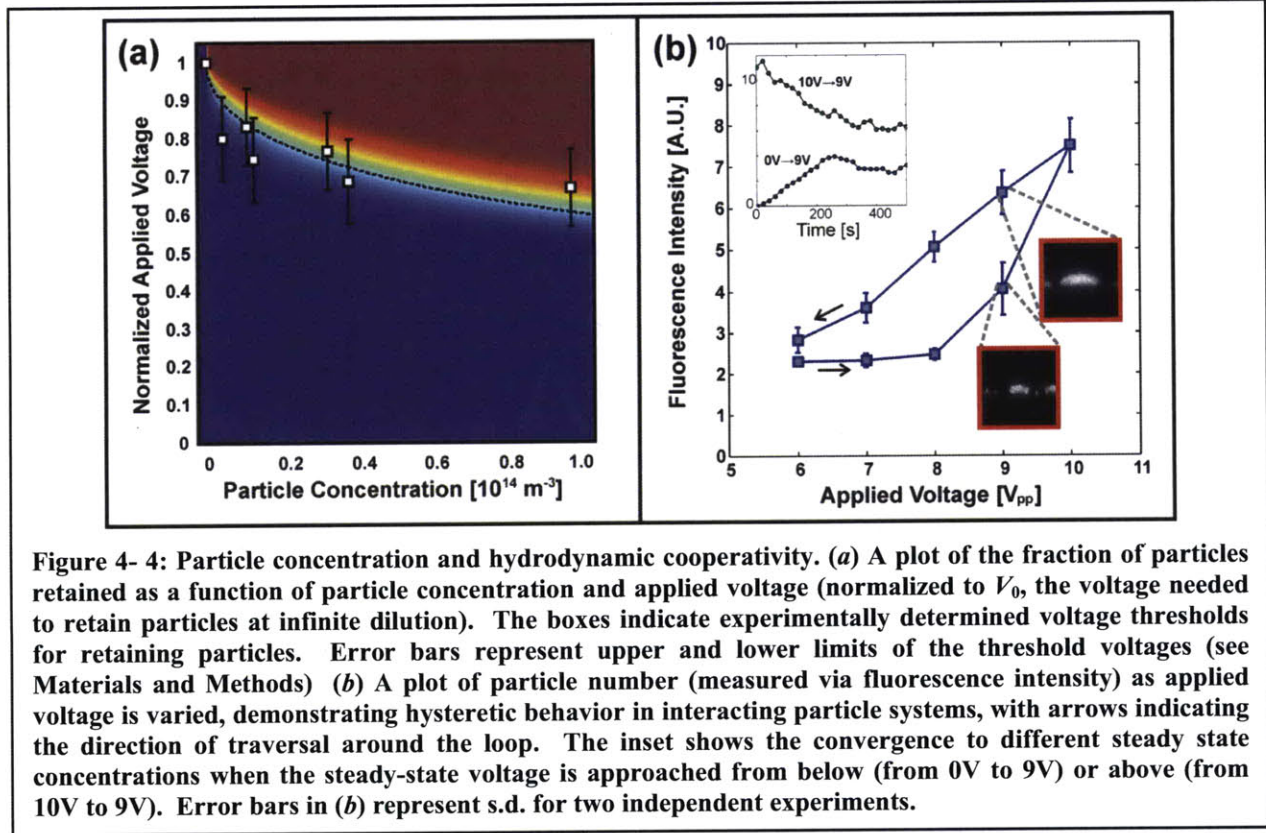


Figure 4- 4: Particle concentration and hydrodynamic cooperativity. (a) A plot of the fraction of particles retained as a function of particle concentration and applied voltage (normalized to V_0 , the voltage needed to retain particles at infinite dilution). The boxes indicate experimentally determined voltage thresholds for retaining particles. Error bars represent upper and lower limits of the threshold voltages (see Materials and Methods) (b) A plot of particle number (measured via fluorescence intensity) as applied voltage is varied, demonstrating hysteric behavior in interacting particle systems, with arrows indicating the direction of traversal around the loop. The inset shows the convergence to different steady state concentrations when the steady-state voltage is approached from below (from 0V to 9V) or above (from 10V to 9V). Error bars in (b) represent s.d. for two independent experiments.

Separating Particles. While cooperation between particles is advantageous in making a relatively dilute suspension more concentrated, it generally has adverse effects on separations, where the objective is to get components of a mixture to exhibit different behavior in a common environment. To see how particle interactions affect separations, we consider two general separation schemes; those with constant and those with time-varying operating conditions. The first separation scheme is analogous to chromatographic separations, in which particles are sorted according to their different mobilities in a (macroscopically) homogeneous environment. In this case, the statistical model we presented for concentrating particles can be applied by accounting for the interaction force of each component of the mixture separately and then combining each of these contributions into a total interaction force. Specifically, we generalize equation (4- 8) to apply to heterogeneous mixtures by defining the distributions $p_i(f_{int})$ for particles of type i contributing to the net interaction force, f_{int} :

$$p_i(f_{int}) = e^{-c_i} \left[\delta(f_{int}/F_i) + \frac{c_i k e^{-f_{int}/F_i}}{\sqrt{c_i k (f_{int}/F_i)}} \left[I_1 \left\{ 2\sqrt{c_i k (f_{int}/F_i)} \right\} \right] \right] \quad (4- 23)$$

Here, f_{int} denotes the net interaction force, while F_i denotes the external force applied to the i^{th} particle. We can then find the probability distribution for the total interaction force acting on a particle by convolving the distributions associated with each component of the mixture: $p(f_{int}) = p_1(f_{int}) * p_2(f_{int}) * \dots * p_k(f_{int})$ (here, k denotes the number of components in the mixture). To calculate the fraction of a given particle type (j) that is retained, we integrate f_{int} from $(u_0 - \mu_j F_j)$ to infinity:

$$\Theta_j(c_j) = \int_{u_0 - \mu_j F_j}^{\infty} p(f') df' \quad (4-24)$$

This result is analogous to equations (4-9) or (4-10) for a heterogeneous mixture of particles. Comparison of this model with experimental results for the separation of polystyrene beads (0.8 μm and 0.5 μm radius) is given in Figure 4-5.

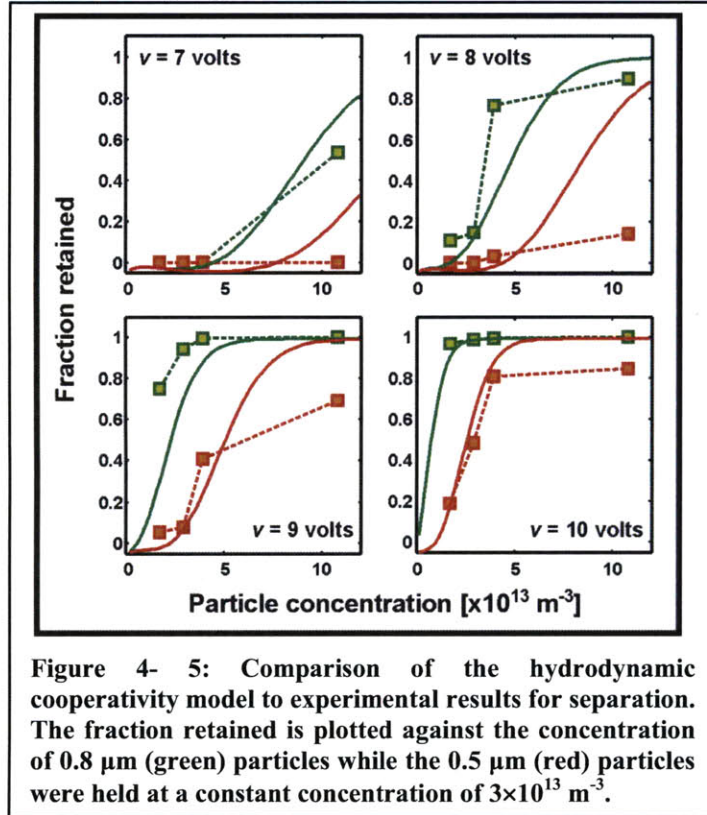


Figure 4- 5: Comparison of the hydrodynamic cooperativity model to experimental results for separation. The fraction retained is plotted against the concentration of 0.8 μm (green) particles while the 0.5 μm (red) particles were held at a constant concentration of $3 \times 10^{13} \text{ m}^{-3}$.

force is modulated; in state *B*, the electric field frequency (and thus particle polarizability) is changed, whereas in state *C*, the electric field magnitude is reduced by reducing the applied voltage. Although the external electrical force is identical in states *B* and *C*, the strength of interactions between particles is not; since the external force scales as $\sim KV^2$ while electrical interactions scale as $\sim K^2V^2$, reducing *K* has a proportionally larger effect on the strength of interactions between particles than on the external force. Accordingly, differences in separation performance associated with varying polarizability as opposed to varying voltage can be attributed specifically to electrical (as opposed to hydrodynamic) interactions between particles. Furthermore, by comparing separations in which a single operating state is maintained to those in which it is varied (i.e. $A \rightarrow B$ or $A \rightarrow C$), we can determine the implications of hysteresis for these simple dynamic separation schemes.

Although this approach is useful for chromatographic separations where the operating conditions do not change throughout the separation, it cannot be directly applied to *dynamic* separation methods, where the force experienced by particles varies over space or time. When this is the case, hysteresis can significantly affect separation performance.

To explore the relationship between particle interactions and separation performance, we perform numerical simulations of a binary separation operating in one of three distinct states. In one state (*A*), only one of the particle types (quantified by n_1) is retained at infinite dilution (i.e. in the absence of interactions). In the other two states (*B* or *C*), the external electrical force is reduced to $\sim 44\%$ of its magnitude in state *A*, with the result that neither particle type is retained at infinite dilution. States *B* and *C* are distinguished from each other by the mechanism through which the external

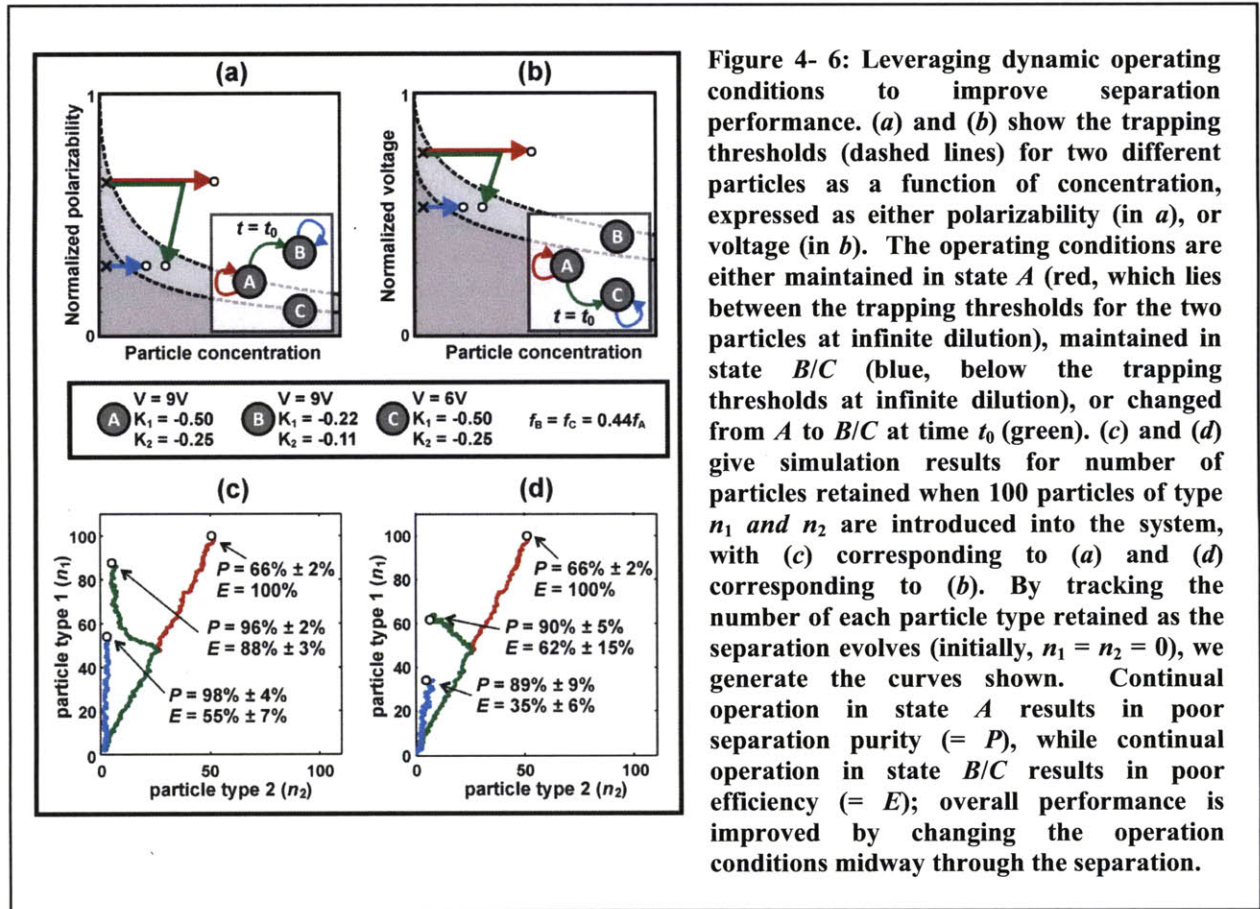


Figure 4- 6: Leveraging dynamic operating conditions to improve separation performance. (a) and (b) show the trapping thresholds (dashed lines) for two different particles as a function of concentration, expressed as either polarizability (in a), or voltage (in b). The operating conditions are either maintained in state A (red, which lies between the trapping thresholds for the two particles at infinite dilution), maintained in state B/C (blue, below the trapping thresholds at infinite dilution), or changed from A to B/C at time t_0 (green). (c) and (d) give simulation results for number of particles retained when 100 particles of type n_1 and n_2 are introduced into the system, with (c) corresponding to (a) and (d) corresponding to (b). By tracking the number of each particle type retained as the separation evolves (initially, $n_1 = n_2 = 0$), we generate the curves shown. Continual operation in state A results in poor separation purity ($= P$), while continual operation in state B/C results in poor efficiency ($= E$); overall performance is improved by changing the operation conditions midway through the separation.

Figure 4- 6 illustrates the specific schemes we simulate, in which 100 particles of type n_1 and n_2 are introduced into the system. In the first case (Figure 4- 6a), either state A or state B is maintained throughout, or there is a transition $A \rightarrow B$ midway through the separation. Correspondingly, Figure 4- 6b illustrates continuous operation in either state A or state C, or a transition $A \rightarrow C$. While states B and C are both below the threshold for retaining particles at infinite dilution, there is some probability that particles of either type will be retained in state B or C if the concentration is sufficiently high. This sub-threshold operation leads to high purity ($P \equiv n_1/(n_1+n_2)$, where n_2 is the quantity of non-target particles retained), but poor efficiency ($E \equiv n_1/100$, referring to the fraction of desired input particles that are retained) (Figure 4- 6c & d, blue lines); alternatively, continual operation in state A leads to high efficiency, but relatively poor purity (Figure 4- 6c & d, red lines). Changing the operating conditions (from $A \rightarrow B$ or $A \rightarrow C$) improves performance overall (Figure 4- 6c & d, green lines); this results from the ability to efficiently concentrate particles in state A, which gradually reduces the threshold for retention of both particle types. Reducing the external electrical force then preferentially releases non-target particles relative to target particles. The superior performance of separations based on varying polarizability (Figure 4- 6c) as opposed to varying voltage (Figure 4- 6d) derives from the ability to leverage interactions between particles when they are desirable (i.e. to initially increase the concentration), and suppress them when they are not (i.e. to preferentially release non-target particles); because external electrical forces scale relative to electrical interactions as $\sim K^{-1}$, lowering the polarizability leads to greater disaggregation in a mixture of closely coupled particles, and thus higher purity separation.

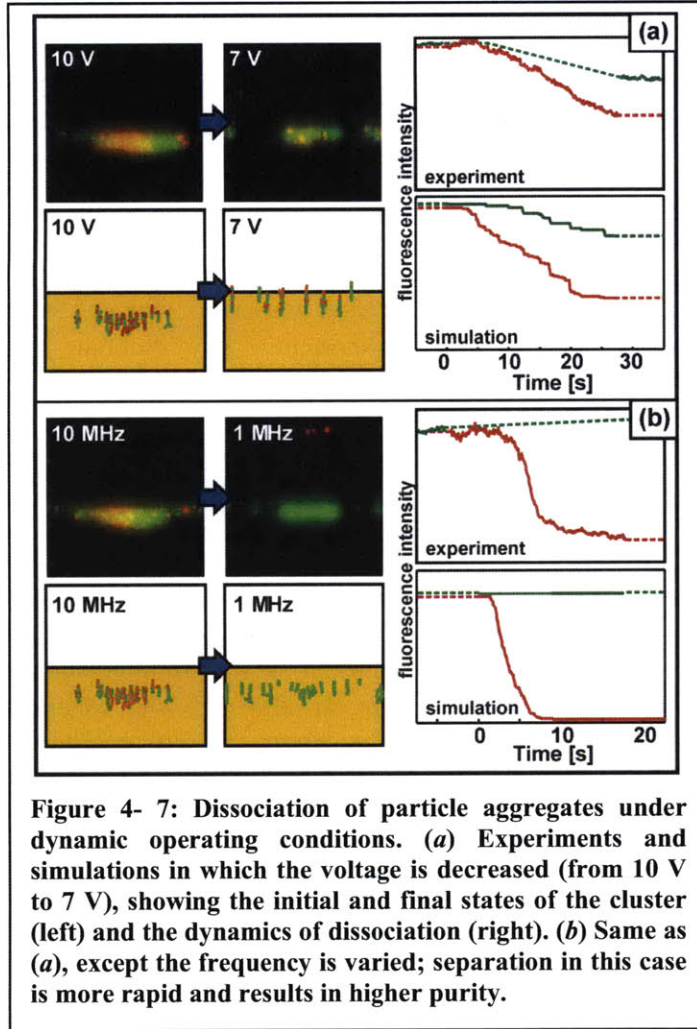


Figure 4- 7: Dissociation of particle aggregates under dynamic operating conditions. (a) Experiments and simulations in which the voltage is decreased (from 10 V to 7 V), showing the initial and final states of the cluster (left) and the dynamics of dissociation (right). (b) Same as (a), except the frequency is varied; separation in this case is more rapid and results in higher purity.

disaggregate (Figure 4- 7a and b).

Interactions between non-spherical particles. The general approach we have taken in modeling interactions between spherical particles can be extended to more complex shapes by introducing forces to constrain assemblies of (spherical) particles to predetermined arrangements. One of the simplest and most relevant cases is that of rod-shaped particles, potentially useful for modeling several species of bacteria (e.g. *E. coli*) or yeast (e.g. *S. pombe*), as well as approximating cells in the process of dividing. To implement this approximation of rod-shaped particles, we introduce spring-like forces that resist deformation (both bending and stretching) of particles grouped into a single object. To prevent stretching deformations, we introduce a force given by:

$$\mathbf{f}_N^S = \xi(\mathbf{x}_{N+1} - \mathbf{x}_N) \frac{|\mathbf{x}_{N+1} - \mathbf{x}_N| - 2a}{|\mathbf{x}_{N+1} - \mathbf{x}_N|} - \xi(\mathbf{x}_N - \mathbf{x}_{N-1}) \frac{|\mathbf{x}_N - \mathbf{x}_{N-1}| - 2a}{|\mathbf{x}_N - \mathbf{x}_{N-1}|} \quad (4- 25)$$

Here, the force is acting on the N^{th} particle in the chain; if the particle is at either end of the chain, the expression for the force consists of only one term. The coefficient ξ reflects the effective stiffness of the rod, and is chosen to achieve sufficient rigidity of the rod without compromising numerical stability. For the force that imparts bending stiffness to the rod, we use:

To better understand the process of disaggregation when polarizability or voltage is changed, we performed experiments and simulations involving polystyrene beads with different sizes and polarizabilities. Figure 4- 7 illustrates how the relationship between external and interaction forces influences separation of these particles when the operating conditions vary in time. Here, a mixture of the particles is subjected to conditions under which a fraction of both components is retained before the operating conditions (either applied voltage or particle polarizability, experimentally controlled through the electric field frequency) are suddenly changed. When the voltage is decreased, the external and interaction forces decrease proportionally; as a result, dissociation of the particle cluster is incomplete, with the loss of target particles as well as the retention of background (Figure 4- 7a). Alternatively, varying the frequency affects the polarizability of background particles (a change in K from -0.46 to ~ 0) considerably more than the target particles (a change from -0.48 to -0.36), enabling higher purity separation (Figure 4- 7b). Additionally, simulations of particle dissociation accurately predict the dynamics with which clusters of particles

$$\mathbf{f}_N^B = \zeta(\mathbf{x}_{N+1} - 2\mathbf{x}_N + \mathbf{x}_{N-1}) \quad (4-26)$$

In the above, ζ has the same interpretation as before. Other than the introduction of these forces, all of the calculations (i.e. those covering self-consistent electrostatics and hydrodynamics) are identical to those used for a suspension of purely spherical (but potentially polydisperse) particles.

One question that this extension allows us to explore is the role of shape in the separation of particles. For example, if we have a binary mixture consisting of spherical particles (with radius a_1) and prolate spheroidal particles (with major axis a and minor axis b), we can study the purity and efficiency with which we are able to separate them. For example, if we constrain volume to be conserved, then $ab^2 = a_1^3$. Approximating the rod as a chain of n spheres with radius a_2 gives $a_2 = n^{-1/3}a_1$. Running this simulation at moderately high particle concentrations with the sphere and subunit polarizabilities set to equal values allows us to estimate how shape influences separations in the presence of particle interactions (Figure 4- 8a & b).

The reduced retention of rod-shaped particles relative to spherical particles of equal volume is to be expected; the effective polarizability of a prolate ellipse aligned to the electric field is generally lower in magnitude than that of a sphere, while the drag coefficient for an ellipsoid with low to modest eccentricity aligned with the flow is very similar to that given by Stoke's law. Specifically, a homogeneous sphere with polarizability K_1 will result in a corresponding ellipsoid with polarizability $K_2 = K_1/[1 + K_1(3l_{\parallel} - 1)]$. Here, l_{\parallel} is the depolarization factor of the ellipsoid, which (for a rod-shaped prolate particle) will be $< 1/3$. To test the accuracy of approximating an ellipsoid with spherical subunits, we can compare the effective polarizability of a particle chain (as determined self-consistently using the Greens function for a point dipole) with that of an ellipsoid with the same volume and aspect ratio. For example, a prolate ellipsoid with $a = 2b$ has a depolarization factor $l_{\parallel} \approx 0.17$, so that $K_{eff} \approx K/[1 - K/2]$, whereas a chain of two spheres with radius b yields $K_{eff} \approx K/[1 - K/4]$. This quantitative discrepancy persists for chains and ellipsoids of arbitrary eccentricity, although there is good qualitative agreement for $K < 0$ (Figure 4- 8c). We will return to the role of shape in cell separations in a more specific context in Chapter 5.

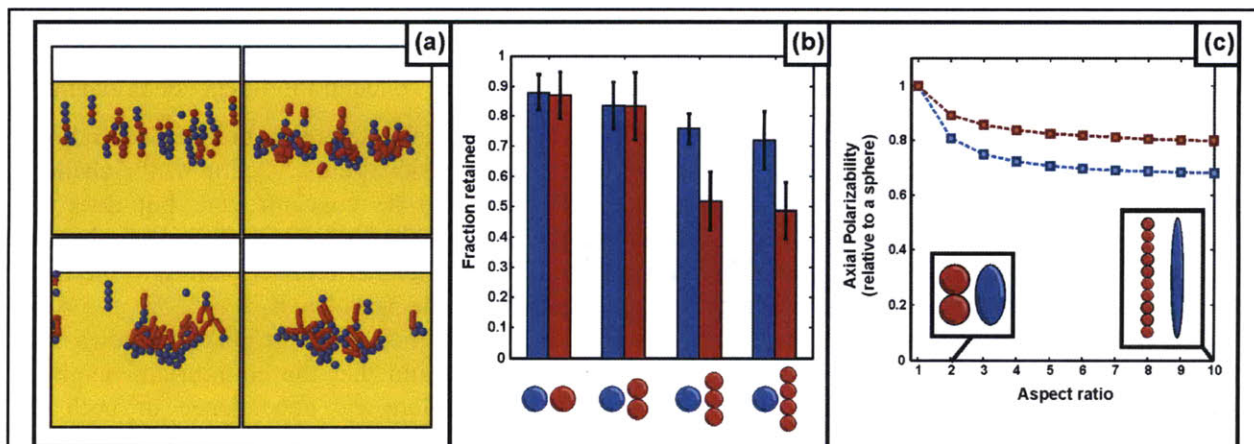


Figure 4- 8: Interactions between non-spherical particles. (a) Simulations of mixtures of spherical and non-spherical particles, constructed through spherical subunits constrained to move as a rigid rod as described in the text. Top left, two spheres; top right: spheres (blue) and rods (red) with $n = 2$; bottom left, rods with $n = 3$; bottom right, rods with $n = 4$. (b) Compiled results of simulations as in (a), showing the fraction of spheres (blue) and rods (red) retained under different conditions. The polarizability of the blue spheres and red spherical subunits are identical in all cases, illustrating the tendency of elongated particles to be less effectively retained. (c) Comparing the depolarization factor of a true ellipse (blue) and an approximation constructed from spherical subunits (red). The prediction is in good qualitative agreement, but under-predicts the effects of elongation on polarizability.

Particle interactions case study: Dielectrophoretic Field Flow Fractionation (DEP-FFF).

To better understand the significance of particle interactions in specific approaches to cell separation, we performed two case studies. The first case study focuses on a variant of field flow fractionation (FFF) that uses dielectrophoresis to levitate particles above a substrate, where a parabolic velocity profile gives rise to different elution times for particles with different equilibrium levitation heights (Figure 4- 9).

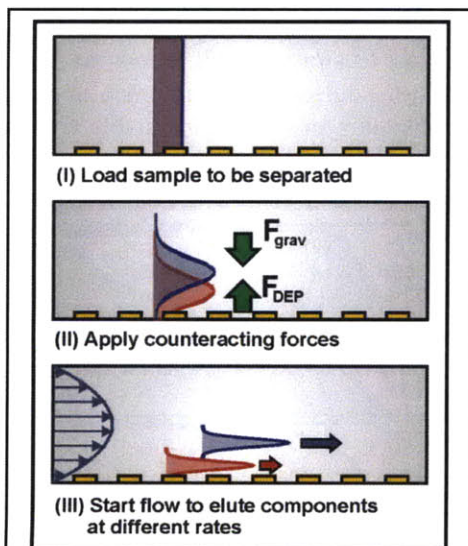


Figure 4- 9: Dielectrophoretic field flow fractionation (DEP-FFF). A sample of particles is loaded (I) and allowed to settle to an equilibrium height under counteracting forces (II); pressure-driven flow elutes particles at different heights at different rates, leading to separation.

One key feature of DEP-FFF is that it is typically performed as a batch mode separation (techniques related to field flow fractionation that operate under continuous flow are generally described as split flow techniques¹¹⁸). The cells to be separated are introduced into the device as a concentrated plug, confined to as small a volume as possible (Figure 4- 9, (I)). Flow in the channel is then stopped, as cells within this plug are allowed to settle to an equilibrium height above the substrate, determined by the balance of gravitational and dielectrophoretic forces (Figure 4- 9, (II)). Typically, the upward-directed DEP force is created by an array of interdigitated electrodes lining the floor of the separation chamber, and operated at a frequency such that cells are repelled. Once the cells reach equilibrium, a pressure gradient is applied to the channel, causing cells at different heights to be eluted (and collected) at different times (Figure 4- 9, (III)).

The effects of particle interactions in DEP-FFF are most significant during the sedimentation / levitation stage, where

the cell concentration is highest. Although hydrodynamic interactions do not influence the equilibrium heights of cells, they do alter the rate at which cells approach this equilibrium. In contrast, electrostatic interactions alter both equilibrium and the approach to equilibrium in a concentration-dependent manner.

Figure 4- 10 shows the results of simulations of DEP-FFF at three different particle concentrations. For simplicity, we have constrained these simulations to a two-dimensional cross section of the channel, taken along its length and depth; this increases the effective particle concentration, but does not qualitatively alter the conclusions. Figure 4- 10a shows the patterns that arise as different numbers of particles ($N = 50, 100,$ and 200) approach three distinct equilibrium heights (corresponding to the three dashed lines and determined from the differences in polarizability of the particles, $K_1 = -1/2, K_2 = -1/4, K_3 = -1/8$) in the presence (upper and lower left, lower right) or absence (upper right) of electrostatic interactions. Note that we are simulating a polydisperse mixture, and that the equilibrium height is independent of the size of the particle; this arises from the volumetric dependence of both the gravitational and DEP forces, which counteract each other. Although chains of particles following the electric field are visible even at lower concentrations ($N = 50$), most particles converge to their equilibrium heights for $N = 50$. For $N = 100$ and $N = 200$, however, simulations predict the formation of large aggregates in which particles become stably held away from what would be their equilibrium height at infinite dilution. Particles in these cases can be thought of as occupying a frustrated energy landscape; neighboring particles disturb the electric field creating many local minima in which a particle can become stuck before reaching its minimum energy position. This frustration has a significant effect on the ability to perform separations. Figure 4- 10b shows the fraction of particles eluted as a function of time for $N = \{50, 100, 200\}$. As the particle concentration increases, the overlap in the elution profiles for the three types of particles increases as well. To quantify this effect, we define the separation *purity* (P) as the percentage of a collected sample corresponding to the targeted particle type, and the separation *efficiency* (E) as the percentage of a targeted particle type that is collected. With these figures of merit, one definition of separation quality is the geometric mean of purity and efficiency, \sqrt{PE} . Gating the separation so as to maximize this parameter across the three types of particles, we find that the separation quality decreases from 95% to 77% to 71% as concentration increases. Interestingly, the elution step (i.e. when flow is initiated after particles have converged as closely as frustration will allow to their equilibrium heights) appears to mitigate the effects of particle interactions during the sedimentation step, even though the electric field remains on throughout the simulations; this may be attributable to the dilution of particles as they become dispersed in the spatially non-uniform flow.

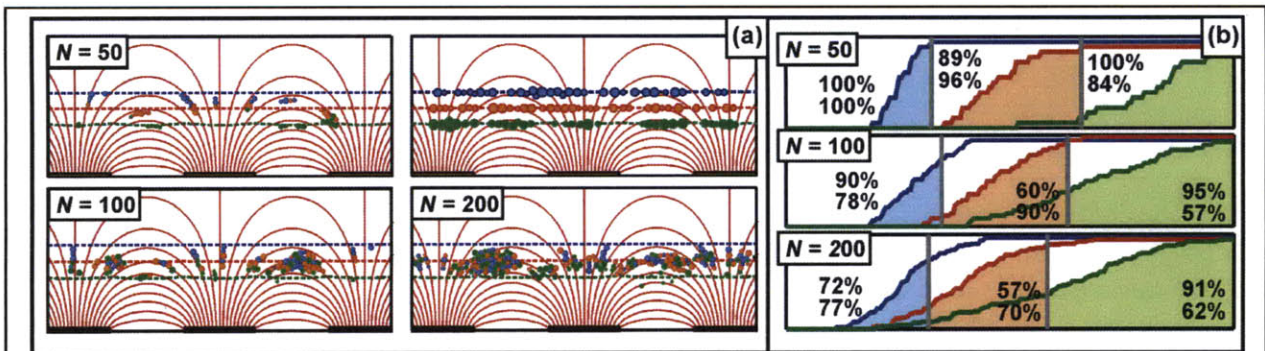
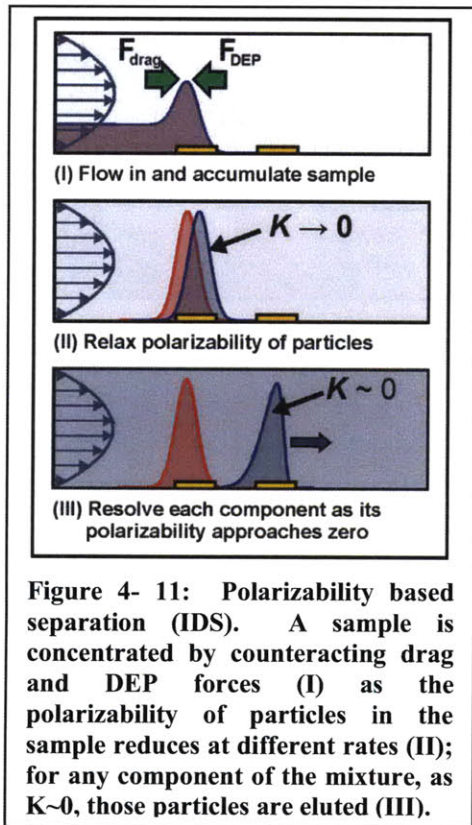


Figure 4- 10: Simulations of DEP-FFF using different numbers of particles. (a) shows the arrangements of different numbers of particles ($N = 50, 100,$ and 200) in the presence of electrostatic interactions after they have reached steady state under counteracting dielectrophoretic and gravitational forces. In the upper right panel, the simulation is run without electrostatic interactions, illustrating ideal convergence of each particle to its equilibrium height (dashed lines). The red streamlines depict the applied electric field. (b) shows the fraction of particles eluted (vertical axis) versus time (horizontal axis) for the three cases in (a) after flow has started. The different samples are optimally gated (see accompanying text) at times denoted by the horizontal lines, and the numbers correspond to the purity and efficiency with which each sample is collected. These results are obtained by averaging 20 ($N = 50$), 10 ($N = 100$) and 5 ($N = 200$) simulations.

Particle interactions case study: Isodielectric Separation. As the second part of the case study, we apply our simulations to a separation approach analogous to that used in IDS. Similar to examples discussed earlier in this Chapter (for example, Figure 4- 7b), we consider a coplanar pair of electrodes used to create a dielectrophoretic force opposing an external flow (Figure 4- 11, (I)). This force concentrates particles impinging on the barrier according to their size and polarizability; by varying this polarizability continuously over time, it is possible to preferentially elute one type of particle (Figure 4-



11, (II) & (III)). This situation is directly analogous to IDS if we choose a reference frame moving with particles as they are deflected by the electrodes, so that spatial differences in medium conductivity transform into temporal differences in particle polarizability.

Figure 4- 12 gives results of simulations in which varying numbers of three types of particles are initially retained by the electrode barrier. Initially, all three types of particles have identical polarizabilities ($K_1 = K_2 = K_3 = -1/2$). Allowing these values to evolve differently over time according to $K_i = -1/2[1 - 2^{i-1}at]$ leads to separation, as particles pass through the barrier at different times in a manner that depends on the initial number of particles (Figure 4- 12a). Figure 4- 12b shows the fraction of each type of particle eluted as a function of time, similar to Figure 4- 10b for DEP-FFF. Here, however, the trend for separation quality ($\equiv \sqrt{PE}$) is opposite that predicted for DEP-FFF, with quality increasing from 67% to 79% to 91% with increasing particle concentration.

Although the absolute numbers quantifying separation performance for both DEP-FFF and IDS will vary with the geometry and operating conditions assumed in the simulations, the general trends are independent of these considerations and can be understood in terms of earlier discussions in this chapter. Electrostatic and hydrodynamic interactions act to distribute the force on one particle to all of its nearest neighbors, so that particles that could be easily distinguished by an external force at infinite dilution tend to respond homogeneously to the same external force at higher concentrations. This gives rise to a form of hysteresis (Figure 4- 4b), where particles that are concentrated into aggregates under one set of operating conditions do not readily dissociate even when these operating conditions are changed. In the case of DEP-FFF, particle aggregates form during the sedimentation/levitation stage of the separation and persist throughout the elution stage, although the concentration becomes less as the particles are dispersed in the flow. In the case of IDS, particle aggregates also form at high concentrations; however, by modulating the polarizability of the particles, it is possible to effectively suppress electrostatic interactions, so that closely packed aggregates are able to dissociate. Additionally, simulations suggest that at higher concentrations, this dissociation becomes less spread out over time for each particle type. This is illustrated in Figure 4- 12b, where the fraction of particles eluted changes from 0 to 1 over a narrower time as the size of the initial aggregate increases. This narrowing of the elution peak is the reason for improved separation performance as concentration increases.

A simple one-dimensional model for the external and interaction electrostatic forces acting on the i^{th} particle helps to explain this observation. The total electrostatic force can be expressed as a sum of the

external and interaction components, giving $f_i^{ES} = \alpha_i K_i v^2 + \sum_j w_{ij} K_i K_j v^2$. The sign of the coupling coefficient, w_{ij} , is such that the force is directed towards the higher concentration of particles, whereas the sign of the coefficient α_i depends on the electric field gradient. The form of f_i^{ES} suggests defining an effective polarizability, $K_i' = K_i [1 + \alpha_i^{-1} \sum_j w_{ij} K_j]$. For a particle that begins to leave the aggregate, the contribution of the interaction term will act to return it to the aggregate. This contribution will persist until $K_i = 0$, when the electrostatic force vanishes. Accordingly, electrostatic coupling at high concentrations effectively acts to make the approach of K_i to zero more abrupt, decreasing the time over which particles with polarizability K_i are separated.

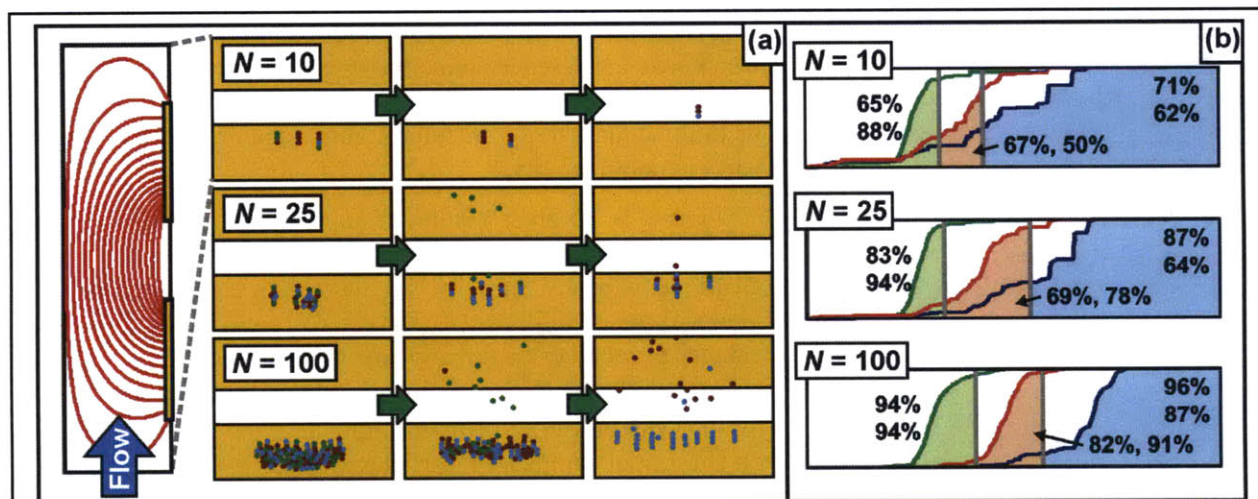


Figure 4- 12: Simulations of polarizability based separations using different numbers of particles. (a) Each row shows the progression of a simulation starting with different numbers of particles (10, 25, and 100) accumulated at the electrodes. The columns represent different time points (identical across the three simulations) in the separation, illustrating the sequence in which different components of the mixture elute. (b) shows the fraction of particles eluted (vertical axis) versus time (horizontal axis) for the three cases in (a) as the polarizabilities are reduced. The different samples are optimally gated (see accompanying text) at times denoted by the horizontal lines, and the numbers correspond to the purity and efficiency with which each sample is collected. These results are obtained by averaging 20 ($N = 50$), 10 ($N = 100$) and 5 ($N = 200$) simulations.

The improved performance of IDS with increasing particle concentration requires that hydrodynamic and electrostatic cooperativity aid in the initial retention of particles without interfering with their eventual elution. While the above argument regarding dipole interactions suggests that these will not inhibit performance at arbitrarily high concentrations (since electrostatic interactions vanish as particles approach their dielectrophoretic equilibrium), such is not necessarily the case for hydrodynamic and steric interactions. If particles become too closely coupled through these mechanisms (or, in an extreme case, stick together through van der Waals or hydrophobic forces), separation performance will sharply diminish. As a result, there is an inevitable upper bound at which performance begins to decrease with particle concentration; this will depend, however, on factors we have not considered here (*e.g.* the surface properties of the particles), and more work – both experimental and theoretical – is needed to determine where this upper bound lies.

Discussion.

Complex systems are often characterized by global patterns emerging as a consequence of local interaction rules propagating across increasing length scales¹¹⁹. In the case of microfluidic systems, we find that the laws governing interactions between particles give rise to forms of cooperativity, hysteresis, and dynamical frustration on scales ranging from a few (<10) to many thousands of particles. The hierarchy of behaviors that emerge over these length scales ultimately affect device performance. In this

context, we have used simulations and experiments to better understand the global patterns emerging in the microfluidic concentration and separation of colloidal particles as well as some of the underlying dynamics that act on a smaller (local) scale. In particular, we have found that cooperativity quantitatively changes the ability to concentrate particles, while dynamical frustration leads to dynamic patterns in particle clusters. Additionally, since the concentration of particles in a device both affects and is affected by interaction forces, microfluidic devices exhibit a form of hysteresis. The significance of this hysteresis is determined by the relationship between external and interaction forces, and can be modulated by varying the operating conditions (e.g. voltage and frequency). One practical consequence of this is that two-stage separations - those in which particles are first concentrated under one set of conditions and then sorted by switching to a second set of conditions - may be a more effective than streaming separations in which the operating conditions are maintained constant throughout.

In the disaggregation of particle clusters, the concept of dynamical frustration may play a critical role. One source of dynamical frustration, arising in protein folding and other applications^{97,120}, is an energy landscape with a well-defined global minimum but riddled with many local minima in which the system may become trapped. Interactions between neighboring particles within a cluster give rise to a large number of local energy minima in which particles may be retained, despite the presence of more favorable states which exist at a larger scale. Convergence to the global minimum depends in part on the rate at which alternate arrangements of particles are sampled. Because large aggregates of particles are not static but rather recirculate continually, the ensemble of particles is able to sample a large number of configurations that would be inaccessible in a static, “frozen” system. Although the applications that we have focused on involve size and energy scales at which entropy does not play a significant role, we propose that the frustrated dynamics of interacting particle systems may act as a surrogate for thermal forces in helping a system to achieve a form of steady state. In the context of separation, this state could be characterized by, for example, the separation’s purity.

Our approach to modeling particle interactions provides insight into some of the considerations that arise when concentrated suspensions are subjected to external forces. Despite some of the inherent limitations in accuracy (e.g. truncation of multipolar electric and hydrodynamic interactions), our simulations suggest a high degree of qualitative and quantitative agreement with experiments, allowing us to use these models predictively, including for the design of new separation techniques that leverage particle interactions to improve performance.

Materials and Methods

Device Fabrication, Packaging and Preparation. Electrodes for the microfluidic devices were fabricated on 6” Pyrex wafers using e-beam evaporation (2000-Å Au/100-Å Ti adhesion layer) and a standard liftoff process. Final electrode spacing and line width are 55 μm and 45 μm , respectively. For the microfluidic channels, we use PDMS replica molding from an SU-8 patterned silicon master (SU-8 2015, Microchem, Newton MA) to create channels with a width of 2 mm and a height of from 18 μm , achieving ~5% uniformity in film thickness over the area of the wafer. Electrical signals are created by a function generator (33220A, Agilent, Palo Alto, CA) and monitored by an oscilloscope (Tektronix, Richardson, TX). To make fluidic connections between the device and a syringe pump (KD Scientific 200, Holliston, MA), we use Tygon tubing (ID 0.02”, OD 0.06”, VWR, Brisbane, CA) press fit into the PDMS.

Particle characterization. In all experiments, we use polystyrene beads (09719, Polysciences, Inc. Warrington, PA, $1.646 \pm 0.069 \mu\text{m}$ true diameter; F-8819 and F-8825, Molecular Probes Eugene, OR, 1.0 and 2.0 μm true diameters, respectively, ~1% CV estimated by manufacturer) suspended in a medium with a conductivity of 0.5 mS/m adjusted to the density of polystyrene using sucrose; to determine the polarizability of particles in this medium, we first determined the particles’ effective conductivities using crossover frequency measurements. For the particles displayed in Figure 4- 7, these measurements (fitted to a single shell surface conductance model) predict polarizabilities of approximately -0.48 and -

0.36 for the 1.6 μm green fluorescent beads and -0.46 and 0 for the 1.0 μm red fluorescent beads at frequencies of 10 MHz and 1 MHz, respectively. We control flowrates in the microfluidic device using a syringe pump set to generate an average fluid velocity of 45 $\mu\text{m/s}$, except where stated otherwise.

Fluorescence imaging. To determine the threshold for particle trapping (Figure 4- 4a), we use fluorescent microscopy to visually inspect the area of the device over which the external force is applied. After activating the electrodes at a particular voltage, we wait five minutes before inspecting the field for the presence of particle aggregates. Extending the waiting time was not observed to affect the trapping voltage. To find the voltage threshold, we repeat this process at a lower or higher voltage until upper and lower limits on the threshold within 1 V of each other are determined (this corresponds to the error bars in Figure 4- 4a). To measure the fraction of particles retained under different conditions (Figure 4- 5), we use fluorescent microscopy along with a particle counting algorithm to measure the particle flux downstream of the electrodes with the electric field off, and again three minutes after the electrodes are activated. We then use the change in flux to calculate the fraction of particles retained.

To track the formation and dissociation of particle clusters (as in Figure 4- 4b and Figure 4- 7), we use the intensity of the fluorescent signal under constant imaging conditions to quantify the change in composition of the aggregate over time. For separations (Figure 4- 7), we allow a mixture of particles to form an aggregate prior to introducing a step change in either voltage or frequency. Because we are only able to record images from one fluorescent channel at a time, during the period of disaggregation, we image those particles (1.0 μm red fluorescent beads in Figure 4- 7) which we expect to be preferentially released from the cluster. Before and after disaggregation, we image from the alternate channel (in this case, the 1.6 μm green fluorescent beads).

Appendix to Chapter 4

Matlab Scripts

The following are Matlab scripts representative of those used throughout this thesis. Although in some cases more specialized functions were used, these provide the basic framework for simulating interactions between two different particle types with different sizes and polarizabilities. A listing and brief description of the scripts included here follows.

interaction_sim.m: Simulates a binary mixture with different sizes and polarizabilities impinging on a coplanar dielectrophoretic barrier. The operating conditions, particle properties, and the number and concentration (volume fraction) of particles can be adjusted. The output 'P' is an $N \times 3 \times M$ three-dimensional matrix of particle positions for N particles and M frames. The output 's0' is an $N \times M$ matrix containing ± 1 to identify whether a particle is of type 1 or 2. This function calls `field_constants.m`.

mixed_rods.m: Simulates a binary mixture of particles comprised of different numbers of spherical subunits, where the size and polarizability of the two types of subunits can be adjusted. Otherwise, the simulation matches that of `interaction_sim.m`. The outputs 'P' and 's0' are defined as in `interaction_sim.m`, with N corresponding to the number of subunits. The outputs 'a1' and 'a2' give the radii of these subunits. This function calls `field_constants.m`.

dep_fff.m: Simulates the levitation/sedimentation and elution of particles with three distinct polarizabilities over an array of interdigitated electrodes with adjustable parameters. The output 'P' is an $N \times 2 \times M$ three-dimensional matrix of particle positions for N particles and M frames. The output 'K' is an $N \times M$ matrix containing the polarizability of each of the N particles.

field_constants.m: Called by `interaction_sim.m` and `mixed_rods.m` to determine parameters based on the conformal mapping solution to the coplanar electrode geometry.

```

function [P s0] = interaction_sim()
warning off
c = 0.001;           % Particle volume fraction
H = 20e-6;          % Channel height
d = 45e-6;          % Electrode width
g = 55e-6;          % Electrode gap
U = 5e-5;           % Average fluid velocity
em = 80*8.85e-12;   % Medium permittivity
mu = 1e-3;          % Medium viscosity

V0 = 8;             % Applied voltage
K1 = -1/2;          % Polarizability of particle type 1
K2 = -1/4;          % Polarizability of particle type 2
a1 = 0.8e-6;        % Radius of particle type 1
a2 = 1.0e-6;        % Radius of particle type 2 (>= a1)
level = 1/2;        % Relative fraction of type 1 vs. type 2
M = 100;            % Total number of particles
m = 10;             % Sampling frequency (i.e. save every mth iteration)
a0 = sqrt(a1*a2);
Dc = 2*a0;

[C D B k0] = field_constants(H,d,g);
Ew = 1/(4*ellipke(k0^2));

prob = rand(1);
s = (prob>level) - (prob<=level);

W = 4*H;    x0 = W/4;    y0 = -4*H;
p(1,1) = x0*(rand(1)-1/2);
p(1,2) = y0;
p(1,3) = a2;

dt0 = a1/abs(40*U);
T = 4/3*pi*a0^3*M/(c*dt0*U*W/4*H);
m_steps = sort(round(T*rand(M,1)));

Nmax = M + 1;
countdown = 3000;

P = zeros(Nmax,3,round((max(m_steps)+countdown)/m));
s0 = zeros(Nmax,round((max(m_steps)+countdown)/m));
t = 0;    k = 1;

while (countdown > 0)
if (size(p,1) > 0)
    N = size(p,1);
    diags = [0:N-1]*(N+1) + 1;
    i1 = 1:N;

    A0 = zeros(3*N,3*N);
    G = zeros(3*N,3*N);
    ex0 = zeros(1,N); ey0 = zeros(1,N);

    a = a1*(s==1) + a2*(s==-1);

```

```

K = K1*(s==1) + K2*(s==-1);
b = 2*em./(3*mu*a);
aa = a*ones(size(a'));
aa = aa';

%=====
% Display the simulation and save the current iteration:
%=====
if mod(round(t/dt0),m)==0

    ind1 = find(s == 1);
    ind2 = find(s == -1);
    plot(p(ind1,1),p(ind1,2),'o','MarkerSize',round(25*a1/4e-6),...
        'MarkerFaceColor',[0,0.5,1],'MarkerEdgeColor',[0,0,0.75],...
        'LineWidth',1);
    if(~isempty(ind1)); hold on; end
    plot(p(ind2,1),p(ind2,2),'o','MarkerSize',round(25*a2/4e-6),...
        'MarkerFaceColor',[0.75,0,0],'MarkerEdgeColor',[1,0.5,0],...
        'LineWidth',1);
    axis equal; xlim([-W/2 W/2]); ylim([-4*H 0]);
    drawnow;
    hold off

    P(1:size(p,1),:,k) = p;
    s0(1:size(p,1),k) = s;
    k = k + 1;
end

%=====
% Calculate the baseline electric field here:
%=====
delta = H/100000;
x = [p(:,2) p(:,2)+delta p(:,2)];
y = [H-p(:,3) H-p(:,3) H-p(:,3)+delta];
z = x+i*y;
u = sinh(pi/H*(z-i*H/2));
v = (u+B)./(C*u+D);
dudz = pi/H*cosh(pi*z/H - i*pi/2);
dvdu = (D-B*C)./(D+C*u)./(D+C*u);
dwdv = 1./sqrt(1-k0*k0.*v.*v)./sqrt(1- v.*v);
Ez = V0*Ew.*conj(dwdv).*conj(dvdu).*conj(dudz);

Ex = real(Ez); Ey = imag(Ez);
ex0((x(:,1)<0)) = -Ex((x(:,1)<0));
ex0((x(:,1)>=0)) = Ex((x(:,1)>=0));
ey0((x(:,1)<0)) = -Ey((x(:,1)<0));
ey0((x(:,1)>=0)) = Ey((x(:,1)>=0));
Ex((x<0)) = -Ex((x<0));
Ex((x>=0)) = Ex((x>=0));
Ey((x<0)) = -Ey((x<0));
Ey((x>=0)) = Ey((x>=0));
ey = ex0'; ez = ey0'; ex = 0*ez;

Eyy = (Ex(:,2)-Ex(:,1))/(delta);
Eyz = -(Ex(:,3)-Ex(:,1))/(delta);
Ezz = -(Ey(:,3)-Ey(:,1))/(delta);

```

```

clear ex0 ey0 x y z u v Ex Ey Ez
%=====
% Take care of overlapping particles:
%=====
dx = p(:,1)*ones(1,N) - ones(N,1)*p(:,1)';
dy = p(:,2)*ones(1,N) - ones(N,1)*p(:,2)';
dz = p(:,3)*ones(1,N) - ones(N,1)*p(:,3)';
r = sqrt(dx.^2 + dy.^2 + dz.^2);
A = a*ones(1,N) + ones(N,1)*a';
flags = (r<A); flags(diags) = 0;

p0 = p;
while sum(sum(flags))>0
    r = r.*(r<A) + 2e6*a2*(r>=A);
    fx = dx./r; fx(diags) = 0;
    fy = dy./r; fy(diags) = 0;
    fz = dz./r; fz(diags) = 0;
    p = p + 1e-5*[(a1./a).*sum(fx,2) (a1./a).*sum(fy,2) (a1./a).*sum(fz,2)]*dt0;
    dx = 0; dy = 0; dz = 0;
    dx = p(:,1)*ones(1,N) - ones(N,1)*p(:,1)';
    dy = p(:,2)*ones(1,N) - ones(N,1)*p(:,2)';
    dz = p(:,3)*ones(1,N) - ones(N,1)*p(:,3)';
    r = sqrt(dx.^2 + dy.^2 + dz.^2);
    flags = (r<A); flags(diags) = 0;
    p((p(:,1)<-W/2+a2),1) = -W/2+a2;
    p((p(:,1)>W/2-a2),1) = W/2-a2;
    p((p(:,3)<a2),3) = a2;
    p((p(:,3)>=H-a2),3) = H-a2;
end
us = (p - p0)/dt0;

dZ1 = -((-p(:,3))*ones(1,N) - ones(N,1)*p(:,3)');
R1 = sqrt(dx.^2 + dy.^2 + dZ1.^2);

k1 = 1./R1; k3 = k1.^3; k5 = k1.^5;
q1 = 1./r; q3 = q1.^3; q5 = q1.^5;
q1(diags) = 0; q3(diags) = 0; q5(diags) = 0;

%=====
% Update the electric field here:
%=====
e0 = [ex;ey;ez];

A0(i1,i1) = (q3+k3) - 3*dx.^2.*(q5+k5);
A0(i1+N,i1+N) = (q3+k3) - 3*dy.^2.*(q5+k5);
A0(i1+2*N,i1+2*N) = (q3-k3) - 3*(dz.^2.*q5 - dZ1.^2.*k5);
A0(i1,i1+N) = -3*dx.*dy.*(q5+k5);
A0(i1+N,i1) = A0(i1,i1+N);
A0(i1,i1+2*N) = -3*dx.*(dz.*q5 - dZ1.*k5);
A0(i1+2*N,i1) = -3*dx.*(dz.*q5 + dZ1.*k5);
A0(i1+N,i1+2*N) = -3*dy.*(dz.*q5 - dZ1.*k5);
A0(i1+2*N,i1+N) = -3*dy.*(dz.*q5 + dZ1.*k5);
A0 = -diag([K;K;K].*[a;a;a].^3)*A0;

```

```

e = (eye(3*N)-A0)\e0;
e0 = []; A0 = [];
px = diag(a.^3.*K.*e(il));
py = diag(a.^3.*K.*e(il+N));
pz = diag(a.^3.*K.*e(il+2*N));

%=====
% Electrostatic Green's Functions:
%=====
p_r = (px*dx + py*dy + pz*dz);
p_R1 = (px*dx + py*dy - pz*dZ1);
p_ri = p_r.*q1.^7;
p_R1i = p_R1.*k1.^7;

exx = (6*px*dx + 3*p_r).*q5 - 15*(dx.^2).*(p_ri + p_R1i) + ...
      (6*px*dx + 3*p_R1).*k5;
eyy = (6*py*dy + 3*p_r).*q5 - 15*(dy.^2).*(p_ri + p_R1i) + ...
      (6*py*dy + 3*p_R1).*k5;
ezz = (6*pz*dz + 3*p_r).*q5 - 15*(dz.^2).*p_ri - ...
      (-6*pz*dZ1 + 3*p_R1).*k5 + 15*(dZ1.^2).*p_R1i;
exy = 3*(px*dy + py*dx).*(q5+k5) - 15*(dx.*dy).*(p_ri+p_R1i);
eyx = exy;
exz = 3*(px*dz + pz*dx).*q5 - 15*dx.*(dz.*p_ri - dZ1.*p_R1i) - ...
      3*(px*dZ1 - pz*dx).*k5;
ezx = 3*(px*dz + pz*dx).*q5 - 15*dx.*(dz.*p_ri + dZ1.*p_R1i) + ...
      3*(px*dZ1 - pz*dx).*k5;
eyz = 3*(py*dz + pz*dy).*q5 - 15*dy.*(dz.*p_ri - dZ1.*p_R1i) - ...
      3*(py*dZ1 - pz*dy).*k5;
ezy = 3*(py*dz + pz*dy).*q5 - 15*dy.*(dz.*p_ri + dZ1.*p_R1i) + ...
      3*(py*dZ1 - pz*dy).*k5;

U0 = 6*U*p(:,3)/H.*(1 - p(:,3)/H);
ux = b.*(exx*diag(px) + exy*diag(py) + exz*diag(pz));
uy = b.*(eyx*diag(px) + eyy*diag(py) + eyz*diag(pz)) + b.*(py*Eyy + pz*Eyz);
uz = b.*(ezx*diag(px) + ezy*diag(py) + ezz*diag(pz)) + b.*(py*Eyz + pz*Ezz);

ux = ux + us(:,1);
uy = uy + us(:,2);
uz = uz + us(:,3);
u = [ux;uy;uz];

%=====
% Lubrication:
%=====
D0 = ((a*a')./A).^2.*(1./(r-A) - 1./Dc)./(r.^2);
D0(diags) = 0;
D0((D0<0)) = 0;
D0 = diag(1./a)*D0;
Sxx = D0.*(dx.*dx); Syy = D0.*(dy.*dy); Szz = D0.*(dz.*dz);
Sxy = D0.*(dx.*dy); Syz = D0.*(dy.*dz); Sxz = D0.*(dx.*dz);
S = [Sxx Sxy Sxz ;
     Sxy Syy Syz ;
     Sxz Syz Szz];
S0 = [diag(Sxx*ones(N,1)) diag(Sxy*ones(N,1)) diag(Sxz*ones(N,1)) ;
      diag(Sxy*ones(N,1)) diag(Syy*ones(N,1)) diag(Syz*ones(N,1)) ;
      diag(Sxz*ones(N,1)) diag(Syz*ones(N,1)) diag(Szz*ones(N,1))];

```

```

u = (eye(3*N) + S0 - S)\u;

%=====
% Hydrodynamic Green's Functions:
%=====
G1 = -2*p(:,3)*p(:,3)';
dri1 = q1 - k1;
dri3 = q3 - k3;

G(i1,i1)      = dri1 + dx.^2.*dri3 + G1.*(k3 - 3*dx.^2.*k5);
G(i1+N,i1+N)  = dri1 + dy.^2.*dri3 + G1.*(k3 - 3*dy.^2.*k5);
G(i1+2*N,i1+2*N) = dri1 + (dz.^2.*q3 - dZ1.^2.*k3) + ...
                    G1.*(-k3 + 3*dZ1.^2.*k5);
G(i1,i1+N)    = dx.*dy.*dri3 - 3*dx.*dy.*k5.*G1;
G(i1+N,i1)    = G(i1,i1+N);
G(i1,i1+2*N)  = dx.*dz.*dri3 + 3*dx.*dZ1.*k5.*G1;
G(i1+2*N,i1)  = dx.*dz.*dri3 - 3*dx.*dZ1.*k5.*G1;
G(i1+N,i1+2*N) = dy.*dz.*dri3 + 3*dy.*dZ1.*k5.*G1;
G(i1+2*N,i1+N) = dy.*dz.*dri3 - 3*dy.*dZ1.*k5.*G1;

G = 3/4*[aa aa aa; aa aa aa ; aa aa aa].*G;
u = u + G*u;    G = [];

%=====
% Update positions:
%=====
p = p + dt0*[u(i1) u(i1+N)+U0 u(i1+2*N)];
p((p(:,1)<-W/2+a2),1) = -W/2+a2;
p((p(:,1)>W/2-a2),1) = W/2-a2;
p((p(:,3)<a2),3) = a2;
p((p(:,3)>=H-a2),3) = H-a2;

if sum(p(:,2)>y0+4*H)>0;
    s((p(:,2)>y0+4*H)) = [];
    p((p(:,2)>y0+4*H),:) = [];
end
end

if(size(m_steps,2)==0)
    countdown = countdown - 1;
elseif (round(t/dt0) == m_steps(1))
    while (size(m_steps,2)~=0)&&(round(t/dt0) == m_steps(1))
        new = [x0*(rand(1)-1/2),y0,H/4*(rand(1))];
        p = [p;new];
        prob = rand(1);
        s = [s ; (prob>level)-(prob<=level)];
        m_steps(1) = [];
        size(m_steps,1)
    end
end
t = t + dt0;
dx = 0; dy = 0; dz = 0; u = 0;
end
% EOF interaction_sim.m

```

```

function [P s0 a1 a2] = mixed_rods()
warning off
c = 0.001;           % Particle volume fraction
H = 20e-6;          % Channel height
d = 45e-6;          % Electrode width
g = 55e-6;          % Electrode gap
U = 5e-5;           % Average fluid velocity
em = 80*8.85e-12;   % Medium permittivity
mu = 1e-3;          % Medium viscosity

V0 = 7;             % Operating voltage
xi = 100;           % Spring stiffness joining the rods
L1 = 2;             % Number of spheres comprising particle type 1
L2 = 3;             % Number of spheres comprising particle type 2 (>=L1)
K1 = -1/4;          % Subunit polarizability for particle type 1
K2 = -1/4;          % Subunit polarizability for particle type 2
a1 = 0.8e-6;        % Subunit size for particle type 1
a2 = a1*(L1/L2)^(1/3); % Subunit size for particle type 2 (<=a1)
d0 = 2.01*min([a1 a2]);
a0 = sqrt(a1*a2);
Dc = 2*a0;

level = 1/2;        % Relative fraction of type 1 vs. type 2
M = 100;            % Total number of particles
m = 100;            % Sampling frequency (i.e. save every mth iteration)
N = 1*L1;

[C D B k0] = field_constants(H,d,g);
Ew = V0/(4*ellipke(k0^2));

prob = rand(N,1);
s = (prob>level)-(prob<=level);
s(1:L1) = 1;

W = 4*H;
x0 = W/4;
y0 = -4*H;
p(1:N,1:3) = 0;
p(1:L1:N,1) = x0*(rand(round(N/L1),1)-1/2);
p(1:L1:N,2) = y0;
p(1:L1:N,3) = a1;
h = 2*pi*rand(round(N/L1),1);
for ind = 2:L1
    p(ind:L1:N,1:3) = p(ind-1:L1:N,1:3) + d0*[cos(h), sin(h), 0];
end

xi1 = xi*ones(N,3);    xi1(L1:L1:end,:) = 0;
xi2 = xi*ones(N,3);    xi2(1:L1:end,:) = 0;    xi2(L1:L1:end,:) = 0;

dt0 = a1*10/abs(4*U*xi);
T = 4/3*pi*a1^3*M/(c/L1*dt0*U*W/4*H);
m_steps = sort(round(T*rand(M,1)));

Nmax = M + 1;

```

```

countdown = 10000;

P = zeros(Nmax,3,round((max(m_steps)+countdown)/m));
s0 = zeros(Nmax,round((max(m_steps)+countdown)/m));

t = 0;
k = 1;
while (countdown > 0)
if (size(p,1) > 0)
    N = size(p,1);
    diags = [0:N-1]*(N+1) + 1;
    i1 = 1:N;

    A0 = zeros(3*N,3*N);
    G = zeros(3*N,3*N);
    ex0 = zeros(1,N); ey0 = zeros(1,N);

    a = a1*(s==1) + a2*(s==-1);
    K = K1*(s==1) + K2*(s==-1);
    b = 2*em./(3*mu*a);
    aa = a*ones(size(a));
    aa = aa';

if mod(round(t/dt0),m)==0

    ind1 = find(s == 1);
    ind2 = find(s == -1);
    plot(p(ind1,1),p(ind1,2),'o','MarkerSize',round(25*a1/4e-6),...
        'MarkerFaceColor',[0,0.5,1],'MarkerEdgeColor',[0,0,0.75],...
        'LineWidth',1);
    if(~isempty(ind1)); hold on; end
    plot(p(ind2,1),p(ind2,2),'o','MarkerSize',round(25*a2/4e-6),...
        'MarkerFaceColor',[0.75,0,0],'MarkerEdgeColor',[1,0.5,0],...
        'LineWidth',1);
    axis equal; xlim([-W/2 W/2]); ylim([-4*H 0]);
    drawnow;
    hold off

    P(1:size(p,1),:,k) = p;
    s0(1:size(p,1),k) = s;
    k = k + 1;
end

%=====
% Calculate the baseline electric field here:
%=====
delta = H/100000;
x = [p(:,2) p(:,2)+delta p(:,2)];
y = [H-p(:,3) H-p(:,3) H-p(:,3)+delta];
z = x+i*y;
u = sinh(pi/H*(z-i*H/2));
v = (u+B)./(C*u+D);
dudz = pi/H*cosh(pi*z/H - i*pi/2);
dvdu = (D-B*C)./(D+C*u)./(D+C*u);
dwdv = 1./sqrt(1-k0*k0.*v.*v)./sqrt(1- v.*v);

```



```

Ez = Ew.*conj(dw dv) .*conj(dv du) .*conj(du dz);

Ex = real(Ez);  Ey = imag(Ez);
ex0((x(:,1)<0)) = -Ex((x(:,1)<0));
ex0((x(:,1)>=0)) = Ex((x(:,1)>=0));
ey0((x(:,1)<0)) = -Ey((x(:,1)<0));
ey0((x(:,1)>=0)) = Ey((x(:,1)>=0));
Ex((x<0)) = -Ex((x<0));
Ex((x>=0)) = Ex((x>=0));
Ey((x<0)) = -Ey((x<0));
Ey((x>=0)) = Ey((x>=0));
ey = ex0';  ez = ey0';  ex = 0*ez;

Eyy = (Ex(:,2)-Ex(:,1))/(delta);
Eyz = -(Ex(:,3)-Ex(:,1))/(delta);
Ezz = -(Ey(:,3)-Ey(:,1))/(delta);

clear ex0 ey0 x y z u v Ex Ey Ez
%=====
% Take care of overlapping particles:
%=====
dx = p(:,1)*ones(1,N) - ones(N,1)*p(:,1)';
dy = p(:,2)*ones(1,N) - ones(N,1)*p(:,2)';
dz = p(:,3)*ones(1,N) - ones(N,1)*p(:,3)';
r = sqrt(dx.^2 + dy.^2 + dz.^2);
A = a*ones(1,N) + ones(N,1)*a';
flags = (r<A);  flags(diags) = 0;

p0 = p;
while sum(sum(flags))>0
    r = r.*(r<A) + 2e6*a1*(r>=A);
    fx = dx./r;  fx(diags) = 0;
    fy = dy./r;  fy(diags) = 0;
    fz = dz./r;  fz(diags) = 0;
    p = p + 1e-5*[(a2./a).*sum(fx,2) (a2./a).*sum(fy,2) (a2./a).*sum(fz,2)]*dt0;
    dx = 0;  dy = 0;  dz = 0;
    dx = p(:,1)*ones(1,N) - ones(N,1)*p(:,1)';
    dy = p(:,2)*ones(1,N) - ones(N,1)*p(:,2)';
    dz = p(:,3)*ones(1,N) - ones(N,1)*p(:,3)';
    r = sqrt(dx.^2 + dy.^2 + dz.^2);
    flags = (r<A);  flags(diags) = 0;
    p((p(:,1)<-W/2+a1),1) = -W/2+a1;
    p((p(:,1)>W/2-a1),1) = W/2-a1;
    p((p(:,3)<a1),3) = a1;
    p((p(:,3)>=H-a1),3) = H-a1;
end
us = (p - p0)/dt0;

dZ1 = -((-p(:,3))*ones(1,N) - ones(N,1)*p(:,3)');
R1 = sqrt(dx.^2 + dy.^2 + dZ1.^2);

k1 = 1./R1;  k3 = k1.^3;  k5 = k1.^5;
q1 = 1./r;  q3 = q1.^3;  q5 = q1.^5;
q1(diags) = 0;  q3(diags) = 0;  q5(diags) = 0;

```

```

%=====
% Update the electric field here:
%=====
e0 = [ex;ey;ez];

A0(i1,i1) = (q3+k3) - 3*dx.^2.*(q5+k5);
A0(i1+N,i1+N) = (q3+k3) - 3*dy.^2.*(q5+k5);
A0(i1+2*N,i1+2*N) = (q3-k3) - 3*(dz.^2.*q5 - dZ1.^2.*k5);
A0(i1,i1+N) = -3*dx.*dy.*(q5+k5);
A0(i1+N,i1) = A0(i1,i1+N);
A0(i1,i1+2*N) = -3*dx.*(dz.*q5 - dZ1.*k5);
A0(i1+2*N,i1) = -3*dx.*(dz.*q5 + dZ1.*k5);
A0(i1+N,i1+2*N) = -3*dy.*(dz.*q5 - dZ1.*k5);
A0(i1+2*N,i1+N) = -3*dy.*(dz.*q5 + dZ1.*k5);
A0 = -diag([K;K;K].*[a;a;a].^3)*A0;

e = (eye(3*N)-A0)\e0;
e0 = []; A0 = [];
px = diag(a.^3.*K.*e(i1));
py = diag(a.^3.*K.*e(i1+N));
pz = diag(a.^3.*K.*e(i1+2*N));

%=====
% Electrostatic Green's Functions:
%=====
p_r = (px*dx + py*dy + pz*dz);
p_R1 = (px*dx + py*dy - pz*dZ1);
p_ri = p_r.*q1.^7;
p_R1i = p_R1.*k1.^7;

exx = (6*px*dx + 3*p_r).*q5 - 15*(dx.^2).*(p_ri + p_R1i) + ...
      (6*px*dx + 3*p_R1).*k5;
eyy = (6*py*dy + 3*p_r).*q5 - 15*(dy.^2).*(p_ri + p_R1i) + ...
      (6*py*dy + 3*p_R1).*k5;
ezz = (6*pz*dz + 3*p_r).*q5 - 15*(dz.^2).*p_ri - ...
      (-6*pz*dZ1 + 3*p_R1).*k5 + 15*(dZ1.^2).*p_R1i;
exy = 3*(px*dy + py*dx).*(q5+k5) - 15*(dx.*dy).*(p_ri+p_R1i);
eyx = exy;
exz = 3*(px*dz + pz*dx).*q5 - 15*dx.*(dz.*p_ri - dZ1.*p_R1i) - ...
      3*(px*dZ1 - pz*dx).*k5;
ezx = 3*(px*dz + pz*dx).*q5 - 15*dx.*(dz.*p_ri + dZ1.*p_R1i) + ...
      3*(px*dZ1 - pz*dx).*k5;
eyz = 3*(py*dz + pz*dy).*q5 - 15*dy.*(dz.*p_ri - dZ1.*p_R1i) - ...
      3*(py*dZ1 - pz*dy).*k5;
ezy = 3*(py*dz + pz*dy).*q5 - 15*dy.*(dz.*p_ri + dZ1.*p_R1i) + ...
      3*(py*dZ1 - pz*dy).*k5;

U0 = 6*U*p(:,3)/H.*(1 - p(:,3)/H);
ux = b.*(exx*diag(px) + exy*diag(py) + exz*diag(pz));
uy = b.*(eyx*diag(px) + eyy*diag(py) + eyz*diag(pz)) + b.*(py*Eyy + pz*Eyz);
uz = b.*(ezx*diag(px) + ezy*diag(py) + ezz*diag(pz)) + b.*(py*Eyz + pz*Ezz);

ux = ux + us(:,1);
uy = uy + us(:,2);
uz = uz + us(:,3);

```

```

%=====
% Spring-Like Forces:
%=====
if N>1
dp = diff(p);
d = sqrt(sum(dp.^2,2));
f = (xi1(1:end-1,:)).*dp.*([d d d]-d0)./([d d d]);
ddp = [dp./[d d d];0,0,0]-[0,0,0;dp./[d d d]];
u = [f;0,0,0] - [0,0,0;f] + xi2*d0.*ddp;
ux = ux + u(:,1);
uy = uy + u(:,2);
uz = uz + u(:,3);
end
u = [ux;uy;uz];

%=====
% Lubrication:
%=====
D0 = ((a*a')./A).^2.*(1./(r-A) - 1./Dc)./(r.^2);
D0(diags) = 0;
D0((D0<0)) = 0;
D0 = diag(1./a)*D0;
Sxx = D0.*(dx.*dx);   Syy = D0.*(dy.*dy);   Szz = D0.*(dz.*dz);
Sxy = D0.*(dx.*dy);   Syz = D0.*(dy.*dz);   Sxz = D0.*(dx.*dz);
S = [Sxx Sxy Sxz ;
     Sxy Syy Syz ;
     Sxz Syz Szz];
S0 = [diag(Sxx*ones(N,1)) diag(Sxy*ones(N,1)) diag(Sxz*ones(N,1)) ;
      diag(Sxy*ones(N,1)) diag(Syy*ones(N,1)) diag(Syz*ones(N,1)) ;
      diag(Sxz*ones(N,1)) diag(Syz*ones(N,1)) diag(Szz*ones(N,1))];
u = (eye(3*N) + S0 - S)\u;

%=====
% Hydrodynamic Green's Functions:
%=====
G1 = -2*p(:,3)*p(:,3)';
dri1 = q1 - k1;
dri3 = q3 - k3;

G(i1,i1)      = dri1 + dx.^2.*dri3 + G1.*(k3 - 3*dx.^2.*k5);
G(i1+N,i1+N) = dri1 + dy.^2.*dri3 + G1.*(k3 - 3*dy.^2.*k5);
G(i1+2*N,i1+2*N) = dri1 + (dz.^2.*q3 - dZ1.^2.*k3) + ...
                    G1.*(-k3 + 3*dZ1.^2.*k5);
G(i1,i1+N)    = dx.*dy.*dri3 - 3*dx.*dy.*k5.*G1;
G(i1+N,i1)    = G(i1,i1+N);
G(i1,i1+2*N)  = dx.*dz.*dri3 + 3*dx.*dZ1.*k5.*G1;
G(i1+2*N,i1)  = dx.*dz.*dri3 - 3*dx.*dZ1.*k5.*G1;
G(i1+N,i1+2*N) = dy.*dz.*dri3 + 3*dy.*dZ1.*k5.*G1;
G(i1+2*N,i1+N) = dy.*dz.*dri3 - 3*dy.*dZ1.*k5.*G1;

G = 3/4*[aa aa aa; aa aa aa ; aa aa aa].*G;
u = u + G*u;   G = [];

%=====

```

```

% Update positions:
%=====
p = p + dt0*[u(i1) u(i1+N)+U0 u(i1+2*N)];
p((p(:,1)<-W/2+a1),1) = -W/2+a1;
p((p(:,1)>W/2-a1),1) = W/2-a1;
p((p(:,3)<a1),3) = a1;
p((p(:,3)>=H-a1),3) = H-a1;

if sum(p(:,2)>1*H)>0;
    j1 = [];
    j0 = find(p(:,2)>1*H);
    type = s(j0);
    L = L1*(type==1) + L2*(type==-1);
    if xil(j0)==0; j1 = (j0-L+1):j0;
    else j1 = j0:(j0+L-1); end
    K(j1) = [];
    s(j1) = [];
    xil(j1,:) = [];
    xi2(j1,:) = [];
    p(j1,:) = [];
end
end

if(size(m_steps,2)==0)
    countdown = countdown - 1;
elseif (round(t/dt0) == m_steps(1))
    while (size(m_steps,2)~=0)&(round(t/dt0) == m_steps(1))
        prob = rand(1);
        type = (prob>level)-(prob<=level);
        L = L1*(type==1) + L2*(type==-1);
        h = 2*pi*rand(1);
        new(1,:) = [x0*(rand(1)-1/2),y0,H/4*(rand(1))];
        s = [s ; type];
        for ind = 2:L
            new(ind,:) = new(ind-1,:) + 2.01*(a1*(type==1) + a2*(type==-1))*[cos(h),sin(h),0];
            s = [s ; type];
        end
        p = [p;new];
        xil_vec = xi*ones(L,3); xil_vec(L,:) = 0;
        xi2_vec = xil_vec; xi2_vec(1,:) = 0;
        xil = [xil ; xil_vec];
        xi2 = [xi2 ; xi2_vec];

        m_steps(1) = [];
        size(m_steps,1)
        new = [];
    end
end

t = t + dt0;
dx = 0; dy = 0; dz = 0; u = 0;
end
% EOF mixed_rods.m

```

```

function [P K] = dep_fff()
warning off
d1 = 100e-6;           % Width of electrode
d2 = 100e-6;           % Spacing between electrodes
d = (d1+d2)/2;
q = d1/(2*d);
.[k0,junk] = ellipke(cos(pi*q/2));

H = 400e-6;           % Channel height
a = 6.e-6;            % Particle radius
Dc = 2*a;
U = 0e-3;
V0 = 2.5;             % Applied voltage
em = 80*8.85e-12;    % Medium permittivity
mu = 1e-3;           % Medium viscosity
b = 2*em/(3*mu*a);
drho = 1060-1000;    % Density difference between particles and medium
g = 9.8;             % Acceleration due to gravity

N = 50;
W = 2*d;
p(1:N,1) = 2*W*(rand(N,1)-1/2);
p(1:N,2) = 3*a + H/8*rand(N,1);

K1 = -1/4;           % Polarizability of particle type 1
K2 = -1/2;           % Polarizability of particle type 2
K3 = -1/8;           % Polarizability of particle type 3
prob = rand(N,1);
K = K1*(prob<1/3) + K2*(prob>1/3) .* (prob<2/3) + K3*(prob>2/3);
ind1 = find(K == K1);
ind2 = find(K == K2);
ind3 = find(K == K3);

dt0 = 1*a/2e-3;

scrsz = get(0,'ScreenSize');
figure('Position',[100 100 scrsz(3)/1.25 scrsz(4)/1.25])
drawnow;
pause(1);
t = 0;
k = 1;
k_final = 1200;
init = 0;

P = zeros(N,2,k_final);

while k<=k_final

    if (k == 800);
        U = 0.2/60*1e-6/(H*25e-3);
    end

    N = size(p,1);
    diags = [0:N-1]*(N+1) + 1;
    i1 = 1:N;

```

```

A0 = zeros(2*N,2*N);
G = zeros(2*N,2*N);

if mod(round(t/dt0),10)==0

    plot(p(ind1,1),p(ind1,2),'o','MarkerSize',round(250*a/100e-6),...
        'MarkerFaceColor',[0,0.5,1],'MarkerEdgeColor',[0,0,0.75],...
        'LineWidth',1);
    if (size(ind1>0)); hold on; end
    plot(p(ind2,1),p(ind2,2),'o','MarkerSize',round(250*a/100e-6),...
        'MarkerFaceColor',[1,0.5,0],'MarkerEdgeColor',[0.75,0,0],...
        'LineWidth',1);
    plot(p(ind3,1),p(ind3,2),'o','MarkerSize',round(250*a/100e-6),...
        'MarkerFaceColor',[0.25,0.75,0],'MarkerEdgeColor',[0,0.5,0],...
        'LineWidth',1);
    axis equal; ylim([0 H]);
    drawnow;
    hold off;

    P(1:size(p,1),:,k) = p;
    k = k + 1
end

%=====
% Calculate the baseline electric field here:
%=====
delta = d/100000;
x = [p(:,1) p(:,1)+delta p(:,1)];
y = [p(:,2) p(:,2) p(:,2)+delta];
z = exp(pi*(i*x-y)/d);
v = (z./(1-2.*z*cos(q*pi)+z.^2)).^(1/2);
S = 2*((cos(pi/2*x/d)>0)-1/2);
Ex = S*pi*V0/(k0*d).*imag(v);
Ey = S*pi*V0/(k0*d).*real(v);

ex = Ex(:,1); ez = Ey(:,1);

Exx = (Ex(:,2)-Ex(:,1))/(delta);
Exz = (Ex(:,3)-Ex(:,1))/(delta);
Ezz = (Ey(:,3)-Ey(:,1))/(delta);

clear x y z v Ex Ey

%=====
% Take care of overlapping particles:
%=====
dx = p(:,1)*ones(1,N) - ones(N,1)*p(:,1)';
dz = p(:,2)*ones(1,N) - ones(N,1)*p(:,2)';
r = sqrt(dx.^2 + dz.^2);
flags = (r<(2*a)); flags(diags) = 0;

p0 = p;
while sum(sum(flags))>0
    r = r.*(r<(2*a)) + 2e6*a*(r>=(2*a));
    fx = dx./r; fx(diags) = 0;
end

```

```

fz = dz./r; fz(diags) = 0;
p = p + 1e-5*[sum(fx,2) sum(fz,2)]*dt0;
dx = 0; dz = 0;
dx = p(:,1)*ones(1,N) - ones(N,1)*p(:,1)';
dz = p(:,2)*ones(1,N) - ones(N,1)*p(:,2)';
r = sqrt(dx.^2 + dz.^2);
flags = (r<(2*a)); flags(diags) = 0;
p((p(:,2)<a),2) = a;
p((p(:,2)>=H-a),2) = H-a;
end

us = (p-p0)/dt0;

dZ = -((-p(:,2))*ones(1,N) - ones(N,1)*p(:,2)');
R = sqrt(dx.^2 + dZ.^2);

k1 = 1./R; k3 = k1.^3; k5 = k1.^5;
q1 = 1./r; q3 = q1.^3; q5 = q1.^5;
q1(diags) = 0; q3(diags) = 0; q5(diags) = 0;

%=====
% Update the electric field here:
%=====
e0 = [ex;ez];

A0(i1,i1) = (q3+k3) - 3*dx.^2.*(q5+k5);
A0(i1+N,i1+N) = (q3-k3) - 3*(dz.^2.*q5 - dZ.^2.*k5);
A0(i1,i1+N) = -3*dx.*(dz.*q5 - dZ.*k5);
A0(i1+N,i1) = -3*dx.*(dz.*q5 + dZ.*k5);
A0 = -a.^3*diag([K;K])*A0;

e = (eye(2*N)-A0)\e0;
e0 = []; A0 = [];
px = diag(a^3.*K.*e(i1));
pz = diag(a^3.*K.*e(i1+N));

%=====
% Electrostatic Green's Functions:
%=====
p_r = (px*dx + pz*dz);
p_R = (px*dx - pz*dZ);
p_ri = p_r.*q1.^7;
p_Ri = p_R.*k1.^7;

exx = (6*px*dx+3*p_r).*q5 - 15*(dx.^2).*(p_ri+p_Ri) + (6*px*dx+3*p_R).*k5;
ezz = (6*pz*dz+3*p_r).*q5 - 15*(dz.^2).*(p_ri - (-6*pz*dZ+3*p_R).*k5 + 15*(dZ.^2).*(p_Ri);
exz = 3*(px*dz+pz*dx).*q5 - 15*dx.*(dz.*p_ri-dZ.*p_Ri) - 3*(px*dZ-pz*dx).*k5;
ezx = 3*(px*dz+pz*dx).*q5 - 15*dx.*(dz.*p_ri+dZ.*p_Ri) + 3*(px*dZ-pz*dx).*k5;

U0 = 6*U*p(:,2)/H.*(1 - p(:,2)/H);
ux = b*(exx*diag(px) + exz*diag(pz)) + b*(px*Exx + pz*Exz);
uz = b*(ezx*diag(px) + ezz*diag(pz)) + b*(px*Exz + pz*Ezz) - 2/9*a^2/mu*drho*g;

ux = ux + init*us(:,1);
uz = uz + init*us(:,2);

```

```

init = 1;
u = [ux;uz];

%=====
% Lubrication:
%=====
D0 = (a/4)*(1./(r-2*a) - 1./Dc)./(r.^2);
D0(diags) = 0;
D0((D0<0)) = 0;
Sxx = D0.*(dx.*dx); Szz = D0.*(dz.*dz); Sxz = D0.*(dx.*dz);
S = [Sxx Sxz ;
     Sxz Szz];
S0 = [diag(Sxx*ones(N,1)) diag(Sxz*ones(N,1)) ;
      diag(Sxz*ones(N,1)) diag(Szz*ones(N,1))];
u = (eye(2*N) + S0 - S)\u;

%=====
% Hydrodynamic Green's Functions:
%=====
G1 = -2*p(:,2)*p(:,2)';
dri1 = q1 - k1;
dri3 = q3 - k3;

G(i1,i1) = dri1 + dx.^2.*dri3 + G1.*(k3 - 3*dx.^2.*k5);
G(i1+N,i1+N) = dri1 + (dz.^2.*q3 - dZ.^2.*k3) + ...
                G1.*(-k3 + 3*dZ.^2.*k5);
G(i1,i1+N) = dx.*dz.*dri3 + 3*dx.*dZ.*k5.*G1;
G(i1+N,i1) = dx.*dz.*dri3 - 3*dx.*dZ.*k5.*G1;

G = 3/4*a*G;
u = u + G*u;

%=====
% Update positions:
%=====
p = p + dt0*[u(i1)+U0 u(i1+N)];
p((p(:,2)<a),2) = a;
p((p(:,2)>=H-a),2) = H-a;

t = t + dt0;
dx = 0; dy = 0; dz = 0;
end
% EOF dep_fff.m

```



```

function [C D B k] = field_constants(h,d,g)

z1 = i*h;
z2 = 0;
z3 = g/2;
z4 = g/2 + d;
u1 = sinh( pi/h * ( z1-i*h/2 ));
u2 = sinh( pi/h * ( z2-i*h/2 ));
u3 = sinh( pi/h * ( z3-i*h/2 ));
u4 = sinh( pi/h * ( z4-i*h/2 ));

tmp1 = -u2*u2+u1*(u2+u3-u4-u4)+2*sqrt((u1-u2)*(u1-u3)*(u2-u4)*(u3-u4))+u2*u4+u3*(u4-u3);
tmp2 = (u2-u3)*(-u1+u2+u3-u4);

C = tmp1/tmp2;
C = real(C);
D = (u3*(1-C)-u2*(1+C))/2;
D = i*imag(D);
B = -u2*(1+C)-D;
v4 = (u4+B)/(C*u4+D);
k = 1/v4;
k = real(k);
% EOF field_constants.m

```


Chapter 5: Genome-wide electrical profiling in *Saccharomyces cerevisiae*

This chapter describes the genome-wide analysis of electrical properties in the budding yeast *Saccharomyces cerevisiae*. In analogy to more traditional studies of global genetic characteristics, we refer to this process as electrogenomic profiling. The preliminary electrogenomic profile presented in this chapter consists of a pilot screen, in which we survey a subset of the *Saccharomyces cerevisiae* deletion collection (comprising ~2% of the total viable deletion strains), followed by the expansion of this screen to the analysis of the complete collection through the sequencing of DNA “barcodes” associated with each strain. Our initial genome-wide survey has identified ~50 gene deletions associated with distinct electrical phenotype in yeast. Comparing strains identified in our screen to existing datasets describing morphology, function, and genetic interactions suggests possible underlying mechanisms for electrical differences between cells. In particular, our results suggest that cell morphology, disruptions in the RIM101 pathway, and disruptions in the dynein-dynactin pathway may each play an important role in determining a cell’s electrical phenotype. Although more work is necessary to confirm and understand the potential role of the genes identified here in determining electrical properties, this chapter presents our initial findings and discusses their possible interpretation.

The work presented in this chapter was performed with much help and guidance from Dr. Peter Svensson and Dr. Laia Quiros Pseudo, both post doctoral associates in Prof. Leona Samson’s lab. In particular, Dr. Svensson and Dr. Pseudo provided valuable consultation in planning both the pilot screen and full genetic screen, in addition to providing all yeast strains and the complete pooled deletion collection.

Introduction.

The electrical properties of a cell encode biophysical information related to that cell’s intrinsic structure and biological state. Although this feature of electrical properties has led to their use as biomarkers^{29,121} as well as handles for sorting different cell types^{30,122}, most applications have focused on cases where the differences between the cells being studied are dramatic. As a result, a precise and systematic understanding of how genotype affects electrical phenotype is lacking. Discovering the connections between a cell’s gene expression and its electrical properties at a genome-wide scale and with high resolution could potentially establish electrical properties as a biologically relevant metric by which to study and characterize cells, enabling and motivating their broader use. Towards this end, we have pursued the electrical characterization of the *Saccharomyces cerevisiae* deletion collection, a library comprised of ~5000 yeast strains with systematic deletions of single, non-essential genes.

The budding yeast *S. cerevisiae* is ideally suited for an initial survey of electrical phenotypes for a number of reasons. First, the relative ease of genetic manipulations in yeast has resulted in them becoming the most well-studied eukaryotic organism. This has facilitated the creation of numerous systematic libraries (including the deletion collection that is the focus of this work), and has resulted in the characterization of roughly 4500 genes (~75% of the genome) to date¹²³. Many of these genes (including entire gene families and genetic pathways) are conserved and have homologues in higher eukaryotes, allowing information derived from yeast to be generalized to a wide variety of organisms. The ability to extrapolate from yeast to humans and other higher eukaryotes has driven the use of yeast as model organisms in studying DNA damage response¹²⁴, cell cycle control¹²⁵, and cell signaling¹²⁶. In addition, this ability to generalize is multidirectional; not only can studies in yeast substitute for those in more complex organisms, but yeast also serve as a convenient platform for the study of genes that originate in higher eukaryotes. This is illustrated by the use of human cDNA libraries in yeast to study protein-protein interactions through two-hybrid screening¹²⁷. The advantages of yeast for these prior genomic and proteomic studies extend to studies of their electrical properties as well; discoveries made in yeast may be generalized to a variety of organisms, and genes of interest in other organisms can be expressed in yeast.

In addition to being excellent genetic models in which a large fraction of the genome has been characterized, yeast also stand out for the *high content* of this characterization. This goes considerably beyond gene annotation to include, for example, a study of the quantity and localization of over 4000 yeast proteins¹²⁸. In cases where the protein appears in sufficiently high copy numbers to have a direct affect on the electrical properties of a cell, this could prove useful in attempting to understand the mechanism by which a gene deletion results in a distinct electrical phenotype. In addition to studies involving individual genes or proteins, *S. cerevisiae* has also been at the center of much work involving interactions between different proteins¹²⁹. For cases in which changes to a cell's electrical properties arise through pleiotropic effects, the large datasets generated by these studies could help to understand the underlying basis for this pleiotropy. This abundance of high content genomic and proteomic information, both for individual genes as well as gene networks, combined with the flexibility and relative ease of genetic manipulation, makes *S. cerevisiae* uniquely well-suited for large-scale electrical phenotyping.

A great variety of yeast libraries have been the focus of recent research. These include libraries for the surface display of proteins¹³⁰; the overexpression¹³¹, knockdown, or knockout of genes (including double deletion mutants¹³²); and the recently developed possibility of using RNAi based libraries¹³³. Amid all of this diversity, we have elected to focus on the deletion collection for a number of reasons. First, by suppressing gene expression at a genomic level (as opposed to at the level of transcription or translation), the deletion collection enables the unambiguous elimination of the protein a gene codes for. Second, the deletion collection has the distinct advantage of containing molecular barcodes uniquely identifying each strain³. This is achieved by replacing each gene to be deleted with an antibiotic resistance cassette (KanMX4) flanked by upstream and downstream barcodes (UPTAG and DNTAG, respectively). These barcodes are themselves flanked by universal sequences that can act as primers to amplify each barcode from genomic DNA. This enables one to quantify (through quantitative PCR, microarray hybridization, or sequencing) the abundance of each deletion strain within a mixed sample. The ability to universally amplify DNA specific to each strain is a powerful tool that makes the deletion collection amenable to pooled genetic screens¹³⁴.

One limitation of the haploid deletion collection is that it is fundamentally restricted to non-essential genes, roughly 80% of the genome. This is not easily circumvented by working with the heterozygous diploid library, since decreasing expression of even an essential gene by ~50% often has no observable impact on phenotype. As an alternative means of studying the electrical properties conferred by essential genes, we have supplemented our studies of the deletion library with DAmP strains, in which destabilization of mRNA transcripts of specific genes decreases their expression by up to ten-fold⁴. This increases the potential coverage of the electrogenomic profile by providing access to an additional ~1000 strains.

Collectively, the properties of yeast in general, and the deletion collection in particular, motivate our choice of this system for electrogenomic profiling. Furthermore, our work investigating the specificity, resolution, and throughput capable with IDS (described in previous chapters) supports the feasibility of using this technology as a platform for genetic screening. The following sections describe our progress towards this goal as well as preliminary results we have obtained demonstrating the existence of electrically distinct strains within the deletion and DAmP collections. To offer possible interpretations of this first genome-wide survey of electrical properties in the deletion collection, we have compared our data to existing datasets on morphology, function, and genetic interactions. These results demonstrate the feasibility of electrogenomic profiling and suggest potentially interesting directions to pursue in the future.

Results

Selection of strains for the pilot screen. In order to guide the genome-wide study, we began by selecting 82 target strains which we hypothesized might exhibit distinct electrical phenotypes. Based upon our previous characterization of yeast using IDS (described in Chapter 3), we focused on genes

related to the cell wall. These can be broadly categorized as genes coding for glycoproteins; genes involved in glycosylation; genes involved in cell wall biosynthesis; and genes whose deletion results in a “low-dye-binding” phenotype¹³⁵ (the name refers to the positively charged dye alcian blue, whose association with the cell wall is used as a measure of cell wall charge). In addition, we selected a number of genes associated with osmoregulation; this was motivated by the hypothesis that cytoplasmic conductivity would vary in strains unable to effectively regulate the transport of water across their membrane. The final genes we chose to investigate in the pilot screen were those associated with distinct morphology. These were selected based upon classifications reported in the original survey of the yeast deletion collection³; any strain scoring ‘4’ (defined as a strong difference from wildtype) for the morphological categories “elongate”, “round”, “small”, “large”, or “football” were included in the pilot screen. We excluded strains scored as “clumpy” due to difficulties we anticipated in working with large cell aggregates in our devices. A complete listing of the strains used in the pilot screen is included in the Appendix to this chapter.

Crossover frequency measurements of candidate strains. In order to obtain a general idea of the distribution of electrical properties across the deletion strains selected for the pilot screen, we performed crossover frequency (COF) measurements on the strains at a medium conductivity of 0.05 S/m, comparable to that used for separations based upon differences in cell wall and membrane properties. Despite the genetic homogeneity of the cell suspension for each measurement, we observed considerable variability in crossover frequency across the suspension (typically 200-300 kHz). To account for this variability, we recorded two frequencies, corresponding to the approximate frequencies at which ~70%

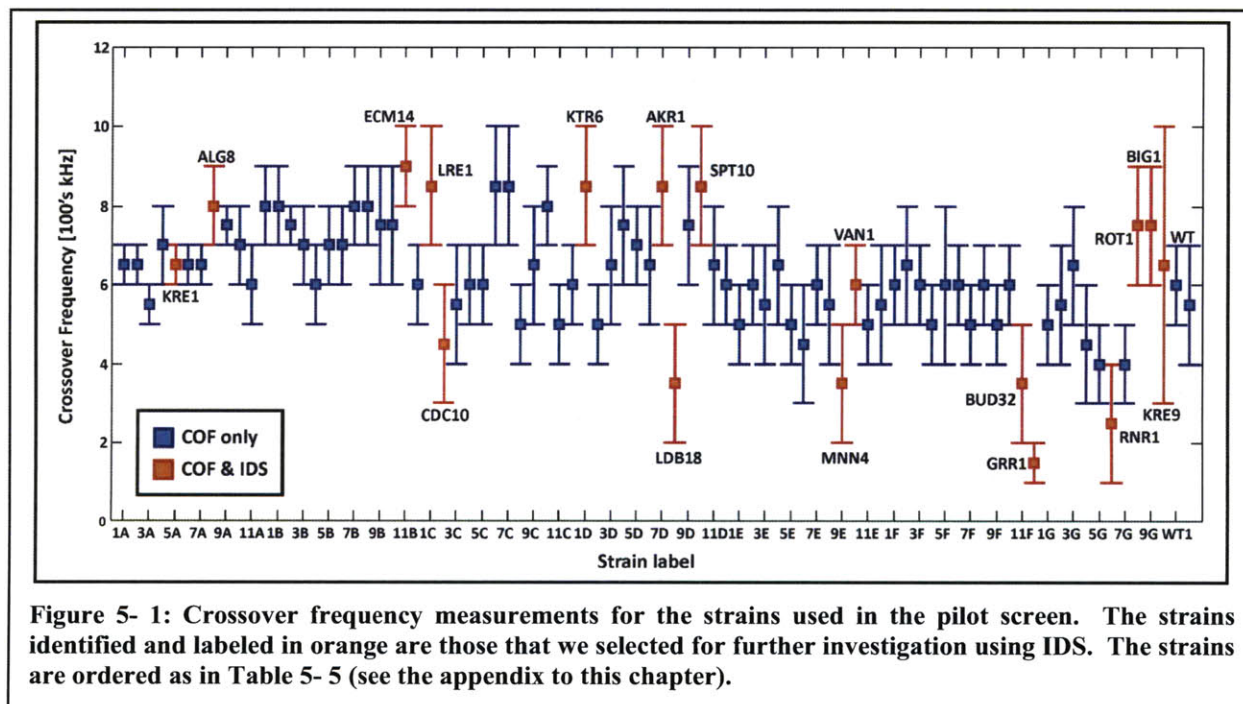


Figure 5- 1: Crossover frequency measurements for the strains used in the pilot screen. The strains identified and labeled in orange are those that we selected for further investigation using IDS. The strains are ordered as in Table 5- 5 (see the appendix to this chapter).

underwent n-DEP in the first case, and ~70% underwent p-DEP in the second case. The results of these measurements are plotted across the different strains in Figure 5- 1, where the error bars represent the high and low frequency bounds on the crossover frequency for a single measurement. Despite the coarse nature of this preliminary characterization (e.g. the growth phase of the cells was controlled for only approximately and cell cycle phase was distributed randomly – see Materials and Methods for growth conditions), a number of strains emerged as possibly exhibiting a distinct electrical phenotype, either being more conductive or less conductive than wildtype. We selected these strains (labeled orange in Figure 5- 1) for further investigation, using IDS to compare them directly to wildtype cells.

IDS analysis of strains with distinct crossover frequencies. Following COF measurements, we chose an initial 13 strains (later expanded to 17) for direct comparison to wildtype using IDS. The majority of these strains were selected as a result of their having either higher (*ALG8*, *ECM14*, *LRE1*, *KTR6*, *AKR1*, *SPT10*) or lower (*CDC10*, *LDB18*, *MNN4*, *BUD32*, *GRR1*, *RNR1*) COFs than the wildtype strain. The one exception to this is a haploid strain containing a DAmP allele⁴ for the gene *KRE9*, which was chosen due to the substantial variability of COFs observed for a suspension of these cells.

Figure 5- 2 shows the results of IDS pairwise comparisons between deletion strains and wildtype, covering the 13 strains chosen based on COF measurements, plus four additional strains (*KRE1*, *VAN1*, *ROT1*, *BIG1*) selected based upon IDS results (discussed momentarily). This figure plots the differences between deletion (Δ) and wildtype (wt) strains, calculated as one minus the correlation coefficient between their distributions at the outlet of the device (p_{wt} and p_{Δ} , respectively). The dashed line gives the negative control, calculated by correlating time-offset distributions of wildtype cells recorded under the same conditions (see Materials and Methods for details of these calculations). These experiments identified four strains exhibiting electrical properties strongly distinct from wildtype (*GRR1*, *CDC10*, *KRE9*, *RNR1*), in addition to a number of strains exhibiting possible differences (*BUD32*, *ALG8*, *LDB18*). Among these strains, *ALG8* was the only one that appeared to exhibit lower conductivity than wildtype under the range of operating conditions we used. Accordingly, we select *GRR1* as our high conductivity control, and *ALG8* as our low conductivity control in our subsequent experiments, with the caveat that the results we obtained for the *ALG8* deletion strain were not fully conclusive.

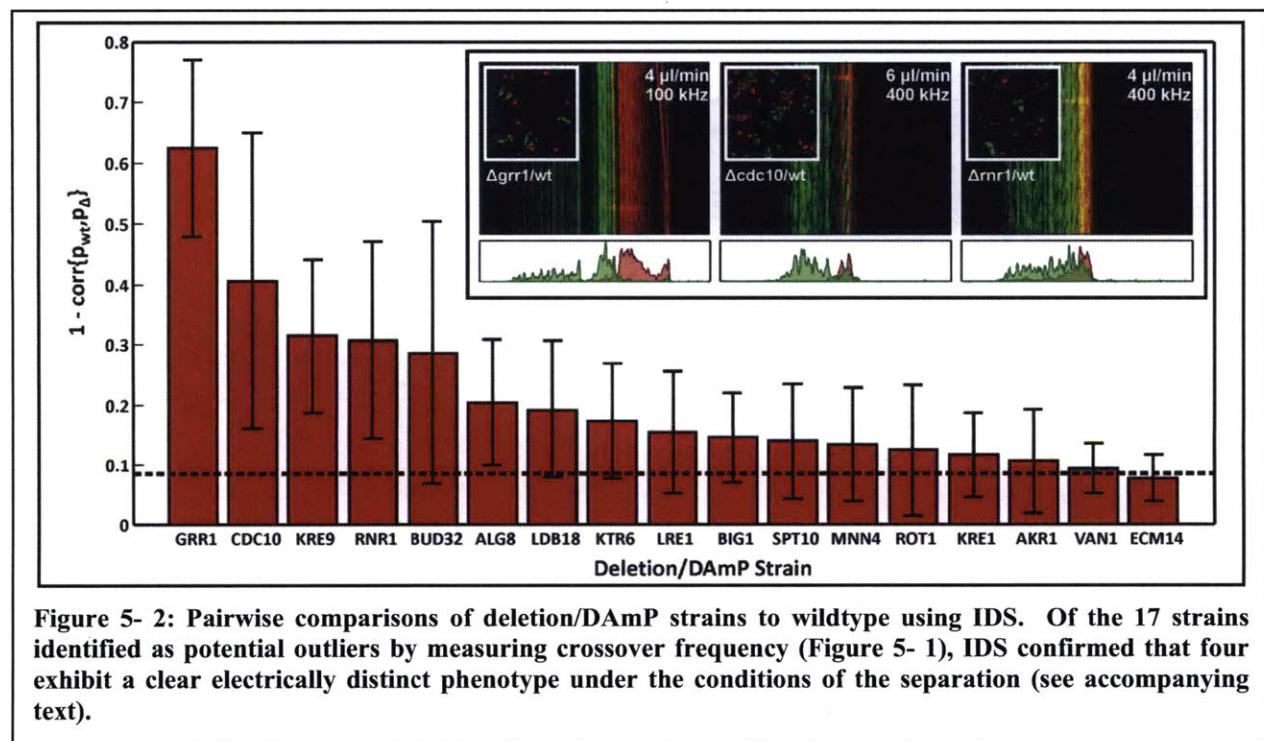
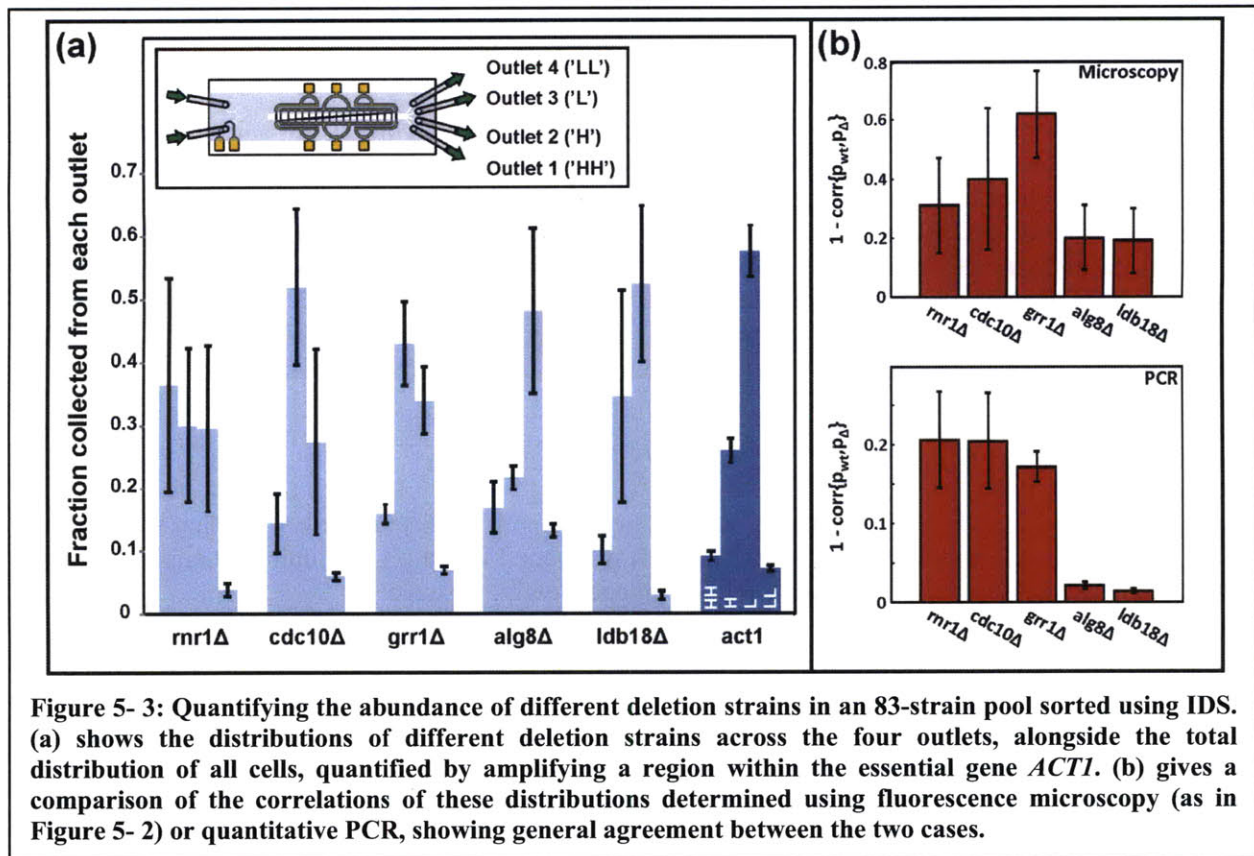


Figure 5- 2: Pairwise comparisons of deletion/DAmP strains to wildtype using IDS. Of the 17 strains identified as potential outliers by measuring crossover frequency (Figure 5- 1), IDS confirmed that four exhibit a clear electrically distinct phenotype under the conditions of the separation (see accompanying text).



Corroboration of pairwise results with pooled separations. Before proceeding to the full deletion collection, we compared the results obtained through pairwise separations of single deletion strains and wildtype (quantified via fluorescence microscopy) with results obtained by simultaneously sorting a pool of the 83 pilot screen strains (Figure 5- 3). These experiments required the construction of a balanced pool and a means for quantifying the abundance of specific strains collected at each of four outlets. We elected to use real-time PCR for strain quantification; this allowed us to construct a coarse-grained distribution of the cells across the four outlets, which could then be correlated with the overall distribution of cells, analogous to the procedure we followed in the pairwise experiments. To quantify the total number of cells, we chose primers that amplify a region of the essential gene *ACT1*. To determine the abundance of individual deletion strains, we choose primers that amplify a region spanning the end of the KanMX4 deletion cassette. One potential difficulty with this approach to quantifying deletion strains is the possibility for amplification across genes; we assured that this was avoided by checking the reaction product for amplicons longer than expected (either through gel electrophoresis or a melting curve). Although this proves not to be an issue for the subset of the library studied in the pilot screen, this is not necessarily the case for experiments working with the complete deletion pool; accordingly, for experiments involving the complete library, we pursue an alternate quantification strategy, discussed in a subsequent section.

Collecting sorted fractions from the 83 strain pool and quantifying the abundance of different strains across the four outlets ('HH', 'H', 'L', and 'LL' in the order of descending conductivity) gives results in general agreement with those obtained using fluorescence microscopy. Figure 5- 3a shows the distributions of several deletion strains across the four outlets alongside the overall distribution of cells, as determined by amplifying a region within the essential gene *ACT1*. As in the pairwise comparisons, we see a substantial enrichment of the *grr1Δ* strain at high conductivity, with comparable enrichments also observed for the *rnr1Δ* and *cdc10Δ* strains. Although we do not observe significant enrichment in any

outlet for our low conductivity positive control, $alg8\Delta$, this may be due to the less dramatic electrical differences observed for this strain compared to three high conductivity positive controls (see, for example, Figure 5- 2).

The complete pooled deletion library: sampling strains in collection and sequencing. In moving from the pilot screen to experiments involving the complete pooled deletion collections, we must address the question of how many cells need to be sorted to achieve robust statistics. In this section, we address this question and discuss some additional considerations relevant to sample collection. We begin by addressing the issue of strain sampling; in effect, how many cells does one need to collect to obtain at least K samples of each strain with a certainty of $X\%$?

If a particular strain occurs in the library with frequency f , the probability density function for the number of times it has been sampled ($= k$) when N cells have been collected is given by:

$$p[k] = \binom{N}{k} (f)^k (1-f)^{N-k} \approx \frac{1}{\sqrt{2\pi fN}} \exp\left\{-\frac{(k-fN)^2}{2fN}\right\} \quad (5-1)$$

The corresponding cumulative distribution function gives the probability that $k > K$, so that the sampling of this strain satisfies our criterion for redundancy. If we require that this criterion be satisfied for each of M total strains and assume the strains are sampled independently, we have:

$$[P(k \geq K)]^M \approx \frac{1}{2^M} \left[1 - \operatorname{erf}\left\{\frac{(K-fN)}{\sqrt{2fN}}\right\}\right]^M \geq X \quad (5-2)$$

Here, X ($0 < X < 1$) reflects the desired level of certainty in having sampled each strain at least K times during cell collection. To solve for N , we first define $q \equiv (fN - K)/\sqrt{2fN}$, and use the large x expansion $\operatorname{erf}(x) \sim 1 - \exp(-x^2)/\sqrt{\pi}x$ along with the approximation, valid for large M , $(1+x)^M \sim \exp(Mx)$. This gives:

$$\frac{1}{2^M} [1 + \operatorname{erf}(q)]^M \approx \exp\left\{-\frac{Me^{-q^2}}{2\sqrt{\pi}q}\right\} \geq X \quad (5-3)$$

Solving for q involves a transcendental equation, $q = [\log\{M/(2\sqrt{\pi}q \log(X^{-1}))\}]^{1/2}$. Although we cannot solve this exactly, it is possible to iteratively construct an accurate approximation by noting that the right-hand side is only weakly dependent on the denominator inside the logarithm:

$$q_0 \approx [\log(M)]^{1/2} \rightarrow q_1 \approx \left[\log\left\{\frac{M}{2\sqrt{\pi} \log(M) \log(1/X)}\right\}\right]^{1/2} \rightarrow \dots \quad (5-4)$$

This iterative procedure converges rapidly; for our purposes, the first approximation, q_0 , is sufficient.

Finally, the number of cells N that must be collected to satisfy our requirements is:

$$N \approx M \left[K + \log(M) + \sqrt{2K \log(M)} \right] \quad (5-5)$$

This equation assumes that all strains are present at the same frequency, $1/M$. In the more general case, where each strain may be present in the library at a different frequency ($= f_i$), we would have $q_i \equiv (f_i N - K)/\sqrt{2f_i N}$ and the number of cells we need to collect would be determined by solving $\sum_{i=1}^M \exp(-q_i^2)/2\sqrt{\pi}q_i = \log(1/X)$. If we further assume that the representation of different strains differ significantly (as is the case if the pooled library is grown for several generations), then N will be determined almost entirely by the number and frequency of the slowest growing strain(s). Despite its simplifications, equation (5- 5) provides a reasonable guideline for the number of cells one must collect to

sample each of M total strains at least K times. Note that, to leading order, the level of certainty, X , does not matter; this is because equation (5- 2) transitions from 0 to 1 over a very narrow range of N when M is large. Also worth noting is that requiring that all strains be sampled at least K times is not much more stringent than requiring that one particular strain be sampled K times; this effectively increases N by an amount $M\sqrt{2K \log M} \ll MK$.

Determining the number of cells we need to collect in a typical separation requires determining an appropriate value for the necessary redundancy of each strain, K . Specifically, we want K to be large enough that the frequency of each strain in the collected samples is an accurate representation of the ideal frequency (i.e. the frequency we would observe if we collected infinitely many cells). It is worth mentioning that undersampling strains is potentially an issue in both cell collection as well as in barcode sequencing. However, undersampling in cell collection is a more critical concern; once the barcodes from the collected cells are amplified, any information regarding the actual number of cells the barcodes originate from is essentially lost. Accordingly, in addressing the possibility of sampling error, our primary concerns are those regarding cell collection.

Given that we collect K cells of a particular strain from a single outlet, the probability distribution for the *actual* frequency ($=f$) of these cells (i.e. the frequency we would observe if we collected infinitely many cells) under the given conditions is:

$$p(f) = N \binom{N}{K} (f)^K (1-f)^{N-K} \approx \frac{N(fN)^K}{K!} \exp\{-fN\} \quad (5- 6)$$

The first and second moments of this distribution are $\langle f \rangle = (K + 1)/N$ and $\langle f^2 \rangle = (K + 1)(K + 2)/N^2$, so that the uncertainty in f decreases relative to the mean as $\sim K^{-1/2}$. Therefore, to assure that the sensitivity of the screen is not limited by the number of cells we collect, a reasonable level of redundancy is to require $K \sim 400$, corresponding to a detection limit of $\sim 5\%$ (other unrelated factors may increase this limit). Since the haploid deletion library is comprised of ~ 5000 strains, this requires collecting about 2.5 million cells from each outlet. In practice, typically 90% of the cells are collected in two of the four outlets, making it difficult to satisfy this requirement in all cases; nonetheless, we treat this as a rough guideline, and attempt to collect $\sim 10^7$ cells in each experiment. Falling below this threshold does not preclude obtaining useful results, but may decrease the sensitivity of the screen.

Assuming each strain has been adequately sampled during the separation, the potential concern of undersampling during sequencing remains. This consideration determines the number of samples that can be multiplexed in a single lane for sequencing. If one lane is capable of generating N_R reads and each experiment consists of five samples (four outlets plus the original cell mixture), then the number of experiments that can be multiplexed is roughly $N_R/5KM$, where K (~ 400) and M (~ 5000) are the sampling requirement and strain number, as before. Since $N_R \sim 20$ million in current technology, two experiments can be pooled to obtain ~ 400 reads for a typical strain in any sample. However, since the five samples per experiment are divided evenly into UPTAG and DNTAG barcodes, only ~ 200 of these reads would be matching. The multiplexing strategy and primers we use are described in the appendix to this chapter.

The complete pooled deletion library: corroboration with the 83 strain pilot screen.

In progressing from the 83 strain pool to the complete pool of ~ 5000 strains, it became necessary to adopt a modified quantification strategy. For an expanded pool, the same amount of genomic DNA contains roughly $1/60^{\text{th}}$ the number of copies of a particular DNA barcode. As a result, primers that yielded relatively clean PCR products in the pilot screen yielded no product or a product of the wrong size (suggesting that the primers have dimerized). To circumvent this, we adopted a two-stage approach to quantitative PCR, in which a first (non-quantitative) reaction amplified a universal region containing the strain barcodes, while a second (quantitative) reaction primed off of the barcode itself to produce an

amplicon in only the targeted strain (Figure 5- 4a; see the appendix to this chapter for primer sequences). Although this strategy improved the reliability of the quantification, not all barcodes proved sufficient; as a result, only a subset of the strains could be reliably quantified in this way (see Figure 5- 10 in the appendix to this chapter). As additional quality control, we record and inspect melting curves after each reaction to verify the amplification of a single product of appropriate length.

To determine the possible extent to which amplifying barcodes might bias our quantification, we compared fractions collected from the 83 strain pool using both PCR strategies (Figure 5- 4). We find a correlation coefficient between amplified and unamplified distributions of >0.95, compared to an average correlation of 0.83 across unrelated samples. This suggests that amplification is not likely to introduce any large systematic bias in our experiments; nonetheless, we keep the number of cycles for which the barcode is amplified relatively low (< 25; see the appendix to this chapter for more detailed PCR protocols).

After validating our PCR strategy and determining reliable primers, we sought to corroborate the results of our pilot screen with separations of the complete pooled deletion library. Because each strain is ~60× more dilute than in the pooled pilot screen, these experiments have more stringent requirements for cell collection. Although the specific number of cells necessary depends on the technique used to quantify their abundance, it is possible to place a lower bound on the minimum number of cells needed from each outlet by considering only the sampling of strains during collection, independent of how they will be quantified. As discussed in the previous section, we take ~10⁷ cells as an approximate guideline for the total number of cells collected, or >10⁶ cells as the approximate number of cells needed from each outlet. These numbers assume roughly equal representation of strains within the

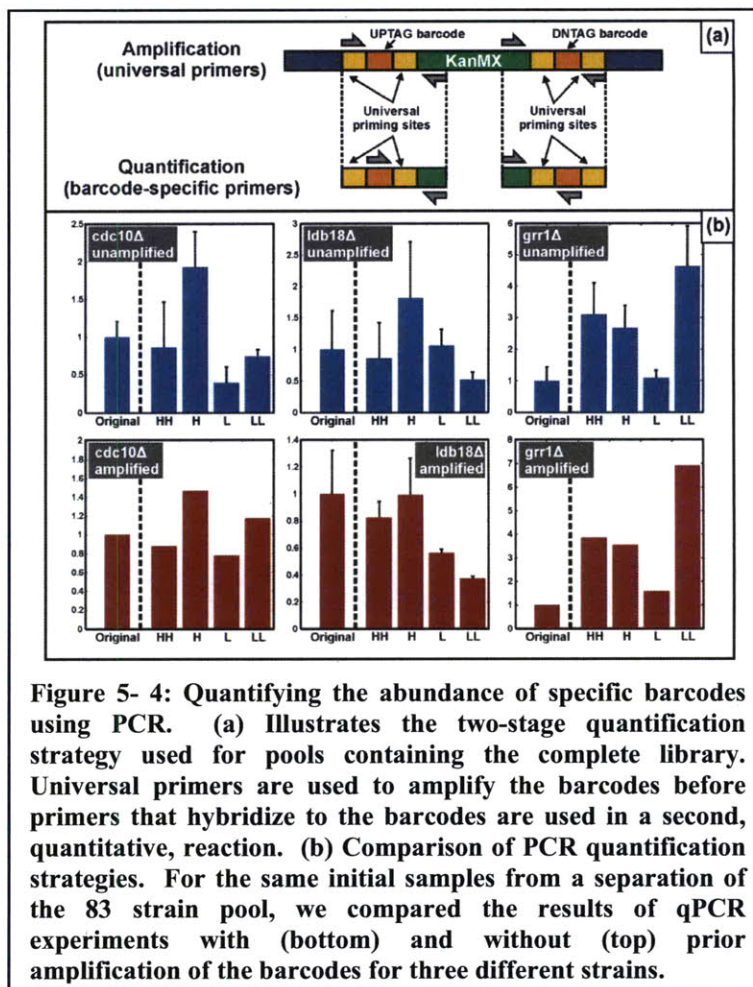


Figure 5- 4: Quantifying the abundance of specific barcodes using PCR. (a) Illustrates the two-stage quantification strategy used for pools containing the complete library. Universal primers are used to amplify the barcodes before primers that hybridize to the barcodes are used in a second, quantitative, reaction. (b) Comparison of PCR quantification strategies. For the same initial samples from a separation of the 83 strain pool, we compared the results of qPCR experiments with (bottom) and without (top) prior amplification of the barcodes for three different strains.

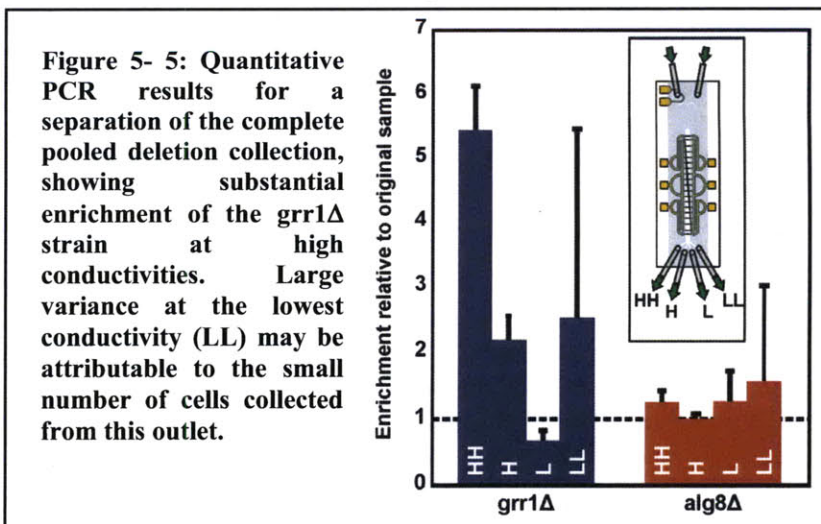


Figure 5- 5: Quantitative PCR results for a separation of the complete pooled deletion collection, showing substantial enrichment of the *grr1Δ* strain at high conductivities. Large variance at the lowest conductivity (LL) may be attributable to the small number of cells collected from this outlet.

library, which will only be true if the cells are not given opportunity to divide after thawing the pooled aliquot. For all separations using quantitative PCR to quantify strain abundance, we sort cells directly after thawing them on ice. This results in relatively poor viability (~50% as determined by staining with propidium iodide and counting cells). However, non-viable cells typically exhibit significantly reduced effective conductivity and thus should not interfere substantially with quantification of strains with the high conductivities typical of those identified in the pilot screen. Accordingly, rather than risk losing slow-growing strains to dilution, we do not allow cells enough time to divide after thawing.

Results from pooled experiments are shown in Figure 5- 5, where the abundance of cells in each of four outlets has been normalized to their abundance in the original pool. Note that because we have amplified the strain barcodes from each outlet separately prior to quantifying particular strains, the enrichment or depletion of strains across the four outlets is no longer conserved. Significant differences in the number of cells collected from each outlet may explain the large variation associated with the fourth outlet (error bars in Figure 5- 5 give s.d. for two independent experiments); observationally, very few cells were collected under this condition. This makes it difficult to determine if there is any significant enrichment of the *alg8Δ* strain - our low conductivity control - in the lowest conductivity outlet (*LL*). However, in the two higher conductivity outlets (*HH* and *H*), we obtain substantial enrichment of the *grr1Δ* strain, strongly identified as electrically distinct in our pilot screen (Figure 5- 2).

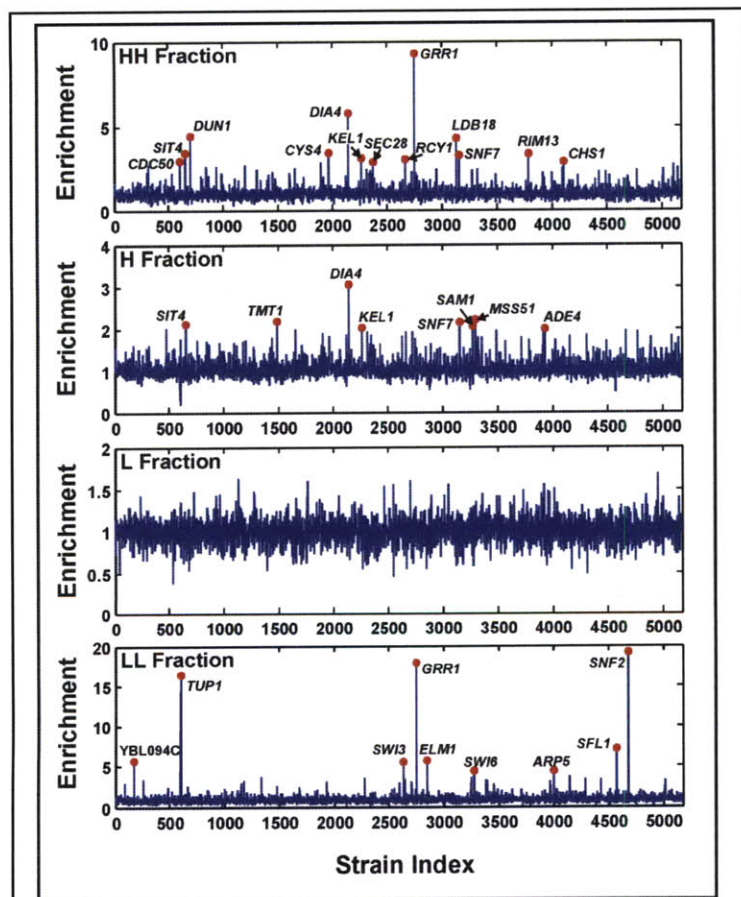


Figure 5- 6: Enrichment of deletion strains across four sorted fractions relative to the original unsorted pool. Plotted here is the geometric mean of enrichment across two independent experiments and two sets of barcodes (UPTAG and DNTAG). Strains enriched 6 s.d. or more above the mean are labeled and marked in red.

The comprehensiveness of these experiments is limited largely by the robustness of our quantitative PCR strategy, which is in turn determined by the quality of barcode-specific primers and the quantity of genomic DNA available for amplification. Nonetheless, the emergence of the *grr1Δ* strain as electrically distinct in all three phases of the preliminary genetic screen suggest its value as a positive control in proceeding to sequencing-based quantification of the complete library.

Sequencing results for the pooled deletion collection. For our initial sequencing experiment, we multiplexed fractions collected from two independent separations performed using the same operating conditions (conductivity ranging from 0.075 - 0.01 S/m, a flowrate of 6μl/min, and a frequency 300 kHz) on cells grown for ~2 generations. This identified 58 candidate strains (~1% of the total screened) exhibiting distinct electrical properties across any of the four outlet fractions (*HH*, *H*, *L*, *LL*) or combined pools of the two higher (*HH+H*) and lower (*L+LL*) conductivities. Figure 5- 6 shows the consensus enrichment (relative to the unsorted sample) across all strains for the four different fractions, highlighting

30 of the strains with enrichments six standard deviations above the mean. Here, a baseline value (equal to one tenth the sample mean) has been added to the strain frequencies in each sample before calculating the enrichment; this removes spurious hits due to strains with low representations (see Materials and Methods for a complete description of data analysis). We observe the greatest enrichment for *grr1Δ*, the strain that emerged as a positive control for electrical phenotype in our pilot screen. Also as in the pilot screen, the majority of these strains (44 of the total 58, or 21 of the strains highlighted in Figure 5- 6) are enriched in the high conductivity fraction, with the remaining strains showing enrichment in the lowest conductivity (*LL*); we find that no strains are significantly enriched within the *L* fraction, perhaps because the majority of cells were collected here. The comparatively high enrichments in the *LL* sample (including, interestingly, the *grr1Δ* strain; perhaps due to the occasional formation of multi-budded aggregates in this strain) are likely due to the small number of cells collected from this outlet. A complete listing of candidate strains identified through sequencing is given in the appendix to this chapter.

Strain	HH	H	L	LL
<i>GRR1</i>	9.2998	1.7549	1.1472	18.0489
<i>CDC10</i>	0.6261	1.3282	0.3604	1.2943
<i>RNR1</i>	[---]	[---]	[---]	[---]
<i>BUD32</i>	[---]	[---]	[---]	[---]
<i>ALG8</i>	0.5619	0.857	1.1076	2.2198
<i>LDB18</i>	4.3401	1.3786	0.5982	0.7669
<i>KTR6</i>	0.7161	0.7512	0.9336	0.7339
<i>LRE1</i>	1.1257	1.0337	0.964	0.9411
<i>SPT10</i>	[---]	[---]	[---]	[---]
<i>MNN4</i>	0.7072	0.9275	1.0973	1.1493
<i>KRE1</i>	1.2691	1.1374	0.9462	1.1229
<i>VAN1</i>	1.281	0.829	1.0701	1.2905
<i>ECM14</i>	1.3123	0.9234	1.2398	1.0148

Table 5- 1: Enrichment of strains from the pilot screen determined through barcode sequencing of the complete pooled deletion collection.

Comparing the results of the complete screen to the pilot screen suggests reasonable agreement, although barcodes associated with some strains (*RNR1*, *BUD32*, and *SPT10*) were not detected at sufficient levels during sequencing to reliably quantify. Table 5- 1 summarizes the sequencing results for the pilot strains, showing a few noteworthy features. First, an enrichment of the *grr1Δ* strain is detected at the lowest conductivity (*LL*), similar to previous results (Figure 5- 4 and Figure 5- 5). Although this may be due to the low number of cells collected in this outlet, another possible explanation involves cell shape, and is discussed in the following section. A second feature of the sequencing results for the pilot strains is the emergence of the *ldb18Δ* mutants as a possible high conductivity strain; this agrees with COF measurements (Figure 5- 1), but was not strongly borne out by separation results (Figure 5-

2 and Figure 5- 3). Finally, sequencing results suggest that the *alg8Δ* strain that served as a low conductivity control may in fact be enriched at low conductivities, although not significantly enough to qualify as an outlier within the ~5000 strain pool.

Discussion

Cell morphology and electrical phenotype. A strong predictor of electrical differences in our survey of the deletion collection is morphology; strains scoring as highly elongated have consistently lower crossover frequencies and separate at consistently higher conductivities. This can be understood by approximating elongated cells as prolate ellipsoids sheathed by confocal ellipsoids representing the cell membrane and wall²³. For a prolate ellipsoidal cell comprised of three confocal layers with major axis a_i , minor axis c_i , and eccentricity $e_i^2 = 1 - c_i^2/a_i^2$, (where $i = 1,2,3$ for cytoplasm, membrane, and cell wall, respectively), the polarizability can be determined using the depolarization factors, (ℓ_i^\perp and ℓ_i^\parallel) to reduce the layered ellipsoid to an equivalent, homogeneous ellipsoid. Specifically, the effective permittivity of a particle aligned parallel to the electric field can be determined by iteratively using (for each of n cell layers, where n increases in the external direction):

$$\underline{\varepsilon}'_n = \underline{\varepsilon}_n \left[\frac{\underline{\varepsilon}_n + (\underline{\varepsilon}'_{n-1} - \underline{\varepsilon}_n) \ell_{n-1}^{\parallel} + (a_{n-1} c_{n-1}^2 / a_n c_n^2) (\underline{\varepsilon}'_{n-1} - \underline{\varepsilon}_n) (1 - \ell_n^{\parallel})}{\underline{\varepsilon}_n + (\underline{\varepsilon}'_{n-1} - \underline{\varepsilon}_n) \ell_{n-1}^{\parallel} - (a_{n-1} c_{n-1}^2 / a_n c_n^2) (\underline{\varepsilon}'_{n-1} - \underline{\varepsilon}_n) \ell_n^{\parallel}} \right] \quad (5-7)$$

From this, the polarizability can be calculated using:

$$\underline{K} = \left[\frac{\underline{\varepsilon}'_p - \underline{\varepsilon}_m}{3(\underline{\varepsilon}_m + (\underline{\varepsilon}'_p - \underline{\varepsilon}_m) \ell_p^{\parallel})} \right] \quad (5-8)$$

Here, the complex permittivity is given by $\varepsilon_i = \varepsilon_i + \sigma_i / i\omega$ and the depolarization factors are given by:

$$\ell_i^{\parallel} = \frac{c_i^2}{2a_i^2 e_i^3} \left[\log \left\{ \frac{1+e_i}{1-e_i} \right\} - 2e_i \right] ; \quad \ell_i^{\parallel} + 2\ell_i^{\perp} = 1 \quad (5-9)$$

Equations (5- 7) and (5- 8) can be modified for a particle perpendicular to the field by replacing ℓ_i^{\parallel} with ℓ_i^{\perp} everywhere. Note that, in assuming that the cell layers are confocal, the cell wall and cell membrane thickness vary over the surface of the cell. For two confocal ellipsoids, the distance between their surfaces along the major and minor axes are $\Delta_a = (a^2 + \xi^2)^{1/2} - a$ and $\Delta_c = (c^2 + \xi^2)^{1/2} - c$, respectively, where surfaces of constant ξ describe confocal ellipsoids. If we choose to define Δ_c as the wall/membrane thickness, the thickness along the major axis will be approximately smaller by a factor of c/a ; accordingly, this approximation may become inaccurate for strongly elongated ellipsoids. Nonetheless, the salient feature of these equations is that, as a particle becomes increasingly elongated, $\ell_i^{\parallel} \rightarrow 0$ and $\ell_i^{\perp} \rightarrow 1/2$. This amounts to a shift *up* in the dielectric spectrum of a cell aligned with the field, and a shift *down* for a particle perpendicular to the applied field (Figure 5- 7). Although cells will initially have arbitrary orientation, application of a strong field will exert a torque that tends to align their major axis in the direction of the field (although under some special conditions, they may align perpendicular to the field²³, this is not the case here). This alignment (although not complete in the presence of fluid flow exerting an additional torque on elongated cells) can be directly observed in our experiments. The result is that the dielectric spectrum of essentially all elongated cells will shift upwards, increasing their apparent conductivity and decreasing their COF. This explains qualitatively the results of our pilot screen; cells possessing the most extreme case of elongated morphology (the *GRR1* deletion strain) also exhibit the lowest COF and most conductive IDP (Figure 5- 1 and Figure 5- 2). Less dramatically elongated cells (such as *CDC10* and *RNR1* deletion strains) exhibit a less dramatic increase in effective conductivity. A possible exception to this argument applies to cases where cells are prevented by steric constraints (i.e. crowding from other cells) to align to the external field. If this is the case, elongated cells will exhibit *lower* effective conductivities. This may give rise to the enhancement we observe for the highly elongated *grr1Δ* strain at the lowest conductivity (Figure 5- 4 and Figure 5- 5, as well as Table 5- 1).

An additional morphological dependence can arise through differences in cell size; for a given cell wall thickness, a larger cell will generally exhibit a higher effective conductivity than a smaller one. This may be partially responsible for the relatively high effective conductivities of the *RNR1* and *BUD32* deletion strains. In an effort to see if this reasoning could be applied to the only strain from the preliminary survey possessing a “small” morphology, we performed a comparison of the *VANI* deletion strain with wildtype, detecting no noticeable difference (Figure 5- 2).

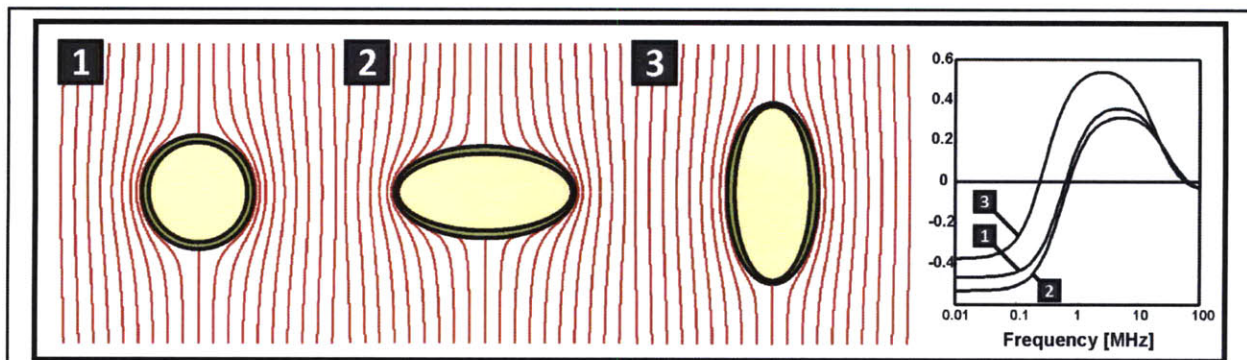


Figure 5- 7: Cell shape and the dielectric spectra. Modeling the cell as confocal ellipsoids representing the cell wall, membrane and cytoplasm, we can approximate how the spectrum is altered by elongation and orientation. A prolate ellipsoidal cell aligned perpendicular to the applied field (“2”) has more negative polarizability at low frequencies, whereas a cell of the same shape aligned parallel to the applied field (“3”) has more positive polarizability. In these calculations, the cell volume is held constant.

Electrical Phenotype of the *KRE9* DAmP Strain. Aside from morphological differences, the most distinct strain emerging from the pilot screen is one deficient in the gene *KRE9*. This gene is one of three essential genes included in the pilot screen (the others being *ROT1* and *BIG1*), and thus unavailable in the haploid deletion collection. To circumvent this limitation, we analyzed strains with mutations in this gene constructed through a DAmP (Decreased Abundance through mRNA Perturbation) strategy⁴. Very briefly, DAmP reduces the amount of protein synthesized from a particular gene by destabilizing its mRNA; this destabilization is achieved either by inserting an antibiotic resistance cassette immediately after the stop codon of a particular gene (disrupting its 3’ untranslated region) or by additionally inserting a tag (a degron) that targets the transcript for protease degradation. The DAmP strategy has been shown to decrease the amount of protein from 2- to 10-fold, with the addition of the degron leading to an additional 2- to 10-fold reduction⁴.

The *KRE9* DAmP strain was unique in the pilot screen for its broad distribution of crossover frequencies and relatively weak overall dielectrophoretic response at 0.05 S/m. These characteristics were also observed using IDS to compare this strain to wildtype (Figure 5- 8). Across the experimental frequencies (100 – 700 kHz) and flowrates (3 – 6 μ l/min), a majority of *KRE9* deficient cells separate at the highest conductivity (0.075 S/m) with a subpopulation more closely resembling wildtype, but separating at a slightly *lower* conductivity. This bimodal distribution of cells is uncommon among the

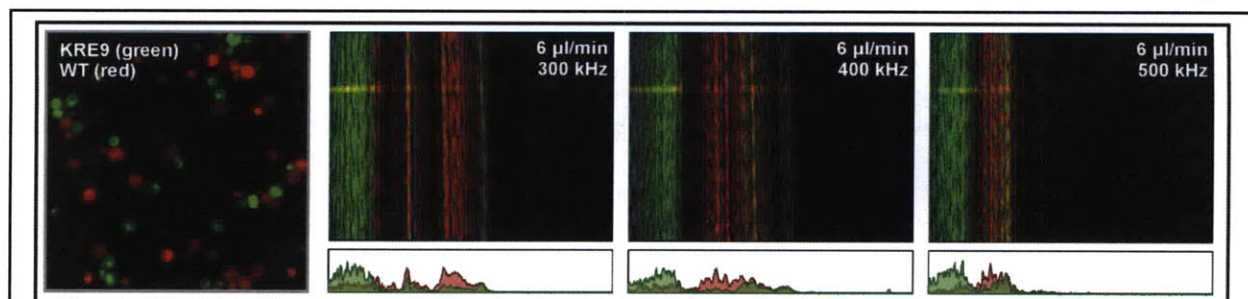


Figure 5- 8: Pairwise comparisons between wildtype (red) and *KRE9* DAmP strains (green). The *KRE9* DAmP strain is the only one found in the pilot screen with electrical properties significantly different from wildtype (right panels) but exhibiting no obvious morphological difference (left panel). The distribution of *KRE9* DAmP cells is noteworthy for appear bimodal, with cells localizing at both higher (to the left side, in the fluorescent images) and lower conductivities than wildtype.

strains selected for the pilot screen and may be attributable to a number of factors, including the presence

of a significant number of non-viable cells comprising the low conductivity fraction. More interestingly, it could be related to the broad distribution of crossover frequencies observed for these cells, and a consequence of phenotypic heterogeneity. This is supported by the large variability we observe in COF measurements of this strain (Figure 5- 1).

To determine if this heterogeneity was perhaps intrinsic to DAmP strains (in which the amount of synthesized protein is not as tightly controlled as for a complete gene deletion), we performed IDS experiments with the other DAmP strains present in our pilot screen (*ROT1* and *BIG1*); these strains, however, appear to exhibit electrical properties indistinguishable from wildtype. Similarly, the *KRE1* deletion strain did not appear distinct from wildtype in follow-up experiments motivated by our findings regarding *KRE9*. Unfortunately, the DAmP library (in contrast to the deletion library) lacks barcodes identifying each strain, and is thus not amenable to the type of pooled genetic screen suitable for IDS. Accordingly, although the underlying mechanism through which knocking down *KRE9* effects a cell's electrical properties remains unknown, the DAmP library remains a potentially interesting subject for future work.

Candidate strains identified through barcode sequencing. Our initial electrogenomic profile of the yeast deletion library yielded 58 strains exhibiting potentially distinct electrical phenotypes. In an effort to interpret these results, we have categorized these strains according to their morphology, biological function, and genetic interactions, as reported in the literature.

Categorization of candidate strains by morphology.

In the morphological screen accompanying the initial characterization of the deletion collection, ~15% of the strains were found to exhibit morphology distinct from wildtype³. At ~43%, the frequency is much higher for strains identified in our screen as having distinct electrical properties. This suggests that, as in the pilot screen, cell morphology is a primary indicator of altered electrical phenotype. In particular, we find a high frequency of “elongate” and “football” morphologies at high conductivities,

Morphology	Frequency (Total Library)	Frequency (High σ)	Frequency (Low σ)
Elongate	0.027	0.21	0.29
Football	0.0254	0.14	0.00
Clumpy/Chain	0.0055	0.02	0.21
Small	0.0368	0.05	0.00
Round	0.0459	0.00	0.14
Large	0.0329	0.02	0.00

Table 5- 2: Comparison of strain morphology frequencies in the total library with corresponding frequencies in high and low conductivity fractions.

consistent with the lower depolarization factor of elongated cells aligned to an electric field (Table 5- 2). Somewhat less clear is the role, if any, that morphology plays in low conductivity strains. Although we see an enrichment of “clumpy” and “round” morphologies at low conductivities that may be explained by arguments similar to those underlying the increased conductivity of elongated strains, we also see a relatively high frequency of elongated strains in the low conductivity fractions. Given the relatively small number of low conductivity strains identified in this screen (14), it may be difficult to reach any conclusions without more specific and detailed characterization. Nonetheless, the ambiguities we observe with respect to morphology emphasize the potential subtlety of electrical phenotypes; although the general correlation between higher conductivity and more elongated morphology is consistent with the model presented above, in many cases, there may be additional factors competing with or complementing the effects of shape alone. As a result, it could be interesting to focus our attention on strongly elongate strains that do not exhibit increased conductivity, or to more thoroughly characterize the correlation between shape and conductivity on a single cell level. A complete listing of the morphological screening results reported for strains identified in our study is included in the Appendix to this chapter (Table 5- 9).

Categorization of candidate strains by biological function. In addition to looking at the morphological categorization of the identified deletion strains, we also explored possible functional

groupings they might share through the Gene Ontology (GO) biological processes associated with each gene. We began by categorizing each gene according to the general processes in which it was involved (see Table 5- 10 in the Appendix to this chapter). This resulted in prominent groups involved in metabolism, transcription, and protein modification and sorting. Interestingly, of the eight low conductivity strains we were able to categorize, five appear to be involved in regulating transcription. This may suggest that decreased electrical conductivity requires more significant changes in gene expression than increased conductivity, and is primarily incurred only when genes controlling the expression of multiple other genes are deleted.

Filtering the 58 electrically distinct strains through the GO Term Finder (available through the Saccharomyces Genome Database, <http://www.yeastgenome.org/cgi-bin/GO/goTermFinder.pl>) identified only one statistically significant group ($P < 10^{-2}$) of similar GO annotations. This group is comprised of four genes: *STP22*, *VPS36*, *SNF7*, and *SNF8*, associated with the protein sorting through the multivesicular body pathway. Although it is not immediately obvious what role these genes could potentially play in determining electrical properties, one possibility is discussed in the following section.

Genetic interactions and electrical phenotype. To determine the extent to which genes whose deletion confers a distinct electrical phenotype interact with each other, we filtered the high conductivity strains identified in our screen through a database summarizing the results of 5.4 million digenic interactions¹²⁹. Of the 44 gene deletions associated with high conductivity, 8 (*RIM8*, *RIM13*, *RIM20*, *WHI2*, *LDB18*, *CLB2*, *GPH1*, *SCS2*) share strong genetic interactions with other deletions conferring high conductivity at a rate greater than would be expected by chance ($P < 0.02$). In total, genetic interactions contained in the data set we have used connect 12 of the 44 high conductivity deletion strains. Figure 5- 9 gives a reduced illustration of the interactions between genes associated with increased conductivity.

Interactions between pairs of genes can be categorized as positive or negative, depending upon whether the double deletion mutant exhibits greater or lesser fitness than would be expected from the multiplicative effect of two single gene deletions acting independently. For example, a negative interaction could suggest that two particular genes act in parallel, performing overlapping tasks, whereas a positive interaction could indicate that the genes act in series, so that deleting multiple genes from the cascade has a diminished effect relative to the first deletion (since the cascade is substantially disrupted by deleting any one of its components). Accordingly, deleting individual genes linked by positive interactions may produce similar phenotypes, since they may act as part of a pathway. By this reasoning, the subnetwork of interactions among genes whose deletion results in increased conductivity suggests the possible role of the RIM101 pathway in creating a distinct electrical phenotype. This pathway is associated with the alkaline pH signaling response and involves *RIM8*, *RIM9*, *RIM13*, *RIM20*, *RIM21*, and *DFG16*; interestingly, disruption of the RIM101 cascade has been shown to result in cell wall defects¹³⁶. Of course, as a transcription factor that acts as both a repressor and activator of different genes, *RIM101* is highly pleiotropic¹³⁷. Nonetheless, the proposed role of this pathway in the regulation

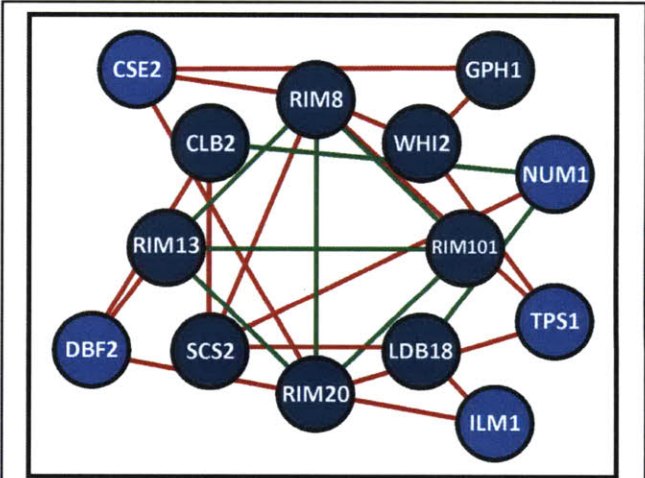


Figure 5- 9: Illustration of a subnetwork of interactions among genes whose deletion confers increased electrical conductivity. Edges denote strong positive (green) and negative (red) interactions as determined in Costanzo *et al.*, 2010. Dark blue and light blue nodes denote strains with enrichment >5 s.d. and >3 s.d. above the mean at high conductivity, respectively. Dangling nodes are excluded for clarity.

of cell wall biosynthesis and reorganization would be consistent with the enrichment of strains lacking different components of the RIM101 signaling cascade at high conductivities (Table 5- 3); a thinner or more porous cell wall could produce such a phenotype.

Supporting the hypothesis that perturbations to the RIM101 pathway result in increased electrical conductivity - but through a mechanism other than cell wall assembly - is recent evidence connecting *RIM8* and *RIM101* to the ESCRT (endosomal sorting complex required for transport) machinery¹³⁸. This evidence suggests that several components of the ESCRT machinery identified in our screen and grouped according to their GO annotations (*STP22*, *SNF7*, *SNF8*, and *VPS36*; see previous section), are necessary for alkaline pH signal transduction through the RIM101 pathway. Since our separations for this screen were performed at a pH of ~7.4 (whereas pH > 7.6 is generally associated with the strong activation of the RIM101 cascade¹³⁶), it is unclear if the enrichment of these strains at high conductivity arises through a deficiency in the pH stress response. Although more work is necessary to understand the electrical phenotypes we observe for strains associated with RIM101 signaling, the ability demonstrated by this screen

to identify clusters of genetic interactions correlating with electrical phenotype suggests that using IDS to study the physical implications of perturbing genetic networks is feasible. Towards this end, screening cells subjected to a variety of environmental conditions during their separation, analogous to functional profiling, could provide deeper understanding of the effects of genotype on cell structure, as measured through electrical phenotype.

In addition to suggesting that the RIM101 pathway is associated with electrical phenotype, filtering our screening results through the genetic interactions dataset also suggests a link between *CLB2*, *NUM1*, and *LDB18* deletion strains, which are linked by positive interactions (Figure 5- 9). Although *LDB18* is largely uncharacterized, recent work suggests that it, along with *NUM1*, may be a component of the dynein-dynactin pathway¹³⁹. Interestingly, the reading frame of *NUM1* overlaps with an uncharacterized ORF, YDR149C; deletions of either of these ORFs results in significant enrichment at high conductivities (>3 s.d. above the mean for *NUM1* in the (HH+H) outlets, >6 s.d. above the mean for YDR149C in the HH outlet). Checking other genes associated with the dynein-dynactin pathway in our screening results (Table 5- 4) suggests that deletions from this group may have a similar effect on electrical phenotype, although this is less strongly supported than the correlations between genes within the RIM101 pathway ($P = 0.11$ as opposed to $P = 0.023$; see Materials and Methods for a description of the statistical analysis).

The results of this screen, though preliminary, suggest a number of potentially interesting directions to pursue. First, it will be necessary to confirm the strains identified

ORF	Alias	(HH+H)	(LL+L)
YGL045W	<i>RIM8</i>	2.0234	0.3727
YGL046W	<i>RIM8*</i>	2.1971	0.5335
YMR063W	<i>RIM9</i>	1.2255	1.2072
YMR154C	<i>RIM13</i>	2.4253	0.3312
YOR275C	<i>RIM20</i>	1.8866	0.4606
YNL294C	<i>RIM21</i>	1.5345	0.8896
YOR030W	<i>DFG16</i>	[---]	[---]
YHL027W	<i>RIM101</i>	1.9856	0.5905

Table 5- 3: Correlated electrical phenotype in strains lacking different components of the RIM101 cascade, determined through barcode sequencing. The phenotype exhibited by this grouping of 6 genes (excluding *DFG16* which received too few barcode reads to quantify) is statistically significant with $P = 0.023$. (*Overlapping ORF)

ORF	Alias	(HH+H)	(LL+L)
YLL049W	<i>LDB18</i>	2.4461	0.6773
YDR149C	[---]	1.7143	1.1274
YDR150W	<i>NUM1</i>	1.6172	0.5569
YHR129C	<i>ARP1</i>	1.5148	0.7294
YMR294W	<i>JNM1</i>	1.4733	0.4924
YKR054C	<i>DYN1</i>	1.0178	1.0811
YDR424C	<i>DYN2</i>	0.8932	0.9733
YPL174C	<i>NIP100</i>	1.1437	0.7484
YDR488C	<i>PAC11</i>	0.9815	0.6996
YOR269W	<i>PAC1</i>	1.2096	0.7836
YMR299C	<i>DYN3</i>	1.4895	0.6497

Table 5- 4: Correlated electrical phenotype in strains lacking different components of the dynein-dynactin spindle orientation pathway. The phenotype exhibited by this grouping of 11 genes borders on statistical significance ($P = 0.11$).

here as being electrically distinct through experiments with finer resolution (*e.g.* pairwise comparisons with wildtype) and by restoring the deleted genes to see if wildtype electrical properties are restored. Beyond this, it may prove interesting to explore the apparent clustering of genes associated with elongated morphology, the RIM101 pathway, and (more tentatively) the dynein-dynactin pathway by performing the screen under different conditions. For example, performing separations at higher conductivities and frequencies can suppress the sensitivity to cell shape (see, for example, the bottom row of Figure 1- 5). Similarly, changing the pH of the separation medium may help to clarify the mechanism through which genes in the RIM101 pathway alter electrical phenotype. We have performed separations using YPD as the high conductivity medium which could potentially address both of these questions simultaneously. Further exploration of the genetic basis of electrical properties may yield additional avenues for research.

Materials and Methods

Measuring Crossover Frequencies. For crossover frequency experiments, we removed a small inoculum from the frozen stock for each individual strain and added it to 2ml of YPD plus 100 $\mu\text{g/ml}$ G418. We cultured the strains separately in 14ml round bottom tubes overnight (~ 24 hrs.) at 30°C . In the case of some slow growing strains, we extended the culture time an additional 24 hours, so that the cell concentration at the time of the COF measurement was comparable for all strains. Immediately prior to the COF measurement, we harvested and centrifuged 200 μl of each strain, which we then resuspended in 1ml of a solution adjusted to 0.05 S/m by the addition of PBS (~ 1.5 S/m). We then used ~ 10 μl of this suspension to fill a 250 μm -thick, hand-cut PDMS gasket which we placed on a set of interdigitated electrodes (pitch and spacing = 50 μm). We capped the gasket with a glass coverslip and made electrical connections to a function generator. To minimize electrothermal convection, we used a voltage of $3V_{pp}$ (at which no convection was observed) and varied the frequency to determine the approximate range over which the cells transitioned from undergoing negative dielectrophoresis (at lower frequencies) to positive dielectrophoresis (at higher frequencies).

Pairwise Comparison of Strains Using IDS. To perform IDS-based pairwise comparisons of wildtype and deletion strains, we cultured cells as described in the previous section, harvesting cells for separation in mid- to late-exponential phase. In order to visualize the distribution of the two strains, we stained wildtype and deletion strains for 10 minutes in solutions of 5 μM Syto 63 and Syto 9 fluorescent nucleic acid stains (S11345 and S34854, Invitrogen), respectively. After staining, we washed the cells $3\times$ in the high conductivity buffer (0.075 S/m, 0.5% BSA), and loaded them into the device along with the low conductivity buffer (0.01 S/m, 0.5% BSA). To eliminate bubbles, we placed a piece of scotch tape temporarily over the outlets of the device as it was continually loaded; this drove any bubbles out through the gas permeable PDMS. After allowing flow through the device to equilibrate, we sequentially visualized cells at the device outlet through FITC (Syto 9) and TRITC (Syto 63) filters, recording each strain for approximately 10s under each condition. To minimize the effects of drift (*i.e.* low frequency fluctuations in the distribution of cells over time), we recorded video continuously, switching the filter cube during the process; this minimized the time offset between recordings of the red and green channels. For each experiment, we varied both flowrate and frequency; typically, we recored data at flowrates of 3, 4.5, and 6 $\mu\text{l/min}$, and at frequencies of 100-600 kHz in 100 kHz intervals.

As in previous experiments, we processed the recorded videos using a first-order difference filter across the frame number index, and applied a threshold to equalize the intensity of each cell. We then averaged the result across the number of frames to obtain a two-dimensional image, and averaged the red and green channels of these images to obtain one-dimensional distributions of cells across the width of the channel. To compare distributions of deletion and wildtype strains under given conditions, we first normalize the one-dimensional distributions, $p(x)$, so that they represent the probability density for

finding a cell at position x along the channel width. We then calculate the correlation between the distribution of deletion ($p_{\Delta}(x)$) and wildtype ($p_{wt}(x)$) strains according to:

$$\text{corr}\{\mathbf{p}_{\Delta}, \mathbf{p}_{wt}\} = \frac{\mathbf{p}_{\Delta} \cdot \mathbf{p}_{wt}}{|\mathbf{p}_{\Delta}| |\mathbf{p}_{wt}|} \quad (5-10)$$

We then take $1 - \text{corr}\{\mathbf{p}_{\Delta}, \mathbf{p}_{wt}\}$ as a measure of the difference between a particular deletion strain and wildtype. For each strain, we average this quantity across all experiments and experimental conditions (frequency and flowrate). An important consequence of choosing to quantify differences between strains in this way is that it discards any information regarding whether the deletion strain in question is more or less conductive than wildtype; however, since our present goal is to determine electrically distinct strains to serve as controls for a larger study of the deletion library, this is sufficient for our purposes.

A potential hazard of this microscopy-based approach arises from our inability to image the differentially stained deletion and wildtype strains simultaneously. As a result, we must switch the microscopes filter cube to image them sequentially, introducing a time offset between the distributions that could give rise to lower correlations due to drift in the device's operation. As a negative control for pairwise comparisons, we therefore correlate distributions of wildtype cells measured 1-2 seconds apart. This provides an approximate baseline for the difference in correlation coefficients introduced by fluctuations in the devices operation over short times. The result of this correlation (averaged over different experiments) is plotted as a dashed line in Figure 5- 2.

Separations of the Pooled Pilot Screen Strains. To create a pool with equal representation of each strain, we grew the 83 strains to stationary phase in separate wells of a 96-well plate. After all strains had reached stationary phase, we pooled the wells and froze 1 ml aliquots in 15% glycerol, with one aliquot to be used for each experiment. We chose the operating conditions for these pooled separations to optimize both the separation of the electrically distinct strains as well as the overall number of cells collected from each of the four outlets. For a conductivity ranging from 0.075 S/m to 0.01 S/m and a flowrate of 6 μ l/min, this is achieved at a frequency of around 300 kHz.

Separations of the Pooled Deletion Collection. For separations of the complete pooled deletion collection where we use quantitative PCR to measure strain abundance, we do not allow cells within the pooled library to divide after thawing but before separation. This assures equal representation of strains in the library, whereas an extended growth period could result in the loss of slow growing strains to dilution. To achieve an appropriate number of cells, we resuspend the contents of 3-4 aliquots ($\sim 2 \times 10^6$ cells each) in 1 ml of the higher conductivity medium and proceed with the separation.

For separations in which the final readout of strain abundance will be performed by barcode sequencing (thus affording higher sensitivity than quantitative PCR), we allow the cells to undergo ~ 2 rounds of division prior to sorting them. This reduces the fraction of non-viable cells present in the sample by a factor of four. To limit growth to two generations, we inoculate cells at an OD_{600} of ~ 0.5 in 400 μ l of YPD containing 100 μ g/ml G418 and allow them to grow overnight (~ 12 hours). Although this not a precise means of controlling growth, we set aside a sample of the culture (containing $\sim 2 \times 10^6$ cells) immediately prior to sorting to be quantified along with the sorted fractions. This internal control allows us to account for variation in strain representation from experiment to experiment by normalizing the abundance of strains in the separated sample to their abundance in the original sample after ~ 2 generations of growth.

Once the cells have been prepared for sorting, the separation proceeds identically regardless of the intended method of quantification (i.e. quantitative PCR or sequencing). For separations of the complete library, we explore two sets of operating conditions; the first matches the conditions of the pilot screen (conductivity ranging from 0.075 - 0.01 S/m, a flowrate of 6 μ l/min, and a frequency 300 kHz), while the second uses fresh YPD plus 100 μ g/ml G418 as the high conductivity buffer (~ 0.25 S/m), a low

conductivity buffer adjusted to 0.04 S/m, and a frequency of 1MHz. In all cases when working with the complete deletion collection, we run the separation for three hours, corresponding to the collection of $\sim 10^7$ cells, distributed across the four outlets.

Analysis of Sequencing Results. In our initial sequencing experiments, we submitted twenty samples (ten each for UPTAG and DNTAG barcodes, representing two independent experiments), labeled using ten multiplexing tags to be combined on a single lane in an Illumina flowcell. This yielded ~ 21 million reads, with samples receiving from between a minimum of 310,000 reads and maximum of 1.7 million reads. To analyze this data, we parsed the text file containing all of the reads into twenty separate files according to the first five bases; the first four bases give the multiplexing tag, while the fifth base determines if the barcode is an UPTAG ('G') or a DNTAG ('C'). We discard any sequence in which these bases do not perfectly match a multiplexing tag followed by G or C, preserving $\sim 95\%$ of the total reads. We then compare the data in these separate files to either the 5169 UPTAG barcodes or to the 5004 DNTAG barcodes, as appropriate.

Within each UPTAG sequencing read, the final 13 bases correspond to the first 13 bases of the reverse complement of the barcode as listed in the reference provided by the curators of the deletion library (http://www-sequence.stanford.edu:16080/group/yeast_deletion_project/). For each DNTAG read, the final 14 bases correspond to the first 14 bases of the barcode, ordered as listed in the above reference. To identify the barcodes, we create a 5169×13 (or 5004×14) matrix of characters corresponding to the barcodes, and sequentially read in the final 13 (or 14) characters from each line in one of the text files. Using this read, we create a binary matrix equal in size to the barcode matrix, in which '1' corresponds to a base match, and '0' corresponds to a mismatch between the sequence read and a particular barcode. Summing over the columns of this matrix gives a vector of scores representing how well the sequencing read matches each barcode. We take the maximum of this vector, and if it is correct to within two bases, we increment the count of the corresponding strain. Since for both UPTAGs and DNTAGs, $\sim 75\%$ of the sequencing reads are perfect matches, with $\sim 12\%$ being off by a single base, this relaxed criteria for matching a barcode is not essential. However, since some of the barcodes have been shown to differ from their original listings¹⁴⁰, and some of the sequencing reads contain ambiguous base calls ('N'), we tolerate small discrepancies. The final result is a vector for each of the 20 samples containing the number of counts for each strain.

To identify strains exhibiting atypical electrical phenotype, we normalize the vectors of counts to obtain frequencies for each strain, which we then compare across samples. For each of the two experiments, both UPTAG and DNTAG, we calculate the ratio of frequencies HH/O , H/O , L/O , and LL/O , where 'O' denotes the original, unsorted fraction. Because each sample contains ~ 500 -1000 strains for which there were few to no detected barcodes, we add a baseline value to each vector of frequencies to eliminate spurious hits arising from poorly represented strains. The larger this baseline, the more robust the enrichment of a particular strain must be to be detected. Experimenting with baselines ranging from $1/100^{\text{th}}$ to $1/2$ the sample mean, we find that baselines greater than one tenth the sample mean ($= 1/10M$, for M strains) yield consistent results that exclude all poorly represented strains (this is equivalent to adding 10-20 pseudocounts to the unnormalized vector of counts). For each separation condition (HH , H , L , LL), we then have four numbers (two experiments with two sets of barcodes); taking the geometric mean gives us a consensus across the different barcodes and experiments. Strains showing enrichment of six standard deviations above the mean for these consensus vectors are identified as candidate strains exhibiting potentially distinct electrical phenotypes. We perform this analysis on each of the four samples, as well as on the geometric mean of the (HH , H) and (LL , L) samples. For these ($HH+H$) and ($LL+L$) vectors, we set five standard deviations above the mean as the criteria for enrichment.

Mapping Genetic Interactions to Electrical Phenotype. Using recently published¹²⁹ genetic interaction data available through the *Saccharomyces* Genome Database, we obtain lists of the genes that interact strongly with each of the genes associated with high conductivity. Of the 44 genes identified in our screen, 34 of them exhibit interactions listed in the dataset. This generates 34 lists of partner genes

that interact with a particular gene identified in our screen. We search each of these lists to identify the number of interacting partners that are also associated with high conductivity (corresponding to enrichment at high conductivity of ≥ 3 s.d. above the mean); if the number is statistically significant ($P < 0.02$), we count this grouping of genes as linked both through electrical phenotype as well as genetic interactions. To determine statistical significance, we calculate the probability that a gene with a given number of total interactions would include the observed number of interactions with other genes associated with high conductivity.

To determine the statistical significance of correlated electrical properties within groups of genes participating in known pathways (specifically, RIM101 and dynein-dynactin), we assume that the strain enrichments follow a log-normal distribution. Using the mean and variance determined from the log of the strain enrichments, we calculate the probability that the geometric mean enrichment of a random grouping of genes would be greater than that observed in the high conductivity fraction ($HH+H$) and lower than that observed in the low conductivity fraction ($LL+L$).

Appendix to Chapter 5

Strains used in the Pilot Screen.

ORF	Alias	Description (SGD)
YAL053W	FLC2	Protein of unknown function
YLL052C	AQY2	Aquaporin water channel protein, member of major intrinsic protein (MIP) family of transmembrane channels, has strong similarity to aquaporin Aqy1p
YLL043W	FPS1	Glycerol channel protein, member of the major intrinsic protein (MIP) family of transmembrane channel proteins
YML016C	PPZ1	Protein serine/threonine phosphatase required for normal osmoregulation, member of the PPP family of protein phosphatases and related to PP1 phosphatases
YNL322C	KRE1	Cell wall protein needed for cell wall beta-1,6-glucan assembly, probably involved in side-chain addition to form mature beta-1,6-glucan
YOR010C	TIR2	Cold-shock induced protein of the PAU1 family
YOR002W	ALG6	Glucosyltransferase involved in the synthesis of dolichol-linked oligosaccharide precursor
YOR067C	ALG8	Glucosyltransferase of the endoplasmic reticulum; has a role in adding glucose to the dolichol-linked oligosaccharide precursor prior to transfer to protein
YPL230W	USV1	Protein with similarity to yeast and human zinc finger transcription factors; has a C2H2-type zinc finger
YPL221W	FLC1	Protein of unknown function
YPL161C	BEM4	Bud emergence protein that interacts with Rho-type GTPases
YBR205W	KTR3	Alpha-1,2-mannosyltransferase of the KRE2 family
YBR199W	KTR4	Alpha-1,2-mannosyltransferase of the KRE2 family
YDR055W	PST1	Protein with similarity to members of the Sps2p-Ecm33p-Ycl048p family
YBR229C	ROT2	Catalytic (alpha) subunit of glucosidase II
YDR364C	CDC40	Protein required for the second catalytic step of mRNA splicing, member of WD (WD-40) repeat family
YDR123C	INO2	Basic helix-loop-helix (bHLH) transcription factor required for derepression of phospholipid synthetic genes
YDR436W	PPZ2	Protein serine/threonine phosphatase involved in osmoregulation, member of the PPP family of protein phosphatases and related to PP1 phosphatases
YDR414C	ERD1	Protein required for retention of luminal ER proteins
YDR420W	HKR1	Hansenula mrakii K9 killer toxin-resistance protein
YER011W	TIR1	Stress-induced cell wall structural protein of the PAU1 family
YGR217W	CCH1	Putative voltage-gated calcium channel
YHR132C	ECM14	Protein possibly involved in cell wall structure or biosynthesis
YCL005W	LDB16	Protein of unknown function, can mutate to confer daunomycin resistance
YCL051W	LRE1	Protein involved in laminarinase resistance
YCR002C	CDC10	Septin, component of 10 nm filaments of mother-bud neck, involved in cytokinesis
YKL048C	ELM1	Serine/threonine protein kinase regulating pseudohyphal growth
YKL164C	PIR1	Protein required for tolerance to heat shock, member of the Pir1p/Hsp150p/Pir3p family
YKL163W	PIR3	Protein with similarity to members of the Pir1p/Hsp150p/Pir3p family

YKL096W	CWP1	Mannoprotein of the cell wall; member of the PAU1 family
YOR134W	BAG7	Putative GTPase-activating protein (GAP)
YGR104C	SRB5	Component of the RNA polymerase II holoenzyme and Kornberg's mediator (SRB) subcomplex; required for basal transcription
YOR247W	SRL1	Protein with similarity to Svs1p
YJL158C	CIS3	Cell wall protein with similarity to members of the Pir1p/Hsp150p/Pir3p family
YLR233C	EST1	Putative component of telomerase
YPL086C	ELP3	subunit of elongator/RNAPII holoenzyme, has histone acetyltransferase activity
YPL053C	KTR6	Mannosyltransferase of the KRE2 family
YPL049C	DIG1	MAP kinase-associated protein involved in negative regulation of invasive growth
YGR227W	DIE2	Glucosyltransferase involved in the terminal glucosylation step of the lipid-linked oligosaccharide
YPR192W	AQY1	Aquaporin water channel protein, member of the MIP (major intrinsic protein) family of aquaglyceroporin transmembrane channels
YNL160W	YGP1	Secreted glycoprotein produced in response to nutrient limitation
YKR061W	KTR2	Mannosyltransferase of KRE2 family, involved in N-linked glycosylation
YDR264C	AKR1	Ankyrin repeat-containing protein; has an inhibitory effect on signaling in the pheromone pathway
YLL049W	LDB18	Protein of unknown function
YJL093C	TOK1	Two-domain outwardly-rectifying voltage-gated potassium channel
YJL127C	SPT10	Protein that amplifies the magnitude of transcriptional regulation at various loci
YJL062W	LAS21	Protein required for addition of a side chain to the glycosylphosphatidylinositol (GPI) core structure
YKR100C	SKG1	Protein of unknown function
YLR443W	ECM7	Protein possibly involved in cell wall structure or biosynthesis
YDL240W	LRG1	GTPase-activating protein of the rho/rac family, expressed highest in sporulating cells
YJR051W	OSM1	Mitochondrial soluble fumarate reductase involved in osmotic regulation
YNL029C	KTR5	Putative mannosyltransferase of the KRE2 family
YBR005W	RCR1	Protein of unknown function
YNL025C	SSN8	Cyclin C homolog, component of RNA polymerase holoenzyme complex and Kornberg's mediator (SRB) subcomplex
YBR067C	TIP1	Cold- and heat-shock induced mannoprotein of the cell wall, member of the PAU1 family
YBR023C	CHS3	Chitin synthase III; responsible for chitin ring at base of bud and chitin in the lateral cell walls
YKL201C	MNN4	Protein required for transfer of mannosylphosphate to core and outer chain portions of N-linked oligosaccharides
YML115C	VAN1	Vanadate resistance protein; component of mannan polymerase M-Pol I, which includes Mnn9p and Van1p
YNR052C	POP2	Component of the CCR4 complex required for glucose derepression
YDL049C	KNH1	Putative secreted protein with similarity to Kre9p
YBR171W	SEC66	Component of ER protein-translocation subcomplex; with Sec62p, Sec63p, Sec66p, and Sec72p
YDR456W	NHX1	Late endosomal Na ⁺ /H ⁺ antiporter
YDR528W	HLR1	Protein of unknown function
YIL085C	KTR7	Putative mannosyltransferase of the KRE2 family

YOL148C	SPT20	Component of the nucleosomal histone acetyltransferase (Spt-Ada-Gcn5-Acetyltransferase or SAGA) complex, member of TBP class of SPT proteins
YDR351W	SBE2	Protein required for bud growth
YHR103W	SBE22	Protein required for bud growth
YOR099W	KTR1	Mannosyltransferase of KRE2 family involved in N-linked and O-linked glycosylation
YJR040W	GEF1	Voltage-gated chloride channel, has effects on intracellular iron metabolism
YPL031C	PHO85	Cyclin-dependent protein kinase that interacts with cyclin Pho80p to regulate phosphate pathway, also interacts with other Pho80p-like cyclins
YGR262C	BUD32	Protein with similarity to apple tree calcium/calmodulin-binding protein kinase
YJR090C	GRR1	F-box protein that targets G1 cyclins and Gic1p and other proteins for degradation by the SCF-Grr1p complex (Skp1p-Cdc53p-Cdc34p-Grr1p); also required for glucose repression and for glucose and cation transport
YDR245W	MNN10	subunit of the Anp1p-Hoc1p-Mnn10p-Mnn11p-Mnn9p mannosyltransferase complex, M-Pol II
YLR337C	VRP1	Proline-rich protein verprolin, involved in cytoskeletal organization and cellular growth
YNL084C	END3	Protein required for endocytosis and cytoskeletal organization
YPR072W	NOT5	Protein that negatively regulates transcription of TATA-less promoters and has similarity to Not3p
YNL059C	ARP5	Actin-related protein
YER070W	RNR1	Ribonucleotide reductase (ribonucleoside-diphosphate reductase) large subunit; converts deoxyribonucleoside diphosphate to ribonucleoside diphosphate
YEL036C	ANP1	Protein of the cis Golgi with a role in retention of glycosyltransferases in the Golgi, subunit of the Anp1p-Hoc1p-Mnn11p-Mnn9p mannosyltransferase complex
YMR200W	ROT1	DAMP HAP 9
YHR101C	BIG1	DAMP HAP 6
YJL174W	KRE9	DAMP HAP 7

Table 5- 5: A listing of yeast strains used in the pilot screen, including a description of the protein that has been deleted (or knocked down, in the case of *ROT1*, *BIG1*, and *KRE9*) obtained from the Saccharomyces Genome Database (www.yeastgenome.org).

DNA Extraction and Purification. After separation, we extracted DNA from the four collected fractions (*HH*, *H*, *L*, *LL*) in addition to an aliquot from the original pool (*O*) using a YeaStar Genomic DNA Kit (D2002, Zymo Research) and following Protocol I (chloroform-based) in the kit's manual. For the final elution step, we used 80µl of TE buffer, so that the final product consists of purified genomic DNA in 80µl of TE. These samples were then used directly as the template in subsequent PCR amplifications.

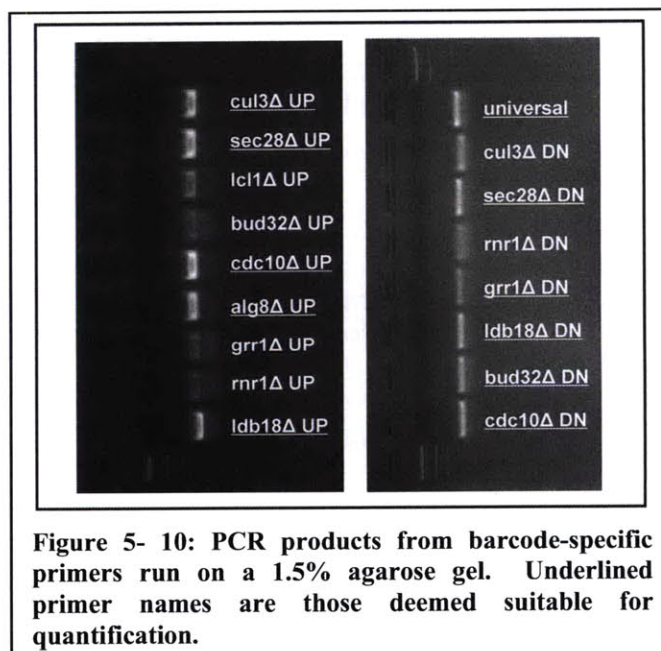
Amplification of Strain Barcodes for Quantitative PCR. To corroborate the results of full library separations with the pilot screen, we adopted a two-stage PCR approach, in which a universal region around the barcodes was amplified in the first stage, followed by a second reaction in which one primer hybridized directly to the barcode to give strain-specific amplification. Primer sequences used for these experiments are listed in Table 5- 6. Primers labeled “universal” are those used in the first reaction, while the strain-specific primers are used with “universal (R)” primers in the second reaction. Note that while the “universal (L)” primers reside directly 5' of the barcodes, the “universal (R)” primers lie within the KanMX cassette for both UPTAG and DNTAG barcodes. We chose to do this (rather than using the default universal priming sites flanking the barcodes) to get better compatibility (i.e. melting temperature, G-C content, low complementarity) across as many primers as possible.

For the first reaction, we used 112 μ l purified water, 35.2 μ l template DNA (~100ng), 12.8 μ l primer mix (forward and reverse each at 10 μ M), and 160 μ l of Taq 2X Master Mix (M0270, New England BioLabs). We then divided this mixture into eight separate 40 μ l aliquots for amplification, mixing them back together after the reaction.

Priming off of UPTAGS (5'-3')		Priming off of DNTAGS (5'-3')	
universal (L)	ATGGATGTCCACGAGGTCTCT	universal (L)	ACGGTGTCGGTCTCGTAG
universal (R)	ACATGGGGATGTATGGGCTA	universal (R)	TCATGCGTCAATCGTATGTG
<u>grr1Δ</u> (L)	CTGAGTAGTCAGCATTCGTTCG	<u>grr1Δ</u> (L)	GGGAGCGAGCGTCATATTT
<u>rnr1Δ</u> (L)	TCTCCGCCATAGTAATAGAGATCC	<u>rnr1Δ</u> (L)	GACGCTCTACGATGCTGCT
<u>cdc10Δ</u> (L)	CTCTCCGTGTCCAGAACTAGAATA	<u>cdc10Δ</u> (L)	GCATTACCGAACATGGCGTA
<u>ldb18Δ</u> (L)	CTCTGCATGTGACTAATCTACGAG	<u>ldb18Δ</u> (L)	CGTAGCATAGACCTGAAGCCATAG
<u>bud32Δ</u> (L)	CGTGTGGAATCATATTGACG	<u>bud32Δ</u> (L)	GGCTATTTATACAGTCTCCCGATC
<u>alg8Δ</u> (L)	CTCTCAGATCATGGAATATCACG	<u>sec28Δ</u> (L)	CAGCAGCATGAACCAGTGA
<u>sec28Δ</u> (L)	AGCACGTCTTCAATGCGA	<u>cul3Δ</u> (L)	CTTGGACTGACGGCGTTT
<u>cul3Δ</u> (L)	AAGACGGGCGAATTTCTT		
<u>lcl1Δ</u> (L)	TCTCTTAGTAATCGACAGTGAGGTC		

Table 5- 6: Primer sequences used for barcode-specific quantitative PCR. The “universal (R)” primer is used as the right primer in all reactions.

To determine which barcode primers yield reasonably pure PCR products, we ran the products on an agarose gel. Figure 5- 10 shows the results, for both UPTAG and DNTAG barcodes, with underlined primers corresponding to those deemed reliable for quantification. In addition to strains from the pilot screen, we added negative control strains to the group that we quantify (*lcl1 Δ* , *cul3 Δ* , and *sec28 Δ*), selected at random (*i.e.* using a random number generator) from the *Saccharomyces* Genome Database (<http://www.yeastgenome.org/>).



Amplification of Strain Barcodes for Sequencing.

The procedures we followed for amplifying barcodes for sequencing matches that used for quantitative PCR, with a different set of primers. These were designed as described in¹⁴⁰, with minor modifications for the multiplexing sequence, and are listed in Table 5- 7.

Primers for Illumina Sequencing (5'-3')	
UPTAG (F)	CAAGCAGAAGACGGCATAACGAGCTCTTCCGATCTGATGTCCACGAGGTCTCT
UPTAG (R)	AATGATACGGCGACCACCGAC <u>ACTCTTTCCCTACACGACGCTCTTCCGATCT</u> NNNN GTCGACCTGCAGCGTACG
DNTAG (F)	CAAGCAGAAGACGGCATAACGAGCTCTTCCGATCTGAAAACGAGCTCGAATTCATCG
DNTAG (R)	AATGATACGGCGACCACCGAC <u>ACTCTTTCCCTACACGACGCTCTTCCGATCT</u> NNNN CGGTGTCGGTCTCGTAG

Table 5- 7: UPTAG and DNTAG primers used for multiplexed Illumina sequencing. The underlined sequence corresponds to the sequencing primer, and the red “NNNN” corresponds to the multiplexing sequence used to identify each sample.

The multiplexing sequence consists of four nucleotides immediately adjacent to the sequencing primer hybridization site (underlined in Table 5- 7). Since each experiment consists of five samples (four from the separation plus the original pool), four nucleotides is sufficient to uniquely multiplex 51 experiments. However, due to concerns of undersampling rare strains in the sequencing analysis, we elected to pool only two experiments and adopt a multiplexing scheme in which the first two bases encode the experiment (either ‘AG’ or ‘TC’) and the second two bases encode the samples within that experiment (Original pool, *O* = ‘TC’, Highest conductivity, *HH* = ‘AC’, High conductivity, *H* = ‘CA’, Low conductivity, *L* = ‘TG’, Lowest conductivity, *LL* = ‘GT’). Because the UPTAG and DNTAG barcodes are all unique, the same multiplexing tags were used for each sample regardless of which barcode was amplified.

These primers were then used in the following PCR protocol: 33.6µl purified water, 33.6µl template DNA (~100ng), 12.8µl primer mix (forward and reverse each at 10µM), and 80µl of Taq 2X Master Mix (M0270, New England BioLabs). This mixture was created for both UPTAG and DNTAG samples, with each sample receiving the appropriate multiplexing primer, and then divided into four tubes containing 40µl each. The amplification was carried out using the following parameters: 4 minutes at 95°C; 25 cycles of 30s at 95°C, 30s at 50°C, 30s at 72°C; and finally 7 minutes at 72°C. The end result is 10 samples containing 160µl PCR product. Although these samples could theoretically be combined, we did not do so, so as to assure that the concentration of each sample can be normalized separately immediately prior to sequencing.

Purification of PCR Product for Sequencing. In order to remove any residual primers or primer-dimers created during the amplification of the barcodes, we purified the reaction products on a 4-20% polyacrylamide gel (161-1237, Bio-Rad Laboratories) using a Bio-Rad Mini PROTEAN 3 Cell (operated at a constant current of 15mA for ~ 1 hour). To size the product, we run a 50 base pair ladder (N3236S, New England BioLabs) in parallel with the samples. Each well in the gel that we use can hold 50µl of sample. We fill this to capacity, purifying the same sample multiple times as needed (up to 3×, since the PCR amplification yields ~160µl).

To extract the DNA from the gel, we locate the appropriate areas to remove using UV shadowing. After running the gel, we place it in

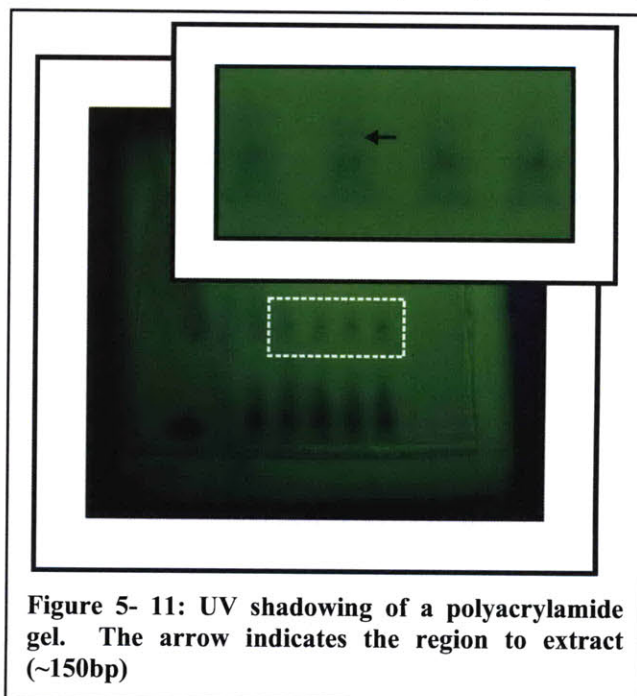


Figure 5- 11: UV shadowing of a polyacrylamide gel. The arrow indicates the region to extract (~150bp)

between two sheets of Saran wrap, and rest this on a fluor-coated TLC plate (AM10110, Ambion). Shining a shortwave (254 nm) UV light through the gel illuminates the plate except where DNA absorbs the light, leaving a shadow. Although this is a considerably less sensitive means of detecting bands than staining, it has the advantage of not using any stains (e.g. ethidium bromide) that would need to be subsequently removed from the DNA before using it in a sensitive downstream application like sequencing or microarray analysis. Figure 5- 11 shows an image of a gel during UV shadowing, in which the band to be excised is barely visible (highlighted in the inset). Analysis of the dark bands beneath the region to be excised revealed that they were 70-100 base pair primers or primer-dimers left over from the barcode amplification. After marking the areas to cut on the top layer of Saran wrap with a marker, we flip the gel over, removing the unmarked Saran wrap, and cut out (with a clean razor blade) the marked regions. Each gel fragment is typically ~2-mm × 5-mm or smaller. Despite the faintness of the desired bands, our typical yield after following the steps listed below is ~100ng of DNA with the correct adaptors for sequencing and of the expected length (~150bp).

After cutting the appropriate band out of the gel, we extract the DNA using a crush and soak procedure, followed by ethanol precipitation, to concentrate and de-salt the sample. Because ethanol precipitation is more efficient at higher concentrations of DNA, we typically combine multiple gel slices of the same sample during the crush and soak step, to increase the amount of DNA by two- or three-fold. For the gel elution buffer we use 120µl of 0.3M sodium acetate and 2mM disodium EDTA, added to the gel slices. To crush the gels, we heat the end of a 1000µl pipette tip, press fit the molten tip into the bottom of an empty microcentrifuge tube, and allow it to solidify. This forms a pestle that can be used to finely crush the gel and to which DNA will not non-specifically bind. We soak the crushed gel overnight at 37°C before removing the gel fragments using a cellulose acetate centrifuge filter. We take the ~100µl this yields for each sample and add 300µl of 100% ethanol, storing at -20°C overnight to allow the DNA to aggregate. Ethanol precipitation is completed by centrifuging at maximum speed (~14000 rpm) on a benchtop centrifuge for 40 minutes, aspirating down to ~20µl, adding 400µl of 75% ethanol, centrifuging at maximum speed again for 40 minutes, aspirating to ~20µl, and allowing the residual solution to evaporate. To resuspend the DNA, we add 20µl of 1× TE buffer, for a final concentration of ~5ng/µl. These samples are then submitted directly for sequencing.

Electrically Distinct Strains Identified from Barcode Sequencing.

ORF	Alias	Sample	Description (SGD)
YCR094W	<i>CDC50</i>	HH, (HH+H)	Endosomal protein that interacts with phospholipid flippase Drs2p; interaction with Cdc50p is essential for Drs2p catalytic activity; mutations affect cell polarity and polarized growth; similar to Ynr048wp and Lem3p
YDL047W	<i>SIT4</i>	HH, H, (HH+H)	Type 2A-related serine-threonine phosphatase that functions in the G1/S transition of the mitotic cycle; cytoplasmic and nuclear protein that modulates functions mediated by Pkc1p including cell wall and actin cytoskeleton organization
YDL101C	<i>DUN1</i>	HH, (HH+H)	Cell-cycle checkpoint serine-threonine kinase required for DNA damage-induced transcription of certain target genes, phosphorylation of Rad55p and Sml1p, and transient G2/M arrest after DNA damage; also regulates postreplicative DNA repair
YDR042C	[---]	HH, (HH+H)	Putative protein of unknown function; expression is increased in ssu72-ts69 mutant
YGL046W	<i>RIM8</i>	HH, H, (HH+H)	Protein involved in proteolytic activation of Rim101p in response to alkaline pH; interacts with ESCRT-1 subunits Stp22p and Vps28p; essential for anaerobic growth; member of the arrestin-related trafficking adaptor family (overlapping ORF)
YGR058W	<i>PEF1</i>	HH, (HH+H)	Penta-EF-hand protein required for polar bud growth and cell wall abscission; binds calcium and zinc with different affinity; localizes to bud site in G1, bud neck in G2
YGR155W	<i>CYS4</i>	HH, (HH+H)	Cystathionine beta-synthase, catalyzes synthesis of cystathionine from serine and homocysteine, the first committed step in cysteine biosynthesis; responsible for hydrogen sulfide generation; mutations in human ortholog cause homocystinuria

YHR011W	<i>DIA4</i>	HH, H, (HH+H)	Probable mitochondrial seryl-tRNA synthetase, mutant displays increased invasive and pseudohyphal growth
YHR158C	<i>KEL1</i>	HH, H, (HH+H)	Protein required for proper cell fusion and cell morphology; functions in a complex with Kel2p to negatively regulate mitotic exit, interacts with Tem1p and Lte1p; localizes to regions of polarized growth; potential Cdc28p substrate
YIL007C	<i>NAS2</i>	HH, H, (HH+H)	Proteasome-interacting protein involved in the assembly of the base subcomplex of the 19S proteasomal regulatory particle (RP); similar to mammalian proteasomal modulator subunit; non-essential gene; interacts with Rpn4p
YIL076W	<i>SEC28</i>	HH, (HH+H)	Epsilon-COP subunit of the coatomer; regulates retrograde Golgi-to-ER protein traffic; stabilizes Cop1p, the alpha-COP and the coatomer complex; non-essential for cell growth
YJL204C	<i>RCY1</i>	HH, (HH+H)	F-box protein involved in recycling plasma membrane proteins internalized by endocytosis; localized to sites of polarized growth
YJR090C	<i>GRR1</i>	HH, (HH+H), LL	F-box protein component of the SCF ubiquitin-ligase complex; involved in carbon catabolite repression, glucose-dependent divalent cation transport, high-affinity glucose transport, morphogenesis, and sulfite detoxification
YLL049W	<i>LDB18</i>	HH, (HH+H)	Protein of unknown function; required for nuclear migration; null mutant shows a reduced affinity for the alcian blue dye suggesting a decreased net negative charge of the cell surface
YLR025W	<i>SNF7</i>	HH, H, (HH+H)	One of four subunits of the endosomal sorting complex required for transport III (ESCRT-III); involved in the sorting of transmembrane proteins into the multivesicular body (MVB) pathway; recruited from the cytoplasm to endosomal membranes
YMR154C	<i>RIM13</i>	HH, (HH+H)	Calpain-like cysteine protease involved in proteolytic activation of Rim101p in response to alkaline pH; has similarity to <i>A. nidulans</i> palB
YNL192W	<i>CHS1</i>	HH	Chitin synthase I, requires activation from zymogenic form in order to catalyze the transfer of N-acetylglucosamine (GlcNAc) to chitin; required for repairing the chitin septum during cytokinesis; transcription activated by mating factor
YPR119W	<i>CLB2</i>	HH, (HH+H)	B-type cyclin involved in cell cycle progression; activates Cdc28p to promote the transition from G2 to M phase; accumulates during G2 and M, then targeted via a destruction box motif for ubiquitin-mediated degradation by the proteasome
YBR134W	[---]	HH, (HH+H)	Dubious open reading frame unlikely to encode a functional protein, based on available experimental and comparative sequence data
YDR149C	[---]	HH	Dubious open reading frame unlikely to encode a functional protein, based on available experimental and comparative sequence data; overlaps the verified gene NUM1; null mutation blocks anaerobic growth
YDR477W	<i>SNF1</i>	HH, (HH+H)	AMP-activated serine/threonine protein kinase found in a complex containing Snf4p and members of the Sip1p/Sip2p/Gal83p family; required for transcription of glucose-repressed genes, thermotolerance, sporulation, and peroxisome biogenesis
YPR160W	<i>GPH1</i>	HH, (HH+H)	Non-essential glycogen phosphorylase required for the mobilization of glycogen, activity is regulated by cyclic AMP-mediated phosphorylation, expression is regulated by stress-response elements and by the HOG MAP kinase pathway
YCL008C	<i>STP22</i>	H, (HH+H)	Component of the ESCRT-I complex, which is involved in ubiquitin-dependent sorting of proteins into the endosome; homologous to the mouse and human Tsg101 tumor susceptibility gene; mutants exhibit a Class E Vps phenotype
YER175C	<i>TMT1</i>	H	Trans-aconitate methyltransferase, cytosolic enzyme that catalyzes the methyl esterification of 3-isopropylmalate, an intermediate of the leucine biosynthetic pathway, and trans-aconitate, which inhibits the citric acid cycle
YGL045W	<i>RIM8</i>	H, (HH+H)	Protein involved in proteolytic activation of Rim101p in response to alkaline pH; interacts with ESCRT-1 subunits Stp22p and Vps28p; essential for anaerobic growth; member of the arrestin-related trafficking adaptor family
YHL027W	<i>RIM101</i>	H, (HH+H)	Transcriptional repressor involved in response to pH and in cell wall construction; required for alkaline pH-stimulated haploid invasive growth and sporulation; activated by proteolytic processing; similar to <i>A. nidulans</i> PacC

YIL050W	<i>PCL7</i>	H, (HH+H)	Pho85p cyclin of the Pho80p subfamily, forms a functional kinase complex with Pho85p which phosphorylates Mmr1p and is regulated by Pho81p; involved in glycogen metabolism, expression is cell-cycle regulated
YJR060W	<i>CBF1</i>	H, (HH+H)	Helix-loop-helix protein that binds the motif CACRTG, which is present at several sites including MET gene promoters and centromere DNA element I (CDEI); required for nucleosome positioning at this motif; targets Isw1p to DNA
YLR180W	<i>SAM1</i>	H, (HH+H)	S-adenosylmethionine synthetase, catalyzes transfer of the adenosyl group of ATP to the sulfur atom of methionine; one of two differentially regulated isozymes (Sam1p and Sam2p)
YOR275C	<i>RIM20</i>	H, (HH+H)	Protein involved in proteolytic activation of Rim101p in response to alkaline pH; PalA/AIP1/Alix family member; interaction with the ESCRT-III subunit Snf7p suggests a relationship between pH response and multivesicular body formation
YLR203C	<i>MSS51</i>	H	Specific translational activator for the mitochondrial COX1 mRNA; loosely associated with the matrix face of the mitochondrial inner membrane; influences both COX1 mRNA translation and Cox1p assembly into cytochrome c oxidase
YMR300C	<i>ADE4</i>	H, (HH+H)	Phosphoribosylpyrophosphate amidotransferase (PRPPAT; amidophosphoribosyltransferase), catalyzes first step of the 'de novo' purine nucleotide biosynthetic pathway
YDR074W	<i>TPS2</i>	(HH + H)	Phosphatase subunit of the trehalose-6-phosphate synthase/phosphatase complex, which synthesizes the storage carbohydrate trehalose; expression is induced by stress conditions and repressed by the Ras-cAMP pathway
YER120W	<i>SCS2</i>	(HH + H)	Integral ER membrane protein that regulates phospholipid metabolism via an interaction with the FFAT motif of Opi1p, also involved in telomeric silencing, disruption causes inositol auxotrophy above 34 degrees C, VAP homolog
YIL006W	<i>YIA6</i>	(HH + H)	Mitochondrial NAD ⁺ transporter, involved in the transport of NAD ⁺ into the mitochondria (see also YEA6); member of the mitochondrial carrier subfamily; disputed role as a pyruvate transporter; has putative mouse and human orthologs
YIL028W	[---]	(HH + H)	Dubious open reading frame unlikely to encode a protein, based on available experimental and comparative sequence data
YIL041W	<i>GVP36</i>	(HH + H)	BAR domain-containing protein that localizes to both early and late Golgi vesicles; required for adaptation to varying nutrient concentrations, fluid-phase endocytosis, polarization of the actin cytoskeleton, and vacuole biogenesis
YIL053W	<i>RHR2</i>	(HH + H)	Constitutively expressed isoform of DL-glycerol-3-phosphatase; involved in glycerol biosynthesis, induced in response to both anaerobic and, along with the Hor2p/Gpp2p isoform, osmotic stress
YIL065C	<i>FIS1</i>	(HH + H)	Protein involved in mitochondrial membrane fission and peroxisome abundance; required for localization of Dnm1p and Mdv1p during mitochondrial division; mediates ethanol-induced apoptosis and ethanol-induced mitochondrial fragmentation
YOR043W	<i>WHI2</i>	(HH + H)	Protein required, with binding partner Psr1p, for full activation of the general stress response, possibly through Msn2p dephosphorylation; regulates growth during the diauxic shift; negative regulator of G1 cyclin expression
YPL002C	<i>SNF8</i>	(HH + H)	Component of the ESCRT-II complex, which is involved in ubiquitin-dependent sorting of proteins into the endosome; appears to be functionally related to SNF7; involved in glucose derepression
YLR234W	<i>TOP3</i>	(HH + H)	DNA Topoisomerase III, conserved protein that functions in a complex with Sgs1p and Rmi1p to relax single-stranded negatively-supercoiled DNA preferentially, involved in telomere stability and regulation of mitotic recombination
YLR417W	<i>VPS36</i>	(HH + H)	Component of the ESCRT-II complex; contains the GLUE (GRAM Like Ubiquitin binding in EAP45) domain which is involved in interactions with ESCRT-I and ubiquitin-dependent sorting of proteins into the endosome
YNL171C	[---]	(HH + H)	Dubious open reading frame unlikely to encode a functional protein, based on available experimental and comparative sequence data
YCR084C	<i>TUP1</i>	LL, (LL + L)	General repressor of transcription, forms complex with Cyc8p, involved in the establishment of repressive chromatin structure through interactions with histones H3 and H4, appears to enhance expression of some genes
YEL072W	<i>RMD6</i>	LL	Protein required for sporulation

YJL176C	<i>SWI3</i>	LL, (LL + L)	Subunit of the SWI/SNF chromatin remodeling complex, which regulates transcription by remodeling chromosomes; required for transcription of many genes, including ADH1, ADH2, GAL1, HO, INO1 and SUC2
YOR140W	<i>SFL1</i>	LL, (LL + L)	Transcriptional repressor and activator; involved in repression of flocculation-related genes, and activation of stress responsive genes; negatively regulated by cAMP-dependent protein kinase A subunit Tpk2p
YOR290C	<i>SNF2</i>	LL, (LL + L)	Catalytic subunit of the SWI/SNF chromatin remodeling complex involved in transcriptional regulation; contains DNA-stimulated ATPase activity; functions interdependently in transcriptional activation with Snf5p and Snf6p
YNL059C	<i>ARP5</i>	LL	Nuclear actin-related protein involved in chromatin remodeling, component of chromatin-remodeling enzyme complexes
YLR182W	<i>SWI6</i>	LL, (LL + L)	Transcription cofactor, forms complexes with DNA-binding proteins Swi4p and Mbp1p to regulate transcription at the G1/S transition; involved in meiotic gene expression; localization regulated by phosphorylation; potential Cdc28p substrate
YKL048C	<i>ELM1</i>	LL, (LL+L)	Serine/threonine protein kinase that regulates cellular morphogenesis, septin behavior, and cytokinesis; required for the regulation of other kinases; forms part of the bud neck ring
YLR131C	<i>ACE2</i>	LL, (LL+L)	Transcription factor that activates expression of early G1-specific genes, localizes to daughter cell nuclei after cytokinesis and delays G1 progression in daughters, localization is regulated by phosphorylation; potential Cdc28p substrate
YJR092W	<i>BUD4</i>	(LL+L)	Protein involved in bud-site selection and required for axial budding pattern; localizes with septins to bud neck in mitosis and may constitute an axial landmark for next round of budding; potential Cdc28p substrate
YBL094C	[--]	LL, (LL + L)	Dubious open reading frame unlikely to encode a protein, based on available experimental and comparative sequence data; partially overlaps uncharacterized ORF YBL095W
YDR442W	[--]	LL, (LL+L)	Dubious open reading frame unlikely to encode a functional protein, based on available experimental and comparative sequence data
YHR177W	[--]	LL	Putative protein of unknown function; overexpression causes a cell cycle delay or arrest
YNR068C	[--]	(LL+L)	Putative protein of unknown function

Table 5- 8: A list of the 58 strains identified as significantly enriched in one or more of the sorted fractions, using a baseline of 1/10th the mean and ½ the mean to remove spurious hits with different stringency. The “Sample” column lists the fractions – *HH, H, L, LL, (HH+H)* or *(LL+L)* - in which that particular strain was found to be enriched. The descriptions are quoted directly from the *Saccharomyces* Genome Database.

Classification of Strains by Morphology.

WT			Elongate		
Alias	Sample(s)	Score	Alias	Sample(s)	Score
YDR042C	HH, (HH+H)	[---]	<i>DUN1</i>	HH, (HH+H)	2
<i>RIM8</i>	HH, H, (HH+H)	[---]	<i>DIA4</i>	HH, H, (HH+H)	3
<i>NAS2</i>	HH, H, (HH+H)	[---]	<i>KEL1</i>	HH, H, (HH+H)	3
<i>SEC28</i>	HH, (HH+H)	[---]	<i>GRR1</i>	HH, (HH+H)	4
<i>RCY1</i>	HH, (HH+H)	[---]	<i>CLB2</i>	HH, (HH+H)	3
<i>LDB18</i>	HH, (HH+H)	[---]	<i>RHR2</i>	(HH + H)	2
<i>SNF7</i>	HH, H, (HH+H)	[---]	<i>TOP3</i>	(HH + H)	2
<i>RIM13</i>	HH, (HH+H)	[---]	<i>SNF2</i>	LL, (LL + L)	2
<i>CHS1</i>	HH	[---]	<i>ARP5</i>	LL, (LL + L)	4
<i>SNF1</i>	HH, (HH+H)	[---]	<i>ELM1</i>	LL, (LL + L)	4
<i>GPH1</i>	HH, (HH+H)	[---]	<i>SWI6</i>	LL, (LL + L)	3
<i>STP22</i>	H, (HH+H)	[---]	Football		
<i>RIM8</i>	H, (HH+H)	[---]	<i>CDC50</i>	HH, (HH+H)	2
<i>RIM101</i>	H, (HH+H)	[---]	<i>CYS4</i>	HH, (HH+H)	3
<i>PCL7</i>	H, (HH+H)	[---]	<i>CLB2</i>	HH, (HH+H)	4
<i>CBF1</i>	H, (HH+H)	[---]	<i>GVP36</i>	(HH + H)	3
<i>SAM1</i>	H, (HH+H)	[---]	<i>RHR2</i>	(HH + H)	3
<i>RIM20</i>	H, (HH+H)	[---]	<i>WHI2</i>	(HH + H)	2
<i>MSS51</i>	H	[---]	Clumpy		
<i>ADE4</i>	H, (HH+H)	[---]	<i>SIT4</i>	HH, H, (HH+H)	2
<i>TPS2</i>	(HH + H)	[---]	<i>SWI3</i>	LL, (LL + L)	3
<i>YIA6</i>	(HH + H)	[---]	<i>SFL1</i>	LL, (LL + L)	2
<i>YIL028W</i>	(HH + H)	[---]	<i>ACE2</i>	LL, (LL + L)	3
<i>FIS1</i>	(HH + H)	[---]	Small		
<i>SNF8</i>	(HH + H)	[---]	<i>PEF1</i>	HH, (HH+H)	2
<i>VPS36</i>	(HH + H)	[---]	<i>TOP3</i>	(HH + H)	2
<i>RMD6</i>	LL	[---]	Round		
<i>BUD4</i>	LL, (LL + L)	[---]	<i>TUP1</i>	LL, (LL + L)	3
<i>YBL094C</i>	LL, (LL + L)	[---]	<i>SFL1</i>	LL, (LL + L)	2
<i>YHR177W</i>	LL, (LL + L)	[---]	Large		
<i>YNR068C</i>	(LL+L)	[---]	<i>YDR149C</i>	HH	3

Table 5- 9: Strains identified in the screen categorized according to morphology, as reported by Giaever *et al.*, 2002.

Classification of Strains by Biological Function.

Metabolism and amino acid biosynthesis		Transcription		Protein Modification and Degradation	
Alias	Fraction	Alias	Fraction	Alias	Fraction
CYS4	HH, (HH+H)	SNF1	HH	RIM8	HH, H, (HH+H)
TMT1	H	RIM101	H, (HH+H)	RIM13	HH, (HH+H)
PCL7	H, (HH+H)	CBF1	H, (HH+H)	RIM20	H, (HH+H)
SAM1	H, (HH+H)	TUP1	LL, (LL+L)	NAS2	HH, H, (HH+H)
ADE4	H, (HH+H)	SWI3	LL, (LL+L)	RCY1	HH, (HH+H)
TPS2	(HH+H)	SFL1	LL, (LL+L)	Protein Sorting and Trafficking	
SCS2	(HH+H)	SWI6	LL, (LL+L)	Alias	Fraction
RHR2	(HH+H)	SNF2	LL, (LL+L)	SEC28	HH, (HH+H)
DNA repair and replication		ACE2	LL, (LL+L)	SNF7	HH, H, (HH+H)
Alias	Fraction	ARP5	LL	RIM8	HH, H, (HH+H)
DUN1	HH, (HH+H)	Cell Cycle		STP22	H
TOP3	(HH+H)	Alias	Fraction	SNF8	(HH+H)
Stress response (primarily osmotic)		CLB2	HH, (HH+H)	VPS36	(HH+H)
Alias	Fraction	SIT4	HH, H, (HH+H)		
SNF1	HH	DUN1	HH, (HH+H)		
GPH1	HH	ELM1	LL, (LL+L)		
RHR2	(HH+H)	Mitochondria			
WHI2	(HH+H)	Alias	Fraction		
TPS2	(HH+H)	DIA4	HH, H, (HH+H)		
Cell polarity and morphogenesis		MSS51	H		
Alias	Fraction	YIA6	(HH+H)		
CDC50	HH, (HH+H)	FIS1	(HH+H)		
PEF1	HH, (HH+H)	Cell wall biosynthesis			
KEL1	HH, H, (HH+H)	Alias	Fraction		
GRR1	HH, (HH+H)	SIT4	HH, H, (HH+H)		
GVP36	(HH+H)	CHS1	HH		
BUD4	(LL+L)	RIM101	H, (HH+H)		

Table 5- 10: Strains identified in the screen categorized according to general biological functions, determined based upon functional descriptions listed in the *Saccharomyces* Genome Database.

Chapter 6: Contributions and Future Directions

The underlying objective of this thesis has been the development of a new technology with the performance capabilities necessary to collect genome-wide biological data. The preceding four chapters have been organized to present an approximate chronology for the development of isodielectric separation, from the fundamental concept to its application in a genetic screen. The intent of this concluding chapter is to briefly summarize the contributions that have arisen from this work, and to discuss possible future directions in which IDS could be taken.

Contributions

Design rules for isodielectric separation. One important outcome of this work has been the development of guidelines for designing IDS devices (Chapter 2). This was made possible through comprehensive models of the electric fields, mass transport, and fluid dynamics throughout the device, including the coupling between these different physical domains. Although a single basic geometry is used throughout this thesis, it should be possible for anyone seeking to use IDS for an alternate application to follow these design rules to converge on a device design suitable for the application of interest. In subsequent sections of this chapter, we discuss scenarios in which using IDS to sort bacteria or mammalian cells could be interesting; the design rules in Chapter 2 could be useful for anyone pursuing some of these applications. In addition to delineating design rules for a specific implementation of IDS, we also present some general ideas that could be used in alternate implementations. Accordingly, the work described in this thesis could provide a starting point for the dissemination of IDS to a broader community beyond our lab.

Demonstration of important figures of merit. In setting out to develop a screening platform, we decided that necessary features included *high specificity*, *high resolution*, and *high throughput*. These three requirements shaped our implementation of the device. To assure high specificity, we adopted the principles of equilibrium gradient separations; this helped us to largely overcome the volumetric dependence of the dielectrophoretic force to implement a separation that is insensitive to variations in cell size. Implementing IDS as a gradient method also enabled high resolution, since cells could be separated in a continuum of electrical conductivities. Finally, to maximize the throughput of the device, we sought to make it operate under continuous-flow and high particle concentrations. After creating the first IDS device, our immediate goal was to demonstrate each of these claims, work that is presented in Chapter 2. These early demonstrations validated the further development of IDS into an analytical technique and, eventually, a platform for genetic screening.

Combining analytical and preparative separations using IDS. By extending the models used to *design* devices and applying them to *predict* device performance, we were able to develop IDS into an analytical separation method (Chapter 3). This is of particular importance due to the relative dearth of techniques capable of directly quantifying the intrinsic properties of cells at both single-cell and population-wide levels. Although impedance spectroscopy offers higher spectral resolution than is possible with IDS, it is less well-suited for particle separation, and is not easily amenable to characterizing electrical properties as a function of medium composition. The validation of IDS as a tool for analysis suggests its potential value as a high-content screening platform, capable of quantifying the electrical properties of cells and their distribution across populations. The ability to couple analysis of electrical properties directly to separation further enables multidimensional characterization; separating cells according to electrical properties and then measuring (for example) the gene expression of different collected fractions is at the center of phenotypic mapping, and is only possible using a platform capable of both analytical and preparative separations. We will discuss possible ways to take advantage of this capability in subsequent sections of this chapter.

Tools for understanding particle interactions in microfluidic devices. A critical component of achieving the throughput necessary for a genetic screen is an understanding of how high concentrations of

cells can alter a device's performance. To address this question, we developed numerical tools to study the hydrodynamic and electrostatic interactions between particles (both spherical and non-spherical) in simple microfluidic devices (Chapter 4). After experimentally validating these tools, we used them to study how varying the operating conditions of a separation can significantly improve its performance. Additionally, we supplemented this numerical approach with an analytical model capturing how hydrodynamic coupling between particles leads to a form of cooperativity. Although this work was largely motivated by the specific example of IDS, the simulations we developed can be easily generalized to other separation methods as well. To illustrate this, we performed a case study comparing the influence of particle interactions in DEP-FFF and IDS. The simulation tools we have developed as well as the insights we have obtained from them could be useful in the development and optimization of new high-throughput microfluidic devices.

Identification of yeast strains exhibiting distinct electrical phenotypes. Through a pilot screen comprised of 82 strains from the *S. cerevisiae* deletion and DAmP libraries, we have identified a number of strains exhibiting distinct electrical phenotypes. In many cases, the changes in electrical properties could be qualitatively traced back to differences in cell shape; elongated cells (in particular, the *grr1Δ* strain) exhibit higher effective conductivities, due to their lower depolarization factors when aligned to the external electric field. In our preliminary survey, we also identified a strain exhibiting distinct electrical properties in the absence of any morphological differences with respect to wildtype. These cells, the *kre9* DAmP strain, provide an interesting case for follow-up experiments, as well as suggesting the possible existence of other interesting discoveries within the DAmP library. In addition to demonstrating the ability of single-gene alterations to substantially affect the electrical properties of a cell, the strains identified in this pilot screen provide valuable positive controls for the genome-wide characterization of electrical properties.

Electrogenomic profiling with IDS. Although a fully validated electrogenomic profile of the yeast deletion collection is still in progress, the work presented in this thesis demonstrates the ability to construct such a profile using IDS as a central platform. In particular, by performing separations of the complete library, corroborating the results of these separations with those of a pilot screen, and sequencing DNA barcodes to quantify the enrichment or depletion of deletion strains at different conductivities, we have demonstrated the potential to characterize electrical properties on a genome-wide scale. Our results have identified ~50 strains that appear to exhibit distinct electrical properties, and comparison of these strains with datasets describing genetic interactions has enabled us to identify possible pathways (RIM101 and dynein-dynactin) that play an important role in determining a cell's electrical phenotype. The scientific results made possible by this work, as well as the technical capabilities demonstrated, suggest the potential of microfluidic technologies to address biological questions at the level of an organism's entire genome.

Future Directions

The following sections outline some specific directions that build off of the contributions of this thesis. These include technological and conceptual developments, in addition to new applications to explore. Although pursuing many of these directions may be significantly involving, they present feasible (if large) extensions of capabilities that we have previously demonstrated.

More diverse particle interactions. The numerical simulations we use to study the implications of particle interactions can be generalized to a larger number of forces than we have considered. For example, the inclusion of Coulombic, magnetic, and thermal forces would be straightforward, and could potentially lead to more unexpected phenomena relevant to devices for manipulating concentrated suspensions. Magnetically-driven microfluidic separations in particular have gained prominence recently^{141,142}, and could be analyzed by this approach. From a more exploratory viewpoint, it may also be interesting to study interactions of polarizable, ferromagnetic particles in the presence of superimposed

electrostatic and magnetic fields; combining the anisotropic interactions that each of these fields give rise to could lead to substantially more intricate behaviors than either field induces alone.

Besides exploring the influence of other types of interactions, there are questions beyond those directly relevant to separations that might be addressed focusing exclusively on electrostatic interactions. For example, all of the simulations presented in Chapter 4 involved particles with polarizabilities of $K \leq 0$; when particles have positive or *mixed* polarizabilities, different behaviors arise. Figure 6- 1a gives one example. At 1 MHz (where $K < 0$ for all particles) and 100 kHz (where $K > 0$), sheets of particles in a

hexagonal lattice and linear chains form, respectively. These structures are stable, and do not change over time. In contrast, at frequencies for which the magnitude of the polarizability is low and its sign varies (as occurs at ~ 400 kHz in the present case), the lattice becomes irregular and filled with voids that fluctuate and do not converge to any static equilibrium for as long as we observe them. Additionally, at these intermediate frequencies chains of particles consistently align at an angle (~ 30 - 45°) with respect to the applied field (not shown). The size of these particles ($2\mu\text{m}$) and the operating conditions used suggest that these phenomena are neither primarily Brownian nor hydrodynamic in origin, and may be an example of dynamical frustration arising from the difficulty in finding an energetically satisfactory arrangement of weakly polarized particles of opposite affinity. We have performed preliminary simulations in an effort to capture this behavior with some success (Figure 6- 1a, bottom); more work along these lines could provide an experimentally useful platform for studying dynamical frustration.

A related concept that we have briefly explored is the behavior of particles constrained to a chain with polarizabilities of random sign (Figure 6- 1b). When an electric field is applied, the chain is observed to fold (to some extent) in a manner dependent on the sequence of polarizabilities in the chain. This could be extended by introducing particles of different sizes into the chain to increase the diversity of interactions between the subunits. Experimentally constructing a colloidal chain of this nature is not unreasonable¹⁴³, and could provide an experimentally tractable analog to protein folding. Although more difficult to construct, this approach could provide a better physical analogy than other (macroscopic) implementations of a similar idea¹⁴⁴.

“Carrier” Particles for Improved Separation. One possible means of improving separation performance that exploits particle interactions could be to introduce “carrier” particles to the suspension prior to sorting. Intentionally introducing background particles to a sample for separation can be thought of as a way to adjust the separation environment without needing to alter the device geometry. This could

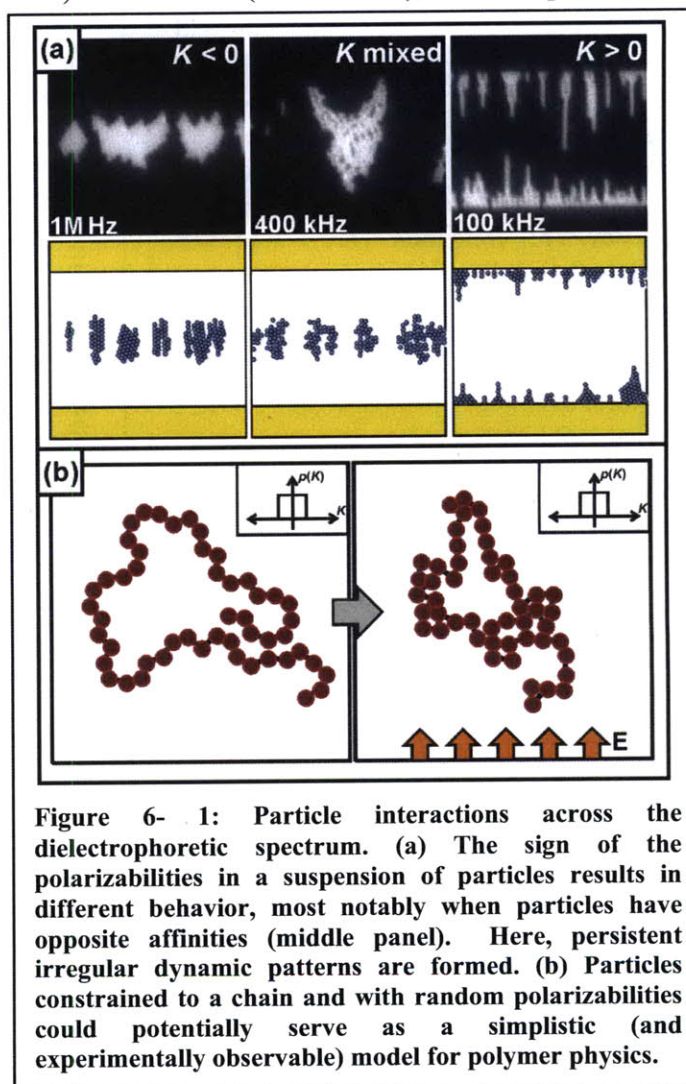
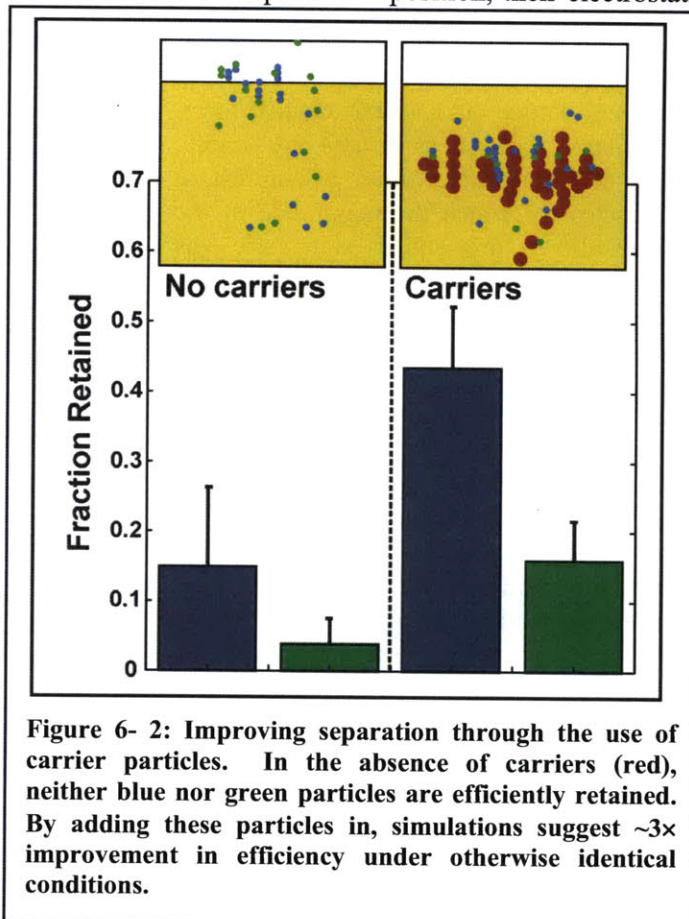


Figure 6- 1: Particle interactions across the dielectrophoretic spectrum. (a) The sign of the polarizabilities in a suspension of particles results in different behavior, most notably when particles have opposite affinities (middle panel). Here, persistent irregular dynamic patterns are formed. (b) Particles constrained to a chain and with random polarizabilities could potentially serve as a simplistic (and experimentally observable) model for polymer physics.

potentially prove useful in bacterial separations. Doping a suspension of cells to be sorted with an appreciable concentration of $\sim 1\text{-}2\ \mu\text{m}$ polystyrene beads can effectively enhance the electric field gradients involved in the separation (through electrostatic interactions), while at the same time reducing the drag on the difficult to retain bacteria (through hydrodynamic coupling). Because IDS operates by varying the polarizability of particles, as the bacteria reach their equilibrium position, their electrostatic coupling to the carrier particles would be suppressed, allowing them to dissociate cleanly. Importantly, the presence of any contaminating beads in the collected samples would not prevent cells from being plated and cultured. Figure 6- 2 shows simulations of a separation with and without carrier particles. In these simulations, both the purity of the eluted samples and the efficiency of retention are improved significantly by the addition of the carriers. Extending these simulations and validating them experimentally could elucidate the conditions in which this approach to separation would be advantageous.

Screening Applications for Isodielectric Separation. Our goal of screening the *S. cerevisiae* deletion collection has been motivated largely by exploration – obtaining a genotype to electrical phenotype map – and the desire to test the feasibility of performing a genetic screen with IDS. Having shown the feasibility of this goal, a number of more directed screening applications could be pursued in the future. In this section, I will outline some screening applications for which IDS may be well suited.



Improving the sensitivity and content of traditional functional assays. The ability to perform genome-wide characterizations of electrical phenotype could serve to complement more traditional assays (such as those based on competitive growth) by providing an additional perspective from which to consider a cell's phenotype. The value of this perspective follows directly from the reasoning that not all cells that are *functionally* indistinguishable are indistinguishable by other metrics. Accordingly, IDS offers a platform to screen for (and quantify the extent of) physiological differences that might be transparent during functional profiling. A potential benefit afforded by quantifying electrical properties in particular is the ability to identify in some cases the cell compartment which has been affected. To take one possible example, using IDS to sort cells under different ranges of frequencies and conductivities could identify cells with altered membranes but wildtype cytoplasmic conductivity. Although this does not compete with the specificity afforded by biochemical methods, it offers a potential advance over characterizing growth rate alone.

Screening Non-Barcoded Libraries. Barcoded libraries in yeast remain largely the exception rather than the rule. Extending the applicability of IDS to libraries without DNA barcodes would enable, for example, the characterization of libraries of strains with depressed expression of essential genes⁴, or systematic overexpression libraries¹³¹. Adapting IDS to these applications would likely involve

substantially re-engineering the device without altering its general principle of operation. Specifically, the implementation of IDS developed in this thesis is largely motivated by high throughput; this enables highly diverse mixtures of cells to be sorted with statistically robust numbers of each strain present in the collected fractions. If large numbers of pairwise comparisons between strains are to be performed, however, parallelization of many lower-throughput devices takes precedence over designing a single, large, high-throughput device. One possible solution is to design an array of devices to interface with a 96- or 384-well plate and its accompanying robotics. This is facilitated by the fact that relaxing the throughput requirement allows the footprint of the device to be reduced considerably; our design rules (e.g. equation (2- 22)) suggest that reducing the flowrate, Q_0 , by an order of magnitude allows the channel length (and width) to be decreased proportionally. The narrower channel would relax the residence time needed to establish a sufficiently smooth conductivity gradient, further reducing a device's overall footprint. Fabricated out of glass or gas-impermeable plastic, an array of these devices connected to a common outlet (with appropriate matching of fluidic resistances) could be driven in parallel by applying vacuum at the shared outlet. Interfacing an array of these devices with scanning optics to monitor spatial distributions of fluorescently labeled cells would allow for the rapid characterization of large libraries with high resolution, in terms of both genetic characterization and electrical characterization.

Large Scale Analytical Separations. In our efforts to develop IDS as an analytical technique (Chapter 3), we relied exclusively on fluorescence microscopy to determine the distributions of cells across conductivity. While this approach has the advantage of offering single-cell resolution, it is limited by the number of samples that one is able to multiplex (typically two or three, as determined by the spectra of the fluorophores and filter set used). One way to address this would be through the implementation of a device array, as described in the previous section, allowing for many pairwise comparisons to be performed in parallel. A second alternative is to determine strain distributions as presented in Chapter 5, by collecting cells from different outlets and quantifying the abundance of particular strains within each collected fraction. Depending on the specific goal, this quantification can be performed on a relatively small number of strains via quantitative PCR, or on entire libraries, using sequencing or microarray technology. Characterizing cells in this way, in addition to being highly parallelized, takes advantage of the ability of IDS to operate as a true label-free technique.

The tradeoff inherent in quantifying strain abundance from collected fractions is the loss of resolution compared to fluorescence microscopy. Specifically, the discretization of a strain's distribution into some number of outlets risks losing valuable information if the number of those outlets is not sufficiently high. Conversely, increasing the number of outlets proportionally *decreases* the number of cells collected in each outlet, leading to less robust sampling of the strains. A simple scaling argument can be used to determine an appropriate number of outlets. In Chapter 5 (equation (5- 5)), we found that sampling each of M distinct strains at least K times requires collecting $N \approx M[K + \sqrt{2K \log M}] \approx MK$ cells in total. If we hold N fixed, the sampling redundancy for a device with Q outlets is $K = N/MQ$, from which the relative sampling noise is $K^{-1/2}$. Balancing this against the approximate quantization error ($\approx 1/Q\Delta$, where $\Delta < 1$ is the fraction of the channel width spanned by the cell distribution) gives $Q \sim [N/M\Delta^2]^{1/3}$. Typical values for N ($\sim 10^6$ - 10^7), M (~ 5000), and Δ (~ 0.3) suggest that Q could be as large as ~ 20 before the error introduced by strain sampling matched the quantization error in reconstructing the distribution from the Q collected fractions. The four-outlet design used in this thesis is better suited for applications in which cells are more uniformly distributed across the width of the device ($\Delta \sim 1$). Accordingly, an easy way to improve the quality of data obtained by quantifying collected fractions would be to increase by several fold the number of outlets.

If temporal fluctuations in the isodielectric points of cells are of larger amplitude than the width of the outlets, increasing the number of these outlets is of little benefit. Accordingly, a complementary effort to increase the sampling resolution of the device is to implement a control system to reduce the temporal fluctuations that arise from gradual changes in the conductivity, flowrate, or cell concentration. Figure 6-

3 illustrates a simple feedback loop, in which a microscope and camera act as a sensor to determine the distribution of cells (from brightfield images) so that the mean ($\langle x \rangle$) can be compared to a reference ($= x_0$), and the error used to adjust the frequency of a function generator (the controller) in an attempt to hold the system output at the reference at all times. The simple differential control scheme proposed here is used only for illustrative purposes, and the design of a better feedback system would need to take into consideration the transfer function of the IDS device itself, a function of the cells being sorted (through their dielectric spectra) as well as the device geometry and operating conditions. Although we have not pursued this, doing so should be conceptually straightforward. The implementation and automation of this type of system could have considerable benefits on the stability and reliability of the device over long separations, and could enable, for example, overnight operation.

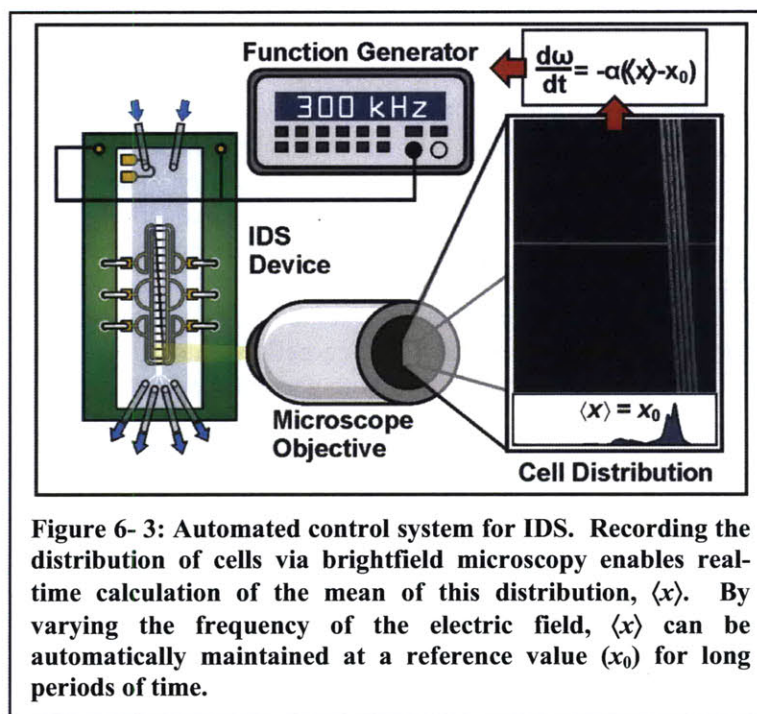


Figure 6- 3: Automated control system for IDS. Recording the distribution of cells via brightfield microscopy enables real-time calculation of the mean of this distribution, $\langle x \rangle$. By varying the frequency of the electric field, $\langle x \rangle$ can be automatically maintained at a reference value (x_0) for long periods of time.

Screening for the enhanced yield of metabolic products. The systematic nature of the DAmP and deletion collections that make them desirable for the type of phenotypic mapping explored in this thesis is less advantageous for other applications. A prominent example is metabolic engineering, where complex biochemical pathways are perturbed in an effort to achieve strain improvement¹⁴⁵. This improvement could consist of increased tolerance to specific environmental conditions, increased production of a particular metabolite, or a combination of multiple desirable phenotypes. In order to elicit this type of strain improvement, knocking down or over-expressing a single gene is seldom sufficient; instead, combinatorial changes in gene expression are generally necessary.

One recently developed approach to generating such combinatorial changes is global transcription machinery engineering (gTME)¹⁴⁶. Here, rather than altering many genes in a systematic way, one or a few genes involved in the regulation of gene expression are subjected to random mutagenesis (through error-prone PCR) to generate strains with varying expression profiles. For example, altering the TATA-binding protein (*SPT15*) in *S. cerevisiae* is known to affect promoter function and specificity, so that libraries of cells with subtle mutations in the gene *spt15* have been created and screened (via selection) for increased ethanol tolerance⁷. The success of this approach and others like it derives from the expanded phenotypic space they allow researchers to explore.

While screening by selection is ideal for random combinatorial libraries in which the desired phenotype involves increased tolerance for an environmental condition, other phenotypes are less amenable to this type of assay, and require cell sorting. This is often the case when increased production of a metabolite or cytokine is sought after. An additional challenge is presented when the biomolecule of interest remains sequestered inside the cell; this has led to the development of assays to fluorescently

label the desired product, so that high-producing cells can be isolated through flow cytometry^{147,148}. However, like methods in which the metabolite is extracted from cells and analyzed chromatographically¹⁴⁹, the process of labeling is often destructive, requiring that cells be fixed and permeabilized. As a non-destructive, label-free separation method capable of probing the internal properties of a cell, IDS could greatly facilitate screens in which the metabolite results in an electrically distinct phenotype. For example, substantial accumulation of biopolymer in a cell's cytoplasm could decrease its effective conductivity; screening a library of cells for low conductivity mutants and plating these cells to obtain clonal populations could identify high-producing strains and significantly reduce the size of the mutant pool. If needed, mutants from this smaller library could be screened by more labor-intensive techniques that offer higher specificity than IDS (e.g. extraction followed by HPLC).

Although efforts to improve metabolite production have been dominated by prokaryotic systems (especially *E. coli*), there has been some work with *S. cerevisiae* demonstrating biopolymer yields comparable to bacterial strains¹⁵⁰. Nonetheless, for IDS to contribute appreciably in screening for metabolite production, an implementation ideally suited for working with prokaryotic organisms is needed. Achieving this is primarily a matter of engineering development, and should be possible with no fundamental changes to the principle of operation explored in this thesis; the analysis in Chapter 2 (for example, Figure 2- 3) could provide useful guidelines towards this end.

Gene Expression Profiling Using IDS. Beyond metabolic engineering, a consistent theme in biotechnology research is the pursuit of convenient markers of cell state. The usefulness of these markers derives from their ability to serve as a relatively small basis set on which the enormous state vector representing a cell's gene expression can be projected. The use of biomarkers has been invaluable in identifying cancer cells¹⁵¹, monitoring stem cells for differentiation or pluripotency¹⁵², and more recently, in discriminating between true induced pluripotent stem cells and those that have only been partially reprogrammed¹⁵³. In each of these examples, the primary challenge is to identify a minimal set of criteria by which *phenotypically heterogeneous* cells can be distinguished within a *genetically homogeneous* background.

One possible new application of IDS could be to search for “electrical” biomarkers; gene expression profiles within a heterogeneous population of cells that can be efficiently represented by those cell's electrical properties under a given set of conditions. The conditions that give rise to heterogeneity are enumerable, and can be categorized as “intrinsic” (i.e. arising spontaneously) or “extrinsic” (i.e. arising through differences in the cell's external environment); in theory, IDS could be applied to any population in which the cells phenotypically diversify, providing a new means of characterizing this diversity and how it evolves across a population over time. Determining groups of genes whose expression levels correlates with higher or lower effective conductivity could potentially have two uses. First, the altered electrical phenotype could serve as a handle for isolating cells with these particular patterns of gene expression, enriching them from the background to facilitate further study. Second, the electrical properties of cells shown to correlate with a particular gene expression state could serve as a proxy for this state, circumventing more involved or costly readout (microarrays or sequencing). This latter concept could be applied in a manner similar to current research characterizing the evolution of cell state over time using flow cytometry¹⁵⁴; collecting a fraction of cells from a narrow range of conductivities and resorting them at a later time could reveal if the electrical phenotype of a population persists over generations, or if it converges to a stationary distribution independent of the distribution of states across the population at an earlier time.

Correlating global gene expression with electrical phenotype would complement studies on libraries of genetically distinct knockout or knockdown strains (such as the one discussed in this thesis). This research direction could have the additional benefit of fitting in well with other projects in our lab, such as those investigating the fate of mouse embryonic stem cells (mESCs) in different growth environments. Using isoelectric separation to sort, characterize, and compare populations of mESCs grown under microfluidic perfusion versus in a static petri dish¹⁵⁵ could provide new avenues for studying the

differences between these populations, as well as the heterogeneity within them. Although projects such as this are highly exploratory, the range of questions to which IDS can be applied is sufficiently large - and the genetic basis of electrical properties sufficiently unknown - that such exploration could prove fruitful.

Bibliography

1. Huang, Y., Hozel, R., Pethig, R. & Wang, X. B. Differences in the AC electrodynamics of viable and non-viable yeast cells determined through combined dielectrophoresis and electrorotation studies. *Phys. Med. Biol.* **37**, 1499-1517 (1992).
2. Abraham, V. C., Taylor, D. L. & Haskins, J. R. High content screening applied to large-scale cell biology. *Trends Biotechnol* **22**, 15-22 (2004).
3. Giaever, G. et al. Functional profiling of the *Saccharomyces cerevisiae* genome. **418**, 387-391 (2002).
4. Breslow, D. K. et al. A comprehensive strategy enabling high-resolution function analysis of the yeast genome. *Nature Methods* **5**, 711-718 (2008).
5. Berns, K. et al. A large-scale RNAi screen in human cells identifies new components of the p53 pathway. *Nature* **428**, 431-437 (2004).
6. Simon, R., Priefer, U. & Puhler, A. A broad host range mobilization system for in vivo genetic engineering: transposon mutagenesis in gram negative bacteria. *Nature Biotechnology* **1**, 784-791 (1983).
7. Alper, H., Moxley, J., Nevoigt, E., Fink, G. R. & Stephanopoulos, G. Engineering yeast transcription machinery for improved ethanol tolerance and production. *Science* **314**, 1565-1568 (2006).
8. Krutzik, P. O. & Nolan, G. P. Fluorescent cell barcoding in flow cytometry allows high-throughput drug screening and signalling. *Nature Methods* **3**, 361-368 (2006).
9. Miltenyi, S., Muller, W., Weichel, W. & Radbruch, A. High gradient magnetic cell separation with MACS. *Cytometry* **11**, 231 (1990).
10. Huang, L. R., Cox, E. C., Austin, R. H. & Sturm, J. C. Continuous particle separation through deterministic lateral displacement. *Science* **304**, 987-990 (2004).
11. Marcos, Fu, H. C., Powers, T. R. & Stocker, R. Separation of Microscale Chiral Objects by Shear Flow. *Physical Review Letters* **102**, 158103 [4 pages] (2009).
12. Davis, J. A. et al. Deterministic hydrodynamics: Taking blood apart. *Proc Natl Acad Sci U S A* **103**, 14779-14784 (2006).
13. Brakke, M. K. Density-gradient centrifugation. *Methods in Virology* **2**, 93-118 (1967).
14. Laurell, T., Petersson, F. & Nilsson, A. Chip integrated strategies for acoustic separation and manipulation of cells and particles. *Chemical Society Reviews* **36**, 492-506 (2007).
15. Golovanov, M. V. in *Cell Electrophoresis* (ed. Bauer, J.) 181-196 (CRC Press, Boca Raton, FL, 1994).
16. Lee, R. S., Arnold, W. M. & Pethig, R. in *2004 Annual Report Conference on Electrical Insulation and Dielectric Phenomena* 352-355 (2004).
17. Markx, G. H., Dyda, P. A. & Pethig, R. Dielectrophoretic separation of bacteria using a conductivity gradient. *Journal of Biotechnology* **51**, 175-180 (1996).
18. O'Farrell, P. H. Separation Techniques Based on the Opposition of 2 Counteracting Forces to Produce a Dynamic Equilibrium. *Science* **227**, 1586-1589 (1985).
19. Evans, L. L. & Burns, M. A. Solute Focusing Techniques for Bioseparations. *Nature Biotechnology* **13**, 46-52 (1995).
20. Righetti, P. G. *Isoelectric focusing: theory, methodology and applications* (Elsevier Biomedical Press, New York, 1983).
21. Giddings, J. C. *Unified Separation Science* (John Wiley & Sons, Inc., New York, 1991).
22. Pohl, H. A. & Crane, J. S. Dielectrophoresis of cells. *Biophysical Journal* **11**, 711-727 (1971).
23. Jones, T. B. *Electromechanics of Particles* (Cambridge University Press, New York, 1995).
24. Gawad, S., Schild, L. & Renaud, P. Micromachined impedance spectroscopy flow cytometer for cell analysis and particle sizing. *Lab on a Chip* **1**, 76-82 (2001).

25. Sun, T., Holmes, D., Gawad, S., Green, N. G. & Morgan, H. High speed multi-frequency impedance analysis of single particles in a microfluidic cytometer using maximum length sequences. *Lab on a Chip* **7**, 1034-1040 (2007).
26. Asami, K. & Yonezawa, T. Dielectric Behavior of wild-type yeast and vacuole-deficient mutant over a frequency range of 10 kHz to 10 GHz. *Biophysical Journal* **71**, 2192 (1996).
27. Holzel, R. Electrorotation of single yeast cells at frequencies between 100 Hz and 1.6 GHz. *Biophys. J.* **73**, 1103-1109 (1997).
28. Weiss, T. F. *Cellular Biophysics Volume 2* (The MIT Press, Cambridge, MA, 1996).
29. Flanagan, L. A. et al. Unique Dielectric Properties Distinguish Stem Cells and Their Differentiated Progeny. *Stem Cells* **26**, 656-665 (2008).
30. Becker, F. F. et al. Separation of human breast cancer cells from blood by differential dielectric affinity. *Proc Natl Acad Sci U S A* **92**, 860-864 (1995).
31. Castellarnau, M., Errachid, A., Madrid, C., Juarez, A. & Samitier, J. Dielectrophoresis as a Tool to Characterize and Differentiate Isogenic Mutants of Escherichia coli. *Biophysical Journal* **91**, 3937-3945 (2006).
32. Hu, X. et al. Marker-specific sorting of rare cells using dielectrophoresis. *Proc Natl Acad Sci U S A* **102**, 15757-15761 (2005).
33. Hawkins, B. G., Smith, A. E., Syed, Y. A. & Kirby, B. J. Continuous-Flow Particle Separation by 3D Insulative Dielectrophoresis Using Coherently Shaped, dc-Biased, ac Electric Fields. *Analytical Chemistry*, Published Online September, 2007. DOI: 10.1021/ac0707277 (2007).
34. Huang, Y., Wang, X.-B., Becker, F. F. & Gascoyne, P. R. C. Introducing dielectrophoresis as a new force field for field-flow fractionation. *Biophysical Journal* **73**, 1118-29 (1997).
35. Gascoyne, P. R. C., Wang, X. B. & Vykoukal, J. in *Solid-State Sensor and Actuator Workshop* 37-38 (Transducers Research Foundation, Inc., Hilton Head Island, South Carolina, 1998).
36. Vahey, M. D. in *Electrical Engineering and Computer Science* 103 (Massachusetts Institute of Technology, Cambridge, 2006).
37. Vahey, M. D. & Voldman, J. An Equilibrium Method for Continuous-Flow Cell Sorting Using Dielectrophoresis. *Analytical Chemistry* **80**, 3135-3143 (2008).
38. Desai, S. P., Vahey, M. D. & Voldman, J. Electrically Addressable Vesicles: Tools for Dielectrophoresis Metrology. *Langmuir* **25**, 3867-3875 (2009).
39. Demierre, N. et al. Characterization and optimization of liquid electrodes for lateral dielectrophoresis. *Lab on a Chip* **7**, 355-365 (2007).
40. Rosenthal, A., Taff, B. M. & Voldman, J. Quantitative modeling of dielectrophoretic traps. *Lab on a Chip* **6**, 508-515 (2006).
41. Oddy, M. H., Santiago, J. G. & Mikkelsen, J. C. Electrokinetic instability micromixing. *Analytical Chemistry* **73**, 5822-5832 (2001).
42. Ajdari, A. Electrokinetic "ratchet" pumps for microfluidics. *Applied Physics A: Materials Science and Processing* **75**, 271-274 (2002).
43. Pethig, R. Dielectrophoretic separation of bacteria using a conductivity gradient. *Journal of Biotechnology* **51**, 175-180 (1996).
44. Bazant, M. Z., Squires, T. M. Induced-Charge Electrokinetic Phenomena: Theory and Microfluidic Applications. *Phys. Rev. Lett.* **92**, 1-4 (2004).
45. Huang, J. P. Dielectrophoresis of charged colloidal suspensions. *Physical Review E* **67**, (7 pages) (2003).
46. Maier, H. Electrorotation of Colloidal Particles and Cells Depends on Surface Charge. *Biophys. J.* **73**, 1617-1626 (1997).
47. Arnold, W. M. Surface Conductance and Other Properties of Latex Particles Measured by Electrorotation. *Journal of Physical Chemistry* **91**, 5093 - 5098 (1987).
48. Khusid, B., Acrivos, A. Effects of interparticle electric interactions on dielectrophoresis in colloidal suspensions. *Physical Review E* **54**, 5428 - 5435 (1996).

49. Angelova, M. I. & Dimitrov, D. S. Liposome electroformation. *Faraday Discuss. Chem. Soc.* **81**, 303-311 (1986).
50. Stachowiak, J. C. et al. Unilamellar vesicle formation and encapsulation by microfluidic jetting. *Proc Natl Acad Sci U S A* **105**, 4697-4702 (2008).
51. Tan, Y.-C., Hettiarachchi, K., Siu, M., Pan, Y.-R. & Lee, A. P. Controlled microfluidic encapsulation of cells, proteins, and microbeads in lipid vesicles. *Journal of the American Chemical Society* **128**, 5656-5658 (2006).
52. Ismagilov, R. F., Ng, J. M. K., Kenis, P. J. A. & Whitesides, G. M. Microfluidic Arrays of Fluid-Fluid Diffusional Contacts as Detection Elements and Combinatorial Tools. *Analytical Chemistry* **73**, 5207-5213 (2001).
53. Nardi, J., Bruinsma, R. & Sackmann, E. Vesicles as Osmotic Motors. *Physical Review Letters* **82**, 5168-5171 (1999).
54. Braschler, T., Demierre, N., Nascimento, E. M., Oliva, A. G. & Renaud, P. Continuous separation of cells by balanced dielectrophoretic forces at multiple frequencies. *Lab on a Chip* **8**, 280-286 (2008).
55. Vahey, M. D. & Voldman, J. Characterization of diverse cell and particle types using iso-dielectric separation. *Analytical Chemistry* **81**, 2446-2455 (2009).
56. Holzel, R. Electrorotation of Single Yeast Cells at Frequencies Between 100 Hz and 1.6 GHz. *Biophysical Journal* **73**, 1103-1109 (1997).
57. Gascoyne, P. R. C. & Vykoukal, J. Particle separation by dielectrophoresis. *Electrophoresis* **23**, 1973-1983 (2002).
58. Voldman, J. Electrical forces for microscale cell manipulation. *Annual Review of Biomedical Engineering* **8**, 425-454 (2006).
59. Vahey, M. & Voldman, J. An Equilibrium Method for Continuous-Flow Cell Sorting Using Dielectrophoresis. *Analytical Chemistry* DOI: 10.1021/ac7020568 (2008).
60. Asami, K., Gheorghiu, E. & Yonezawa, T. Real-Time Monitoring of Yeast Cell Division by Dielectric Spectroscopy. *Biophys. J.* **76**, 3345-3348 (1999).
61. Staben, M. E., Zinchenko, A. Z. & Davis, R. H. Motion of a particle between two parallel plane walls in low-Reynolds-number Poiseuille flow. *Physics of Fluids* **15**, 1711-1733 (2003).
62. Rosenthal, A. D., Voldman, J. Quantitative modeling of dielectrophoretic traps. *Lab on a Chip* **6**, 508-515 (2006).
63. Santiago, J. G. Instability of electrokinetic microchannel flows with conductivity gradients. *Physics of Fluids* **16**, 1922-35 (2004).
64. Hoburg, J. F. & Melcher, J. R. Electrohydrodynamic Mixing and Instability Induced by Colinear Fields and Conductivity Gradients. *Physics of Fluids* **20**, 903-911 (1977).
65. Green, N. G., Ramos, A. & Morgan, H. AC electrokinetics: a survey of sub-micrometre particle dynamics. *Journal of Physics D-Applied Physics* **33**, 632-641 (2000).
66. Batchelor, G. K. Brownian diffusion of particles with hydrodynamic interaction. *Journal of Fluid Mechanics* **74**, 1-29 (1976).
67. Desai, S. P., Taff, B. M. & Voldman, J. A Photopatternable Silicone for Biological Applications. *Langmuir*, Published online December 15, 2007; DOI: 10.1021/la702827v (2007).
68. Nam, J.-M., Thaxton, C. S. & Mirkin, C. A. Nanoparticle-Based Bio-Bar Codes for the Ultrasensitive Detection of Proteins. *Science* **301**, 1884-1886 (2003).
69. Wang, Y.-C. & Han, J. Pre-binding dynamic range and sensitivity enhancement for immunosensors using nanofluidic preconcentrator. *Lab on a Chip* **8**, 392-394 (2008).
70. Wang, X.-B., Vykoukal, J., Becker, F. F. & Gascoyne, P. R. C. Separation of polystyrene microbeads using dielectrophoretic/gravitational field-flow-fractionation. *Biophysical Journal* **74**, 2689-701 (1998).
71. Voldman, J., Braff, R. A., Toner, M., Gray, M. L. & Schmidt, M. A. Holding Forces of Single-Particle Dielectrophoretic Traps. *Biophys. J.* **80**, 531-541 (2001).

72. Jimenez, M. L., Arroyo, F. J., Carrique, F. & Delgado, A. V. Surface conductivity of colloidal particles: Experimental assessment of its contributions. *Journal of Colloid and Interface Science* **316**, 836-843 (2007).
73. Green, N. G., Morgan, H. Dielectrophoresis of Submicrometer Latex Spheres. 1. Experimental Results. *Journal of Physical Chemistry B* **103**, 41-50 (1999).
74. Green, N. G. & Morgan, H. Dielectrophoretic separation of nano-particles. *Journal of Physics D (Applied Physics)* **30**, L41-L44 (1997).
75. Mangelsdorf, C. S. & White, L. R. Effects of stern-layer conductance on electrokinetic transport properties of colloidal particles. *Journal of the Chemical Society, Faraday Transactions* **86**, 2859-2870 (1990).
76. Hughes, M. P., Morgan, H. & Flynn, M. F. The Dielectrophoretic Behavior of Submicron Latex Spheres: Influence of Surface Conductance. *Journal of Colloid and Interface Science* **220**, 454-457 (1999).
77. Asami, K. & Yonezawa, T. Dielectric Behavior of Wild-Type Yeast and Vacuole-Deficient Mutant Over a Frequency Range of 10 kHz to 10 GHz. *Biophysical Journal* **71**, 2192-2200 (1996).
78. Zhou, X. F., Markx, G. H. & Pethig, R. Effect of biocide concentration on electrorotation spectra of yeast cells. *Biochimica et Biophysica Acta (BBA) - Biomembranes* **1281**, 60-64 (1996).
79. Carstensen, E. L. & Marquis, R. E. Passive Electrical Properties of Microorganisms: III. Conductivity of Isolated Bacterial Cell Walls. *Biophysical Journal* **8**, 536-548 (1968).
80. Labeed, F. H., Coley, H. M. & Hughes, M. P. Differences in the biophysical properties of membrane and cytoplasm of apoptotic cells revealed using dielectrophoresis. *Biochimica et Biophysica Acta (BBA) - General Subjects* **1760**, 922-929 (2006).
81. Wang, X., Becker, F. F. & Gascoyne, P. R. C. Membrane dielectric changes indicate induced apoptosis in HL-60 cells more sensitively than surface phosphatidylserine expression or DNA fragmentation. *Biochimica et Biophysica Acta (BBA) - Biomembranes* **1564**, 412-420 (2002).
82. Labeed, F. H., Coley, H. M., Thomas, H. & Hughes, M. P. Assessment of Multidrug Resistance Reversal Using Dielectrophoresis and Flow Cytometry. *Biophysical Journal* **85**, 2028-2034 (2003).
83. Gascoyne, P. R. C., Wang, X.-B., Huang, Y. & Becker, F. F. Dielectrophoretic separation of cancer cells from blood. *IEEE Transactions on Industry Applications* **33**, 670-8 (1997).
84. Yu, S. P., Canzoniero, L. M. & Choi, D. W. Ion homeostasis and apoptosis. *Current Opinion in Cell Biology* **13**, 405-411 (2001).
85. Alberts, B. et al. *Molecular Biology of the Cell 3rd Edition* (Garland Publishing, New York, 1995).
86. Becker, F. et al. Separation of human breast cancer cells from blood by differential dielectric affinity. *Proc Natl Acad Sci U S A* **92**, 860-864 (1995).
87. Morgan, H., Sun, T., Holmes, D., Gawad, S. & Green, N. G. Single cell dielectric spectroscopy. *Journal of Physics D (Applied Physics)* **40**, 61-70 (2007).
88. Cross, M. & Hohenberg, P. Pattern formation outside of equilibrium. *Review of Modern Physics* **65**, 851-1112 (1993).
89. Swinney, H. *Emergence and evolution of patterns* (eds. Fitch, V., Marlow, D. & Dementi, M.) (Princeton University Press, 1997).
90. Turing, A. The chemical basis of morphogenesis. *Bulletin of Mathematical Biology* **52**, 153-197 (1990).
91. Dill, K. A., Fiebig, K. M. & Chan, H. S. Cooperativity in protein-folding kinetics. *Proc Natl Acad Sci U S A* **90**, 1942-1946 (1993).
92. Kikuchi, R. A Theory of Cooperative Phenomena. *Physical Review Letters* **81**, 988-1003 (1951).
93. Perutz, M. F. Stereochemistry of Cooperative Effects in Haemoglobin: Haem-Haem Interaction and the Problem of Allostery. *Nature* **228**, 726-734 (1970).

94. Kellermayer, M. S. Z., Smith, S. B., Granzier, H. L. & Bustamante, C. Folding-Unfolding Transitions in Single Titin Molecules Characterized with Laser Tweezers. *Science* **276**, 1112-1116 (1997).
95. Pikovsky, A., Rosenblum, M. & Kurths, J. *Synchronization: A Universal Concept in Nonlinear Science* (Cambridge U. P., New York, 2002).
96. Strogatz, S. H. Exploring Complex Networks. *Nature* **410**, 268-276 (2001).
97. Onuchic, J. N., Luthey-Schulten, Z. & Wolynes, P. G. Theory of Protein Folding: The Energy Landscape Perspective. *Annual Review of Physical Chemistry* **48**, 545-600 (1997).
98. Bryngelson, J. D. & Wolynes, P. G. Spin glasses and the statistical mechanics of protein folding. *Proc Natl Acad Sci U S A* **84**, 7524-7528 (1987).
99. Binder, P.-M. Frustration in Complexity. *Science* **320**, 322-323 (2008).
100. Prakash, M. & Gershenfeld, N. Microfluidics Bubble Logic. *Science* **315**, 832-835 (2007).
101. Fuerstman, M. J., Garstecki, P. & Whitesides, G. M. Coding/Decoding and Reversibility of Droplet Trains in Microfluidic Networks. *Science* **315**, 828-832 (2007).
102. Schindler, M. & Ajdari, A. Droplet Traffic in Microfluidic Networks: A Simple Model for Understanding and Designing. *Physical Review Letters* **100**, 044501 [4 pages] (2008).
103. Tornay, R. et al. Dielectrophoresis-based particle exchanger for the manipulation and surface functionalization of particles. *Lab on a Chip* **8**, 267-273 (2008).
104. Morton, K. J. et al. Crossing microfluidic streamlines to lyse, label, and wash cells. *Lab on a Chip* **8**, 1448-1453 (2008).
105. Khusid, B. & Acrivos, A. Effects of interparticle electric interactions on dielectrophoresis in colloidal suspensions. *Physical Review E* **54**, 5428 LP - 5435 (1996).
106. Khusid, B. & Acrivos, A. Effects of conductivity in electric-field-induced aggregation in electrorheological fluids. *Physical Review E* **52**, 1669-1693 (1995).
107. Bennett, D. J. et al. Combined field-induced dielectrophoresis and phase separation for manipulating particles in microfluidics. *Applied Physics Letters* **83**, 4866-4868 (2003).
108. Aubry, N. & Singh, P. Influence of particle-particle interactions and particles' rotational motion in traveling wave dielectrophoresis. *Electrophoresis* **27**, 703-715 (2006).
109. Dufresne, E. R., Squires, T. M., Brenner, M. P. & Grier, D. G. Hydrodynamic Coupling of Two Brownian Spheres to a Planar Surface. *Physical Review Letters* **85**, 3317-3320 (2000).
110. Chiou, P. Y., Ohta, A. T. & Wu, M. C. Massively parallel manipulation of single cells and microparticles using optical images. *Nature* **436**, 370-372 (2005).
111. Vahey, M. & Voldman, J. An Equilibrium Method for Continuous-Flow Cell Sorting Using Dielectrophoresis. *Analytical Chemistry* **80**, 3135-3143 (2008).
112. Ermak, D. L. & McCammon, J. A. Brownian dynamics with hydrodynamic interactions. *J. Chem. Phys.* **69**, 1352 (1978).
113. Brady, J. F. & Bossis, G. Stokesian Dynamics. *Annual Review of Fluid Mechanics* **20**, 111-157 (1988).
114. Blake, J. R. & Chwang, A. T. Fundamental singularities of viscous flow. *Journal of Engineering Mathematics* **8**, 23-29 (1974).
115. Happel, J. & Brenner, H. *Low Reynolds Number Hydrodynamics: With Special Applications to Particulate Media* (Kluwer, Boston, 1983).
116. Bender, C. M. & Orszag, S. A. *Advanced Mathematical Methods for Scientists and Engineers* (Springer, New York, 1999).
117. Bhattacharya, S., Blawdziewicz, J. & Wajnryb, E. Far-field approximation for hydrodynamics interactions in parallel-wall geometry. *Journal of Computational Physics* **212**, 718-738 (2006).
118. Giddings, J. C. A System Based on Split-Flow Lateral-Transport Thin (SPLITT) Separation Cells for Rapid and Continuous Particle Fractionation. *Separation Science and Technology* **20**, 749-768 (1985).
119. Sillescu, H. Heterogeneity at the glass transition: a review. *Journal of Non-Crystalline Solids* **243**, 81-108 (1999).

120. Shintani, H. & Tanaka, H. Frustration on the way to crystallization in glass. *Nature Physics* **2**, 200-206 (2006).
121. Gascoyne, P. R. C., Noshari, J., T. J. Anderson & Becker, F. F. Isolation of rare cells from cell mixtures by dielectrophoresis. *Electrophoresis* **30**, 1388-1398 (2009).
122. Vykoukal, D. M., Gascoyne, P. R. C. & Vykoukal, J. Dielectric characterization of complete mononuclear and polymorphonuclear blood cell subpopulations for label-free discrimination. *Integrative Biology* **1**, 477-484 (2009).
123. Pena-Castillo, L. & Hughes, T. R. Why are there still over 1000 uncharacterized yeast genes? *Genetics* **176**, 7-14 (2007).
124. Jelinsky, S. A. & Samson, L. D. Global response of *Saccharomyces cerevisiae* to an alkylating agent. *Proc Natl Acad Sci U S A* **96**, 1486-1491 (1999).
125. Spellman, P. T. et al. Comprehensive identification of cell cycle-regulated genes of the yeast *Saccharomyces cerevisiae* by microarray hybridization. *Mol. Biol. Cell* **9**, 3273-3297 (1998).
126. Davis, R. J. Signal Transduction by the JNK Group of MAP Kinases. *Cell* **103**, 239-252 (2000).
127. Rual, J.-F. et al. - Towards a proteome-scale map of the human protein-protein interaction network. - **437**, - 1178 (2005).
128. Huh, W.-K. et al. Global analysis of protein localization in budding yeast. *Nature* **425**, 686-691 (2003).
129. Costanzo, M. et al. The Genetic Landscape of a Cell. *Science* **327**, 425-431 (2010).
130. Boder, E. T. & Wittrup, K. D. Yeast surface display for screening combinatorial polypeptide libraries. *Nature Biotechnology* **15**, 553-557 (1997).
131. Sopko, R. et al. Mapping pathways by Systematic Gene Overexpression. *Molecular Cell* **21**, 319-330 (2006).
132. Tong, A. H. Y. et al. Systematic Genetic Analysis with Ordered Arrays of Yeast Deletion Mutants. *Science* **294**, 2364-2368 (2001).
133. Drinnenberg, I. A. et al. RNAi in Budding Yeast. *Science* **326**, 544-550 (2009).
134. Pierce, S. E., Davis, R. W., Nislow, C. & Giaever, G. Genome-wide analysis of barcoded *Saccharomyces cerevisiae* gene-deletion mutants in pooled cultures. *Nature Protocols* **2**, 2958-2974 (2007).
135. Corbacho, I., Oliveroa, I. & Hernandez, L. M. Identification of low-dye-binding (ldb) mutants of *Saccharomyces cerevisiae*. *FEMS Yeast Research* **4**, 437-444 (2006).
136. Castrejon, F., Gomez, A., Sanz, M., Durna, A. & Roncero, C. The RIM101 Pathway Contributes to Yeast Cell Wall Assembly and Its Function Becomes Essential in the Absence of Mitogen-Activated Protein Kinase Slt2p. *Eukaryotic Cell* **5**, 507-517 (2006).
137. Lamb, T. M. & Mitchell, A. P. The Transcription Factor Rim101p Governs Ion Tolerance and Cell Differentiation by Direct Repression of the Regulatory Genes NRG1 and SMP1 in *Saccharomyces cerevisiae*. *Molecular and Cellular Biology* **23**, 677-686 (2003).
138. Herrador, A., Herranz, S., Lara, D. & Vincent, O. Recruitment of the ESCRT Machinery to a Putative Seven-Transmembrane-Domain Receptor Is Mediated by an Arrestin-Related Protein. *Molecular and Cellular Biology* **30**, 897-907 (2010).
139. Ye, P. et al. Gene function prediction from congruent synthetic lethal interactions in yeast. *Molecular Systems Biology* **1**, 2005.0026 (2005).
140. Smith, A. M. et al. Quantitative phenotyping via deep barcode sequencing. *Genome Research* **19**, 1836-1842 (2009).
141. Pamme, N. Magnetism and Microfluidics. *Lab on a Chip* **6**, 24-38 (2006).
142. Adams, J. D., Kim, U. & Soh, H. T. Multitarget magnetic activated cell sorter. *Proc Natl Acad Sci U S A* **105**, 18165-18170 (2008).
143. Dreyfus, R. et al. Microscopic artificial swimmers. *Nature* **437**, 862-865 (2005).
144. Reches, M., Snyder, P. W. & Whitesides, G. M. Folding of electrostatically charged beads-on-a-string as an experimental realization of a theoretical model in polymer science. *Proc Natl Acad Sci U S A* **106**, 17644-17649 (2009).

145. Stephanopoulos, G. Metabolic Fluxes and Metabolic Engineering. *Metabolic Engineering* **1**, 1-11 (1999).
146. Alper, H. & Stephanopoulos, G. Global transcription machinery engineering: A new approach for improving cellular phenotype. *Metabolic Engineering* **9**, 258-267 (2007).
147. Jung, T., Schauer, U., Heusser, C., Neumann, C. & Rieger, C. Detection of intracellular cytokines by flow cytometry. *Journal of Immunological Methods* **159**, 197-207 (1993).
148. Tyo, K. E., Zhou, H. & Stephanopoulos, G. High-Throughput Screen for Poly-3-Hydroxybutyrate in Escherichia coli and Synechocystis sp. Strain PCC6803. *Applied and Environmental Microbiology* **72**, 3412-3417 (2006).
149. Smedsgaard, J. Micro-scale extraction procedure for standardized screening of fungal metabolite production in cultures. *Journal of Chromatography A* **760**, 264-270 (1997).
150. Carlson, R. & Sreenc, F. Effects of recombinant precursor pathway variations on poly[(R)-3-hydroxybutyrate] synthesis in Saccharomyces cerevisiae. *Journal of Biotechnology* **124**, 561-573 (2006).
151. Ross, D. T. et al. Systematic variation in gene expression patterns in human cancer cell lines. *Nature Genetics* **24**, 227-235 (2000).
152. Niwa, H., Miyazaki, J. & Smith, A. G. Quantitative expression of Oct-3/4 defines differentiation, dedifferentiation or self-renewal of ES cells. *Nature Genetics* **24**, 372-376 (2000).
153. Chan, E. M. et al. Live cell imaging distinguishes bona fide human iPS cells from partially reprogrammed cells. *Nature Biotechnology* **27**, 1033-1038 (2009).
154. Chang, H. H., Hemberg, M., Barahona, M., Ingber, D. E. & Huang, S. Transcriptome-wide noise controls lineage choice in mammalian progenitor cells. *Nature* **453**, 544-548 (2008).
155. Kim, L. Y., Vahey, M. D., Lee, H.-Y. & Voldman, J. Microfluidic arrays for logarithmically perfused embryonic stem cell culture. *Lab on a Chip* **6**, 394-406 (2006).